

# **Novel PLIF Techniques for Analysis of G-DI Spray Dynamics**

A Thesis Submitted in partial fulfilment  
of the requirements for the degree of

**Doctor of Philosophy**  
**in**  
**Mechanical Engineering**

By

Mario Alberto Alonso Rincon

School of Engineering  
Cardiff University  
April 2009

UMI Number: U585205

All rights reserved

INFORMATION TO ALL USERS

The quality of this reproduction is dependent upon the quality of the copy submitted.

In the unlikely event that the author did not send a complete manuscript and there are missing pages, these will be noted. Also, if material had to be removed, a note will indicate the deletion.



UMI U585205

Published by ProQuest LLC 2013. Copyright in the Dissertation held by the Author.  
Microform Edition © ProQuest LLC.

All rights reserved. This work is protected against  
unauthorized copying under Title 17, United States Code.



ProQuest LLC  
789 East Eisenhower Parkway  
P.O. Box 1346  
Ann Arbor, MI 48106-1346



---

## **Abstract:**

Gasoline direct injection (G-DI) engines offer several advantages over traditional Port Fuel Injection (PFI) engines with regards to achieving substantial improvement in fuel economy and emissions without deteriorating engine performance. The motivation of this thesis is to contribute to the development of new optical techniques for analysis of 'air-fuel' mixing processes occurring in G-DI engines, particularly spray impact and spray evaporation.

A 3-dimensional laser induced fluorescence technique is developed to quantify the thickness and spatial distribution of transient liquid fuel films formed as a result of spray-wall interaction. Calibrated temporally-resolved benchmark results of a transient spray from a gasoline direct injector impinging on a flat quartz crown are presented, with observations and discussion of the transient development of the fuel film. Experimental results for atmospheric and elevated ambient pressures are presented and discussed, providing an insight on the influence of elevated ambient density in the deposition of fuel films. The technique proved successful at characterising, qualitatively and quantitatively, the development of fuel films, particularly describing the transient effect of the fuel film thickness and shape. The calibrated measurements are consistent with previous qualitative studies of spray impact and demonstrate the applicability of the technique for appraisal of CFD predictions.


For the analysis of spray mass transfer, a Laser Induced Exciplex Fluorescence (LIEF) technique is also developed. LIEF is an optical diagnostic technique that generates spectrally separated fluorescence signals from liquid and vapour phases of a spray, providing temporal and spatial resolution of both species simultaneously. Experiments at three sets of ambient conditions are presented to examine the influence of temperature and pressure variations on airborne liquid/vapour mass ratio. Quantitative analysis of vapour concentrations is discussed along with potential limitations for quantitative results, particularly for dense sprays.

Finally, a simulation on a commercially available CFD code is presented to explore the potential of TIR-LIF for validation of spray impingement models. CFD results are compared with TIR-LIF experimental data, showing good comparison of quantitative trends and fuel film characteristics. However, areas for further development are identified and discussed.

---

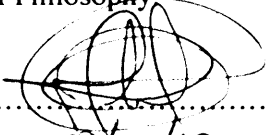
**Declaration:**

This work has not previously been accepted in substance for any degree and is not concurrently submitted in candidature for any degree.

Signed..........(Mario Alonso)  
Date.....29/05/09.....


**STATEMENT 1**

This thesis is being submitted in partial fulfilment of the requirements for the degree of Doctor of Philosophy

Signed..........(Mario Alonso)  
Date.....29/05/09.....


**STATEMENT 2**

This thesis is the result of my own independent work/investigation, except where otherwise stated. Other sources are acknowledged by explicit references.

Signed..........(Mario Alonso)  
Date.....29/05/09.....

**STATEMENT 3**

I hereby give consent for my thesis, if accepted, to be available for photocopying and for inter-library loan, and for the title and summary to be made available to other organisations.

Signed..........(Mario Alonso)  
Date.....29/05/09.....

---

## **Acknowledges:**

I would like to use this space to thank the many people who made this thesis possible.

It is difficult to overstate my gratitude to my supervisor: Prof. Phil Bowen. He provided enthusiasm, inspiration, and guidance throughout the course of my PhD, and I am forever grateful for his patience and support.

I would like to offer special thanks to my friend: Dr. Peter J. Kay. His encouragement and sound advice throughout my studies is greatly appreciated.

I would also like to thank Robert Gilchrist for his guidance and I am forever grateful to Ricardo UK and EPSRC for their financial support.

I wish to thank the many people from the Mechanical Engineering Workshop who provided help and technical support during my experiments. Special thanks to Paul Malpas, Alan Griffiths, Malcolm Seaborne, and Steve Mead.

Lastly, and most importantly, I would also like to express my gratitude to my parents Ida and Mario, my brother Carlos, and my partner Veronica, for helping me get through the difficult times, and for all the emotional support and caring they provided over the years.

---

## **List of Contents:**

### **Chapter 1: Introduction**

1.1. Motivation for the Study	2
1.2. Environmental Challenges	2
1.3. Future of Internal Combustion Engines	5
1.3.1. Key Potential Advantages of Gasoline Direct Injection	8
1.4. Thesis Aims and Objectives	11

### **Chapter 2: Gasoline Direct Injection Review**

2.1. G-DI Combustion System Concepts	13
2.2. Fuel Injector Requirements	15
2.3. Injector Selection	17
2.4. Atomisation and Spray Break-up Principles	20
2.4.1. Primary and Secondary Break-up	23
2.4.2. Droplet Interactions	27
2.4.3. Droplet Vaporisation	29
2.4.4. Spray / Wall Interaction	30
2.5. Chapter Summary	33

### **Chapter 3: Two New LIF Techniques For In-cylinder Diagnostics Under Simulated Engine Conditions**

3.1. Development of a New Rig for Fuel Film Characterisation	35
3.1.1. Previous Work	36
3.1.2. New Optical Configuration	40
3.1.3. Principles of Laser Induced Fluorescence (LIF)	41
3.1.3.1. Tracer Selection	42
3.1.3.2. Quantitative LIF for Fuel Films	44
3.1.3.3. Potential Limitations of LIF for fuel films	46
3.1.4. Total Internal Reflection Method (TIR-LIF)	49
3.1.5. TIR-LIF Calibration	51
3.1.6. TIR-LIF Post-Processing Methodology	52

---

3.2. Development of ‘TIR-LIF’ Rig for Fuel Film Quantification in a High Pressure Environment	54
3.2.1. The High Pressure High Temperature (HP-HT) Rig	55
3.2.2. Modification of TIR-LIF Rig for use within the HP-HT rig	56
3.3. Development of Optical Rig for Characterisation of Vapour Fractions	58
3.3.1. Principles of Laser Induced Exciplex Fluorescence (LIEF)	60
3.3.1.1. Tracer Selection	61
3.3.1.2. Potential Limitations of LIEF for quantitative results	63
3.3.2. Rig Development	64
3.3.3. LIEF Calibration	66
3.3.4. LIEF Post-Processing Methodology	70
3.4. Programme of Work	72
3.5. Chapter Summary	73

#### **Chapter 4: Analysis of Transient Liquid Fuel Films of an Impinging Gasoline Direct Injection Spray on a solid Surface**

4.1. Analysis of Fuel Films of an Impinging Spray at Atmospheric Pressure (0.1 MPa) – Case A	75
4.1.1. Total Mass Deposits	79
4.1.2. Average Fuel Film Thickness	80
4.1.3. Footprint Size	81
4.1.4. Fuel Film Penetration	82
4.1.5. Fuel Film for Multiple Injections	83
4.1.6. Analysis of Fuel Impingement for Case A - Summary	87
4.2. Analysis of Fuel Films of an Impinging Spray at Elevated Ambient Pressure (0.4 MPa) – Case B	87
4.2.1. Total Mass Deposits	90
4.2.2. Average Fuel Film Thickness	91
4.2.3. Footprint Size	92
4.2.4. Fuel Film Penetration	93
4.2.5. Analysis of Fuel Impingement for Case B - Summary	94
4.3. Chapter Summary	94

---

## **Chapter 5: Analysis of Vapour Fractions of a Gasoline Direct Injection Spray at Elevated Ambient Conditions**

5.1. Analysis of an Unconfined Spray at Ambient Pressure 0.14 MPA and Ambient Temperature 423 K – Case 1	99
5.1.1. Spray Penetration	100
5.1.2. Relative Area of Liquid and Vapour Regions	101
5.1.3. Vapour Fractions Quantification	103
5.1.4. Analysis of Case 1 – Summary	105
5.2. Analysis of an Unconfined Spray at Ambient Pressure 0.58 MPA and Ambient Temperature 423 K – Case 2	105
5.2.1. Spray Penetration	105
5.2.2. Relative Area of Liquid and Vapour Regions	107
5.2.3. Vapour Fractions Quantification	108
5.2.4. Analysis of Case 2 – Summary	110
5.3. Analysis of an Unconfined Spray at Ambient Pressure 0.1 MPA and Ambient Temperature 373 K – Case 3	110
5.3.1. Spray Penetration	111
5.3.2. Relative Area of Liquid and Vapour Regions	112
5.3.3. Vapour Fractions Quantification	113
5.3.4. Analysis of Case 3 – Summary	115
5.4. Discussion and Limitations	115
5.5. Chapter Summary	116

## **Chapter 6: CFD modelling of a Gasoline Spray and Spray Impingement**

6.1. Computational Fluid Dynamics	118
6.2. Governing Equations	119
6.3. Spray Impact Modelling	121
6.4. Spray Model Development	125
6.4.1. Mesh Development	125
6.4.2. Spray Model	126
6.5. Preliminary Results of a Simulated Impinging Spray	130
6.6. Chapter Summary	136

---

**Chapter 7: Conclusions and Future Work**

7.1. Conclusions	138
7.2. Recommendations and Future Work	140

<b>List of publications by the Author</b>	<b>141</b>
---	------------

<b>References</b>	<b>142</b>
-------------------	------------

**Appendices**

<b>Appendix A: Transient Fuel Film Measurements for Case A</b>	<b>152</b>
<b>Appendix B: Transient Fuel Film Measurements for Case B</b>	<b>163</b>
<b>Appendix C: Transient Vapour Concentration Measurements for Case 1</b>	<b>174</b>
<b>Appendix D: Transient Vapour Concentration Measurements for Case 2</b>	<b>182</b>
<b>Appendix E: Transient Vapour Concentration Measurements for Case 3</b>	<b>190</b>

---

## **List of Figures:**

---

<b>Figure</b>		<b>page</b>
Figure 1-1:	EU emission Standards – SI passenger Cars (Eichseder et al 2003)	4
Figure 1-2:	CO <sub>2</sub> – Emissions EU fleet average (Eichseder et al 2003)	5
Figure 1-3:	Automobile fuel consumption relative to the 2001 reference vehicle for the evolving baseline vehicle, the gasoline-fueled, hybrid ICE vehicle, and the hydrogen-fueled, hydrogen fuel cell vehicle (Shäfer et al 2006)	7
Figure 1-4:	Schematic of a gasoline direct injection engine running at (a) stratified charge, and (b) homogeneous Charge (SAE)	9
Figure 2-1:	Classification of G-DI combustion systems: (a) spray-guided system, (b) wall-guided system, and (c) air-guided systems	13
Figure 2-2:	Concept evaluation of three typical G-DI injector designs (Zhao et al 1999)	16
Figure 2-3:	Schematic of the internal geometry of a swirl fuel injector: (a) section along centreline, b) plan view of the swirl device (Morris 2003)	18
Figure 2-4:	Development of a hollow-cone pressure-swirl G-DI spray for selected times after start of injection	19
Figure 2-5:	Schematic of spray structure and spatial distribution	21
Figure 2-6:	Schematic of spray atomisation, transport and wall impact (Tropea and Roisman 2006)	23
Figure 2-7:	Schematic of aerodynamic Break-up mechanisms (Khavkin 2004)	25
Figure 2-8:	Drop deformation and secondary breakup regime map for shock wave disturbances (Khavkin 2004)	26
Figure 2-9:	Schematic of possible outcomes after droplet to droplet collisions	28
Figure 2-10:	Schematic of post-impingement regimes	32
Figure 3-1:	Schematic of the Optical Setup Proposed by Kay et al (2006b)	37
Figure 3-2:	Fluorescent images for impingement studies reported by Kay (2006b): (a) Footprint image of fuel film, (b) Side View of the Spray above the quartz piston.	37
Figure 3-3:	Schematic of the principle of total internal reflection	38
Figure 3-4:	Comparison of the illumination of the interrogation zone with and without the UV diffuser.	39
Figure 3-5:	Schematic of the TIR-LIF optical configuration	40
Figure 3-6:	Principle of Laser Induced Fluorescence	42

---



---

Figure 3-7:	Variation of normalised LIF intensity illustrating the (a) Temperature and (b) Pressure effects for several dopants and excitation wavelengths (Fujikawa et al 1999)	43
Figure 3-8:	Fluorescence spectra of 3-pentanone excited at 266nm	44
Figure 3-9:	Schematic of elemental volume illustrating fluorescence	45
Figure 3-10:	Normalised transmittance in the quartz-fuel interface as a function of the incident angle	50
Figure 3-11:	Typical Calibration images from a 10 and 40 mm <sup>3</sup> 3-pentanone fuel films deposited on the measurement plane using a microsyringe	51
Figure 3-12:	Calibration curve obtained recording intensity values for different fuel films of the 3-pentanone and isooctane mixture	52
Figure 3-13:	Image Processing sequence (TIR-LIF image for time = 1.75 ms ASOI and Patm = 0.1 MPa)	53
Figure 3-14:	Schematic of the HP-HT rig: (a) PDA System, (b) Planar Imaging Techniques (e.g. PIV, LIF, etc)	56
Figure 3-15:	Experimental setup for impingement experiments at elevated ambient pressures	57
Figure 3-16:	Schematic showing the system synchronisation: (a) CCD camera trigger, (b) Signal to the injector, (c) Laser Q-switch, (d) Image intensifier trigger	58
Figure 3-17:	Photophysics of the TMPD/Np exciplex system proposed by Melton (a), and Fluorescence Spectra for liquid and vapour phases (b) (Fujimoto et al 2002)	60
Figure 3-18:	Normalised fluorescence spectra of 2% TEA, and 2.9% benzene in isooctane. Note that the fluorescence of the vapour and liquid phases are not in the same scale	62
Figure 3-19:	Schematic of the LIEF optical set-up	64
Figure 3-20:	Limitation of the optical setup: a) Schematic of the optical setup, b) Schematic of pre-processed image showing the obscuration zone	65
Figure 3-21:	Relative fluorescence intensities of the liquid and vapour signals	67
Figure 3-22:	Temperature and Pressure dependence of the vapour fluorescence intensity. a) Temperature dependency (obtained at 0.1 MPa) b) Pressure dependency (obtained at 373 K)	68
Figure 3-23:	Variation of fluorescent intensity with vapour concentration	69
Figure 3-24:	First stage of LIEF images post-processing methodology	70
Figure 3-25:	Second step of the LIEF Image post-processing methodology	71
Figure 4-1:	Schematic of the experimental configuration (Top: Side View, Bottom: Typical footprint image)	76

---

---

Figure 4-2:	Transient fuel film images for different times: (a) 1.00 ms ASOI, (b) 1.25 ms ASOI (left: side view, right: Average footprint image with background subtracted)	77
Figure 4-3:	Transient fuel thickness measurements for different times after start of injection (ASOI): (a) 1.50 ms, (b) 1.75 ms, (c) 2.00 ms, (d) 2.25 ms; (e) 2.50 ms	78
Figure 4-4:	Cumulative total mass deposits for Case A	80
Figure 4-5:	Average and maximum thickness of the fuel film for Case A	81
Figure 4-6:	Fuel film footprint area at atmospheric pressure (Case A)	81
Figure 4-7:	Maximum and minimum horizontal penetration for case A	82
Figure 4-8:	Transient fuel thickness measurements for multiple injections for selected times ASOI: (a) 1.00 ms, (b) 1.25 ms, (c) 1.50 ms, (d) 1.75 ms; (e) 2.00 ms, (f) 2.25 ms	84
Figure 4-9:	Average (a) and Maximum (b) Thickness for multiple injections	85
Figure 4-10:	Comparison between transient fuel thickness measurements under 0.1 and 0.4 MPa ambient pressures for selected times after start of injection	88
Figure 4-11:	Comparison of cumulative total mass deposits at 0.1 and 0.4 MPa ambient pressures	90
Figure 4-12:	Comparison between average and maximum thickness of the fuel film at 0.1 and 0.4 MPa ambient pressures	92
Figure 4-13:	Comparison between footprint area of the fuel film at 0.1 and 0.4 MPa ambient pressures	92
Figure 4-14:	Comparison between maximum and minimum horizontal penetration of the film for $P_a = 0.1$ and 0.4 MPa	93
Figure 5-1:	Development of the gasoline DI pressure swirl spray under three different ambient conditions	97
Figure 5-2:	Randomly selected vapour images from instantaneous measurements at 2.25 ms ASOI for case 1	99
Figure 5-3:	Absolute (a) and relative (b) penetration of liquid and vapour phases for case 1	100
Figure 5-4:	Spatial distribution of liquid and vapour regions (Randomly selected images from instantaneous measurements at 1.50 ms ASOI)	102
Figure 5-5:	Relative area of liquid and vapour regions for case 1	102
Figure 5-6:	Vapour concentration measurements for selected timebins of case 1 (all images are randomly selected from instantaneous measurements)	104
Figure 5-7:	Comparison between spray penetration of liquid and vapour phases for cases 1 and 2	106

---

---

Figure 5-8:	Relative area of liquid and vapour regions for case 2	107
Figure 5-9:	Comparison of vapour concentration measurements for selected timebins of Cases 1 and 2 (all images are randomly selected from instantaneous measurements)	109
Figure 5-10:	Comparison between spray penetration of liquid and vapour phases for cases 1 and 3	111
Figure 5-11:	Relative area of liquid and vapour regions for case 3	113
Figure 5-12:	Comparison of vapour concentration measurements for selected timebins of Cases 1 and 3 (all images are randomly selected from instantaneous measurements)	114
Figure 6-1:	Schematic of the computational mesh used for an impingement spray	125
Figure 6-2:	Variation of mass injection rate with time for the Bosch C2 pressure swirl injector (Kay 2006)	126
Figure 6-3:	Velocity profile input for sac-spray (Kay 2006)	128
Figure 6-4:	Qualitative comparison of the spray side view at 1.00 ms ASOI: (a) Planar laser image, (b) CFD simulation	130
Figure 6-5:	Comparison between (i) TIR-LIF measurements at atmospheric pressure and (ii) CFD predictions using Ricardo VECTIS, for different times after start of injection (ASOI): (a) 1.25 ms, (b) 1.50 ms, (c) 1.75 ms, (d) 2.00 ms, (e) 2.25 ms, (f) 2.50 ms, (g) 3.00ms	132
Figure 6-6:	Comparison of cumulative mass deposits for experiments at atmospheric pressure and CFD simulation	133
Figure 6-7:	Comparison of fuel film thickness	137
Figure 6-8:	Comparison fuel film footprint area for TIR-LIF experiments at atmospheric pressure and corresponding CFD simulation	135

---

## **List of Tables:**

---

<b>Table</b>		<b>page</b>
Table 1-1:	Summary of ways to improve energy consumption on Internal Combustion Engines (Taylor 2008)	6
Table 3-1:	Summary of experimental conditions	72
Table 6-1:	Summary of the comprehensive sub-model used by Ricardo VECTIS	122
Table 6-2:	Summary of the initial conditions and corresponding times for all the different phases of the spray model	127
Table A-A	Summary of experimental conditions for Case A	152
Table A-B	Summary of experimental conditions for Case B	163
Table A-C	Summary of experimental conditions for Case 1	174
Table A-D	Summary of experimental conditions for Case 2	182
Table A-E	Summary of experimental conditions for Case 3	190

---

## Nomenclature:

### Roman Symbols

Symbol	Definition	Units
$A$	Area	$m^2$
$C$	Molar concentration	$mol.kg^{-1}$
$C_d$	Drop drag coefficient	-
$D_n$	Nozzle diameter	m
$D$	Droplet diameter	m
$E$	Energy	J
$h_{fg}$	Latent heat of evaporation	$kJ.kg^{-1}$
$I$	Intensity	-
$I_f$	Fluorescent intensity	-
$I_t$	Transmitted intensity	-
$K$	Evaporation constant	-
$K_m$	Thermal conductivity	$W.m^{-1}.K^{-1}$
$La$	Laplace number	-
$m$	Mass	kg
$Nu$	Nusselt number	-
$M_R$	Instantaneous fuel injection rate	$mg.ms^{-1}$
$n$	Refractive index	-
$Oh$	Ohnesorge number	-
$P$	Pressure	Pa
$Re$	Reynolds number	-
$S$	Spray tip penetration	mm
$t$	Fuel film thickness	m
$t$	Time	ms
$T$	Transmittance	-
$T$	Temperature	K
$t_{bin}$	Timebin duration	ms
$u$	Velocity	$m.s^{-1}$
$V$	Volume	$m^3$
$We$	Webber number	-

---

## Greek Symbols

Symbol	Definition	Units
$\lambda$	Wavelength	nm
$\Delta t$	Time differential	s
$\phi$	Incident Angle	[radians]
$\theta$	Spray Cone angle	[radians]
$\varepsilon$	Molar absorption coefficient	$\text{m}^2 \cdot \text{mol}^{-1}$
$\rho$	Density	$\text{kg} \cdot \text{m}^{-3}$
$\sigma$	Surface tension	$\text{kg} \cdot \text{s}^{-2}$
$\mu$	Dynamic Viscosity	$\text{kg} \cdot \text{m}^{-1} \cdot \text{s}^{-1}$

## Subscripts

Symbol	Definition
<i>a</i>	Air
<i>amb</i>	Ambient
<i>c</i>	Critical
$\rho$	Density
<i>d</i>	Droplet
<i>e</i>	Excitation
<i>g</i>	Gas
<i>i</i>	Initial
<i>l</i>	Liquid
<i>n</i>	Nozzle
<i>o</i>	Original
<i>pixel</i>	Pixel
<i>Q</i>	Quantum efficiency
<i>rel</i>	Relative
<i>t</i>	Time
<i>t</i>	Transmitted

---

## List of Acronyms

---

<b>Abbreviation</b>	<b>Definition</b>
AFR	Air-to-Fuel Ratio
ASOI	After Start of Injection
CARS	Coherent Anti-Stokes Raman Spectroscopy
CCS	Carbon Capture and Storage
CFD	Computational Fluid Dynamics
CI	Compression Ignition
CO	Carbon Monoxide
COV	Coefficient of variance
CO <sub>2</sub>	Carbon Dioxide
DEMA	Diethyl-methyl-amine
DI	Direct Injection
DISI	Direct Injection Spark Ignition
DICI	Direct Injection Compression Ignition
ECU	Engine Control Unit
EOI	End of Injection
EPM	Energy Pulse Monitor
FB	fluorobenzene
FC	Fuel cell
FWHM	Full Width Half Maximum
G-DI	Gasoline-Direct Injection
GHG	Greenhouse Gas
HC	Hydrocarbons
HP-HT	High Pressure- High Temperature
ICE	Internal Combustion Engine
LDA	Laser Doppler Anemometry
LIF	Laser Induced Fluorescence
LIEF	Laser Induced Exciplex Fluorescence
MPI	Multi Point Injection
NO <sub>x</sub>	Oxides of Nitrogen
PDA	Phase Doppler Anemometry
PFI	Port Fuel Injection

---

PISI	Port Injection Spark Ignition
PIV	Particle Image Velocimetry
PLIF	Planar Laser Induced Fluorescence
PM	Particulate Matter
REFV	Reference Vehicle
SI	Spark Ignition
SOI	Start of Injection
tb	timebin
TEA	triethylamine
TIR-LIF	Total Internal Reflection Laser Induced Fluorescence
TMPD	tetramethyl-p-phenylenediamine
UBHC	Un-burnt Hydrocarbons
UV	Ultraviolet



# **Chapter 1:**

## **Introduction**

This chapter describes the motivation for this study, along with environmental challenges for automotive technology and key potential advantages of gasoline direct injection. The chapter also includes the aim and objectives of the study.

### **1.1. Motivation for the Study**

There is now a general consensus among world leading scientists that human-generated carbon emissions are responsible for global warming, influencing the earth's climate (Stern 2008). Human-generated carbon emissions are produced mainly through the combustion of fossil fuels for electricity, heat, transportation and industrial processes. Thanks to the involvement of political leaders (e.g. Kyoto Summit 1997, and soon the Copenhagen Climate Summit 2009), strict targets are being imposed worldwide to reduce carbon emissions, particularly carbon dioxide (CO<sub>2</sub>). For the automotive sector, the legislative targets imposed on engine manufacturers by the regulatory bodies of Europe, Japan, and USA require significant reduction of exhaust emissions and fuel consumption in the forthcoming years. In addition to carbon dioxide reductions, automotive targets require reductions, of carbon monoxide (CO), un-burnt hydrocarbons (HC), oxides of nitrogen (NO<sub>x</sub>) and particulate matter (PM), which are considered harmful to human health. Compliance to these strict targets has lead to an increase in investment on research for more efficient technologies to reduce emissions, and fuel consumption. As a result, the motivation for this study is to contribute to the development of new technologies for analysis of 'air-fuel' mixing processes, such as spray evaporation and spray impact, with particular relevance to automotive gasoline direct injection applications.

### **1.2. Environmental challenges**

Over a decade ago, most countries joined an international treaty - the United Nations Framework Convention on Climate Change (UNFCCC) - to begin to consider what could be done to reduce global warming and to cope with whatever temperature increases are inevitable. Even though the amount of CO<sub>2</sub> emissions caused by man is relatively small as compared to the whole CO<sub>2</sub> emission, this part is classified as climatically relevant. In fact, it has been claimed that this portion of carbon dioxide is responsible for 60 % of the enhanced greenhouse effect (UNFCCC 2009). Acknowledging strong evidence that human generated activity has caused an increased

rate of global warming in the last century, a number of nations approved an addition to the UNFCCC treaty: the Kyoto Protocol, which has more powerful (and legally binding) measures to limit or reduce greenhouse gas (GHG) emissions responsible for global warming. Countries with commitments to limit or reduce GHG emissions under the Kyoto Protocol must meet their targets primarily through national measures. The Kyoto Protocol is generally seen as an important first step towards a truly global emission reduction regime that will stabilize GHG emissions, and provides the essential structure for any future international agreement on climate change. By the end of the first commitment period of the Kyoto Protocol in 2012, a new international framework needs to be negotiated and ratified to deliver further stringent emission reductions. In 2009, there is an opportunity to discuss such framework at the “Copenhagen Climate Summit”, where representatives of more than 170 countries will meet to discuss future global emission targets.

Measures to slow the rate of global warming are heavily dependent on coordinated action by all nations. Among the key instruments that could be applied for mitigation of climate change are:

- *Reducing future emissions:* burning fossil fuels more efficiently, switching to renewable forms of energy such as solar, nuclear, and wind power, and developing new cleaner technologies for industry and transport.
- *Carbon Capture:* avoiding deforestation (the current trend) by planting trees to remove carbon dioxide from the atmosphere, and also developing technologies to capture carbon already in atmosphere. Furthermore, implementing carbon capture and storage technologies (CCS) to contain future emissions of traditional fossil fuel powerplants (e.g. April 2009, UK government announced that four new major coal-fired power stations are to be built with potential for carbon capture (DEEC 2009).
- *Changing lifestyles and rules:* implementing policies and regulations to change the culture and habits of the people, particularly influencing a more efficient use of energy.

Reducing future emissions is arguably the most sustainable route for mitigation of climate change, and therefore the most sustainable way to comply with future emission targets. As a result, there is an international trend to increase investment on research

for development of cleaner and more efficient technologies to reduce emission and fuel consumption.

In addition to global targets for reductions of future carbon dioxide emissions for mitigation of global warming, legislation often involves reductions of other combustion emissions such as carbon monoxide, un-burnt hydrocarbons, oxides of nitrogen and particulate matter, which are considered harmful to human health. For the automotive sector, most of the progress achieved on emission reductions has been obtained by legislative targets imposed on engine manufacturers by the regulatory bodies of Europe, Japan, and USA. In the last 30 years, legal regulations have demanded, and also gained, considerable emission reductions (see Fig. 1-1). In Europe for example, from the year 2005 onwards, passenger cars with spark ignited engines have to fulfil EU-4 limits with HC and NO<sub>x</sub> emissions being only 3% of the values of 1970 (Eichseder et al 2003).

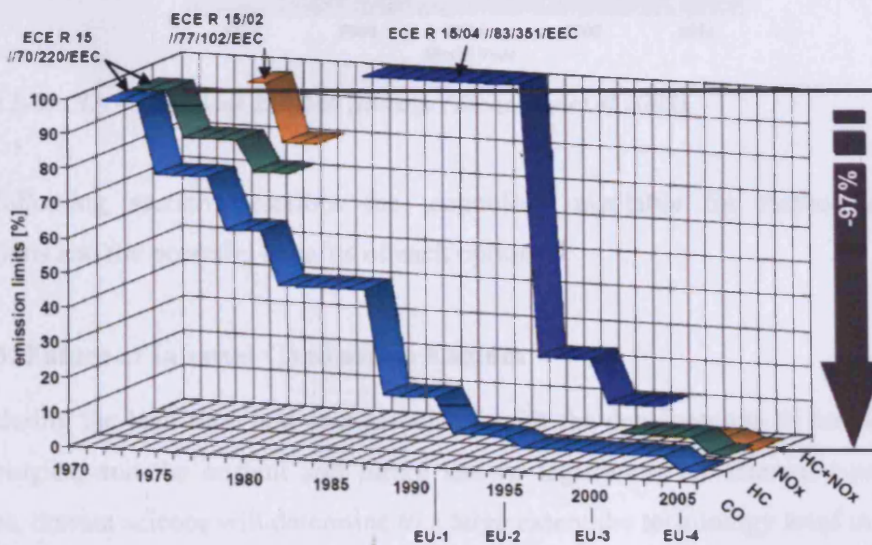


Figure 1-1: EU emission Standards – SI passenger Cars (Eichseder et al 2003)

Even so, cars still account for around 20 % of total European emissions of carbon dioxide (CO<sub>2</sub>), and 23 % in the UK. Therefore, future targets are considered to further reduce engine emissions. A voluntary agreement between the European Union and the ACEA (European Automobile Manufacturers Association), proposed the reduction of 25% of CO<sub>2</sub> emissions of new vehicles till 2008 compared to 1995 (EU-ACEA 1999). Japanese and Korean car producers, represented by JAMA and KAMA, made a similar

commitment for 2009. Furthermore, in 1995, EU heads of state and government set themselves the ambitious goal of reducing emissions of CO<sub>2</sub> from new cars to 120 grams per kilometre (g/km) by 2012 as a measure to combat climate change. This corresponds to fuel consumption of 4.5 litres per 100 km for diesel cars and 5 litres/100 km for petrol cars. Figure 1-2 shows EU commitments for CO<sub>2</sub> emission reductions.

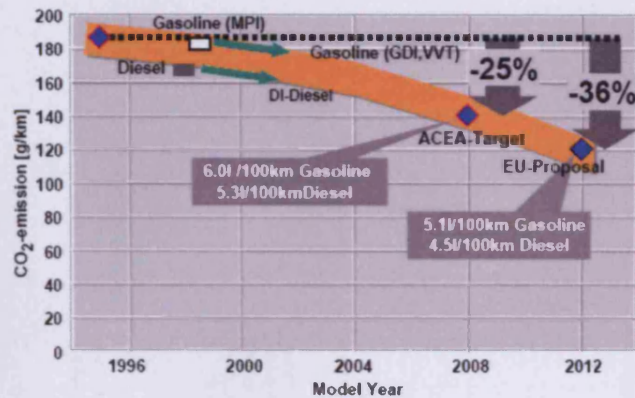


Figure 1-2: CO<sub>2</sub> – Emissions EU fleet average (Eichseder et al 2003)

The following section describes the technology available for further emission reductions and the potential benefits of each option.

### 1.3. Future of Internal Combustion Engines

Considering the lead time and cost associated with the development of future engine technologies, and the current and future known legislation for internal combustion engines, current science will determine to a large extent the technology level in internal combustion engines (ICE) for about the next decade (Taylor 2008). Therefore, an evolved baseline can be drawn considering the evolutionary development of a reference car (Weiss et al 2000). The evolved baseline allows comparison of future (more advanced) technologies with currently available technology. Within Europe, the evolved baseline is made up traditional engine technologies such as:

- Port Injection Spark Ignition Engine (PISI)
- Direct Injection Spark Ignition Engine (DISI)
- Direct Injection Compression Ignition Engine (DICI)



Table 1-1: Summary of ways to improve energy consumption on Internal Combustion Engines (Taylor 2008)

Type	Indicated efficiency	Mechanical efficiency	Volumetric efficiency	Combustion efficiency	Density of incoming charge	Fuel:air ratio	Emissions	Other remarks
Hybrid ICE		Increased electrification of auxiliaries						Improvement in storage of energy and braking power (including by flywheel, by ultra capacitors, by batteries)
PISI	Stratified charge (due to lean-burn effect); <sup>a</sup> variable compression ratio (latter up to 25% gain)	Material and lubrication improvement	20% throttle-minimised engine by: variable displacement, multistroke, downsizing+supercharging, load control by variable valve train	Variable valve train to control residual gases	Variable turbine geometry and improved compressor technology	Direct injection <sup>b</sup>	Additional NO <sub>x</sub> after treatment may be required, NO <sub>x</sub> purging and sulphur regeneration; 2–4% of fuel consumption	Combustion systems tailored to H <sub>2</sub> and natural gas
DISI	Direct injection (lean-burn effect on ratio of specific heat; higher knock resistance); minimised heat loss	Reduction due to high pressure pump	Unthrottled engine; mixture cooling	Deterioration of combustion at high loads/speeds, denying fuel economy, unless homogeneous charge is used			Additional NO <sub>x</sub> after treatment may be required, NO <sub>x</sub> purging and sulphur regeneration; 2–4% of fuel consumption	
CAI/HCCI	Higher compression ratio relative to PISI but lower than DISI			Variable valve train to control residual gases, through negative valve overlap			No need for expensive or heated catalysts? Limited to light loads?	HC and CO emissions, control of transients, ignition timing, idling, low energy exhaust prohibits turbo-charging, part-load application
Light-duty CI	Reduce effective compression ratio by 'early intake valve closing'						DPF and NO <sub>x</sub> control may be avoided by use of advanced fuel injection systems (e.g. split injection systems) non-thermal plasmas for NO <sub>x</sub>	
Heavy-duty CI	Low compression ratio for emission improvement	Lower friction; decoupling auxiliaries from the crank train by using auxiliary power units	Downsizing	Increase combustion efficiency by altering effective compression ratio using variable valve train; improved fuel injection systems			Favour inc. NO <sub>x</sub> , low part (size and number), low fuel consumption, NO <sub>x</sub> adsorber requires injection of fuel; DPF ≈ 3% fuel penalty; bio-fuels have low sulphur; combination of NO <sub>x</sub> and particle trap, H <sub>2</sub> S, N <sub>2</sub> O, NH <sub>3</sub> , aldehydes	Transmission (automate manual transmission, CVT, dual clutch; engine management systems and sensors (cylinder pressure, ion sensing, position sensors) and actuators

<sup>a</sup> The stratified charge using a PISI would be obtained in the manner used by Honda (VTEC) or Toyota (VVT)  
<sup>b</sup> Direct injection enables the use of Gasoline Direct Injection (G-DI) technology, which ultimately leads to improve energy consumption

Even though each of these technologies is expected to evolve over the next decade, they all have different potential for evolution. Table 1-1 provides a detailed summary of ways to improve energy consumption on Internal Combustion Engines, identifying areas of potential development for available internal combustion engine technologies (Taylor 2008).

Recently, Schäfer et al (2006) published a 25 year assessment on life cycle and fleet impact of future fuel cell (FC) and internal combustion engines. He compared the potential evolution of H<sub>2</sub> and gasoline hybrid FCs with the evolved baseline relative to a 2001 reference vehicle (REFV). Figure 1-3 shows the projected 'on-the-road' combined cycle fuel consumption for those technologies relative to the 2001 REFV.

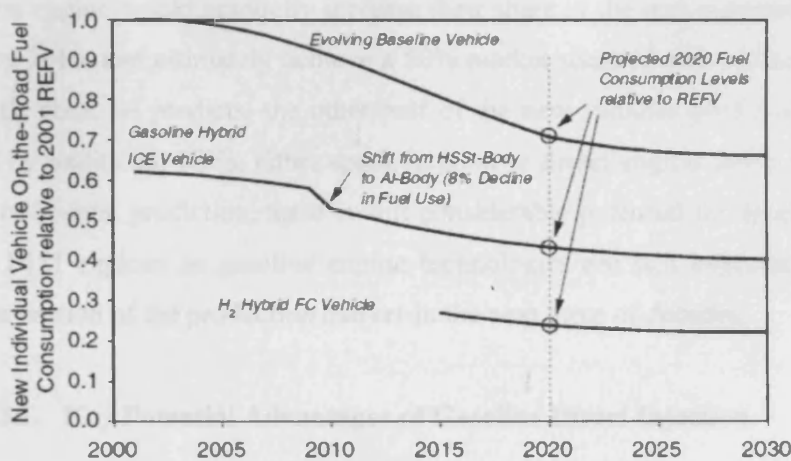


**Figure 1-3:** Automobile fuel consumption relative to the 2001 reference vehicle for the evolving baseline vehicle, the gasoline-fueled, hybrid ICE vehicle, and the hydrogen-fueled, hydrogen fuel cell vehicle (Schäfer et al 2006)

The projection for the evolving baseline vehicle shows an encouraging 30 % reduction in specific fuel consumption for 2020 relative to the 2001 reference vehicle. However, hybrid technologies show considerable more potential for reducing fuel consumption as the projected figures for the gasoline hybrid ICE vehicle and the H<sub>2</sub> hybrid FC vehicle are 45 % and 25 % respectively. Based on this prediction, it is obvious that significant reduction in overall carbon emissions would be significantly easier to achieve using hybrid vehicles. However, the inferior overall performance of hybrid vehicles (compared to traditional ICES) and their significantly higher cost influences negatively on their competitiveness within the automobile market. Therefore, until their cost-competitiveness increases, it is still to be seen if this technology will

ultimately penetrate beyond niche market levels. Once hybrid vehicles become cost competitive, the penetration across new vehicle production will depend upon the willingness of the industry to take risks by increasing production of new hybrid vehicles and the capital available (and required) to expand production volumes of this technology. Additionally, there is generally reluctance by consumers to choose to new engine technologies until they are considerably well developed, for which the market penetration usually takes a few years. For instance, the penetration of high-speed direct-injection diesel engine technology within the European Union has taken some 20 years to capture about 50% of new vehicle market share. ICE hybrid production penetration rates are likely to be slower, since much of the technology is new to the light-duty vehicle market (Shäfer et al 2006). Schäfer estimates that the hybrid internal combustion engine would gradually increase their share in the new automobile market to 2.1% by 2010, and ultimately achieve a 50% market share of new automobiles sold in 2030. By then, he predicts, the other half of the new vehicles produced would be propelled by traditional ICEs, either spark-ignition or diesel engine. Even considering this very optimistic prediction, there is still considerable potential for development of PISI and DISI engines as gasoline engine technologies are still expected to have a significant portion of the production market in the next three of decades.

### **1.3.1. Key Potential Advantages of Gasoline Direct Injection**

Gasoline direct injection (G-DI) engines offer several advantages over traditional Port Fuel Injection (PFI) systems with regards to achieving substantial improvement in fuel economy without deteriorating engine performance. The main difference between the two systems is in the mixture preparation strategy. The G-DI engines are engineered to inject the gasoline directly into the cylinder, in a manner similar to diesel direct injection engines, targeting the injected fuel towards the spark plug. In the PFI engine, fuel is injected into the intake port of each cylinder, and there is an associated time lag between the injection event and the induction of the fuel and air into the cylinder. The main advantage G-DI is that it can operate in two modes:

- i)* Stratified-charge mode, and
- ii)* Homogeneous-charge mode.

Figure 1-4 shows the schematic of a gasoline direct injection engine working at stratified (figure 1-4a) and homogenous (figure 1-4b) modes. When running at



homogeneous mode, the engine operates on the same principle as a regular four-stroke PFI engine, creating a near stoichiometric homogeneous mixture within the cylinder prior to ignition. This is achieved by injecting very early in the compression stroke to allow sufficient time for evaporation and mixing. This strategy is used for high loads. Alternatively, when running at stratified-charge mode only a small fraction of fuel is injected late in the compression stroke creating a rich stratified mixture near the spark plug. This strategy is used for light loads and idle engine conditions allowing significant improvements in fuel economy.

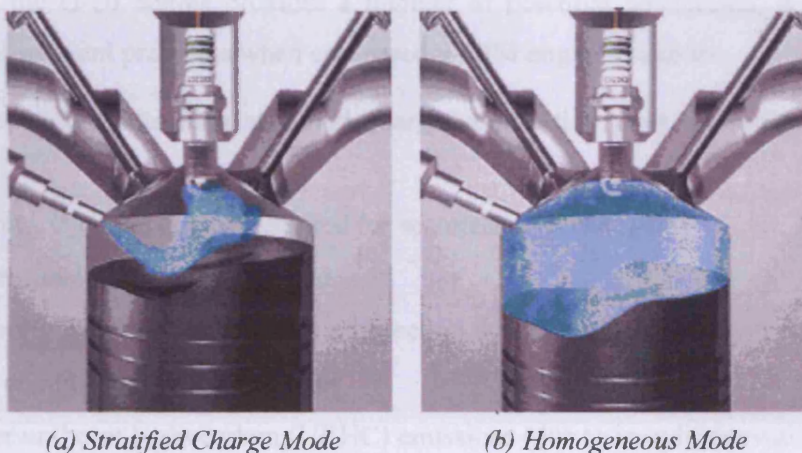


**Figure 1-4:** Schematic of a gasoline direct injection engine running at (a) stratified charge, and (b) homogeneous Charge (SAE).

The theoretical advantages of the GDI engine over the PFI engine are summarized as bellow along with the enabling mechanism (Zhao et al 1999):

- Improved fuel economy resulting from:
  - Less pumping loss: resulting from un-throttled operation at stratified mode
  - Less heat losses: resulting from un-throttled operation at stratified mode
  - Higher compression ratio: due to charge cooling with injection during induction
  - Lower octane requirement: due to charge cooling with injection during induction
  - Increased volumetric efficiency: due to charge cooling with injection during induction
  - Fuel cut-off during vehicle deceleration (no manifold film)
- Improved transient response
  - Less acceleration enrichment required (no manifold film)

- More precise air–fuel ratio control.
  - Quicker starting
  - Less cold-start over-fueling required
- Extended EGR tolerance limit to minimize throttling
- Selective emissions advantages
  - Reduced cold-start UBHC emissions;
  - Reduced CO<sub>2</sub> emissions.
- Enhanced potential for system optimization.

Although the G-DI engine provides a number of potential advantages, it also has a number of inherent problems when compared to PISI engines such as:

- Difficulty in controlling stratified charge combustion over the entire operation range
- Complex injection control required for seamless load changes
- Higher fuel line pressure required
- Relatively high rate of formation of injection deposits and / or ignition fouling
- More complicated injector designs
- Higher un-burnt hydrocarbon (UBHC) emissions (due to in-cylinder wall wetting)
- Increased NO<sub>x</sub> at part loads, and increased soot formation at high-load operation
- More complex injection control / timing.

In a recent science review of internal combustion engines, Taylor (2008) considered that the main improvements to energy efficiency for future gasoline direct injection engines would come from a variety of measures, including:

- a) *Extending the range at which the engine can operate in 'leanburn' mode (stratified charge mode)* -- This will be a considerable challenge considering future regulations on particulate emissions.
- b) *Increasing the compression ratio of G-DI engines relative to a PFI engine* -- This will require improved management of the 'air–fuel' mixture distribution in the vicinity of the spark plug prior to ignition.

Hence, there is a requirement to develop diagnostic tools for analysis of the mixture preparation process to support the development of future fuel injections systems relevant to gasoline direct injection applications.

#### **1.4. Thesis Aim and Objectives**

The aim of this study is to develop planar laser diagnostic techniques towards quantified methodologies to allow comparison with, and improvement of, in-cylinder computational Fluid Dynamic (CFD) models. To enable the delivery of this aim, the primary objectives of this research are:

- To develop a facility and a quantitative planar optical technique for measurement of transient fuel films formed as a result of spray impact.
- To apply the planar optical technique for fuel thickness measurements under atmospheric and elevated ambient conditions, improving the knowledge and understanding of the development of fuel films and the influence on elevated ambient conditions on the resulting film.
- To develop a methodology for quantifying liquid / vapour airborne concentrations.
- To obtain vapour concentration measurements under a range of elevated ambient conditions, investigating the influence of temperature and pressure variations on spray evaporation.
- To compare measurements with contemporary Computational Fluid Dynamic models, and explore potential for sub-model improvements
- To propose future research for further development of both planar techniques.

# **Chapter 2:**

## **Gasoline Direct Injection Review**

This Chapter discusses reviewed literature concerning gasoline direct injection technology, considering fuel systems requirements, injector considerations, and the fundamentals of atomisation and spray break-up.

### 2.1. G-DI Combustion System Concepts

The operating characteristics of an internal combustion engine are governed by the ‘air-mixture’ preparation process, and it has direct influence on its fuel consumption, exhaust emissions, performance, and efficiency. This process is of particular importance for gasoline engines because it is critical to ensure there is a combustible mixture in the vicinity of the spark plug to ignite in every cycle. For gasoline direct injection, the mixture formation process is very restricted due to the confined space and limited amount of time available for fuel evaporation and mixing.

All the gasoline DI combustion systems that have been proposed in the literature so far can be classified into three major groups depending on the primary strategy used to achieve stratification: spray-guided, wall-guided and air-guided systems. Figure 2-1 shows a schematic of the classification of G-DI combustion systems. The specific class assignment depends upon whether the spray dynamics, the spray impingement on a piston surface, or the mixture flow field is the principal mechanism used to achieve stratification at part load. However, regardless of the classification, the stratification is generally achieved by a combination of all three mechanisms, in which the relative contribution of each individual process varies.

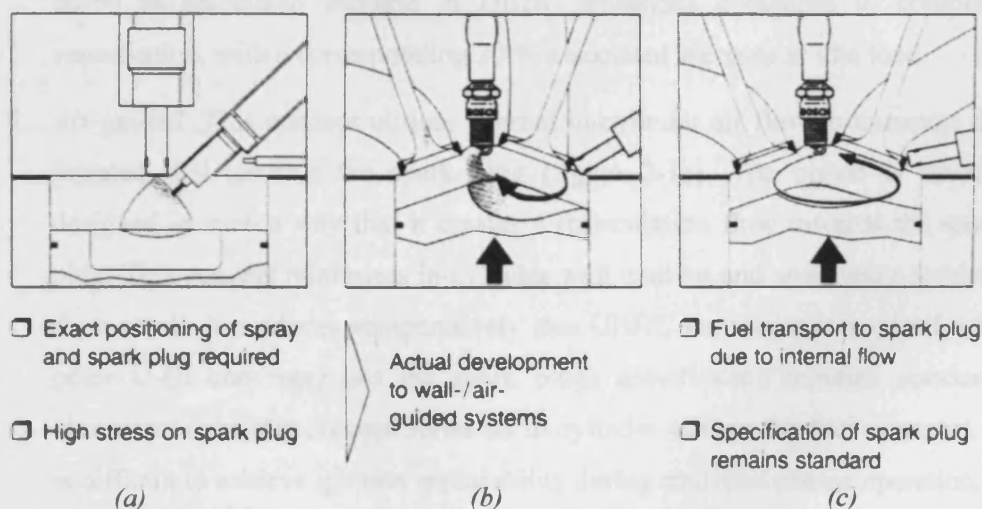


**Figure 2-1:** Classification of G-DI combustion systems: (a) spray-guided system, (b) wall-guided system, and (c) air-guided systems (Zhao et al 1999).

The main characteristics of the different combustion systems concepts are discussed below, along with brief remarks regarding their advantages and deficiencies.

1. *Spray-guided*: The primary strategy used to achieve stratification is spray dynamics (see figure 2-1a). The injector is mounted in such a way that the fuel is injected directly in the vicinity of the spark plug, thus creating a repeatable fuel-rich mixture near the spark plug. The main downside of spray-guided combustion systems is that the spark plugs are more susceptible to fouling due to fuel wetting. Even so, more recently, gasoline DI technology has adopted the 'spray-guided' concept as the preferred option as it extends significantly the speed/load range of stratified charge operation (Fansler and Drake 2006).
2. *Wall-guided*: This system relies on impingement on the piston surface as the primary strategy for stratification (see figure 2-1b). The fuel is injected in the direction of the piston crown, which is used to guide the re-atomised fuel towards the spark plug. For this combustion system, the piston is usually designed in a curved bowl (or similar) shape to assist the transition of the post-impingement fuel towards the spark plug. This concept creates a repeatable mixture in the vicinity of the spark plug, however, the inevitable deposition of fuel films due to in-cylinder wall wetting results in increased UBHC emissions. For instance, experiments by Stanglmaier et al. (1999) and Li et al. (1990) showed that for Gasoline Direct Injection (G-DI) engines working at part load, if 10 % of the mass injected impinges on the piston crown there is a 60-90 % associated increase in UBHC emissions compared to complete vaporisation, with a corresponding 30 % associated increase at idle load.
3. *Air-guided*: This concept utilises internal in-cylinder air flow to transport the injected fuel towards the spark plug (figure 2-1c). The piston is usually designed in such a way that it creates a recirculation flow towards the spark plug. This concept minimises in-cylinder wall wetting and spark plug wetting. As a result, it produces comparatively less UBHC emissions (compared with other G-DI concepts) and the spark plugs specification remains standard. However, since this concept relies on in-cylinder airflow for fuel transport, it is difficult to achieve ignition repeatability during stratified charge operation.

The following section discusses the fuel injector requirements for G-DI applications.

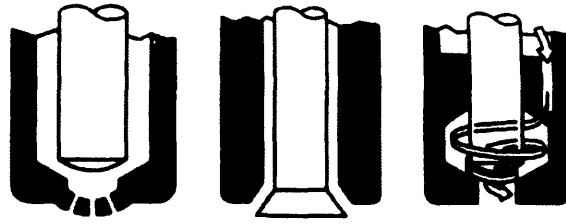
### 2.2. Fuel Injector Requirements

The fuel injection system in a G-DI engine is a key component that must be matched with specific in-cylinder flow field to provide a desired 'air-fuel' mixture in the vicinity of the spark plug for the entire range of engine operation conditions. In general, a well atomised fuel spray must be produced for all operation conditions. Therefore, the atomisation requirements for gasoline direct injection applications are particularly challenging since the engines can operate in two modes, stratified-charge mode and homogenous mode, and the atomisation requirements may vary significantly depending on the operation mode. For instance, for efficient combustion at stratified charge, a stable and compact geometry with relatively high penetration must be achieved. However, for homogeneous mode operation, a highly dispersed mixture with low penetration is desired so that the spray can evaporate completely creating a homogenous mixture prior to ignition. For that reason, a G-DI injector must be capable of providing at least two, and possibly three or more distinct operation modes. The fuel injector is considered to be the most critical element in a G-DI fuel system, and it should have the following characteristics (Zhao et al 1999):

- Accurate fuel delivery
- Desirable and repeatable fuel mass distribution pattern
- Good spray axis-symmetry over the operating range
- Zero fuel leakage, particularly for cold operation
- Small sac volume
- Small pulse-to-pulse variation in fuel quantity and spray characteristics

In addition, the injector should produce a narrow and small drop diameter distribution to ensure vaporisation of the fuel prior to ignition in order to minimise UBHC emissions. Further requirements of G-DI fuel injection systems include:

- Significantly improved level of atomization
- Expanded dynamic operation range to produce different sprays required for all operation modes
- Enhanced resistance to deposit formation
- Ability to operate at higher injector body temperatures
- Stable operation at elevated fuel and ambient pressures
- Minimisation of needle bounce that creates unwanted secondary injections



Criteria	Multi hole concept	Outward opening concept	Inward opening concept
Flexibility of spray pattern	++	+	+
Potential for inclined spray axis	+	-	++
Atomization quality at system pressure = 10 MPa	-	0	++
Robustness against fouling	-	++	+

Figure 2-2: Concept evaluation of three typical G-DI injector designs (Zhao et al 1999)

In order to achieve these requirements, a number of injector concepts have been proposed in the literature. Figure 2-2 provides an evaluation of three of the injector tip designs most commonly used for G-DI applications (Zhao et al 1999). The multi-hole injector tip concept is an adaptation of diesel technology and it uses a simple pencil-jet break-up mechanism to atomise the fuel. During operation, the needle of this injector retracts internally allowing the fuel to exit through the holes. This concept offers great flexibility for creation of different spray patterns, and has potential for off-axis spray design. However, the relatively low injection pressures of G-DI (usually around 10 - 20 MPa) compared to diesel applications (typically 150 - 200 MPa) require significantly smaller hole diameters, which are difficult to manufacture, to achieve satisfactory atomisation. For this reason, this concept offers relatively poor atomisation quality when compared to other G-DI concepts. For the outward opening injector concept, the needle opens outwardly allowing the fuel to exit through the annular section created between the needle and inner tip hole. This concept is arguably the most robust injector type concerning fouling. However, it offers little flexibility for inclined axis (off-axis) designs, which limits its spray-applicability to guided combustion systems (as it limits the capacity of the injector to target the fuel towards the spark plug). The inward opening concept is arguably the best 'all-round' performer as it offers great repeatability, flexibility for different spray patterns including off-axis designs, and good robustness against fouling. For this concept, the



needle of the injector retracts inwardly allowing the fuel to exit through the orifice with a tangential swirl component creating a conical hollow sheet that disintegrates into small droplets. The selection of suitable injector tips depends mainly on the combustion system design (wall, spray, or air guided), as all have different atomisation requirements.

### 2.3. Injector Selection

Many variations of tip designs have been explored for G-DI applications, often producing suitable injectors for operation at stratified-charge, such as: air-assisted injectors, multi-hole injectors, pressure-swirl injectors, fan injectors, and outward opening injectors. Considering the fact that this thesis aims to propose novel optical techniques for G-DI spray diagnostics, any injector concept could have been selected to carry out preliminary experiments. However, an inwards-opening pressure-swirl injector is used mainly for two reasons:

1. *Relevance to G-DI applications* – the pressure-swirl injector concept is commonly used for G-DI applications (particularly to wall-guided applications) because of its enhanced atomisation characteristics.
2. *Significant amount of data available* – detailed information about this spray is available from a previous study by Kay (2006), who used Phase Doppler Anemometry (PDA) to characterise the spray (pre and post impingement) under a wide range of experimental conditions, including the experimental conditions used in this thesis. Kay's work includes temporal and spatial description of the spray in terms of droplet diameter and flow field.

Selecting the same injector used by Kay (a BOSCH C2-70 hollow-cone pressure-swirl atomiser) provides confidence when analysing the performance and results from the techniques proposed in this thesis, since cross-comparison of data from different techniques allows a better understanding of the novel results.

The atomisation mechanism in pressure-swirl injectors is considerably different to the mechanism used by plain orifice multi-hole injectors. For pressure-swirl injectors, the atomization is achieved by the disintegration of a thin conical liquid sheet formed as a result of a strong swirl velocity component achieved by passing the injected fuel through a swirl chamber. Figure 2-3 shows a schematic of the internal geometry of a swirl fuel injector. When the needle retracts, fuel at high pressure is forced to the swirl

chamber through the tangential ports. There, the fuel develops a strong swirl velocity component before leaving the orifice. The swirling flow forms a hollow conical sheet which expands outwards into the air until a critical thickness is achieved, after which the surface tension forces can no longer contain the liquid sheet. As a result, the sheet is disintegrated into ligaments and then into well-atomised droplets. The resulting droplet size is directly proportional to the injector tip characteristics and the thickness of the resulting conical sheet. Due to the strong swirling component the spray also develops a considerable radial velocity component limiting the axial penetration of the spray. As a result, pressure-swirl injectors are able to achieve significantly small droplet diameter distributions with reduced axial spray penetration, which makes them ideal for many G-DI applications.

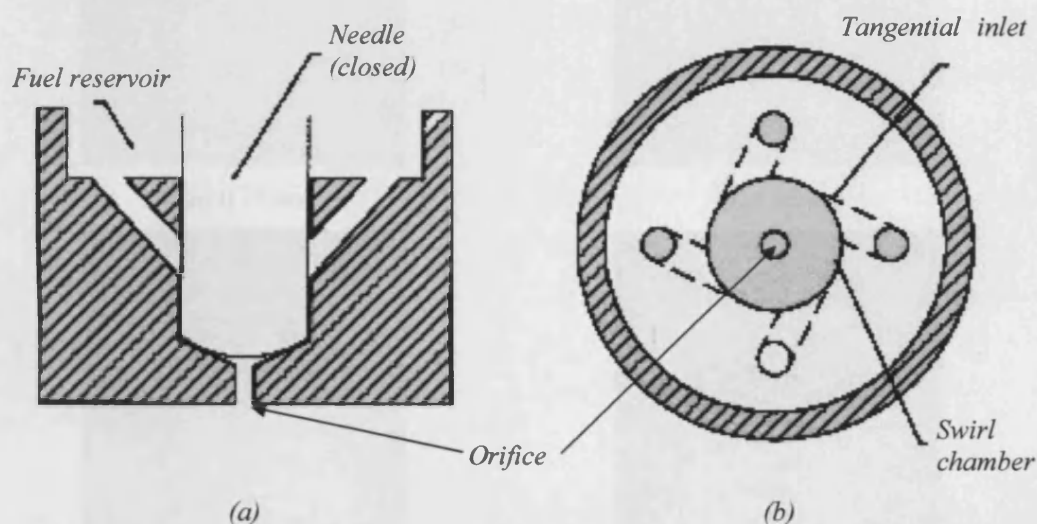


**Figure 2-3:** Schematic of the internal geometry of a swirl fuel injector: (a) section along centerline, (b) plan view of the swirl device (Morris 2003)

The development of a pressure-swirl spray can be divided into four distinct phases, each one describing different spray characteristics (Kay 2006, Morris 2003, Comer 1999). Figure 2-4 shows the development of the BOSCH C2-70 pressure-swirl spray for selected times after start of injection. The four stages of spray development identified for the transient operation of swirl fuel injectors are:

1. **Sac-Spray:** this phase corresponds to injection of the sac volume, which is the small amount of fuel left in the exit tangential ports of the injector tip from the previous injection (see figure 2-4a). The pressure corresponding to the sac

volume is significantly lower than the injection line pressure. Due to the low pressure when entering the swirl chamber, the sac volume develops a very weak swirling velocity component for which it is characteristically poorly atomised. Also, due to poor swirl, the sac volume is characterised for having a strong axial component, and low radial component, for which this fraction of fuel usually displays strong axial penetration (Kay 2006, Gao et al 2005).

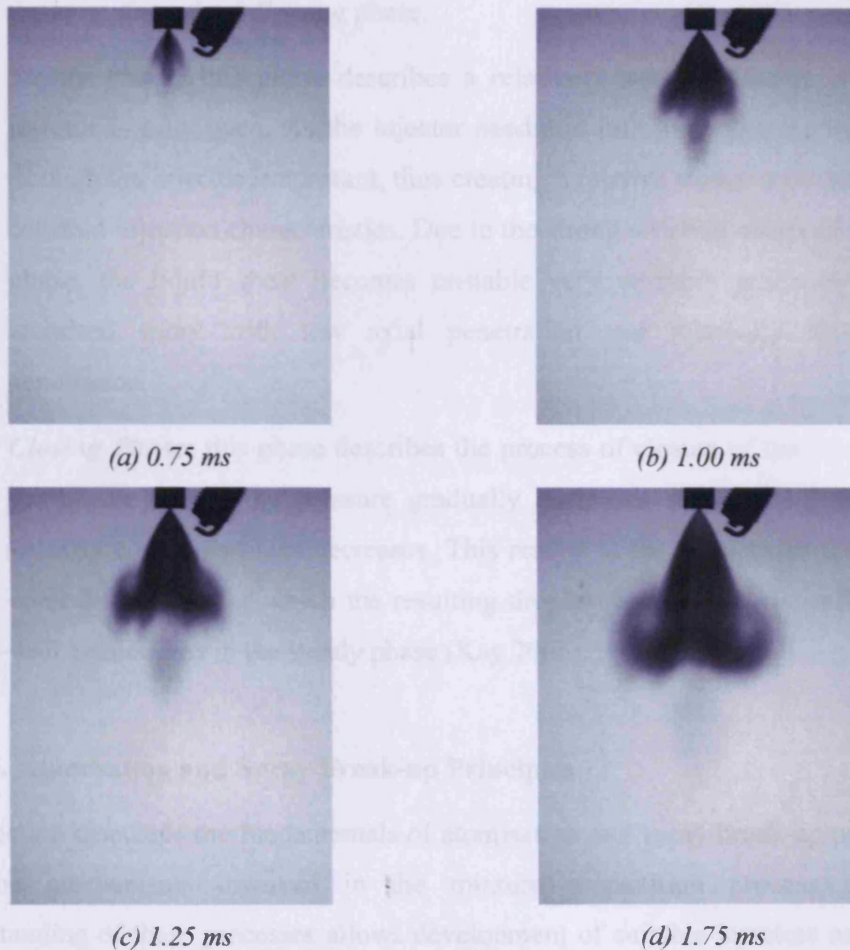


**Figure 2-4:** Development of a hollow-cone pressure-swirl G-DI spray for selected times after start of injection

2. **Opening Phase:** this phase describes the development of the spray as the injector opens (see figure 2-4b). As the needle retracts, fuel enters the swirl chamber at high pressure, and subsequently exits through the tangential ports increasing the swirl component of the spray. As the flow rate increases, the fuel develops an 'air-core' in the centre of the chamber as it has high angular

momentum. This results in the formation of a hollow conical liquid sheet which later disintegrates into ligaments and small droplets. The opening phase describes the development of the hollow cone until the needle is completely retracted and the injector is fully open. Droplets from this phase are significantly smaller than that of the previous phase (Kay 2006). Also, the spray from this phase develops an incremental swirling and radial velocity, which eventually achieve the relatively steady state conditions which describe the spray from the following phase.

3. **Steady Phase:** this phase describes a relatively steady phase in which the injector is fully open. As the injector needle is fully retracted the mass flow through the injector is constant, thus creating a relative steady state phase with constant injection characteristics. Due to the strong swirling component in this phase, the liquid sheet becomes unstable very unstable producing a well atomised spray with low axial penetration and relatively high radial penetration.
4. **Closing Phase:** this phase describes the process of closure of the injector. As the needle closes, the pressure gradually decreases for which the swirling velocity component also decreases. This results in the collapse of the hollow conical structure for which the resulting droplets are characteristically not as well atomised as in the steady phase (Kay 2006).

### 2.4. Atomisation and Spray Break-up Principles

This section discusses the fundamentals of atomisation and spray break-up processes, and the mechanisms involved in the mixture preparation process. A good understanding of these processes allows development of suitable injectors capable of achieving the requirements discussed in the previous section.

Atomisation is the process of conversion of a liquid bulk into a spray or mist by forcing the liquid through a nozzle. Consequently, the nozzle characteristics prove critical at defining the resulting spray. Generally, atomisation is achieved by producing a high relative velocity between the liquid and the gaseous medium into which the liquid is discharged. Although the mechanisms by which the high relative velocity is generated vary significantly depending on the type of atomiser, the

characteristics of the resulting spray can be accurately characterised by the following dimensionless numbers (Lefebvre 1989):

$$Re = \frac{\rho_l u_d D_n}{\mu_l} \quad (2-1)$$

$$We = \frac{\rho_g u_d^2 D_n}{\sigma_l} \quad (2-2)$$

$$Oh = \frac{\mu_l}{\sqrt{\rho_l \sigma_l D_n}} = We_{Dn}^{0.5} \cdot Re_{Dn}^{-1} \quad (2-3)$$

The Reynolds number ( $Re$ ) is the ratio of inertial forces to viscous drag forces acting on the fluid, where  $\rho_l$  is the liquid density,  $u_d$  is the droplet velocity, and  $D_n$  is the diameter of the nozzle. The Reynolds number can be used to describe the velocity profile and the radial velocity component which promotes disintegration of the jet. The Weber number ( $We$ ) is the ratio of inertial forces to surface tension forces, where  $\sigma_l$  is the liquid surface tension, and  $\rho_g$  is the gas density. The Weber and Reynolds numbers are often combined to form the Ohnesorge number ( $Oh$ ), which is the ratio of internal viscosity forces to tension interfacial forces.

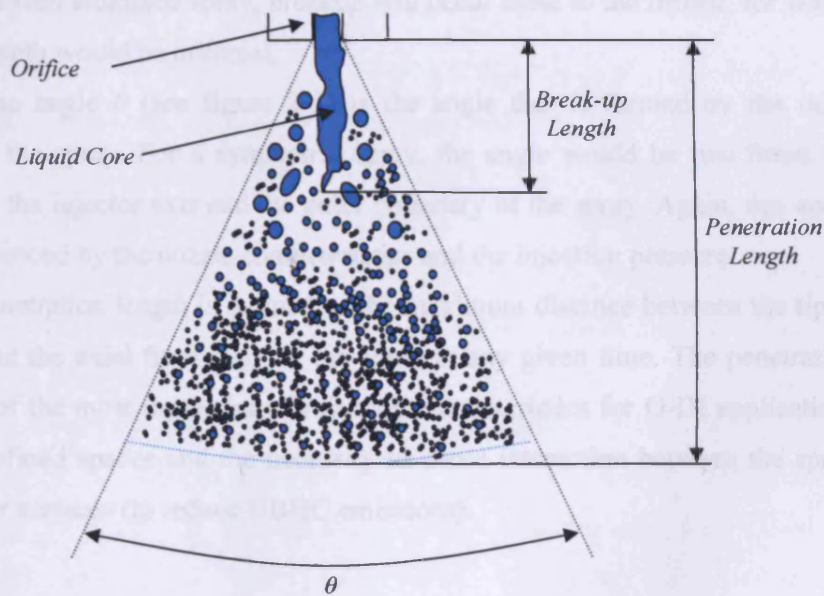


Figure 2-5: Schematic of spray structure and spatial distribution

The structure and spatial distribution of the resulting spray is usually described by three global parameters, the break-up length, the spray cone angle, and the penetration length, all of which vary significantly depending on the nozzle characteristics.

A schematic of the break-up length, spray cone angle ( $\theta$ ), and penetration length is presented in figure 2-5. In general, not all the fluid breaks up once the atomisation begins, hence a boundary between the liquid sheet (and / or ligaments) and the atomised droplets region. The break-up length is the maximum distance from the tip of the injector to the tip of the intact liquid core within the spray. This distance is greatly influenced by a number of parameters, such as: nozzle characteristics, injection velocity, liquid surface tension, liquid viscosity, and aerodynamic forces. Yule and Filipovic (1992) subdivided the break-up zone of a single orifice atomiser into four fairly distinctive areas depending on the level of atomisation. The instant column zone involves the column of liquid emerging from the nozzle, which is at relatively low injection velocity. The peripheral atomised zone is formed by ligaments and dense peripheral layer of droplets resulting from break-up of the liquid due to aerodynamic forces. The ligaments zone is the maximum distance from the nozzle to the tip of the ligaments that are still attached to the liquid column. Finally, the zone detached from ligaments, sheets, and larger droplets, at which the spray is fully atomised. The region where droplets begin to form will depend heavily on the liquid pressure. For a well atomized spray, breakup will occur close to the orifice, for which the breakup length would be minimal.

The spray cone angle  $\theta$  (see figure 2-5) is the angle that is formed by the outer boundaries of the spray. For a symmetric spray, the angle would be two times the angle between the injector axis and the outer boundary of the spray. Again, this angle is greatly influenced by the nozzle characteristics and the injection pressure.

Finally, the penetration length is defined as the maximum distance between the tip of the injector and the axial front edge of the spray at any given time. The penetration length is one of the most important atomisation characteristics for G-DI applications due to the confined spaces and the necessity to avoid interaction between the spray and in-cylinder surfaces (to reduce UBHC emissions).



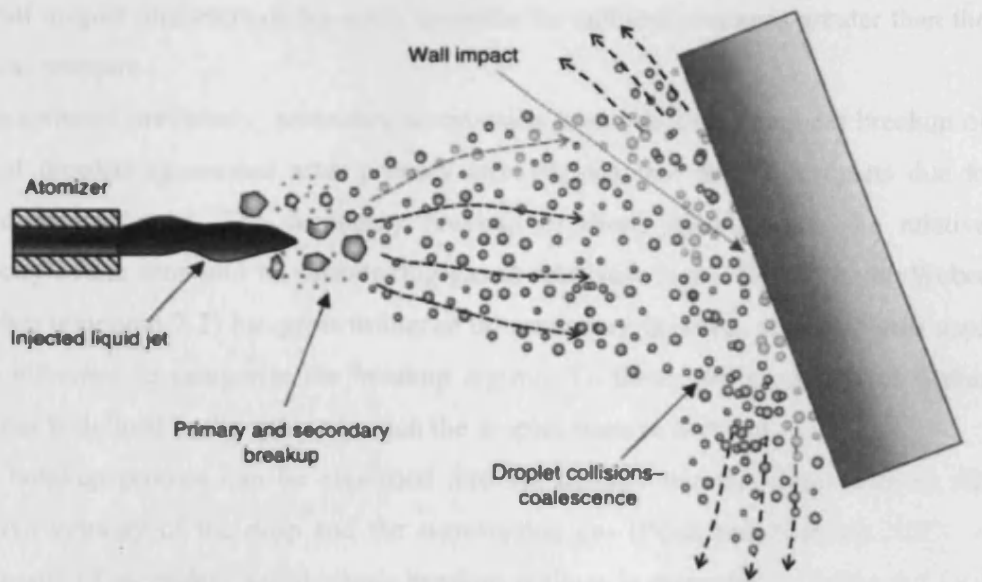


**Figure 2-6:** Schematic of spray atomisation, transport and wall impact (Tropea and Roisman 2006)

Figure 2-6 shows a schematic of the different mechanisms involved in spray atomisation, transport, and wall impact. The following sections (section 2.4.1 to 2.4.4) discuss some of the fundamental of these mechanisms that influence the atomisation process, with particular emphasis to G-DI engine applications.

### 2.4.1. Primary and Secondary Break-up

Primary atomisation is the process that involves the disintegration of the liquid core due to aerodynamic forces, forming fluid particles such as: ligaments, sheets, and large droplets. It marks the first stage in the atomisation process and the initial condition for secondary aerodynamic atomisation, which involves the subsequent breakup of the primary spray into smaller droplets. For that reason, primary atomisation has a significant effect on the resulting droplet size and velocity distribution of the resulting spray.

It is difficult to determine the effect of ambient gas pressure or temperature in the primary atomisation of a spray since these factors also affect subsequent atomisation processes, such as secondary atomisation, droplet evaporation, etc. However, Lefebvre (1989) showed that even though overall droplet diameters increase as ambient pressure increases, there is a critical pressure after which the disintegration forces responsible for primary atomisation become more dominant. As a result,

overall droplet diameters of the spray decrease for ambient pressures greater than the critical pressure.

As mentioned previously, secondary atomisation involves the subsequent breakup of parent droplets (generated after primary atomisation) into smaller droplets due to aerodynamic forces. The secondary breakup of drops occurs when the relative velocity of the drop and its surrounding gas is relatively high. Therefore, the Weber number (equation 2-2) has great influence on secondary breakup, and it is often used as a reference to categorise the breakup regime. To these effects, a critical Weber number is defined as the value at which the droplet starts to breakup.

The breakup process can be classified into six distinct regimes depending on the relative velocity of the drop and the surrounding gas (Pilch and Erdman 1987). A schematic of secondary aerodynamic breakup regimes is presented in figure 2-7, and the different modes are discussed as follows:

- a) *Vibrational breakup*: this type of breakup can occur when the Weber number is small ( $We \leq 12$ ). Oscillations develop at the natural frequency of the drop due to instabilities induced by the gas flow field. Under certain conditions, the amplitude of the oscillations can increase until the drop decomposes into a few large fragments. This mechanism only produces a few relatively large secondary droplets, and the overall breakup time is long compared to other breakup regimes.
- b) *Bag breakup*: usually takes place in the Weber number range of  $12 \leq We \leq 50$ . In this regime, the drop deforms and takes an expanding bag-like shape. A thin hollow bag is blown downstream while being attached to a more robust toroid rim. The bag eventually bursts forming a large number of well atomised secondary droplets. A short time later, the rim disintegrates into a small number or relatively large fragments. This mode is characteristic for drops with low viscosity.
- c) *Bag and Stamen breakup*: this mode has several common features with the bag breakup, and is a transition mechanism that occurs for Weber numbers between 50 and 100. Similar to bag breakup, a thin hollow bag attached to a toroidal rim is blown downstream. However, a column of liquid (stamen) is formed along the flow axis. The bag bursts first, inducing the rupture of the rim. Then, the stamen disintegrates into relatively large drops.



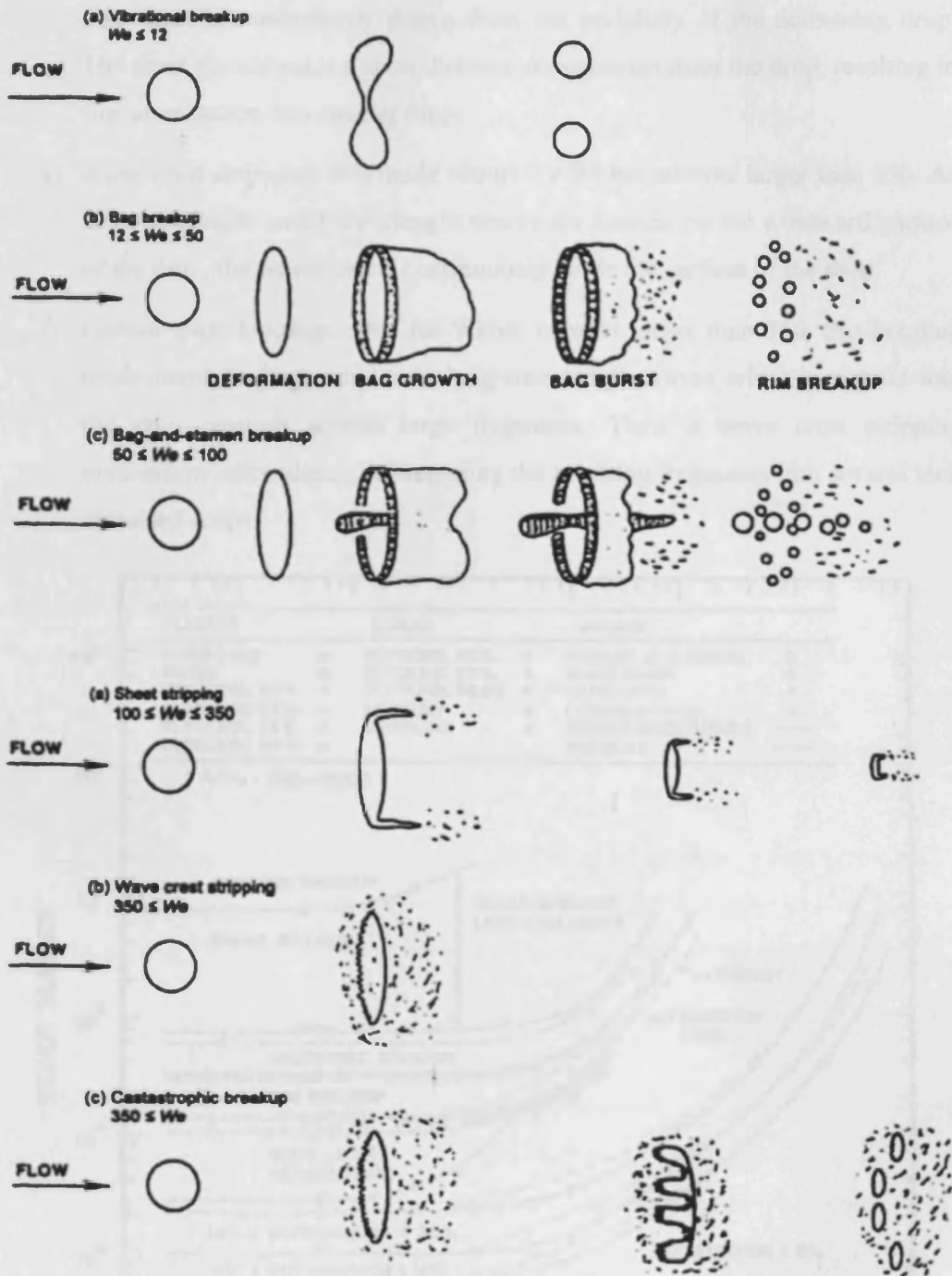


Figure 2-7: Schematic of aerodynamic Break-up mechanisms (Khavkin 2004)

- d) *Sheet stripping breakup*: This mode is distinctively different to the bag breakup mode, and usually occurs at  $100 \leq We \leq 350$ . As the name suggests, a thin sheet is continuously drawn from the periphery of the deforming drop. The sheet disintegrates a short distance downstream from the drop, resulting in fine atomisation into smaller drops.
- e) *Wave crest stripping*: this mode occurs for Weber number larger than 350. As large-amplitude small-wavelength waves are formed on the windward surface of the drop, the waves crests continuously erode the surface of the drop
- f) *Catastrophic breakup*: Also for Weber number larger than 350, this breakup mode involves large-amplitude long-wavelength waves which penetrate into the drop creating several large fragments. Then, a wave crest stripping mechanism takes place, disintegrating the resulting fragments into several well atomised drops.

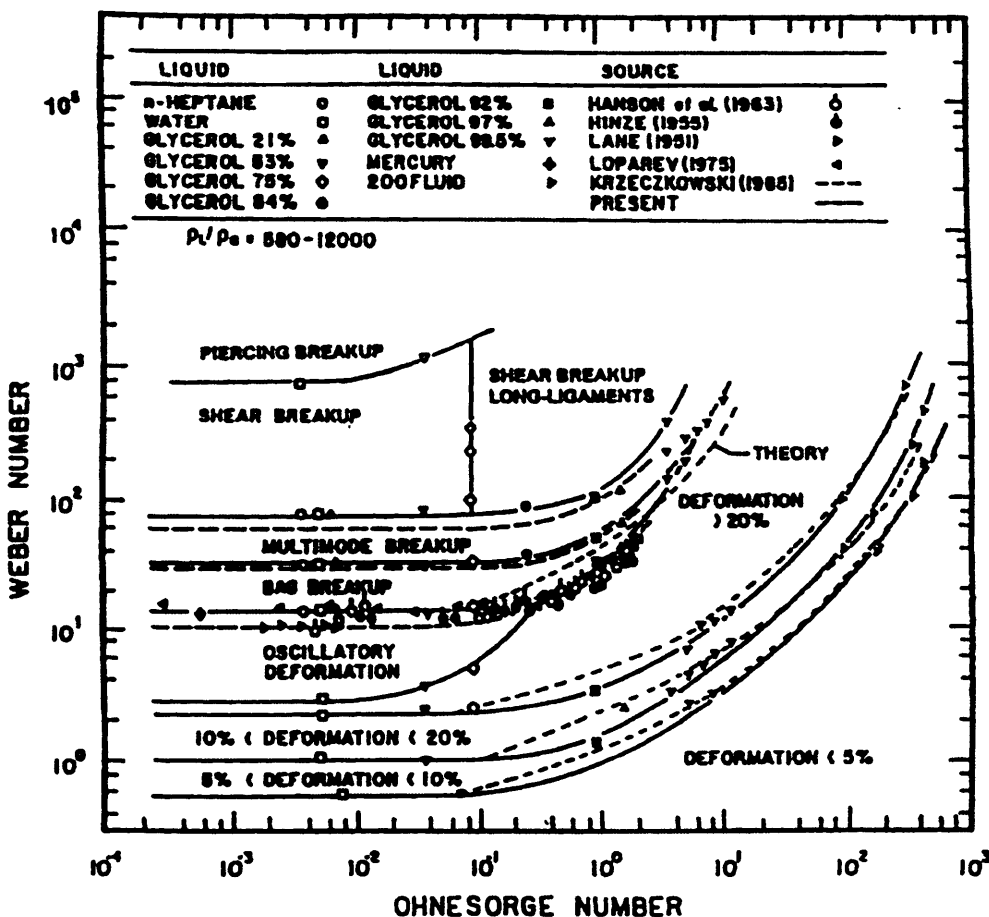


Figure 2-8: Drop deformation and secondary breakup regime map for shock wave disturbances (Khavkin 2004)

The Weber number is not the only dimensionless number that can be used to describe secondary breakup. In fact, the Weber number does not depend on the liquid viscosity, which is an influential parameter in the breakup process. As a result the Ohnesorge number (equation 2-3) is often used in the literature to describe aerodynamic breakup processes. Figure 2-8 shows a drop deformation and secondary breakup regime map as a function of the Ohnesorge and Weber numbers (Khavkin 2004). It shows the significant effect of viscosity on the breakup process.

### 2.4.2. Droplet Interactions

The greater the spray density, the higher probability there will be interaction between droplets. Therefore, it is important to understand the fundamentals of droplet-to-droplet collisions as their outcome can potentially influence the diameter distribution of the spray. For instance, when droplets coalesce (combine) after collision, it leads to the formation of larger droplets which is detrimental for G-DI applications as it increases the evaporation time of the spray.

The outcome of droplet-to-droplet collisions has been investigated by many research groups. Jiang et al (1992) studied the collision of equally sized hydrocarbon droplets, and reported that the outcome of droplet-to-droplet can be categorised into five distinctive categories (see figure 2-9), such as:

1. *Droplet coalescence*: in this regime the colliding droplets merge permanently into a larger droplet. Coalescence usually occurs at low relative velocity between the impacting droplets for which there is little deformation of the resulting droplet.
2. *Droplet bounce*: as the name suggests, in this regime the droplets bounce from each other after impact. It occurs for higher Weber numbers than droplet coalescence. In principle, there is no contact between the droplets due to a gas gap between them. The colliding droplets lose their momentum upon impact, and the surface tension of each droplet return them into their original spherical shape.
3. *Droplet coalescence with significant deformation*: for increased impact energy, the droplets collide similarly to the droplet bounce regime. However, the momentum of the droplets is such that gas gap between the droplets reaches a critical minimum, allowing coalescence between them. However, due to the

increased energy there is significant deformation of the resulting droplet, which oscillates for a period of time until reaching equilibrium as a spherical droplet.

4. *Reflective separation*: for a further increase in the impact energy, the droplets collide similarly to the previous case. The droplets merge temporarily, and the increased energy allows the droplets to breakup into two or more droplets during the oscillation stage as the increased energy overcomes viscous and surface tension forces.

5. *Stretching separation*: this regime occurs for off-axis impact. When two droplets collide off-centre, part of the impact energy generates an angular momentum which changes the direction of the resulting droplets. The droplets usually breakup in a similar fashion to the reflective separation regime, thus creating two or more droplets.

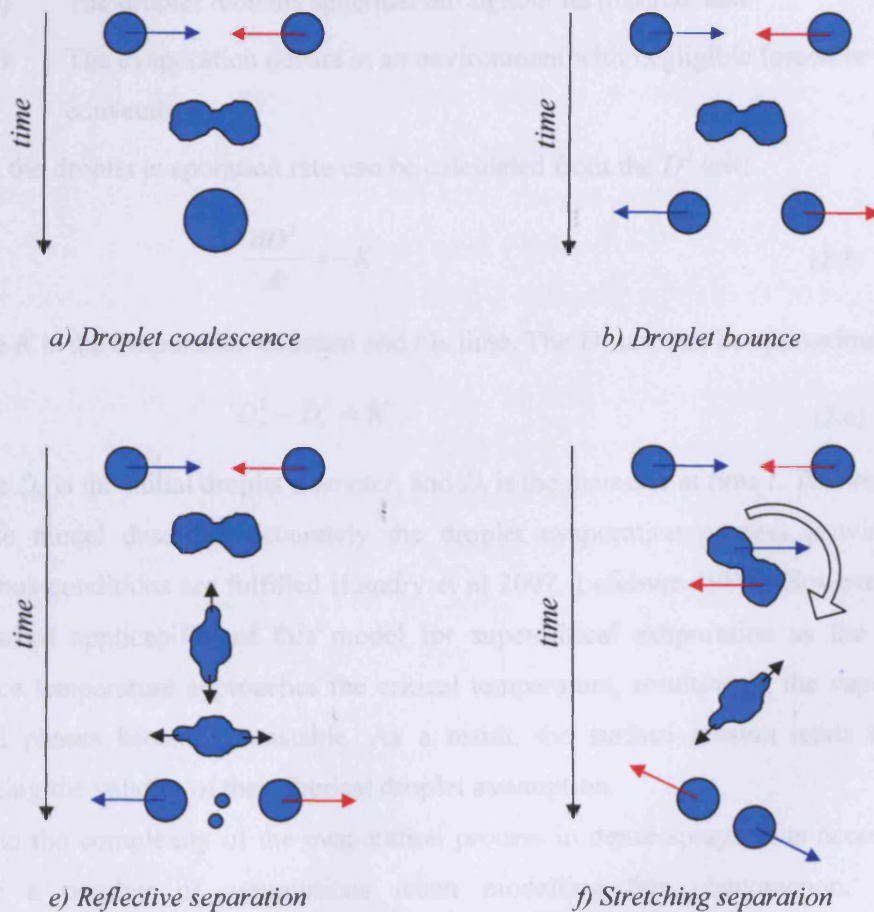


Figure 2-9: Schematic of possible outcomes after droplet to droplet collisions

### 2.4.3. Droplet Vaporisation

The ability to predict droplet evaporation rate is of great importance in the atomisation process, particularly for G-DI applications as there is limited time for evaporation and mixing. The droplet evaporation rate is influenced by the droplet Knudsen number ( $Kn$ ), defined as (Landry et al 2007):

$$Kn = \frac{\lambda}{D} \quad (2-4)$$

where  $\lambda$  is the atomic mean free path near the droplet surface and  $D$  is the droplet diameter. To predict the droplet evaporation rate in the continuum regime ( $Kn \ll 0.1$ ), the hydrodynamic theory can be used to develop the  $D^2$  law, provided that:

- i) The droplet surface temperature is below the critical temperature (i.e., subcritical evaporation)
- ii) The liquid and vapour phases are quasi-steady,
- iii) The droplet remains spherical throughout its lifetime, and
- iv) The evaporation occurs in an environment with negligible forced or natural convection.

Then, the droplet evaporation rate can be calculated from the  $D^2$  law:

$$\frac{dD^2}{dt} = -K \quad (2-5)$$

where  $K$  is the evaporation constant and  $t$  is time. The  $D^2$  law can be approximated to:

$$D_o^2 - D_t^2 = K \quad (2-6)$$

where  $D_o$  is the initial droplet diameter, and  $D_t$  is the diameter at time  $t$ . This relatively simple model describes accurately the droplet evaporation process provided the previous conditions are fulfilled (Landry et al 2007, Lefebvre 1989). However, there is limited applicability of this model for supercritical evaporation as the droplet surface temperature approaches the critical temperature, resulting in the vapour and liquid phases becoming unstable. As a result, the surface tension tends to zero, reducing the validity of the spherical droplet assumption.

Due to the complexity of the evaporation process in dense sprays, it is necessary to make a number of assumptions when modelling this phenomenon. Droplet evaporation models can be categorised into three main types depending on the

approach they take to model the heat transfer to the drop: i) the quasi-steady model (which assumes an uniform steady state temperature), ii) the rapid mixing model (which assumes the temperature to be uniform but time dependent), and iii) the diffusion limit model (in which the heat and mass transport in the liquid is governed by diffusion equations). Additionally, modelling evaporation of dense sprays is particularly challenging as multiple droplets within the spray evaporate simultaneously, saturating the surrounding gas and thus influencing the evaporation of further droplets. Therefore, the selection of a suitable evaporation model and input parameters for any particular application requires careful consideration to allow plausible predictions of spray evaporation.

From all the parameters that affect the droplet evaporation process, the temperature of the liquid and surrounding gas has unquestionably the greatest influence on the evaporation rate. Kay (2006) studied the effect of elevated ambient temperatures and pressures in the evaporation characteristics from a pressure-swirl atomiser. He used a constant volume chamber with independent control of ambient temperatures and pressures to investigate droplet diameter and velocity distributions of the spray under ambient conditions relevant to G-DI applications. At elevated pressures (up to 5.8 bar), Kay reported reduced penetration and larger droplet diameter when comparing the spray to ambient conditions. In contrast, at elevated ambient temperatures (up to 150 °C), he reported a significant reduction in overall droplet sizes resulting from an increased evaporation rate observed at elevated ambient temperatures. In addition, he reported a further increase in droplet evaporation rate for experiments with elevated fuel temperature (as the fuel was pre-heated to 85 °C prior to injection). For a similar experimental setup, Dodge and Biaglow (1985) reported that increasing the ambient temperature has a small effect on droplet diameter distribution close to the nozzle, due to the droplet heat up and evaporation times involved. However, further downstream he observed a significant decrease in overall droplet diameters due to droplet evaporation at elevated ambient temperature.

#### **2.4.4. Spray / Wall Interaction**

Spray/wall interaction upon solid surfaces is an unavoidable phenomenon intrinsic to direct-injection internal combustion engines, influencing greatly the air-fuel mixing and combustion. Impingement is particularly significant in gasoline direct injection

engines working in stratified charge mode, where the fuel is injected late in the compression stroke virtually guaranteeing interaction with in-cylinder surfaces (Zhao et al 1999). Fuel impingement is generally undesirable because its association with unburned hydrocarbon (UBHC) emissions, particulate emissions, and fuel economy. For this reason, it is critical to improve the understanding of the impingement in order to reduce the amount of fuel deposits in gasoline DI engines. To enable an accurate description of the spray impact process, it is necessary to determine correctly two interacting characteristics:

- i) The generation of post-impingement droplets, and
- ii) The accumulation of a liquid fuel film on the wall.

In principle, the outcome of a droplet impacting on a solid surface can be categorised into six post-impingement regimes (Figure 2-10):

- a) **Stick:** generally occurs when the impact energy is very low and the impinging droplet sticks to the impact surface without deformation.
- b) **Rebound:** this describes the phenomenon that occurs when a drop rebounds from the impact surface forming a drop with the same size as the pre-impact drop.
- c) **Spread:** this regime describes the process in which a drop deforms to form a film on the wall, or merges with a pre-existing liquid film. There is no post-impingement airborne mass generated in this process.
- d) **Boiling induced break-up:** describes the process of generation of secondary drops due to boiling. The impacting drops carries low impact energy, which produces an impact within the 'stick' or 'spread' mechanical regime. However, the elevated wall temperature produces rapid boiling of the mass upon impact, generating air-borne post-impingement spray.
- e) **Rebound with break-up:** describes a break-up process of a drop following impact on a hot surface. It occurs when the total mass of the pre-impact drop rebounds from the surface accompanied by break-up into smaller drops.
- f) **Splash:** This regime describes the process that occurs when a drop impinges on a dry surface with higher impact energy than the 'spread' regime. Upon impact, the drop deforms into a film creating a crown or liquid jet form after



the latter part of the drop impinges on the surface. Then, small jets develop on the periphery that becomes unstable and break-up into smaller drops. This regime is also observed when a drop impacts upon a shallow liquid layer. A crown liquid sheet emerges normal to the film as a result of displacement of the centre of impact. For this regime, Yarin et al (1995) observed that the effect of gravity is negligible compared to surface tension and inertia. Additionally, they reported that surface roughness effects are negligible for drops impacting upon liquid films if the film is 'thick' compared to the surface roughness.

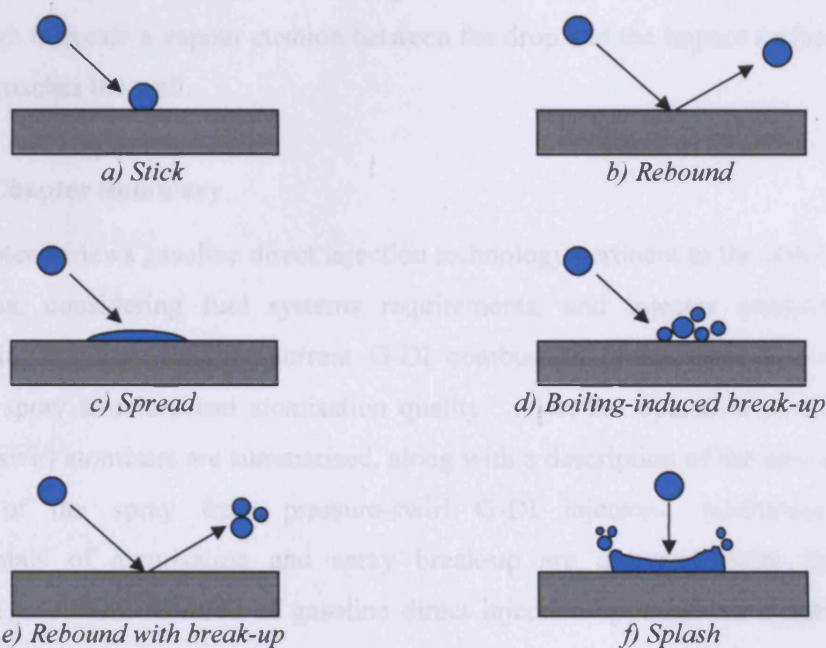


Figure 2-10: Schematic of post-impingement regimes

The relative interaction of the fuel film and secondary post-impact spray is influenced greatly by pre-impact conditions, such as: pre-impinging spray characteristics, ambient conditions, and impact angle, and also surface characteristics such as geometry, temperature and roughness. For G-DI applications, the challenge is to minimise the extent of the fuel film whilst ensuring desirable secondary spray dynamics.



The effect of surface roughness has been studied by many research groups (e.g. Bai et al 1995, Mundo et al 1995, Rioboo et al 2001). The general agreement between researchers is that the impinging droplets are more likely to splash as surface roughness increases. Regarding temperature effects, the impact surface temperature has a significant effect on spray impingement. Fardad and Lamdomatos (1999) investigated the evaporation of impinging drops upon impact on heated surfaces. The authors showed that as the surface temperature increases, there is an increase in heat transfer to the drop, resulting in a reduction in evaporation times. However, for a critical temperature known as the Leidenfrost temperature, the authors reported a decrease in heat transfer and consequently an increase in evaporation time. The Leidenfrost temperature is the surface temperature at which the surface is sufficiently hot enough to create a vapour cushion between the drop and the impact surface as the drop approaches the wall.

### **2.5. Chapter Summary**

This chapter reviews gasoline direct injection technology pertinent to the objectives of this thesis, considering fuel systems requirements, and injector considerations. Atomisation requirements for current G-DI combustion systems are discussed in terms of spray structure and atomisation quality. Also, the operation principles of pressure-swirl atomisers are summarised, along with a description of the development process of the spray from pressure-swirl G-DI injectors. Additionally, the fundamentals of atomisation and spray break-up are discussed with particular relevance to current research of gasoline direct injection applications. Furthermore, important parameters are defined in this chapter, which are regularly used in this thesis to describe spray characteristics in terms of spray structure and atomisation quality. This chapter provides an insight to the different factors that influence the mixture preparation process for gasoline direct injection applications.

# **Chapter 3:**

**Development of New Facilities and New Optical Techniques**

This chapter describes the development of new rigs and temporally-resolved planar optical techniques for characterisation of vapour concentration and post-impingement fuel films of gasoline direct injection sprays. The chapter includes a detailed description of the techniques, calibration process, and post-processing methodologies. In addition, the potential limitations of the techniques are discussed. Finally, the experimental test matrix proposed for this thesis with conditions of relevance to gasoline direct injection applications is presented and discussed.

### **3.1. Development of a New Rig for Fuel Film Characterisation**

As discussed in section 2.4.4, spray/wall interaction upon solid surfaces is an unavoidable phenomenon intrinsic to DI internal combustion engine operation, influencing greatly the air-fuel mixing and combustion. Given the operating conditions of G-DI engines working in stratified charge mode, where high pressure fuel is injected late in the compression stroke virtually guaranteeing interaction with in-cylinder surfaces, the challenge is to minimise fuel film deposits whilst ensuring desirable secondary spray dynamics. Therefore, in order to reduce the amount of fuel deposits in gasoline DI engines, it is crucially important to improve understanding of the impingement process.

In order to quantify this process accurately, it is imperative to determine correctly two interacting characteristics: generation of secondary droplets and the accumulation of a liquid fuel film on the wall. The relative interaction of these characteristics is influenced greatly by pre-impact conditions, such as: pre-impinging spray characteristics, ambient conditions, and impact angle, and also surface characteristics such as geometry, temperature and roughness.

Extensive research has been undertaken to characterise the post-impingement spray using Phase Doppler Anemometry (PDA) (e.g. Pano and Moreira 2007, Cossali et al 2007, Kalantari and Tropea 2007, Kay et al 2005, Chale et al 1997). Although this technique offers considerable potential for quantification of post-impact droplet sizes and flowfield, a full understanding of pre-combustion conditions requires quantification of the fuel mass distribution within the combustion chamber, including the spatial distribution and any residual fuel film. Hence, time-resolved spatial field measurements of droplet size need to be complemented by characterisation of the resulting liquid fuel film on surfaces.

This section describes the development of a temporally-resolved 3-D laser induced fluorescence (LIF) technique to analyse and quantify the transient fuel film formed due to impingement of a pressure swirl G-DI spray on a quartz flat surface. The technique proposes the use of Total Internal Reflection (TIR) to carefully control the propagation of the laser radiation source so as to target the excitation of the liquid fuel film, only and not the airborne droplets above the film.

Calibrated benchmark results reported by Alonso et al (2009a and 2009b) demonstrate the ability of the TIR-LIF technique for spatial and temporal characterisation of fuel films throughout the injection event. Quantitative results reported include time-resolved two-dimensional distribution maps of fuel film thickness, and estimation of total mass deposits. This information, in conjunction with post-impingement PDA characterisation, can be used for development of post-impingement empirical sub-modelling and furthermore, for appraisal of integrated Computational Fluid Dynamics (CFD) predictions of in-cylinder spray impingement. Therefore, the accurate characterisation of fuel films provide valuable information both for contributions to design improvements for current and future gasoline DI engines, and for development of computational techniques for quantitative analysis of this event.

### 3.1.1. Previous Work

The TIR-LIF technique follows work published by Kay et al (2006a and 2006b), who proposed a 3-D LIF technique to quantify the fuel film thickness formed as a result of impingement of a pressure swirl injector on a flat surface. The optical setup proposed by Kay is presented in Figure 3-1. The technique relies on the principle that upon excitation by laser light, the intensity of the fluorescent signal from a suitable dopant is proportional to the film thickness. Initial results reported by Kay (Figure 3-2) show that airborne droplets affect the fluorescent signal from the fuel film. This is due to the fact that the laser continues its path upwards and the light excites the airborne liquid fuel above the piston surface, increasing the fluorescence signal detected by the camera.

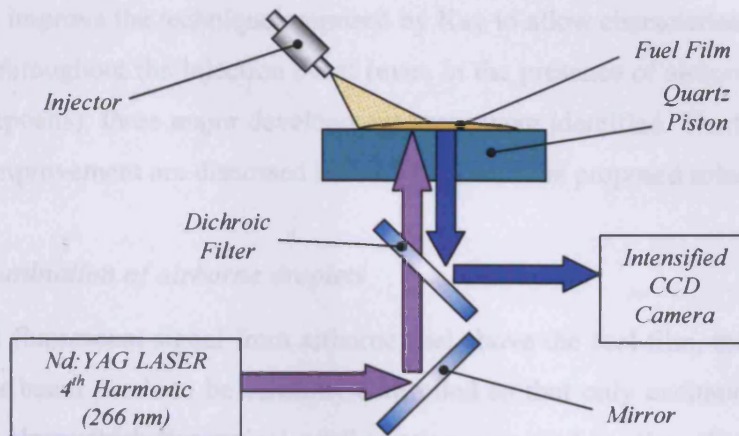


Figure 3-1: Schematic of the Optical Setup Proposed by Kay et al (2006b)

However, a single injection on the quartz piston demonstrated the potential of the technique, as the overall intensity of the fluorescence from the fuel film decreased as the fuel evaporated. Therefore, the main limitation of this technique was present only analysing transient fuel films and multiple injections, where there is airborne fuel above the film. Another limitation of this technique concerns the strong presence of the laser beam pattern in the images, producing bright and dark areas for points with the same thickness introducing errors to the system. These issues contributed to problems experienced in achieving plausible quantitative data in that study.

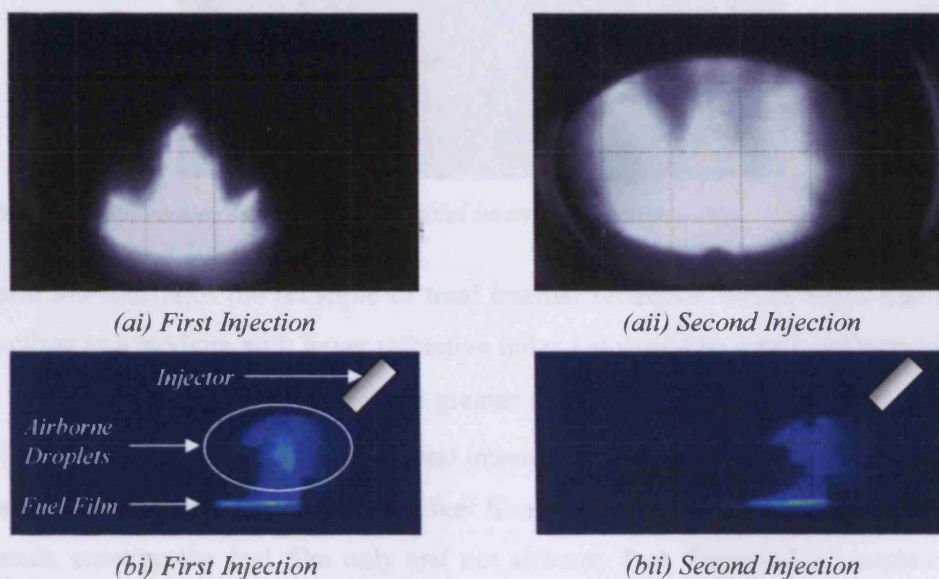
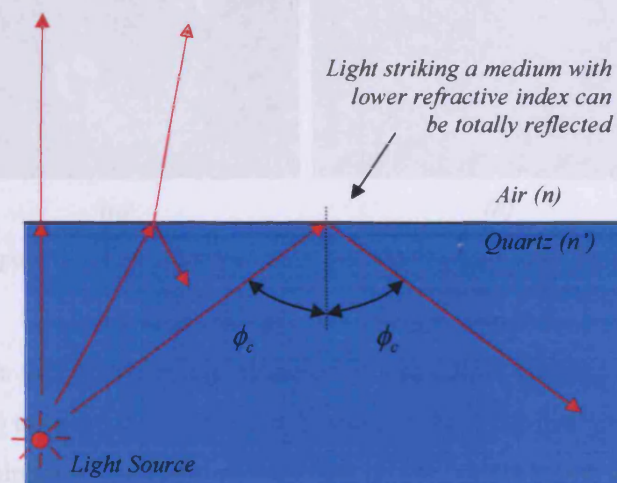


Figure 3-2: Fluorescent images for impingement studies reported by Kay (2006b): (a) Footprint image of fuel film, (b) Side View of the Spray above the quartz piston.

In order to improve the technique proposed by Kay to allow characterisation of liquid fuel films throughout the injection event (even in the presence of airborne fuel above the film deposits), three major development areas were identified. The three areas of potential improvement are discussed below along with the proposed solutions:

*a) Illumination of airborne droplets*

To avoid a fluorescent signal from airborne fuel above the fuel film, the propagation of the laser beam needs to be carefully controlled so that only excitation of the fuel film takes place. With the optical configuration proposed by Kay (Figure 3-1), the optical path of the laser beam is normal to the measurement surface, for which it will always excite airborne droplets above the fuel film, even if the laser power is reduced to a minimum. Therefore, this thesis proposes a new optical configuration which uses total internal reflection to control the propagation of the laser beam.



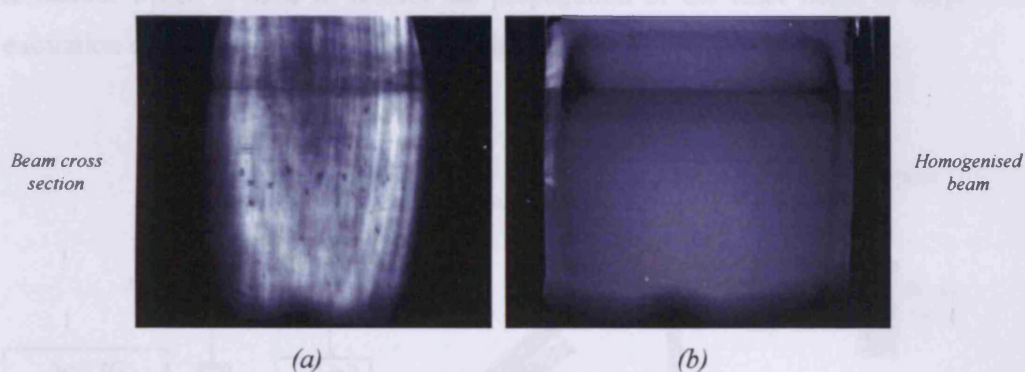
**Figure 3-3:** Schematic of the principle of total internal reflection

Figure 3-3 illustrates the principle of total internal reflection which states that light travelling to a medium with lower refractive index ( $n$ ) would be totally reflected from the interface if the incidence angle is greater than the critical angle  $\phi_c$ . Even if the incident angle is such that it ensures total internal reflection, a fraction of light would cross the 'quartz-fuel' interface of the fuel film due to the similarity in the refractive indexes, exciting the fuel film only and not airborne fuel. Section 3.1.3 explains in detail the benefits of total internal reflection for characterisation of fuel films by LIF.



### b) *Inhomogeneous beam profile*

Significant errors were reported by Kay (2006) concerning the non-uniformity of intensity in the images due to the burning pattern of the laser. Essentially, for a uniform fuel film, there are bright and dark areas in the images due to the Gaussian beam profile of the laser through which the laser power is more concentrated in some areas than others. Figure 3-4a shows the beam profile of the laser when illuminating a uniform fuel film on the interrogation zone. It is clear that there is more concentration of power in the bottom and right of the image. Quantitative results using this beam profile would suggest that the fuel film is thicker on the bottom and right region which makes little sense for an evenly distributed fuel film.



**Figure 3-4:** Comparison of the illumination of the interrogation zone (b) with and (a) without the UV diffuser.

In order to solve this problem it is proposed to use a light shaping UV beam diffuser (described later) to make the beam more homogeneous ('top hat' profile). Figure 3-4b shows the illumination of a uniform fuel film on the interrogation zone using the UV diffuser. The benefit of using the UV diffuser is clear and instantly recognizable as the signal intensity is significantly more uniform across the impingement plane. There is a reduction in laser power when using the UV diffuser (around 30%), which is affordable considering the improvements in laser power distribution.

### c) *'Shot-to-shot' variation of laser power:*

The specification of the Nd:YAG laser available for this experiment states that the nominal energy of this laser can vary up to 9 % between pulses when running at 266 nm. Since the intensity of the fluorescent signal is directly proportional to the laser

power, it is important to account for this variation in the calibration of the images. Therefore, it is proposed to use an Energy Pulse Monitor (EPM) to record the instantaneous power of the laser corresponding to each image, to correct for the 'shot-to-shot' power variation during the calibration process.

### 3.1.2. New Optical Configuration

Figure 3-5 shows the schematic of the optical configuration proposed in this thesis where all the limitations observed in the technique proposed by Kay (2006b) have been addressed. Though all have an appreciable effect in reducing the quantitative significance of the data, probably the most influential, is the principle of total internal reflection which is used to control the propagation of the laser beam to target the excitation of the fuel film only (and not airborne fuel).

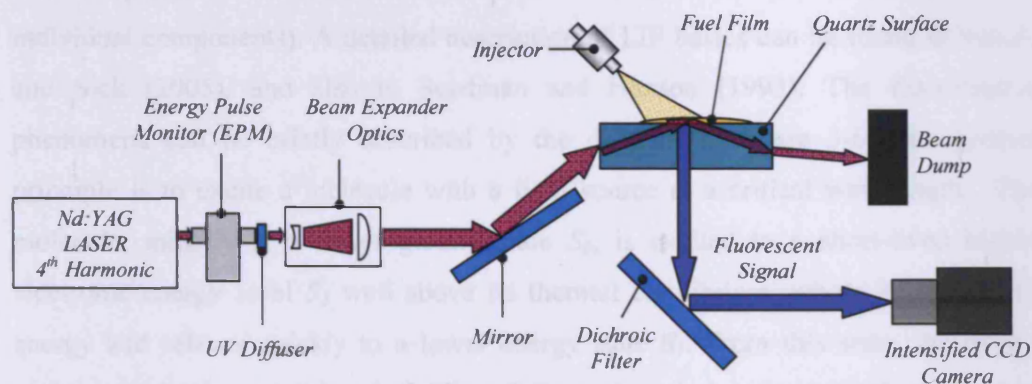


**Figure 3-5:** Schematic of the TIR-LIF optical configuration

A frequency quadrupled Nd:Yag (266 nm) is used as the excitation light source. The laser pulse duration is 5 ns. In order to increase the size of the interrogation area, the nominal beam diameter of 8 mm is expanded to 40 mm using a plano-concave singlet lens (Melles Griot: 01 LQP 003) and a plano-convex singlet lens (Melles Griot: 01LQP027). This allows the illumination of an area large enough to accommodate illumination of the whole fuel film. Fluorescent images are acquired from several cycles and 'phase-averaged' in order to build a full map of the transient fuel film. The fluorescence signal is acquired through a 50mm Nikkor Lens (f/1:4) onto a Hamamatsu gated image intensifier, linked to a Hamamatsu HiSense Mk II CCD camera with a resolution of 1344x1024 pixels. A 400 nm short band pass filter



(Schott BG4 glass) is used to optimise the fluorescence signal from the excited fuel film. In addition, specially coated mirrors are used to maximise the transmittance of both laser the excitation light (266 nm), and the fluorescence signals (400 nm). An Energy Pulse Monitor (EPM) is used before the beam expansion to account for laser power fluctuations ('shot-to-shot' variation). A 5° full width half maximum (FWHM) light shaping UV diffuser optic (Bfi Optilas: L5HPS3-25) is used to attenuate the typically uneven power distribution of the Nd:Yag laser beam pattern. The following sections describe the TIR-LIF technique in detail.

#### 3.1.3. Principles of Laser Induced Fluorescence (LIF)

Laser Induced Fluorescence (LIF) is a widely used and extremely useful technique for quantitative or semi-quantitative analysis of transient flows, providing spatially and temporally resolved information in a desired plane, for example: fuel concentration, fuel temperature, air-to-fuel ratio, and fuel composition (i.e. concentration of individual components). A detailed description of LIF basics can be found in Schulz and Sick (2005), and also in Seitzman and Hanson (1993). The fluorescence phenomena can be briefly described by the diagram in figure 3-6. The general principle is to excite a molecule with a light source at a critical wavelength. The molecule, initially at a lower ground state  $S_0$ , is excited to a short-lived higher electronic energy level  $S_2$  well above its thermal equilibrium, where it loses some energy and relaxes quickly to a lower energy state  $S_1$ . From this state, the excess energy can be lost via chemical (dissociation, photo-induced reaction) or physical processes, such as: radiative processes, non-radiative processes, and collisional quenching. In the radiative process, the excess energy (or part of it) is lost by spontaneous emission of a photon. The emission of a photon (which returns the molecule to its more stable ground state  $S_0$ ) can be observed as fluorescence. For organic molecules, the emission wavelength is usually red-shifted (Stokes-shifted) compared with the absorption wavelength due to non-radiative decay occurring prior to fluorescence (non-radiative decay processes involve the lost of excess energy by vibrational and rotational energy transfer). For practical LIF experiments, the excitation wavelength needs to be carefully selected so it matches with the absorption wavelength of the substance in study.

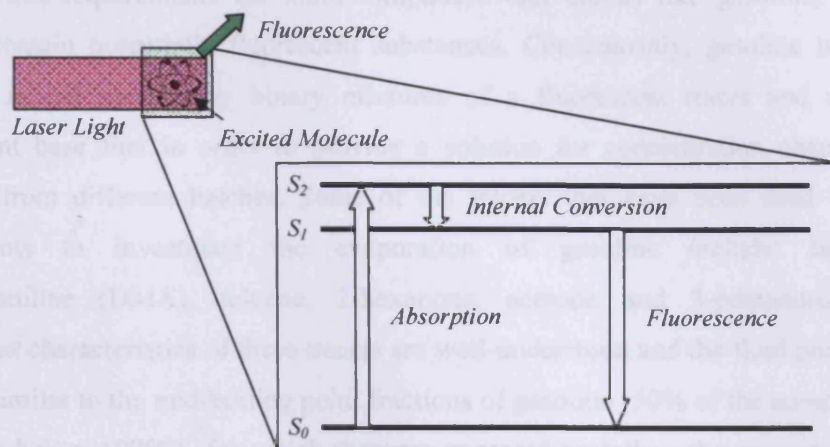


**Figure 3-6:** Principle of Laser Induced Fluorescence

The number of photons emitted is directly proportional to the number of excited molecules and consequently proportional to the concentration of the substance. Therefore, the fluorescence phenomenon can be used to investigate the presence and concentration of a specific component in either the liquid or vapour phase. The Laser induced fluorescence technique has been used extensively as a diagnostic tool in automotive applications, from in-cylinder spray characterisation (e.g. De Sercey et al 2005, Fujikawa et al 1999, Richter et al 1998), fuel film diagnostics (e.g. Cho and Min 2003, Kull et al 1999, Hentshel et al 1997, Le Coz 1994, Meingast et al 2001), and fuel temperature distribution measurements (e.g. Einecke et al 2000, Fujikawa et al 2006) among other in-cylinder characteristics. Depending on the application, the selection of the tracer and tracer concentration is crucial for plausible quantitative results. The following sections discuss the criteria for tracer selection along with potential limitations of LIF for fuel film diagnostics.

### 3.1.3.1. Tracer Selection

The ideal tracer should yield LIF signals that are directly proportional to the desired quantity (e.g. fuel concentration, fuel/air ratio, temperature, fuel composition, residual gas concentration, etc), and the emitted fluorescence should be insensitive to pressure and temperature variations, and also insensitive to the surrounding gas composition (Schulz and Sick 2005). Additionally, the tracer should behave exactly like the fuel to which it is added in terms of evaporation, convection, diffusion, reactivity, and droplet formation. Unfortunately, in practical systems it is virtually impossible to

meet all this requirements for multi-component fuel blends like gasoline, which already contain potentially fluorescent substances. Consequently, gasoline is often replaced in LIF studies by binary mixtures of a fluorescent tracer and a non-fluorescent base fuel in order to provide a solution for concentration changes in gasoline from different batches. Some of the tracers that have been used in LIF experiments to investigate the evaporation of gasoline include: biacetyl, dimethylaniline (DMA), toluene, 2-hexanone, acetone and 3-pentanone. The fluorescent characteristics of these tracers are well-understood and the fluid properties are also similar to the mid-boiling point fractions of gasoline (50% of the components evaporate below 109°C), for which they are expected to follow the evaporation of gasoline effectively.

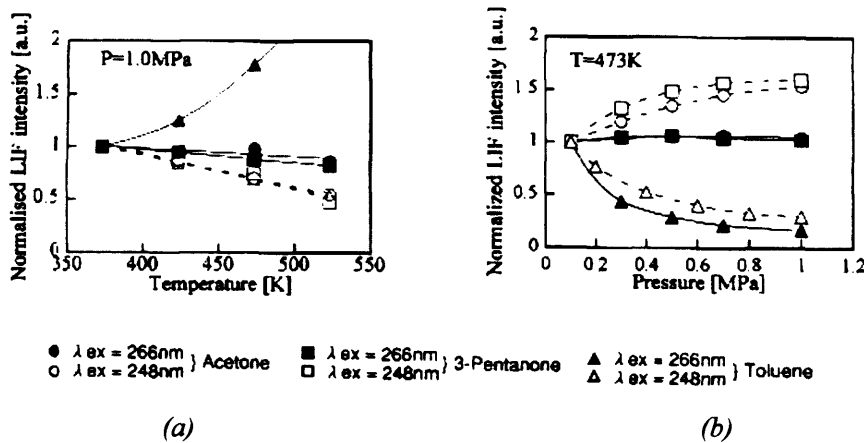


**Figure 3-7:** Variation of normalised LIF intensity illustrating the (a) Temperature and (b) Pressure effects for several dopants and excitation wavelenths (Fujikawa et al 1999)

Fujikawa et al (1999) investigated the fluorescent properties of toluene, acetone, and 3-pentanone under various temperatures and pressures (figure 3-7) and concluded that 3-pentanone fluorescence is the least sensitive to ambient condition changes in typical ranges needed for application in internal combustion engines. For this reason, 3-pentanone is selected as the fluorescence tracer in this study due to its excellent absorption characteristics when excited at 266 nm (Schulz and Sick 2005; Schulz et al 2005). Isooctane, a non-fluorescent component commonly used as a substitute for gasoline in LIF studies, is selected as a base fuel. Consequently, a binary mixture of 10 %(vol) of 3-pentanone in isooctane is used as the model fuel in this study.

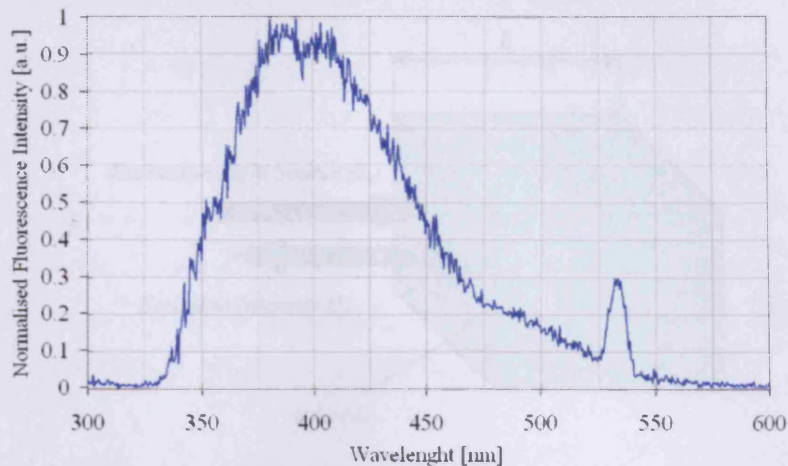


**Figure 3-8:** Fluorescence spectra of 3-pentanone excited at 266nm.

The boiling point of 3-pentanone and isooctane is 99.2 and 102.0 °C respectively, and the heat of vaporisation at 25 °C is 35.1 and 38.5 kJ/mol respectively. This mixture is widely used as a substitute of gasoline in internal combustion systems research, and it has been proven to be chemically stable under typical test conditions (e.g. Schulz and Sick 2005, Sick et al. 2005; Fujikawa et al. 1999; Le Coz and Baritaud 1994). Figure 3-8 shows the fluorescence spectra of 3-pentanone when excited at a wavelength of 266 nm. The fluorescent signal peaks around 400 nm, allowing a sufficient 'red-shift' to facilitate the separation of elastically scattered light and avoid emission reabsorption of the tracer. A second peak is observed at around 532 nm, which is the result of a second order signal at 266 nm. Therefore, by careful selection of optical filters it is possible to eliminate any residual scattering at the excitation wavelength, and any residual emission at 532 nm.

### 3.1.3.2. Quantitative LIF for Fuel Films

The application of laser induced fluorescence for characterisation of fuel films relies on the principle that upon excitation by laser light, the intensity of the fluorescent signal from a tracer is proportional to the concentration of the tracer, and also proportional to the film thickness for 'thin' layers of homogeneous mixtures. A relationship between the fluorescence emission and the excitation laser source can be established considering an elemental volume of liquid with homogeneous concentration as shown in figure 3-9.



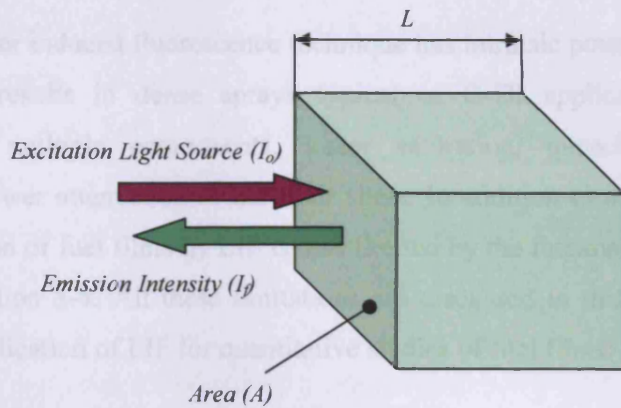


**Figure 3-9:** Schematic of elemental volume illustrating fluorescence

When a collimated light source of intensity  $I_o$  passes through a length of substance  $L$  of molar concentration  $C$ , light with intensity  $I_t$  is transmitted and some with intensity  $I_a$  is absorbed by the substance, as described by the Lambert-Beer law (equation 3-1):

$$I_t = I_o \cdot e^{(-\epsilon \cdot C \cdot L)} \quad (3-1)$$

$$I_a = I_o - I_t = I_o \left(1 - e^{(-\epsilon \cdot C \cdot L)}\right) \quad (3-2)$$

Then, the intensity of the fluorescence signal measured  $I_f$  is given by:

$$I_f = Q \cdot I_o \left(1 - e^{(-\epsilon \cdot C \cdot L)}\right) \quad (3-3)$$

where  $\epsilon$  is the molar absorption coefficient and  $Q$  is the quantum efficiency. Clearly, equation 3-3 is not linearly proportional to the concentration nor the length  $L$  of the substance (thickness for fuel films). However, for a small thicknesses ( $L$ ) and concentrations ( $C$ ), the term  $\epsilon \cdot C \cdot L$  can be considered small. Therefore, the intensity of the fluorescence signal measured can be approximated to:

$$I_f = Q \cdot I_o \cdot \epsilon \cdot C \cdot L \quad (3-4)$$

Thus, the intensity of the fluorescence signal is proportional to the product of molar concentration ( $C$ ) and film thickness ( $L$ ) for homogeneous and optically thin films, as indicated in equation 3-4.

### 3.1.3.3. Potential Limitations of LIF for fuel films

In general, the laser induced fluorescence technique has intrinsic potential limitations for quantitative results in dense sprays typical of G-DI applications, namely: fluorescence of multiple components, tracer saturation, quenching, multiple-scattering, and power attenuation of the laser sheet. In addition to these limitations, the characterisation of fuel films by LIF is also limited by the thickness of the film as indicated in equation 3-4. All these limitations are discussed in this section, in the context of the application of LIF for quantitative studies of fuel films:

a) *Fluorescence of multiple components:*

As mentioned in section 3.1.3.1 (Tracer selection), multi-component fuel blends like gasoline contain many potentially fluorescent substances with different properties in terms of volatility, transport, and especially spectral response which render calibration for quantitative LIF studies a difficult proposition. The presence of multiple fluorescent components makes emission reabsorption the principal limitation for calibration of the fluorescent intensity. This phenomenon occurs when the emission spectrum of one component overlaps the absorption spectrum of another one (or its own absorption spectrum). This has two effects: (i) it increases the fluorescent emission of the second component as, in addition to the excitation light source, it is being excited by the fluorescence of the first component, and (ii) the fluorescent emission of the first component is reduced since it is being reabsorbed by the second component. Therefore, a binary mixture of a tracer (3-pentanone) and a non-fluorescent base fuel (isooctane) is preferred as a substitute of gasoline for G-DI applications. This mixture, used in this thesis for fuel film measurements, provides a homogeneous concentration (also required in equation 3-4) of a single fluorescent component which facilitates calibration for quantitative results.

b) *Tracer Saturation:*

In practical applications, the LIF fluorescence for fuel films increases linearly with tracer concentration up to a saturation point, after which the fluorescence of the tracer decreases (e.g. Schultz and Sick 2005, De Sarcey 2004). For low laser light absorption conditions, molecules throughout control volume are equally illuminated and the whole excited volume contributes to the scattered LIF signal. In this ideal

case, the variation of the LIF signal is linearly proportional to the tracer concentration. However, Greenhalgh et al 2001 reported that in the case of stronger absorption, or stronger tracer concentration, the volume will be only partially illuminated by the laser light, producing non-linear LIF signals. Hardalupas and Domann (1999) reported strong dependency of LIF signals on dye concentration, resulting in noticeable changes in fluorescence spatial distribution for different tracer concentrations. With rising dye concentration, they observed that the fluorescence pattern shows decreasing relevance of intensity enhancement at focusing points of internal light rays and increasing effects of linear absorption on the characteristic features of the distribution. Therefore, successful implementation of LIF relies on careful selection of tracer concentration.

As indicated in equation 3-4, the fluorescence would only be linearly proportional to the concentration of the substance for small tracer concentrations. Therefore, it is crucial to determine an optimum tracer concentration within the operation conditions in study to avoid the saturation phenomenon to occur. The experiments in this thesis use a binary mixture of 10 % (vol) 3-pentanone in isooctane, also used successfully by Kay (2006b) who reported linear calibration of fluorescence and concentration of fuel films with no saturation observed for a similar experimental setup.

#### c) *Quenching:*

Quenching is an influential process which affects the fluorescent emission of an excited molecule. When a group of molecules are excited, there is a non-radiative decay process produced by collisions of excited molecules with each other, which results in the transfer of the excited electron from one molecule to another, introducing a relaxation process without emitting fluorescent light (De Sercey 2004). Quenching, and as a result fluorescence intensity, is dependent on environmental conditions (both ambient temperature and pressure) and surrounding species (e.g. oxygen). Therefore, quenching represents a potential limitation for LIF quantitative studies because it changes the relationship between fluorescence intensity and tracer concentration. For the studies reported within this thesis, both the ambient conditions and surrounding species are kept constant throughout the impingement event, for which the quenching effect is not expected to influence the linear calibration of fluorescence and tracer concentration for quantitative results.

d) *Multiple scattering:*

This phenomenon is observed in the application of laser optical techniques to dense sprays when the path to the signal receiver, the CCD camera for LIF studies, is obstructed by non-excited regions of the dense spray (Berrocal 2006). Essentially, the fluorescent signal emitted by an excited droplet is affected by droplets in the path to the camera, producing undesirable fluorescence from droplets outside the control volume or attenuating the fluorescence emitted by the irradiated drop, thus producing misleading quantitative results. Multiple scattering does not represent a limitation for LIF studies of fuel films with the proposed optical configuration (figure 3-5) since the optical path to the receiver is unobstructed at any given time, even for dense sprays.

e) *Attenuation of the laser sheet:*

The power attenuation of the laser sheet is a phenomenon that occurs in optical diagnostics of dense sprays when the exciting laser sheet is absorbed as it traverses the spray, attenuating the excitation energy available for the further regions of the spray. As a result, images of dense sprays often show a decay in fluorescence intensity as the laser sheet penetrates the spray, producing misleading interpretation of the tracer distribution. For example, for a symmetric dense spray, a LIF intensity image might show one side of the spray brighter than the other suggesting an asymmetric distribution of fuel. For fuel films experiments in this thesis, the current configuration (figure 3-5) ensures that exciting laser beam propagates directly into the fuel film, thus, the laser power should not be significantly affected providing the film is 'optically thin' (discussed below).

f) *Fuel film not optically 'thin':*

Similarly to the tracer saturation phenomenon, the thickness of the film is linearly proportional to the fluorescence intensity only for optically 'thin' fuel films (equation 3-4). Kay (2006b) investigated the relationship between the intensity of the fluorescence signal and film thickness for homogeneous and optically thin films. He reported a linear ratio between thickness and fluorescence signal of 3-pentanone up to 500  $\mu\text{m}$ . Hentschel et al (1997) proved linearly between thickness and fluorescence for gasoline films of up to 300  $\mu\text{m}$ . Initial visualisation tests of the injector in this study provides information concerning the footprint size of the film deposited, and



given that the total mass injected is known, the film thickness is estimated to be smaller than 150 microns, well within the linear regime.

### 3.1.4. Total Internal Reflection Method (TIR-LIF)

In order to avoid a fluorescence signal from airborne droplets, the propagation of the excitation laser beam must be controlled such that only excitation of the fuel film takes place. This thesis proposes using the principle of total internal reflection to eliminate or minimise this source of error (figure 3-3). When light strikes a medium with lower refractive index,  $n$ , from a medium with higher refractive index,  $n'$ , (interface quartz-air), it will be totally reflected if the incident angle is larger than the critical angle determined by the Snell law (equation 3-5).

$$\sin(\phi_c) = \frac{n}{n'} \quad (3-5)$$

Previous work by Alonso et al (2008a), Cho and Min (2003), and Kull et al. (1999), used the LIF technique to visualize fuel films on quartz surfaces, and showed that even if the incident angle of the light is such that it produces total internal reflection, part of the light can propagate from the quartz into the fuel due to the similarity in the refractive indices. This happens because the path of light hardly changes when it propagates into media with similar refractive indices. The proportion of light transmitted into the liquid film can be calculated from the Fresnel equations, so the transmittance of the electromagnetic field for parallel and rectangular polarisation is given by:

$$T_{\parallel}(\phi_i) = \frac{2 \cdot n_{rel} \cdot \cos(\phi_i)}{n_{rel}^2 \cdot \cos(\phi_i) + \sqrt{n_{rel}^2 - \sin^2(\phi_i)}} \quad (3-6)$$

$$T_{\perp}(\phi_i) = \frac{2 \cdot \cos(\phi_i)}{\sqrt{n_{rel}^2 - \sin^2(\phi_i)} + \cos(\phi_i)} \quad (3-7)$$

where  $n_{rel} = n/n'$  and  $\phi_i$  corresponds to the incident angle of light. Additionally, the ratio of the beam areas of the incident and transmitted beams is given by:

$$F_a(\phi_i) = \frac{\sqrt{n_{rel}^2 - \sin^2(\phi_i)}}{n_{rel}^2 \cos^2(\phi_i)} \quad (3-8)$$

Thus, the relative intensity of the laser light penetrating into the liquid film can be written as a function of the incident angle using the following equations:

$$I = T^2(\phi_i) \cdot F_a(\phi_i) \cdot n_{rel} \quad (3-9)$$

$$I_{\perp} = T_{\perp}^2(\phi_i) \cdot F_a(\phi_i) \cdot n_{rel} \quad (3-10)$$

Figure 3-10 shows the transmission in the quartz-fuel interface as a function of the incident angle for a UV graded quartz of refractive index 1.499 and the binary mixture of iso-octane and 3-pentanone of refractive index 1.392. Given that the critical angle to ensure total internal reflection is  $43.81^{\circ}$ , and figure 3-10 shows no transmittance in quartz-fuel interface above  $69^{\circ}$ , the angle of incidence needs to be selected between these values. Based on an iterative experimental process, the optimum angle of incidence found for this experiment is  $65^{\circ}$ , which was the maximum angle at which the fluorescent signal was observed undiminished.

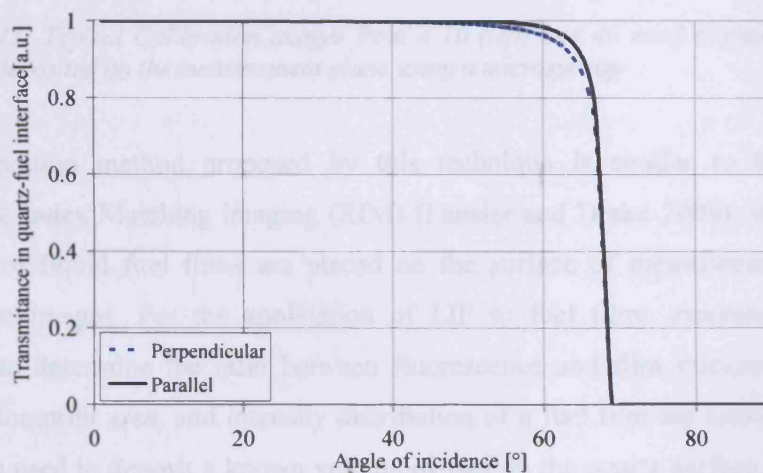


**Figure 3-10:** Normalised transmittance in the quartz-fuel interface as a function of the incident angle.

Cho and Min (2003) showed that after passing the fuel layer and exciting the fuel film, the light interacts with the fuel-air interface, and is totally reflected. They concluded that if the curvature of the fuel film surface is small, the light is totally reflected because of the large difference in the refractive indices. Thus the light only excites the fuel on the piston and there is no fluorescence contribution from airborne droplets.

### 3.1.5. TIR-LIF Calibration

As stated in the previous section, the intensity of fluorescence emitted by 3-pentanone excited at 266 nm would be linearly proportional to its concentration, and hence proportional to the volume for a 'thin' film layer of a homogeneous mixture. Therefore, to calibrate this technique it is essential to determine the ratio between the fluorescence signal emitted and the corresponding liquid film concentration.

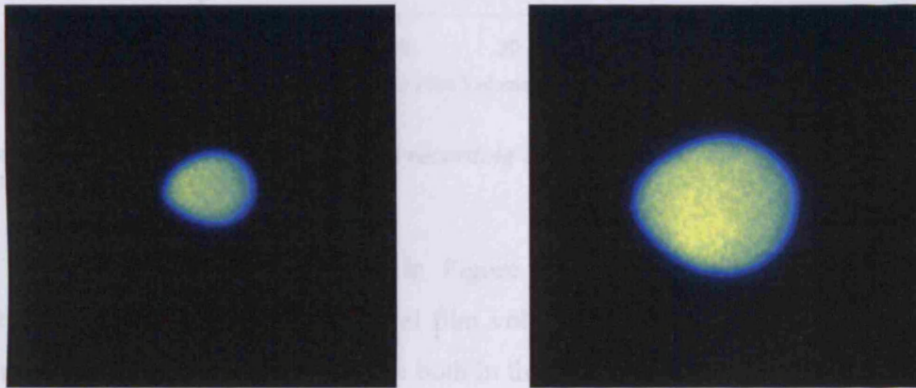


*Figure 3-11: Typical Calibration images from a 10 (left) and 40 mm<sup>3</sup> (right) 3-pentanone fuel films deposited on the measurement plane using a microsyringe*

The calibration method proposed by this technique is similar to that used in Refractive Index Matching imaging (RIM) (Fansler and Drake 2006), where known volumes of liquid fuel films are placed on the surface of measurement to obtain calibration images. For the application of LIF to fuel films measurements, it is possible to determine the ratio between fluorescence and film thickness when the volume, footprint area, and intensity distribution of a fuel film are known. A microsyringe is used to deposit a known volume of fuel on the quartz surface. Figure 3-11 shows a typical image used for the calibration of this technique, after subtracting the background. Given that the injection volume is known, the fluorescent signal of various volumes from 10 to 50 micro-litres is acquired to build a calibration curve representative for each case study.



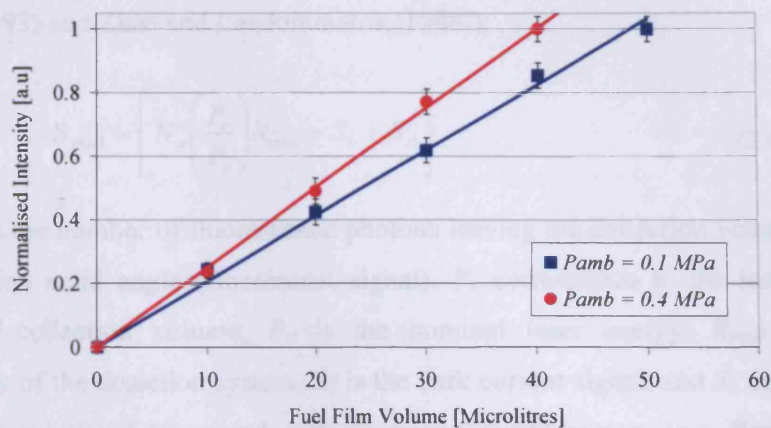


**Figure 3-12:** Calibration curve obtained recording intensity values for different fuel films of the 3-pentanone and isooctane mixture.

The calibration curve is presented in Figure 3-12, which demonstrates a linear relationship between intensity and fuel film volume. Additionally, the output power of the laser is recorded for each image both in the calibration and experimental stages so this information could be used in post-processing.

The minimum film thickness to be measured depends on the calibration of the acquisition system. Depending on the range of thicknesses of interest, the image intensifier is used to amplify (or reduce) the fluorescent intensity to accommodate the signal within the colour range of the camera. In this thesis, the images are processed as 8 bit, which offers 256 colours, or 256 levels of thickness. The system was calibrated to measure fluorescent peaks of up to 200  $\mu\text{m}$  (greater thicknesses would 'white out' the image). Therefore, the minimum thickness to be measured in this thesis is around 1  $\mu\text{m}$ . However, for different applications, or different tracer concentrations, the system could be calibrated for better resolution in a different order of magnitude (i.e. theoretically, for films between 1 and 10 microns, using 256 steps would provide a minimum quantitative measurement of approx. 0.04 microns).

### 3.1.6. TIR-LIF Post-Processing Methodology

In order to obtain quantitative information from TIR-LIF, the raw images require post-processing. The image calibration sequence proposed for the TIR-LIF technique is presented in figure 3-13. The first step of post-processing involves the removal of systematic errors present in the imaging system. The digital signal recorded for a

single pixel of a CCD camera during LIF experiments is expressed as (Seitzman and Hanson (1993) and Zhao and Landommatos (1998)):

$$S_{pixel} = \left[ N_p \left( \frac{P_c}{P_o} \right) R_{total} + S_b + S_d \right] \quad (3-11)$$

where  $N_p$  is the number of fluorescence photons leaving the collection volume within the collection solid angle (fluorescent signal),  $P_c$  corresponds to the laser energy within the collection volume,  $P_o$  is the nominal laser energy,  $R_{total}$  the total responsivity of the detection system,  $S_d$  is the dark current signal, and  $S_b$  corresponds the background signal associated with the laser induced process (e.g. Rayleigh and Mie scatterings, window fluorescence, and ambient light).

Rearranging equation 3-11 for the fluorescence we obtain:

$$N_p = [S_{pixel} - (S_b + S_d)] \cdot \left( \frac{P_o}{P_c} \right) \left( \frac{1}{R_{total}} \right) \quad (3-12)$$

Equation 3-12 suggests a suitable procedure for correcting systematic errors in the recorded image. First, an image combining the background and dark current signals ( $S_b+S_d$ ) is subtracted from the recorded image.

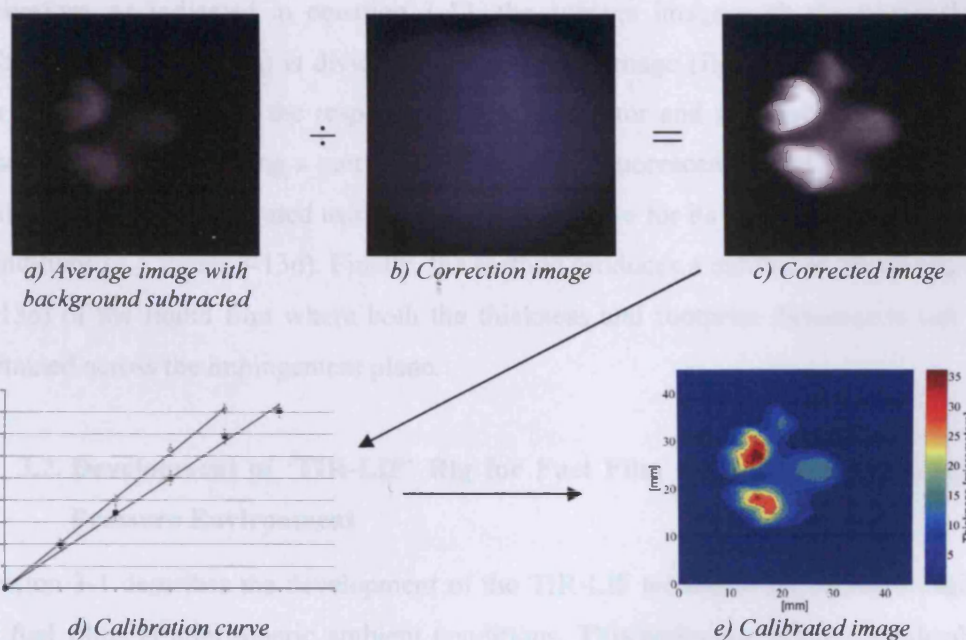


**Figure 3-13: Image Processing sequence (TIR-LIF image for time = 1.75 ms ASOI and  $P_a = 0.1$  MPa)**

This image can be obtained by removing the fluorescent particles from the interrogation area. An average background image is preferred to minimise the effect of shot-to-shot variation. Even though the resolution of the camera is 1344 x 1024 pixels, for the current experimental setup it was impossible to zoom close enough to the interrogation zone to make use of the full resolution within the 45 x 45 mm measurement area. Therefore, all images are cropped to size from slightly bigger images, for which the active resolution of the acquisition system is 675 x 664 pixels. Figure 3-13a shows an average of 20 cropped images resulting from subtracting the average background image from each raw image. Subsequently, the resulting image needs to be multiplied by a correction image to account for the spatial variations in the responsivity of the detector ( $R_{total}$ ), and also multiplied by another corrector factor to account for non-uniformities of the laser source ( $P_c/P_o$ ). Zhao and Landommatos (1998) propose recording the combined effect of the responsivity of the detector and the non-uniformities of the laser source by obtaining an image from a homogeneous mixture containing fluorescent particles ( $S_{uni}$ ) minus the background image ( $S_b+S_d$ ). Thus, the fluorescent signal of each pixel may be rewritten as:

$$N_p = \frac{[S_{pixel} - (S_b + S_d)]}{[S_{uni} - (S_b + S_d)]} \quad (3-13)$$

Therefore, as indicated in equation 3-13, the average image with the background subtracted (figure 3-13a) is divided by a correction image (figure 3-13b) to account for spatial variations in the responsivity of the detector and non-uniformities of the laser sheet, thus obtaining a corrected image of the fluorescent signal (figure 3-13c). This image can be calibrated using the calibration curve for its corresponding ambient conditions (e.g figure 3-13d). Finally, the method produces a calibrated image (figure 3-13e) of the liquid film where both the thickness and footprint dimensions can be obtained across the impingement plane.

### **3.2. Development of 'TIR-LIF' Rig for Fuel Film Quantification in a High Pressure Environment**

Section 3-1 describes the development of the TIR-LIF technique for characterisation of fuel films at atmospheric ambient conditions. This technique offers considerable potential for analysis of fuel films and validation of CFD models at atmospheric

ambient pressure. However, for gasoline direct injection applications at stratified charge, the fuel is injected late in the compression stroke for which it is necessary to investigate the behaviour of the resulting fuel film at elevated ambient pressures. This section describes the development of the 'TIR-LIF' rig for fuel film studies at elevated ambient conditions. In order to control the ambient pressure and temperature independently, the TIR-LIF was adapted for use within an established high-pressure high-temperature (HP-HT) rig.

### 3.2.1. The High Pressure High Temperature (HP-HT) Rig

The Cardiff University high-pressure high-temperature rig (figure 3-14) was designed and commissioned by Comer (1999), and subsequently used by Coleman (2002), Morris (2003), and Kay (2006b) for characterisation of sprays under atmospheric and elevated ambient conditions relevant to G-DI applications. The rig is a constant volume pressure vessel which has been commissioned to allow independent control of ambient temperatures up to 423 K, and ambient pressures up to 1.5 MPa, though the facility is designed to accommodate higher ambient conditions. It has four large windows specifically positioned along its circumference to provide considerable optical access for a wide range of non-intrusive optical diagnostic techniques. All windows are made from fused silica quartz to ensure transmission in a wide range of wavelengths (transmission > 90 % for 200 nm – 2200 nm). The windows are polished to very high tolerances (40 micron scratch / 20 micron dig, flatness 2 lambdas or less) to minimise unwanted reflections. Two of the windows are positioned opposite to each other, and a small window is positioned perpendicular to them to allow laser sheet optical diagnostics (e.g. PIV, LIF), planar imaging and shadowgraphy (figure 3-14b). The other window is set at 70 °; specifically designed for characterisation of gasoline and diesel sprays using Phase Doppler Anemometry (PDA) (figure 3-14a). This angle represents a compromise between the optimum Brewster angle for gasoline (68 °), and for diesel (72 °), which is the angle at which the scattered light is generally collected for PDA applications. The Brewster angle is the angle at which no parallel polarised light is reflected, thus minimising the contribution from reflected light.



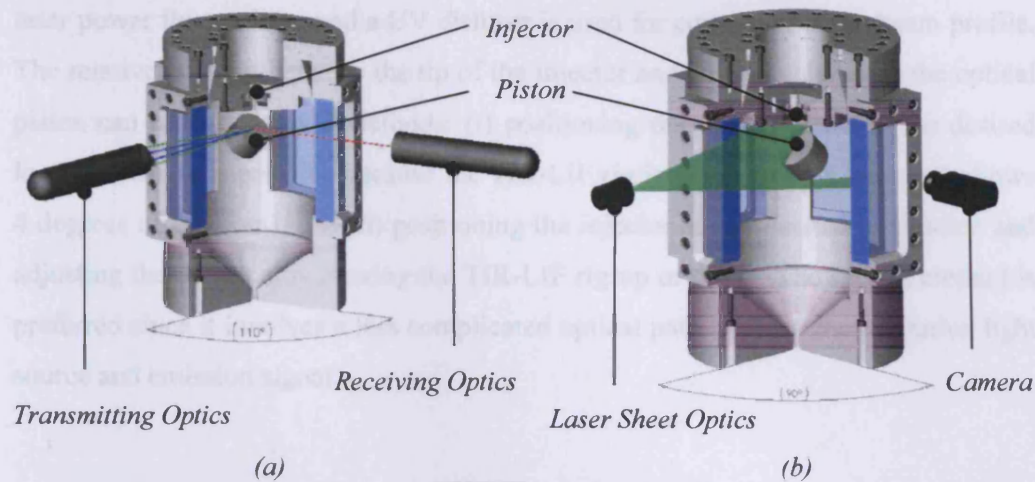


**Figure 3-14:** Schematic of the HP-HT rig: (a) PDA System, (b) Planar Imaging Techniques (e.g. PIV, LIF, etc)

The rig is purged with a constant flow of air (130 l/min) in order to avoid the recirculation of droplets and prevent the build-up of vapour concentration. The air purge also creates an air ‘curtain’ along the windows of the rig which prevents accumulation of fuel on the windows, without disturbing the air around the spray in the centre of the rig (Comer 1999). For experiments at elevated pressure, a high pressure air purge is connected to the rig and ‘throttled’ to control the ambient pressure as desired, ensuring a continuous air flow. For experiments at elevated temperature, a 24 kW electric heater supplied with dry air is connected to the rig to pre-heat the purge air. A PID controller is used to allow accurate control of the heating elements, and thus control of the temperature inside the rig, using feedback from a thermocouple installed near the centre of the rig. Detailed information about the rig design can be found in Comer (1999). Also, further information about the air heater for experiments at elevated temperature may be found in Gruenberger (2000).

### 3.2.2. Modification of TIR-LIF Rig for use within the HP-HT rig

For analysis of fuel films under elevated ambient conditions, the TIR-LIF rig was integrated into the dedicated HP-HT rig to controllably vary the ambient pressure. Figure 3-15 shows the proposed optical setup for experiments at elevated pressures. Similar to the configuration for ambient conditions (figure 3-5), a Nd:YAG laser is used as the excitation light source at wavelength 266 nm. Also, as described in section 3.1.2, the beam is expanded from 8 to 40 mm, an EPM is used to monitor



laser power fluctuations, and a UV diffuser is used for correction of the beam profile. The relative position between the tip of the injector and control volume on the optical piston can be varied via 2 methods: (i) positioning the optical piston at the desired location (which is possible because the TIR-LIF rig is mounted on a joint that allows 4 degrees of freedom), and (ii) positioning the injector at any desired orientation and adjusting the distance by moving the TIR-LIF rig up or down. The second method is preferred since it involves a less complicated optical path both for the excitation light source and emission signal.

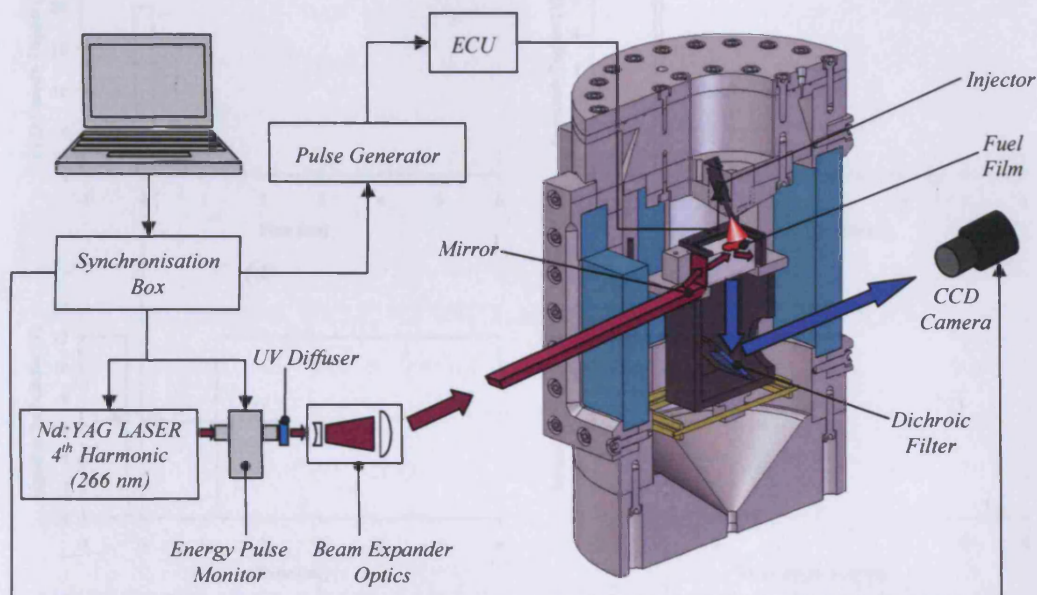


**Figure 3-15:** Experimental setup for impingement experiments at elevated ambient pressures

The CCD camera is positioned on a tripod and focused on the control volume through a 45 ° dichroic mirror. Since the maximum repetition rate of the camera is 5 Hz, images are acquired from several cycles in order to build a full map of the transient fuel film. Therefore, timing of the camera, injector, laser, image intensifier and energy pulse monitor is synchronised as shown in figure 3-16. Essentially, the computer triggers the CCD camera (figure 3-16a), and after a pre-specified delay, it triggers the Q-switch of the laser (figure 3-16c). This ensures that the pulse of the laser (approx. 4-5 ns) is within the corresponding frame (exposure time 5 μs). The image intensifier is triggered from the CCD camera pulse (figure 3-16d), and remains open for 200 ns to include the laser pulse. The camera pulse is also used to trigger the

EPM, which records the laser intensity for the duration of the frame (5  $\mu$ s). Simultaneously, the camera pulse is used again to trigger the injector for the following cycle (figure 3-16b). Therefore, a desired time After Start Of Injection (ASOI) can be achieved setting a user defined delay, given by the frequency of the system (5 Hz) minus the time delay  $\Delta t$ . For example, for synchronisation at 0.25 ms ASOI, the user defined delay to the injector pulse would be 200 ms minus 0.25 ms (199.75 ms).

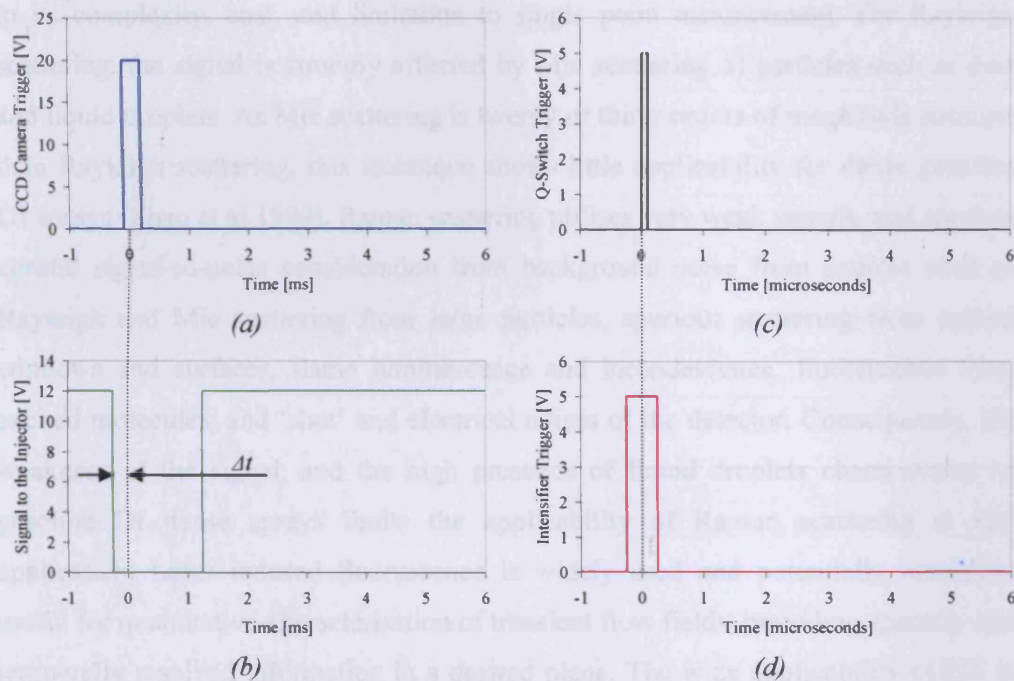


**Figure 3-16:** Schematic showing the system synchronisation: (a) CCD camera trigger, (b) Signal to the injector, (c) Laser Q-switch, (d) Image intensifier trigger.

### 3.3. Development of Optical Rig for Characterisation of Vapour Fractions

The mixture preparation process governs the operating characteristics of an internal combustion engine, and it has direct influence on its fuel consumption, exhaust emissions, performance, and efficiency. This process is of particular importance for gasoline engines because it is crucial to ensure there is a combustible mixture in the vicinity of the spark plug to ignite in every cycle. For this reason it is essential to have a good understanding of the spray development, both temporally and spatially,

particularly of vapour fractions near the spark plug region, in order to contribute to and optimise design improvements for future gasoline DI engines.

Quantifying vapour concentrations in dense gasoline DI sprays is challenging for most contemporary optical diagnostic methods, mainly because the presence of liquid droplets can significantly affect the vapour signal. Some of the techniques available in the literature to quantify vapour fractions in multiphase systems are: Rayleigh scattering, Raman scattering, Coherent Anti Stokes Raman Spectroscopy (CARS), and Laser induced Fluorescence (LIF). CARS is rarely used in engines research due to its complexity, cost, and limitation to single point measurement. For Rayleigh scattering, the signal is strongly affected by Mie scattering of particles such as dust and liquid droplets. As Mie scattering is twenty or thirty orders of magnitude stronger than Rayleigh scattering, this technique shows little applicability for dense gasoline DI sprays (Zhao et al 1999). Raman scattering utilises very weak signals, and requires careful signal-to-noise consideration from background noise from sources such as Rayleigh and Mie scattering from large particles, spurious scattering from optical windows and surfaces, flame luminescence and incandescence, fluorescence from excited molecules, and 'shot' and electrical noises of the detector. Consequently, the weakness of the signal, and the high presence of liquid droplets characteristic of gasoline DI dense sprays limits the applicability of Raman scattering to this application. Laser induced fluorescence is widely used and potentially extremely useful for quantitative characterisation of transient flow fields, providing spatially and temporally resolved information in a desired plane. The wide applicability of LIF is due to the strength of the signal compared to Rayleigh and Raman scattering.

An extension of the LIF diagnostic technique known as Laser Induced Exciplex Fluorescence (LIEF) was proposed by Melton (1983) to investigate the evaporation process of liquid sprays. This technique provides spectral separation of liquid and vapour phases, allowing for independent analysis of the vapour fractions of the spray. The following sections discuss the applicability of LIEF for spark-ignition direct-injection sprays, with detailed consideration of the potential limitations for quantitative results.

### 3.3.1. Principles of Laser Induced Exciplex Fluorescence (LIEF)

The LIEF technique has the unique capability of producing spectrally separated fluorescence signals from both liquid and vapour phases of a spray, providing temporal and spatial resolution of both species simultaneously. The technique requires two tracers to act as an electronic donor and acceptor pair forming an 'excited complex' upon excitation by laser light. The complex only reaches equilibrium in the liquid phase and produces a red-shifted fluorescence which allows characterisation of this phase. Characterisation of the vapour phase is performed by tracking the fluorescence signal of the monomers.

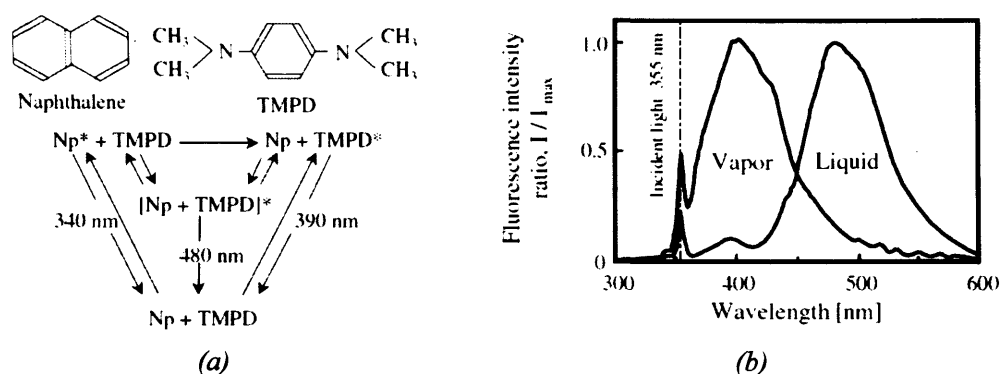


**Figure 3-17:** Photophysics of the TMPD/Np exciplex system proposed by Melton (a), and Fluorescence Spectra for liquid and vapour phases (b) (Fujimoto et al 2002)

Melton (1983) proposed the use of N,N,N',N'- tetramethyl-p-phenyldiamine (TMPD) and naphthalene (Np) as exciplex fluorescent tracers for diesel applications (figure 3-17). Together, they form a loosely bound complex in the liquid phase that produces a red-shifted fluorescence band when excited with UV laser light ( $[TMPD + Np]^*$ ). The monomer fluorescence of these tracers ( $TMPD^*$  and  $Np^*$ ), used as a vapour marker, peaks around 390 nm when excited with laser light at 355 nm. On the other hand, the exciplex compound fluorescence peaks around 480 nm for the same excitation wavelength. Therefore, the liquid and vapour signals can be spectrally separated with careful selection of optical filters. Detailed description of the LIEF technique can be found in Melton (1993), Fujimoto et al (2002), and Melton and Verdieck (1994).

### 3.3.1.1. Tracer Selection

The TMPD-naphthalene exciplex tracer combination has been used extensively in the literature for diesel applications (e.g. Melton and Verdieck (1984), Fujimoto et al (2002), Felton et al (1993), Kim et al (2003), Bruneaux (2001), and Senda et al (1992)). However, the boiling point of these organic compounds is very high compared to the mid-boiling points of gasoline. For this reason, these tracers are poorly suited for characterisation of gasoline sprays, as they would not replicate evaporation effectively. Melton (1993) proposes using a combination of triethylamine (TEA) and fluorobenzene (FB) in isooctane as fluorescence tracers suitable for gasoline applications. Although the co-evaporation of those tracers is excellent to replicate the evaporation process of gasoline, Melton reports considerable interference between the liquid and vapour signals. Ghandhi et al (1994) uses a solution of fluorobenzene and Diethyl-methyl-amine (DEMA) in hexane to investigate a gasoline spray. The boiling point of these components (358, 338, and 342 K respectively) is similar to that of gasoline. They compare the evaporation characteristics of FB/DEMA in hexane with FB/TEA in isooctane and conclude that fluorobenzene displays a better co-evaporation in mixture with DEMA and hexane. Bae et al (2004) also uses DEMA and FB in hexane to investigate a gasoline spray, performing experiments in a nitrogen atmosphere to prevent quenching as fluorobenzene's fluorescence is extremely sensitive to oxygen. For the same tracer, Wieske et al (2006) report that the crosstalk from the liquid phase signal into the spectral detection range of the vapour phase is strongly influenced by the liquid phase temperature. Hence, the liquid temperature is recorded simultaneously in order to correct for this 'crosstalk'.

Leipertz et al (1998) propose TEA and benzene as a suitable exciplex tracer combination for gasoline studies. These tracers have very similar properties to isooctane and thus are excellent choices for simulating the evaporation characteristics of gasoline. They studied the combination of TEA and benzene very thoroughly publishing dependency of the tracers on temperature, partial pressure of nitrogen, partial pressure of oxygen, laser intensity, partial pressure of CO<sub>2</sub> and H<sub>2</sub>O, and air fuel ratio. They report strong fluorescence quenching in oxygen presence, which is used to characterise air/fuel ratio. Again, considerable interference between vapour and liquid signal is reported, but the authors claim to achieve an unambiguous



separation of the liquid phase fluorescence. Following the proposal of this tracer, it has been applied successfully by other researchers to investigate the evaporation of gasoline sprays in direct injection optical engines (e.g. Alonso et al 2008b, Kornmesser et al 2001, Gervais and Gastaldi 2002).

The combination of triethylamine and benzene proposed by Leipertz et al. (1998) was chosen from all the exciplex tracers available in the literature for its similar properties to the mid-boiling point fractions of gasoline. A solution of these tracers in iso-octane can be expected to replicate gasoline vaporisation effectively. Also, the well documented characteristics and reported limitations of this tracer combination inspires confidence for plausible quantitative results.

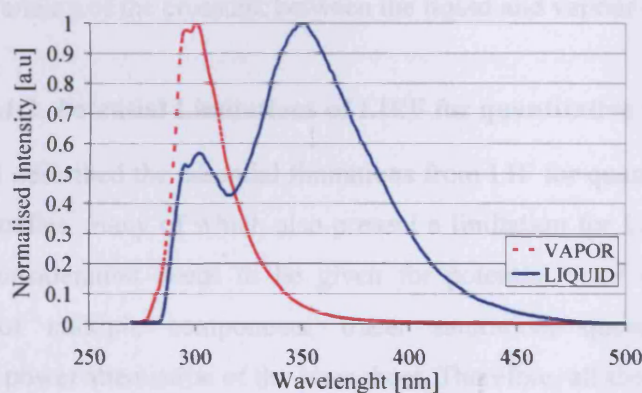


**Figure 3-18:** Normalised fluorescence spectra of 2% TEA, and 2.9% benzene in isooctane. Note that the fluorescence of the vapour and liquid phases are not in the same scale.

The relative concentration of each component used throughout the experiments is: 2% of TEA, 2.9% benzene and 95.1% of iso-octane (all percentages by weight). Figure 3-18 shows the fluorescence spectra for the vapour and liquid phases of the exciplex solution, obtained with a Perkin Elmer LS50B Spectrometer. Although the signals are superimposed in this figure, no conclusions should be drawn regarding the relative intensity of the liquid and vapour signals. The fluorescence spectra on figure 3-18 shows a clear red-shift of the liquid fluorescence of about 50 nm. The vapour fluorescence peaks at 300 nm while the liquid signal peaks at 355 nm. At 355 nm, the vapour fluorescence is negligible, allowing complete separation of the liquid phase. However at 300 nm, some fluorescence of the monomers is still visible in the liquid phase, and its contribution to the fluorescence of the vapour signal is potentially significant. This 'crosstalk' between the liquid and vapour signals makes quantitative

measurements of vapour fractions very challenging. Therefore, a complete separation of the vapour phase emissions is only possible when the liquid phase emissions are recorded simultaneously, and some criterion is used in post-processing stages to identify or ignore liquid contributions in the vapour signal, which will be discussed in more detail later.

Leipertz et al (1998) demonstrated strong quenching of the fluorescence signal by oxygen. For this reason, the experiments discussed in this paper were carried out in a nitrogen atmosphere. For instance, in the presence of oxygen, high intensity could be the result of high fuel concentration, as well as low local quenching rates. For simplicity, it was decided to eliminate the quenching variable in these experiments. Studying the fluorescence in an oxygen-free nitrogen atmosphere would allow a greater understanding of the crosstalk between the liquid and vapour signals.

#### **3.3.1.2. Potential Limitations of LIEF for quantitative results**

Section 3.1.3.3 described the potential limitations from LIF for quantitative results in dense sprays studies, many of which also present a limitation for LIEF applications. Thus, some consideration needs to be given for potential error sources such as: fluorescence of multiple components, tracer saturation, quenching, multiple-scattering, and power attenuation of the laser sheet. Therefore, all these limitations are discussed here:

- The fluorescence of multiple components is an intrinsic characteristic of LIEF, which is exploited to achieve separation of liquid and vapour signals, and thus is not viewed as a limitation for quantitative results.
- The saturation effect is discussed in the calibration section (3.3.3), and shows a linear relationship in between vapour concentration and fluorescent intensity for the chosen operation conditions. No saturation of the tracers is observed for the selected tracer concentration, which was chosen to minimise the crosstalk between liquid and vapour signals.
- To minimise the effects of quenching, the experiments are performed in an 'oxygen-free' nitrogen atmosphere, as oxygen is notorious for quenching the TEA/benzene fluorescent signal.
- To account for power attenuation of the laser sheet, only the first half of the spray cone is processed (both for the liquid and vapour signal images) which

represents a shorter decay distance for the laser sheet. Since the spray structure of the pressure swirl injector in this study is symmetrical, it is assumed that the other half of the spray produces a similar fuel distribution.

In addition to these limitations, the characterisation of vapour fraction by LIEF is also limited by the crosstalk from the liquid phase signal into the spectral detection range of the vapour phase, as shown in figure 3-18. Research indicates that it is possible to achieve an unambiguous separation of the liquid phase fluorescence by careful selection of optical filters (Leipertz et al. (1998)). Therefore, a separation of the vapour signal could be possible if the contribution of liquid fractions in the vapour image is determined. This thesis suggests using a binary image from the liquid signal to determine the location of liquid fractions in the spray. Then, the binary image can be used to identify liquid fractions on a vapour image acquired simultaneously. As a result, liquid fluorescence identified in the vapour image can be disregarded. This procedure is explained later in the post-processing section.

### 3.3.2. Rig Development

A schematic of the optical set-up proposed for this technique is presented in figure 3-19, in which two cameras are used to record spectrally separated fluorescent images of liquid and vapour phases simultaneously. A custom designed camera mount is used to align both cameras in the same plane by means of a mirror.

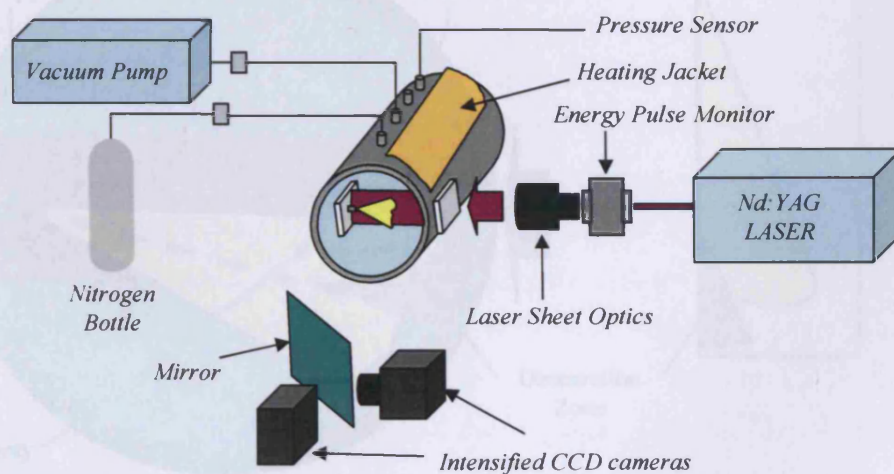
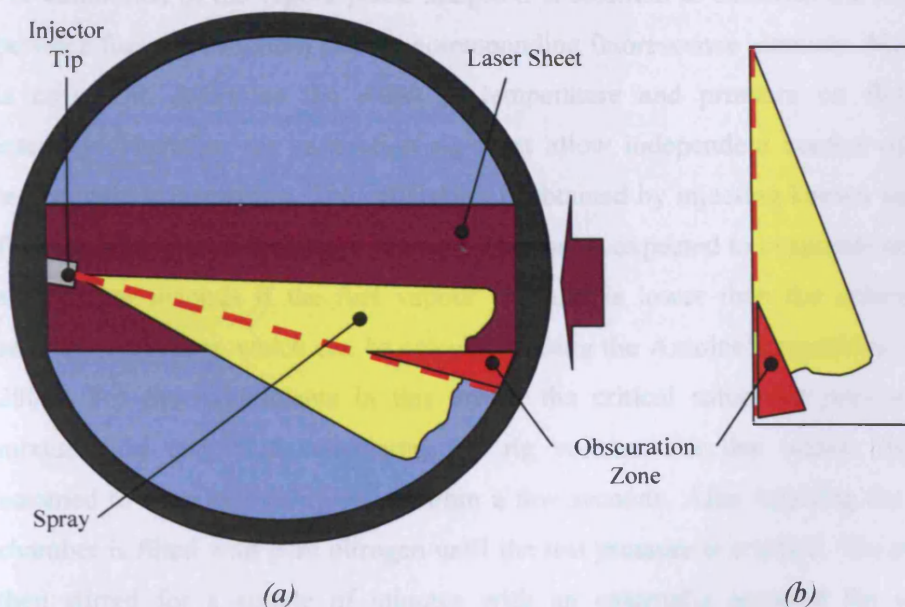


Figure 3-19: Schematic of the LIEF optical set-up



A Nd:Yag laser utilising the fourth harmonic (266 nm) is used as the excitation light source. The laser beam is directed towards the rig and formed into an optically thin collimated laser sheet by means of various UV graded laser sheet optics. The resulting laser sheet has a 35 mm height and a thickness of around 500  $\mu\text{m}$  throughout the interrogation area. In order to account for laser power fluctuations, an energy pulse monitor (EPM) was used to monitor and record the instantaneous laser power throughout the experiments. Even though the repetition rate of the laser is 10 Hz, the maximum repetition rate of the cameras is 5 Hz. Therefore images were acquired from several cycles and 'phase-averaged' in order to build a fuel concentration map for each time-bin. The synchronisation of the cameras, laser, EPM, and injector is achieved using the same method as that discussed in figure 3-16. For both cameras, the fluorescence signal is acquired through UV graded lenses onto a gated image intensifier linked to a HiSense Mk II CCD camera, with a resolution of 1344 x 1024 pixels. For simultaneous detection of liquid and vapour signals, each camera is equipped with different filters to optimise each signal at the peak of its fluorescent emission. A narrow-band interference filter with centre wavelength at 300 nm, and minimum peak transmittance of 20 %, is used to characterise the vapour fractions. For liquid separation, a combination of a long-pass cut-off filter and a narrow band filter is used to ensure no transmission below 350 nm.



**Figure 3-20:** Limitation of the optical setup: a) Schematic of the optical setup, b) Schematic of pre-processed image showing the obscuration zone.

All experiments are carried out in an optical rig which allows independent, accurate control of ambient pressures ( $P_{amb}$ ) up to 1.0 MPa (abs) and ambient temperatures ( $T_{amb}$ ) up to 423 K. A custom designed heating jacket is used to control the temperature inside the rig. A PID controller is used to allow accurate control of the heating elements, and thus control of the temperature inside the rig, using feedback from a thermocouple installed near the centre of the rig. A vacuum pump is used to evacuate the air of the rig between experiments. Then, the chamber is re-filled with nitrogen to create a homogenous oxygen-free nitrogen atmosphere.

In order to avoid fuel deposits in the opposite window of the rig (which allows optical access to the laser sheet), the injector is mounted  $15^\circ$  with respect to the horizontal plane as shown in figure 3-20a. This figure shows a limitation of the optical setup, which is present only for calibration of the fractions of the spray with high penetration along the centre line. Basically, an ‘obscuration zone’ is produced in the control volume as the spray moves away from the laser sheet. As a result, there is an area with no access to the exciting laser sheet. The schematic of a pre-processed image showing the obscuration zone is presented in figure 3-20b, which illustrates the small area where vapour concentration results of are not possible to be calibrated.

#### 3.3.3. LIEF Calibration

For calibration of the vapour phase images it is essential to establish the relationship between fuel concentration and the corresponding fluorescence intensity. Moreover, it is critical to determine the effect of temperature and pressure on fluorescence intensity. Therefore the calibration rig must allow independent control of ambient temperature and pressure. The calibration is obtained by injecting known volumes of fuel into the rig after creating a vacuum. The fuel is expected to evaporate completely after a few seconds if the fuel vapour pressure is lower than the critical vapour saturation pressure, which can be calculated using the Antoine’s equations (Crayford 2004). For the experiments in this thesis, the critical saturation pressure of the mixture was very high considering the rig volume. For that reason, the fuel is assumed to evaporate completely within a few seconds. After injecting the fuel, the chamber is filled with pure nitrogen until the test pressure is reached. The mixture is then stirred for a couple of minutes with an externally actuated fan to ensure homogeneity. The fuel vapour pressure and the final test pressure are measured using

a pressure sensor connected to the rig. Since the fuel partial pressure, the final test pressure, and volume of the rig are known, the mean concentration can be chosen as desired.

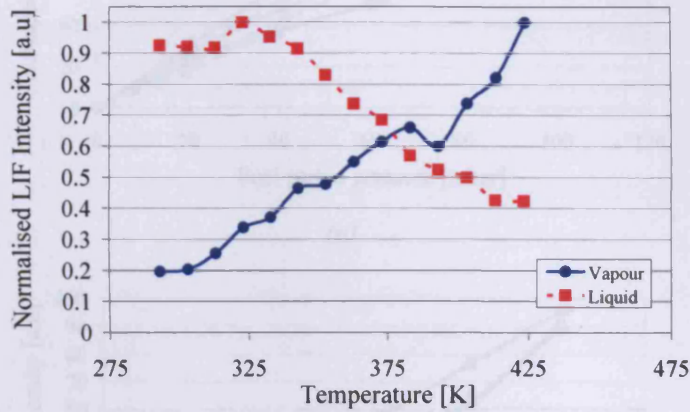
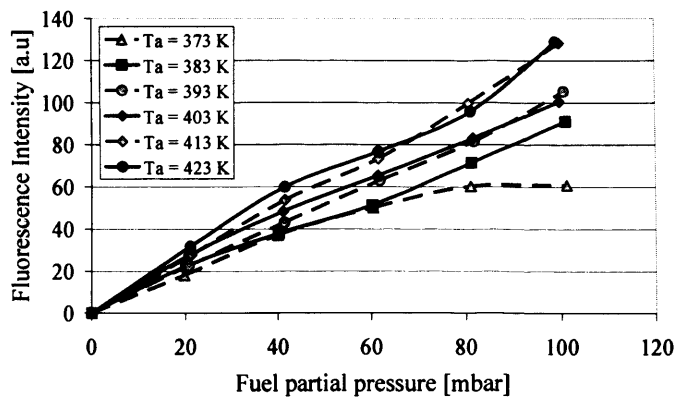
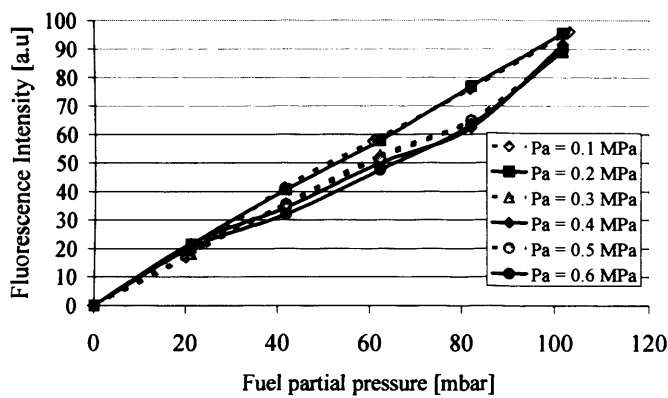


Figure 3-21: Relative fluorescence intensities of the liquid and vapour signals.

A preliminary study of temperature dependence of both monomer and exciplex fluorescence is presented in figure 3-21. The fluorescence of the liquid phase is obtained from a liquid sample of the fuel deposited on a quartz cuvette located within the rig for calibration purposes. The vapour phase fluorescence is obtained independently and is superimposed in this plot for comparative reasons. It should be noted that the normalised fluorescence of the liquid and vapour phases are scaled relative to their respective peak intensities, and hence no conclusion should be drawn regarding the relative intensity of the liquid and vapour signals. Figure 3-21 shows that the intensity of the exciplex fluorescence decreases as temperature increases, in contrast to the intensity of the monomer fluorescence, which increases as temperature rises. For this reason, the test conditions were selected above 373 K in order to minimise the contribution of the exciplex liquid phase signal into the spectral detection range of the vapour phase.



(a)



(b)

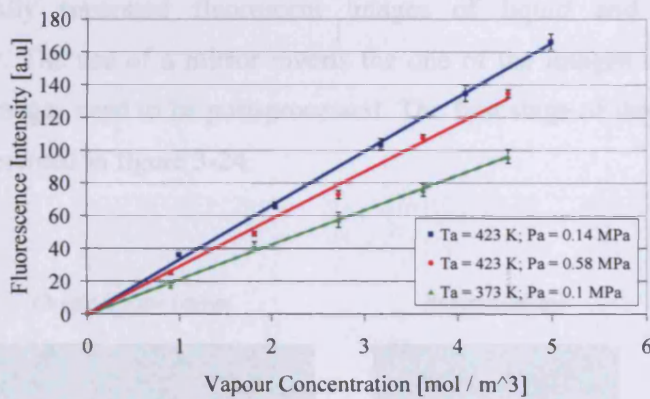
**Figure 3-22:** Temperature and Pressure dependence of the vapour fluorescence intensity. a) Temperature dependency (obtained at 0.1 MPa) b) Pressure dependency (obtained at 373 K).

Figure 3-22 (a & b) show the variation of fluorescent intensity with vapour concentration (expressed as fuel partial pressure) for a range of ambient temperatures and pressures. Figure 3-22a shows that the vapour fluorescence signal is strongly influenced by temperature. As temperature increases, there is a significant increase in the intensity recorded, (more than 50 % increase between 373 K and 423 K) for a high concentration of fuel vapour. In contrast, pressure variations between 0.1 and 0.6 MPa have a small impact in the fluorescence intensity as shown in figure 3-22b. Since the fluorescent signal is pressure and temperature dependent, it needs to be calibrated for each test condition. For internal combustion engine applications, the calibration methodology must account for coupling in-cylinder conditions, both in the calibration and engine operation. Deriving a crank angle resolved calibration, similar to that proposed by De Sarcey et al (2005), allows the calibration of experimental

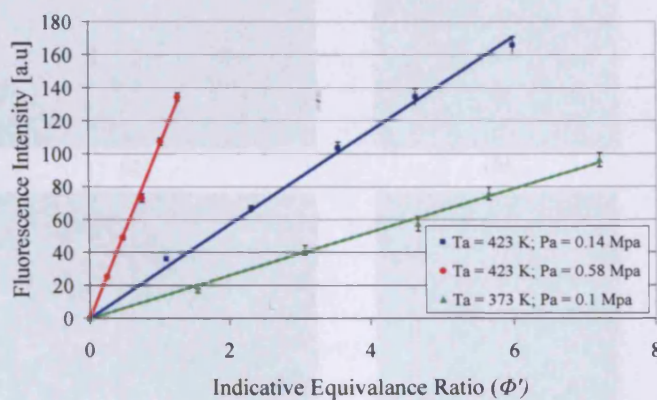


images with its corresponding calibration curve for an equivalent ambient temperature and pressure (crank angle).

Figure 3-23 (a & b) show the calibration of the monomer fluorescence intensity for a range of fuel vapour concentrations. In figure 3-23a, the units used to express vapour concentration are mole of fuel per meter cube ( $\text{mol/m}^3$ ). These units successfully describe the molar concentration of fuel within the rig. However, they fail in describing the ignitability of the mixture, as they do not account for changes in air mass for different ambient pressures. For instance, for a fixed amount of fuel, the calibration in  $\text{mol/m}^3$  would be the same regardless of the pressure in the rig; however, the mass ratio between fuel and nitrogen would decrease as the partial pressure of nitrogen increases. Therefore, an indicative equivalence ratio ( $\Phi'$ ) is defined in order to account for the change in nitrogen mass for different pressures.



(a)



(b)

Figure 3-23: Variation of fluorescent intensity with vapour concentration.

Although the experiments are conducted in a nitrogen atmosphere, the molecular weight of nitrogen can be approximated to the molecular weight of air, for which the measured concentration can be compared to the stoichiometric fuel-to-air ratio to provide an indication of spatial equivalence variation. The stoichiometric fuel-to-air ratio for this tracer mixture is 0.067. In order to allow comparison, a calibration plot of indicative equivalence ratio against fluorescence intensity is presented in figure 3-23b. Both plots show that the fluorescence increases linearly with tracer concentration for all three experimental conditions. To ensure a clear description of vapour concentration, both units are used later in chapter 5 in the discussion of the results.

### 3.3.4. LIEF Post-Processing Methodology

The optical configuration proposed for LIEF experiments (figure 3-19) involves the use of two different cameras, aligned in the same plane by means of a mirror, to record spectrally separated fluorescent images of liquid and vapour phases simultaneously. The use of a mirror inverts the one of the images horizontally, and therefore the images need to be post-processed. The first stage of the post-processing sequence is presented in figure 3-24.

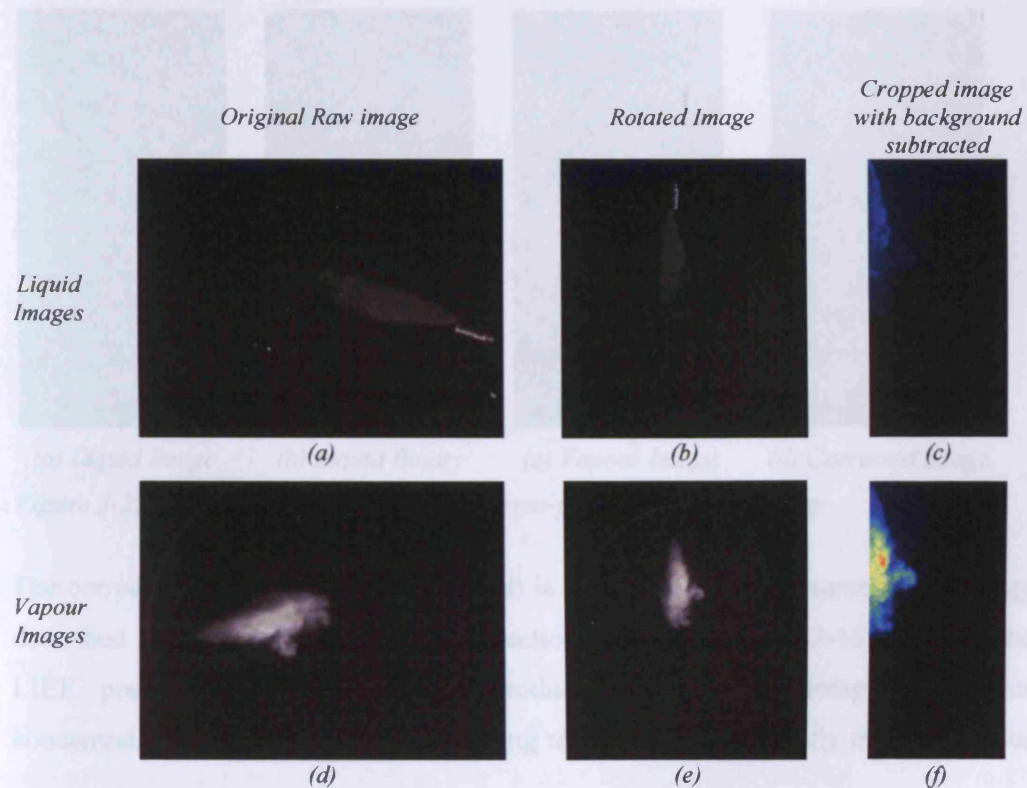
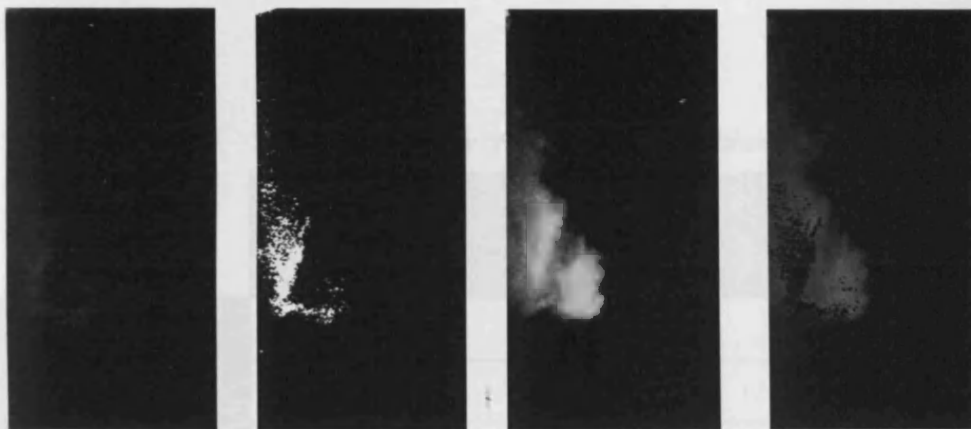


Figure 3-24: First stage of LIEF images post-processing methodology.

It involves flipping the inverted image (figure 3-24d), and rotating the images both the liquid and vapour images to align them and allow future comparison (figure 3-24b and 3-24e). Subsequently, an average background image is subtracted (figure 3-24c and 3-24f) to each raw image to account for the background and dark current signals of the detector (similar to the first step for TIR-LIF post-processing).

After this step, the vapour images need to be corrected for the crosstalk from the liquid phase signal into the spectral detection range of the vapour phase, as indicated by figure 3-18. This thesis proposes using a binary image from the liquid signal to determine the location of liquid fractions in the spray. Later, the binary image can be used to identify liquid fluorescence on a vapour image acquired simultaneously. As a result, liquid fluorescence identified in the vapour image can be disregarded. Figure 3-25 shows the second stage of the post-processing sequence. A binary liquid image (figure 3-25b) is produced from the recorded fluorescent image of the liquid phase minus the background subtracted (figure 3-24c, and figure 3-25a). The binary image is used as a mask to ignore liquid fractions in the vapour image (figure 3-25c). The resulting corrected image (figure 3-25d) can be then calibrated for concentration.



(a) Liquid Image (b) Liquid Binary (c) Vapour Image (d) Corrected Image

**Figure 3-25:** Second step of the LIEF Image post-processing methodology

The corrected vapour image (figure 3-25d) is calibrated using the same methodology described for TIR-LIF experiments in section 3.1.6 (see figure 3-13). Finally, the LIEF post-processing methodology produces a calibrated image of vapour concentration, or air-to-fuel ratio, resolving temporally and spatially the fuel vapour



distribution which highlights the applicability of LIEF for evaluation of the fuel mixture in the vicinity of spark plug for gasoline DI applications.

**3.4. Programme of Work**

The experimental conditions in this thesis were carefully chosen so that both the TIR-LIF and LIEF techniques previously described in this chapter could be examined under ambient pressures and temperatures pertinent to GDI engine operation. Thus, the facilities developed for both techniques enable the interrogation of sprays at elevated ambient pressure and temperatures. The experimental conditions proposed in this thesis are summarised in table 3-1. For impingement studies by TIR-LIF, two conditions were selected to investigate the influence of ambient pressure in the development of the fuel film: an atmospheric benchmark (Case A), and an elevated pressure case pertinent to in-cylinder conditions (Case B). Cases A and B complement post-impingement spray characterisation by Kay (2008b), who used Phase Doppler Anemometry to measure droplet sizes and velocities of the resulting spray for the same configuration. Therefore, the elevated pressure of 0.4 MPa is selected to match Kay’s experimental conditions and allow comparison with this study.

*Table 3-1: Summary of experimental conditions*

	<i>Case</i>	<i>Ambient Pressure [MPa] (abs)</i>	<i>Ambient Temperature [K] (abs)</i>
<i>Fuel Film Studies (TIR-LIF)</i>	<i>A</i>	<i>0.1</i>	<i>293</i>
	<i>B</i>	<i>0.4</i>	<i>293</i>
<i>Vapour Fraction Studies (LIEF)</i>	<i>1</i>	<i>0.14</i>	<i>423</i>
	<i>2</i>	<i>0.58</i>	<i>423</i>
	<i>3</i>	<i>0.10</i>	<i>373</i>

For LIEF studies, three sets of experimental conditions were selected to investigate the characteristics of vapour fraction of the spray at elevated ambient temperatures and pressures: a low pressure high temperature case (Case 1), a high pressure high temperature case (Case 2), and a low pressure mid temperature case (Case 3). The



ambient temperature used in Case 1 and Case 2 was 423 K, which enables analysis of the influence of ambient pressure in the evaporation of the spray. Both Cases 1 and 2 complement temporal and spatial PDA measurements of the spray performed by Kay (2006b). Additionally, a temperature of 373 K is used for Case 3 to investigate the evaporation of the spray at a lower temperature.

### **3.5. Chapter Summary**

This chapter describes in detail the development of new facilities and optical diagnostic techniques for characterisation of the mixture preparation process for G-DI applications. The TIR-LIF technique is developed for characterisation of fuel films formed as a result of impingement of G-DI sprays onto solid surfaces. This information, in conjunction with post-impingement spray characterisation by PDA, can be used to accurately describe the spray/wall interaction process. A new high-pressure optical facility was designed and commissioned to enable quantitative transient TIR-LIF fuel-film measurements under simulated G-DI conditions.

The chapter also describes developments of the LIEF technique for characterisation of vapour fractions of gasoline sprays, which complements current and well-established optical techniques for characterisation of the liquid phase such as PDA, and laser diffraction. It gives novel insight to the applicability of LIEF for quantitative measurements of vapour concentration / air-to-fuel ratios in the vicinity of spark plug for gasoline DI applications. For LIEF studies, a HP-HT rig was successfully redesigned to enable the characterisation of vapour fractions of gasoline sprays under conditions similar to in-cylinder conditions.

The fundamental principles of both techniques are discussed in detail along with potential limitations for quantitative results. Finally, the programme of work is discussed with reference of the experimental conditions selected for all tests discussed in chapter 4 and 5.

# **Chapter 4:**

**Analysis of Transient Liquid Fuel Films from a GDI Spray  
Impinging Upon a Solid Surface**

Quantitative measurements of fuel films formed due to impingement of a G-DI spray on a flat surface are presented and discussed in this chapter. The TIR-LIF technique presented in Chapter 3 is used for characterisation of the fuel films. Experimental results for two different ambient pressures ( $P_{amb}$ ), 0.1 MPa (Case A) and 0.4 MPa (Case B), are presented and discussed, providing an insight on the influence of elevated ambient density in the deposition of fuel films. Observations of the transient development of the 3D liquid fuel films include details of fine surface waves. Results presented include, for the first time, time resolved two-dimensional distribution maps of fuel film thickness, transient average thickness, transient total mass deposit, and footprint area for fuel films.

#### **4.1. Analysis of Fuel Films of an Impinging Spray at Atmospheric Pressure (0.1 MPa) – Case A**

This section describes the transient development of a liquid film formed as a result of impingement on a flat surface, for an experimental setup at atmospheric ambient conditions (0.1MPa and 293 K). A complete dataset of results for these conditions can be found in appendix A, which includes time resolved two-dimensional distribution maps of fuel film thickness, and the corresponding side view image of the spray. Quantitative results presented in this section were obtained using the TIR-LIF technique discussed in Chapter 3. The calibration curve for this case is presented in figure 3-12.

Temporally-resolved fuel film measurements are presented in this section for selected times After Start of Injection (ASOI). They illustrate the development of the liquid film formed as a result of impingement for a BOSCH C2-70 pressure swirl injector mounted 21 mm from the surface and angled at 45° with respect to the normal of the impact surface, as can be seen in figure 4-1 (top). The experiment is conducted with a fuel line pressure of 10 MPa, and injection duration 1.5 ms. Of course these comprise one representative set of conditions for impingement, with a change in any of the stated parameters - easily accommodated within the experimental set up - resulting in a change in fuel film characteristics. For numerical validation purposes, detailed information about the spray (pre and post-impingement) can be found in Kay (2006b), who used Phase Doppler Anemometry to characterise the same injector under a wide range of experimental conditions, including the experimental conditions used in this

## Chapter 4: Analysis of Transient Liquid Fuel Films from a GDI Spray Impinging Upon a Solid Surface

thesis. Kay's work include temporal and spatial description of the spray in terms of droplet diameter and flow field, and provides an excellent tool for formulation of a numerical model of the spray.

The calibrated images presented are the result of the average of twenty injections for each timebin. The main reason for the selection of this number of images is due to the large acquisition time for the data in this experiment (since the surface needs to be cleaned between injections). Therefore the average of twenty images is selected as a compromise. Figure 4-1 (bottom) shows the schematic of a typical footprint image obtained after cropping the raw images on the projection of the tip of the injector in the measurement plane. In the calibrated images, e.g. figure 3-13e, the pre-impinging spray propagates from left to right and the tip of the injector is located in the centre of the left side of the images (figure 4-1).

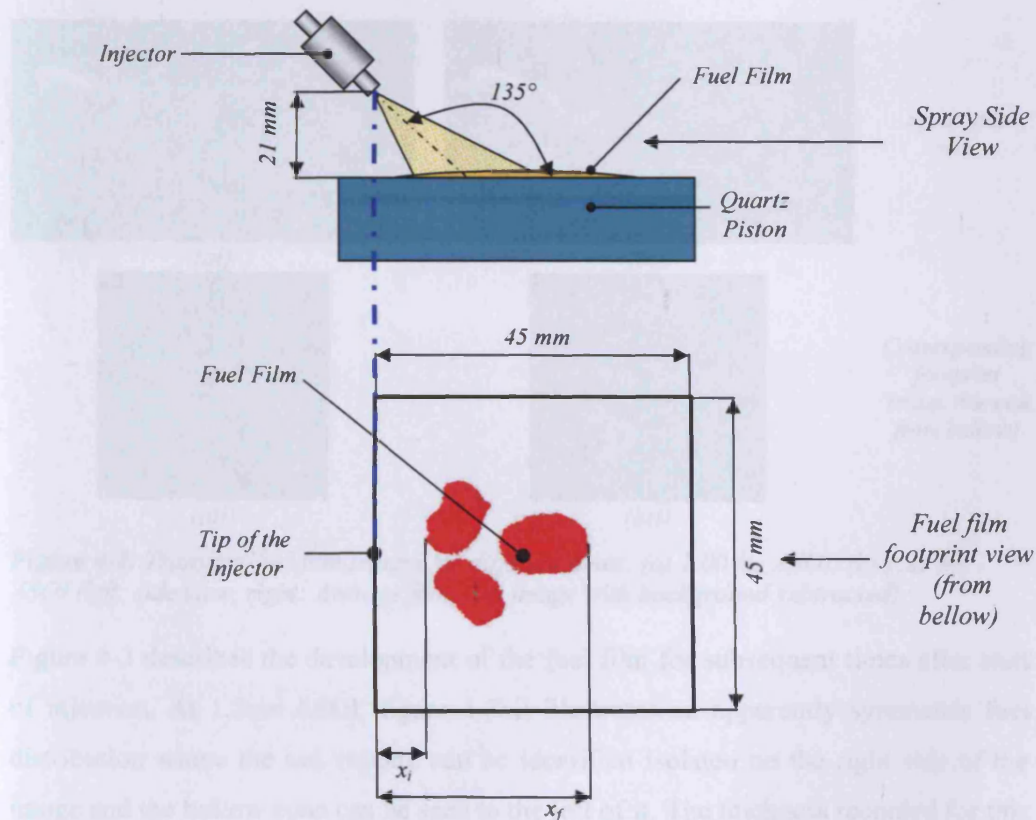


**Figure 4-1:** Schematic of the experimental configuration (Top: Side View, Bottom: Typical footprint image).

Figure 4-2 can be used to illustrate the benefits of using the principle of total internal reflection to illuminate the fuel film. It presents the side view – via a separate Mie-scattering optical set-up - and TIR-LIF footprint image recorded at 1.00 and 1.25 ms ASOI. Figure 4-2ai shows clearly the presence of airborne fuel above the quartz piston; however, no fluorescence signal is recorded in figure 4-2aai implying that early spray has not impacted the piston yet. This figure confirms that fuel is excited only after contacting the piston surface and not from pre-impingement airborne droplets, hence eliminating the potential source of error observed previously by Kay (2006b). By contrast, figure 4-2bii shows the first evidence of impinging fuel 1.25ms after start of injection (ASOI). The sac volume and the bottom half of the hollow cone, which is characteristic of this spray structure, can be identified on this image. The corresponding side view image (figure 4-2bi) affirms the impact of fuel as the film can be seen at the bottom of the image.

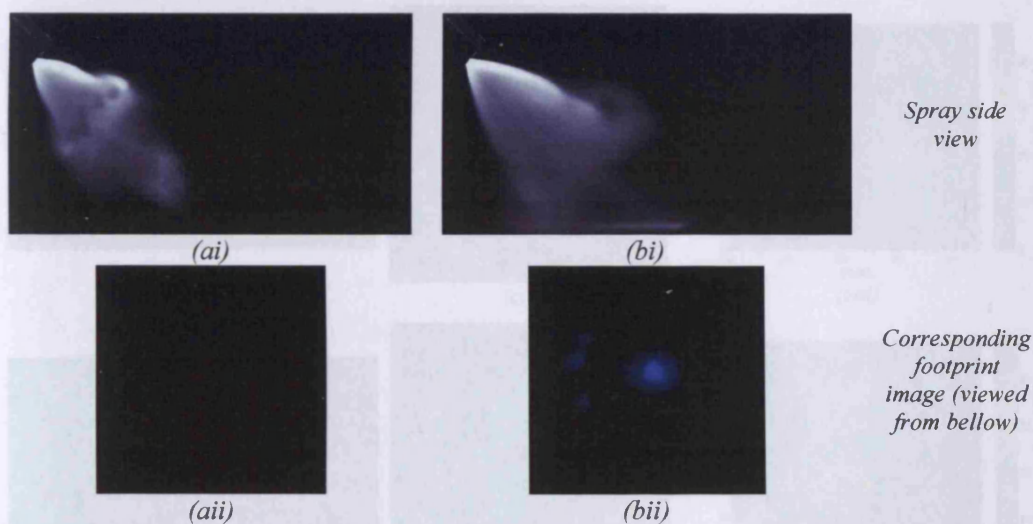


**Figure 4-2:** Transient fuel film images for different times: (a) 1.00 ms ASOI, (b) 1.25 ms ASOI (left: side view, right: Average footprint image with background subtracted)

Figure 4-3 describes the development of the fuel film for subsequent times after start of injection. At 1.5ms ASOI, figure 4-3aii illustrates an apparently symmetric fuel distribution where the sac volume can be identified isolated on the right side of the image and the hollow cone can be seen to the left of it. The thickness recorded for this image is presented in figure 4-3aiii, with average thickness of approximately 10 microns and some peaks at 25 microns. The following calibrated image (figure 4-3bii) shows increased fuel deposits and asymmetric fuel distribution with a tendency for the liquid film to move anticlockwise.



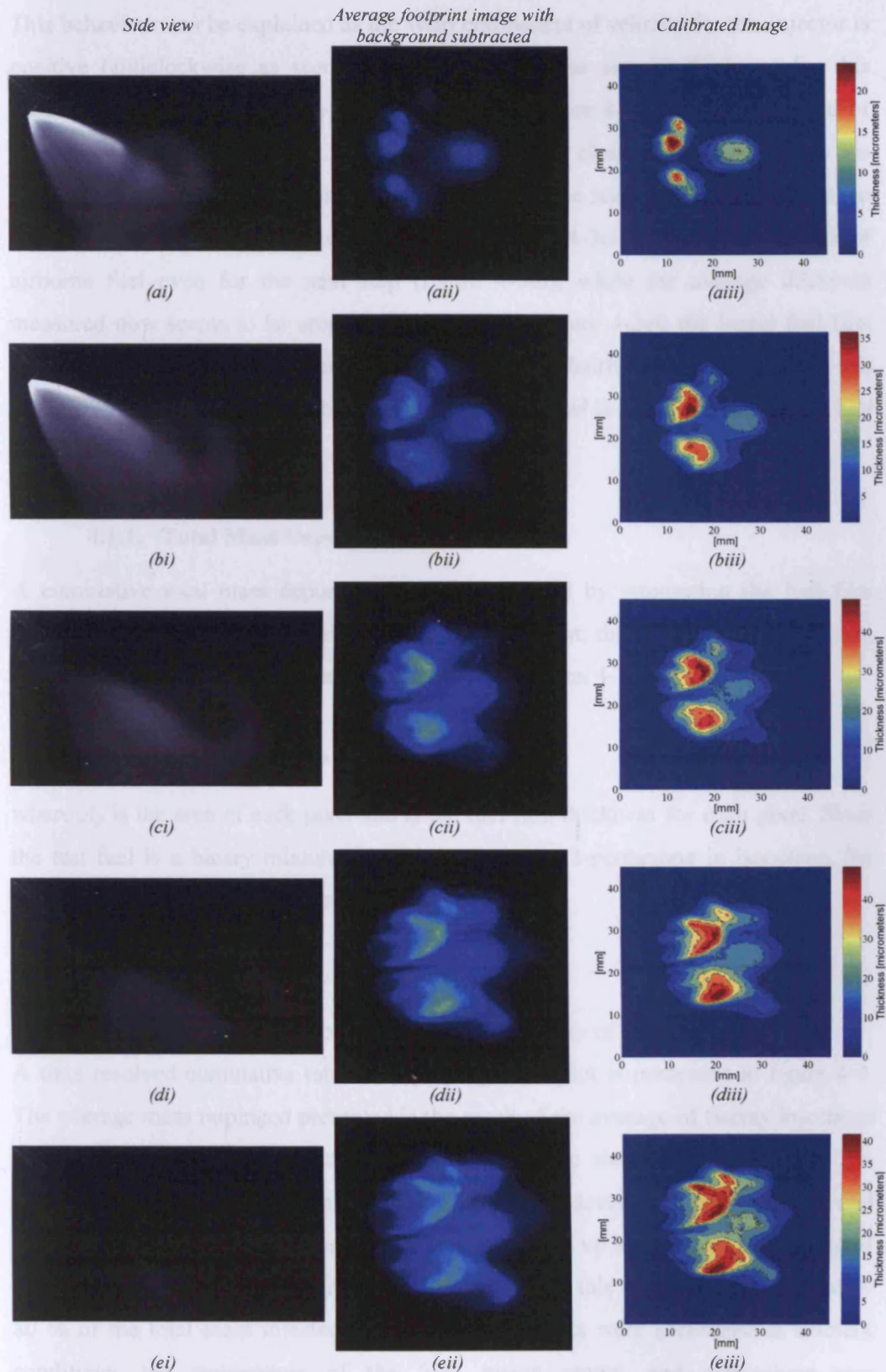


Figure 4-3: Transient fuel thickness measurements for different times after start of injection (ASOI): (a) 1.50 ms, (b) 1.75 ms, (c) 2.00 ms, (d) 2.25 ms; (e) 2.50 ms.

This behaviour can be explained as the swirl component of velocity for this injector is positive (anticlockwise as seen from underneath). The average thickness for this timebin is close to 13 microns. At 2.00 ms ASOI, figure 4-3ci illustrates the end of injection event. At this timebin the injector has already closed and the total mass has been injected, although there is still airborne fuel. The area of the footprint image increases for this instance as can be seen in figure 4-3cii. There is indication of airborne fuel even for the next step (figure 4-3di), while the average thickness measured now seems to be around 18 microns. In Figure 4-3eii the liquid fuel film area has reached its maximum size. The thickness distribution presented for this timebin (figure 4-3eiii) shows that the majority of the fuel is located in the bottom half of the image.

#### 4.1.1. Total Mass Deposits

A cumulative total mass deposits plot can be created by integrating the fuel film thickness over the spatial domain for each timebin. First, the volume of the fuel film for any particular timebin can be calculated from equation 4-1:

$$V = (A_p) \cdot \sum t_p \quad (4-1)$$

where  $A_p$  is the area of each pixel and  $t_p$  the fuel film thickness for each pixel. Since the test fuel is a binary mixture of 10% (by volume) 3-pentanone in isooctane, the total mass deposits can be approximated to:

$$m = V \cdot ((0.9) \cdot \rho_{iso} + (0.1) \cdot \rho_{3-pen}) \quad (4-2)$$

where  $\rho_{iso}$  is the density of isooctane and  $\rho_{3-pen}$  the density of 3-pentanone.

A time resolved cumulative total mass impingement plot is presented in figure 4-4. The average mass impinged presented is the result of the average of twenty injections for each timebin to smooth out unavoidable stochastic shot-to-shot variations. The graph shows clearly the time at which fuel film starts developing, between 1.00 and 1.25 ms ASOI, followed by a rapid accumulation of fuel up to a peak of about 9 mg of fuel deposited on the piston surface at 2.00 ms ASOI; this represents approximately 80 % of the total mass injected. Since the experiments were performed at ambient conditions, the temperature of the fuel, piston crown, and atmosphere was approximately 293 K, which accounts for such large total deposited mass.

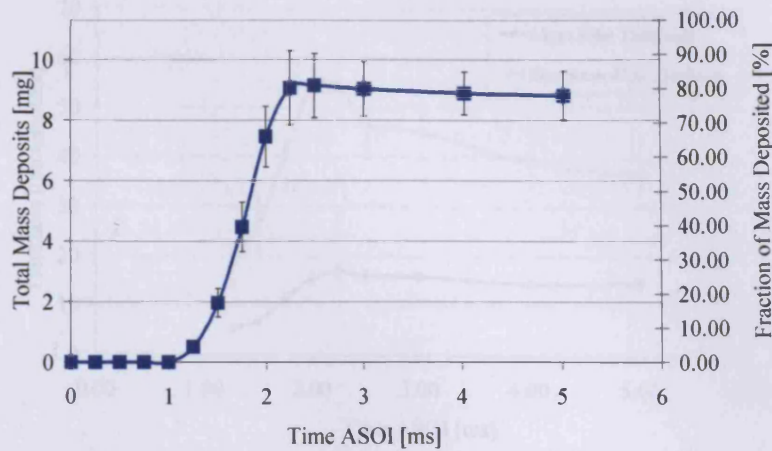


Figure 4-4: Cumulative total mass deposits for Case A

This level of deposited mass for the atmospheric impingement case is also consistent with estimates provided by Kay (2006b) utilising other indicative diagnostic techniques. The final trend shown in figure 4-4 is a relatively slow decay of total mass deposited due to post impingement evaporation.

#### 4.1.2. Average Fuel Film Thickness

Transient measurements of maximum and average thickness of the resulting fuel film are presented in figure 4-5. The maximum thickness recorded for this film is significantly higher than the average thickness due the un-even distribution of the film observed in figure 4-3, with high localised deposits in the region of impact of the cone. The graph shows that both the mean and maximum thickness increase rapidly between 1.25 and 2.25 ms ASOI. During this time there is continuous deposition of fuel on the flat surface. At 2.25 ms the fraction of mass injected in the closing phase of the injection reaches the impact surface, marking the end of the pre-impingement event. After this time the fuel film is redistributed showing a significant decrease in the maximum thickness recorded, while the average thickness reaches a plateau of approximately 15 micrometers. Finally, at 5.00 ms ASOI the maximum and average thickness recorded is approximately 37 and 15 micrometers respectively.



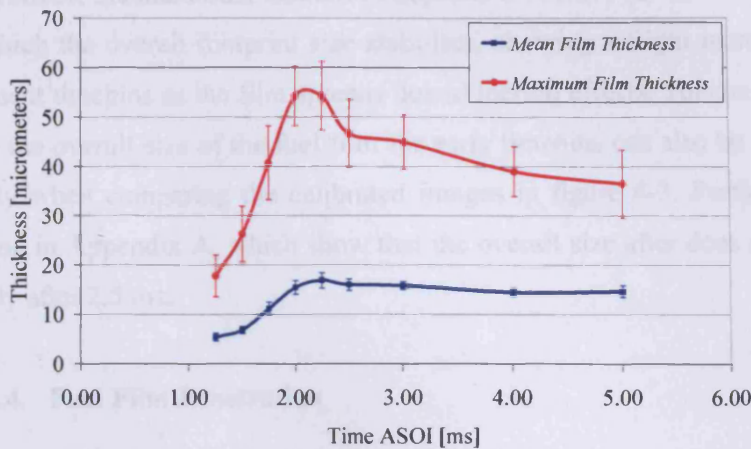


Figure 4-5: Average and maximum thickness of the fuel film for Case A

#### 4.1.3. Footprint Size

The average footprint size is calculated by integrating the number of pixels contained in the fuel film ( $n_p$ ) across the spatial domain, as indicated in equation 4-3.

$$A_{film} = (A_p) \cdot \sum n_p \quad (4-3)$$

Transient measurements of the film footprint area are presented in figure 4-6, which show a sharp increase in the overall footprint size between 1.25 and 2.50 ms. Such increase in footprint size is expected within this timescale as it represents the deposition phase of the injection, also observed in figures 4-4 and 4-5.

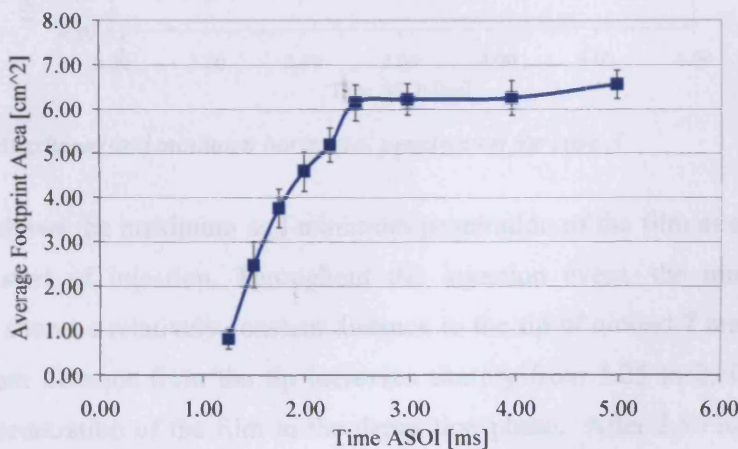


Figure 4-6: Fuel film footprint area at atmospheric pressure (Case A)

At 2.50 ms ASOI, the maximum amount of deposits is reached (as shown in figure 4-4), after which the overall footprint size stabilises, showing a slight increase in size for subsequent timebins as the film spreads due to inertial effects. This trend of sharp increase in the overall size of the fuel film for early timebins can also be appreciated qualitatively when comparing the calibrated images in figure 4-3. Further timebins can be found in Appendix A, which show that the overall size after does not increase significantly after 2.5 ms.

#### 4.1.4. Fuel Film Penetration

The relative position between the fuel film and the tip of injector was investigated to determine the location of the film within the control volume. Therefore, the maximum and minimum penetration of the film was measured as shown in figure 4-1 (bottom). The maximum penetration  $x_f$  is defined as the maximum horizontal distance between the fuel film and the injector tip (see figure 4-1b). In addition, the minimum penetration  $x_i$  represents the shortest horizontal distance from the tip to the film.

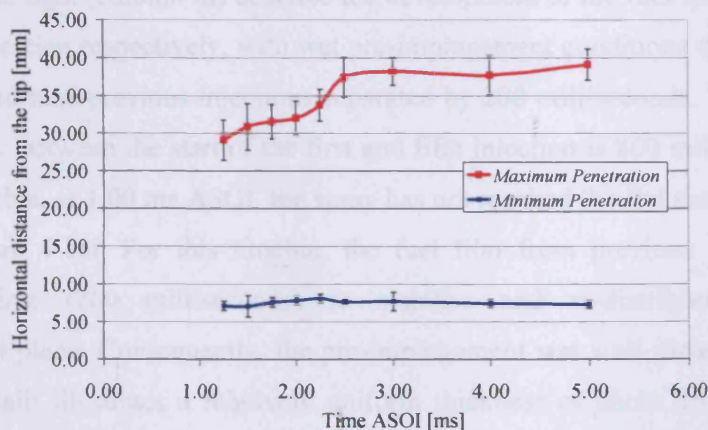


Figure 4-7: Maximum and minimum horizontal penetration for case A

Figure 4-7 shows the maximum and minimum penetration of the film as a function of time after start of injection. Throughout the injection event, the minimum film penetration shows a relatively constant distance to the tip of around 7 mm. However, the maximum distance from the tip increases sharply from 1.25 to 2.50 ms, which marks the penetration of the film in the deposition phase. After 2.50 ms, there is a slight increase in maximum penetration as the film spreads due to inertial effects.

#### 4.1.5. Fuel Film for Multiple Injections

As discussed in Chapter 2, the latest generation of G-DI engines propose the use of multiple injections to enhance pre-ignition mixture preparation, particularly for cold starts. Thus, the study of impingement for multiple injections within one cycle involves the interaction of sprays with pre-impingement wet walls. The ability to characterise such films provides an essential tool for validation of impingement models which consider this scenario to describe the impingement process (e.g. Bai et al 1995, and Mundo et al 1998). Therefore, an analysis of fuel films for multiple injections is presented in this sub-section to demonstrate the applicability of the TIR-LIF technique for analysis of fuel films with wet pre-impingement walls.

Figure 4-8 shows transient fuel thickness measurements for multiple injections for selected times after start of injection: (a) 1.00 ms, (b) 1.25 ms, (c) 1.50 ms, (d) 1.75 ms; (e) 2.00 ms, and (f) 2.25 ms. The first, fifth and tenth injections are shown in this figure, with times referenced to the start of its corresponding injection. The column on the left (column i) illustrates the development of the fuel film for a single injection with dry pre-impingement conditions. The column in the centre (column ii) and the column of the right (column iii) describe the development of the fuel film for the fifth and tenth injection respectively, with wet pre-impingement conditions due to deposits from four and nine previous injections separated by 200 milliseconds. Therefore, the absolute time between the start of the first and fifth injection is 800 milliseconds. For the first timebin, at 1.00 ms ASOI, the spray has not reached the flat surface as can be seen in figure 4-8ai. For this timebin, the fuel film from previous injections has sufficient time (200 milliseconds) to stabilise and re-distribute across the impingement plane. Consequently, the pre-impingement wet wall shown in figure 4-8aai and 4-8aaii illustrates a relatively uniform thickness of about 25 microns with most of the deposits located in the bottom of the image (due to the rotational component of the spray). At 1.25 ms ASOI, the sac volume and the bottom half of the hollow cone can be identified for the first injection (figure 4-8bi), while the sac volume can also be vaguely identified on the fifth and tenth injection as a small hole (thinner region) in the centre of the image (figures 4-8bii and 4-8biii). For the following timebin, 1.50 ms ASOI, figures 4-8cii and 4-8ciii show clearly a 'crater' structure in the centre of the image produced as a result of displacement of mass within the film due to impact of the sac volume with high inertia.



Chapter 4: Analysis of Transient Liquid Fuel Films from a GDI Spray Impinging Upon a Solid Surface

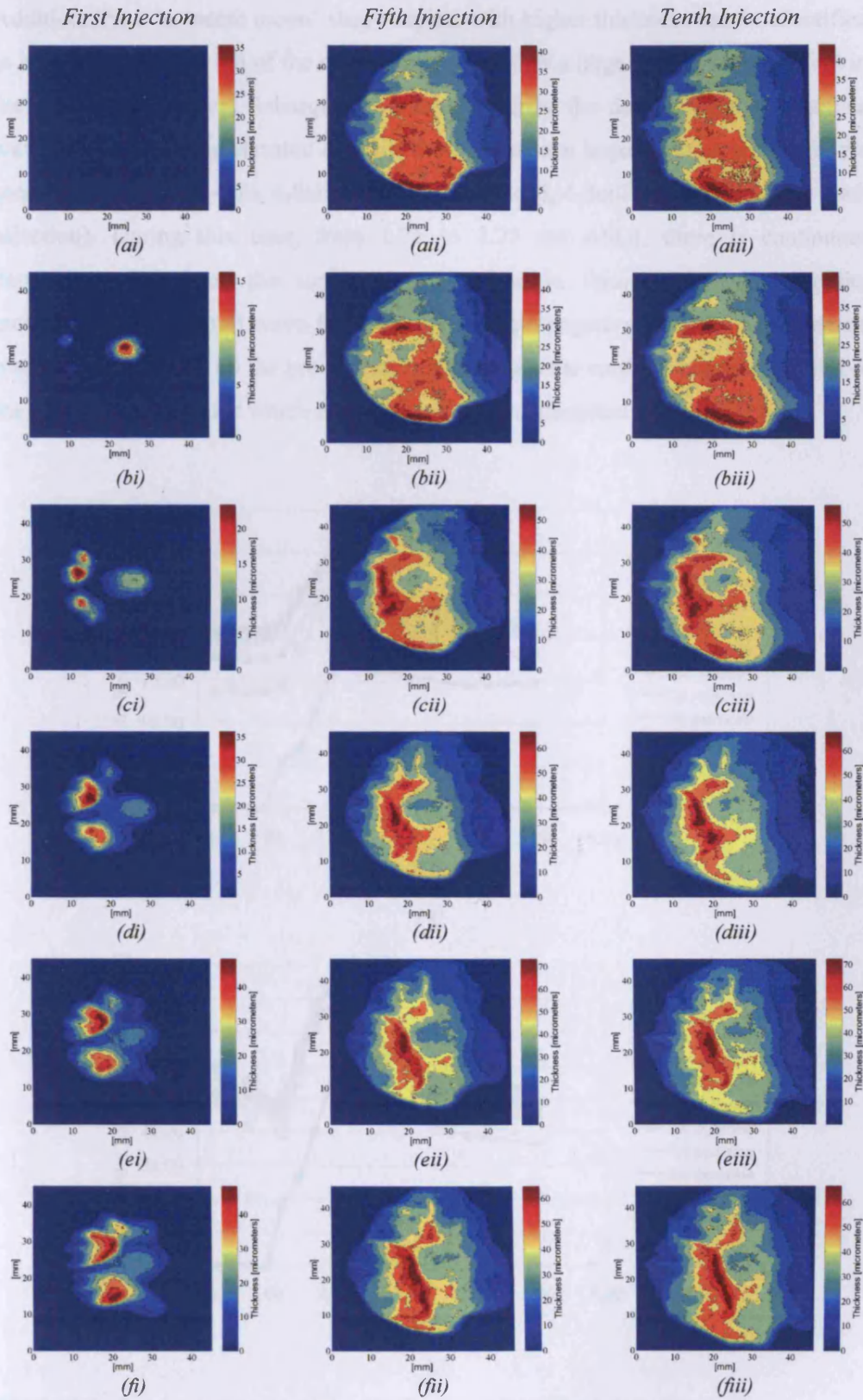
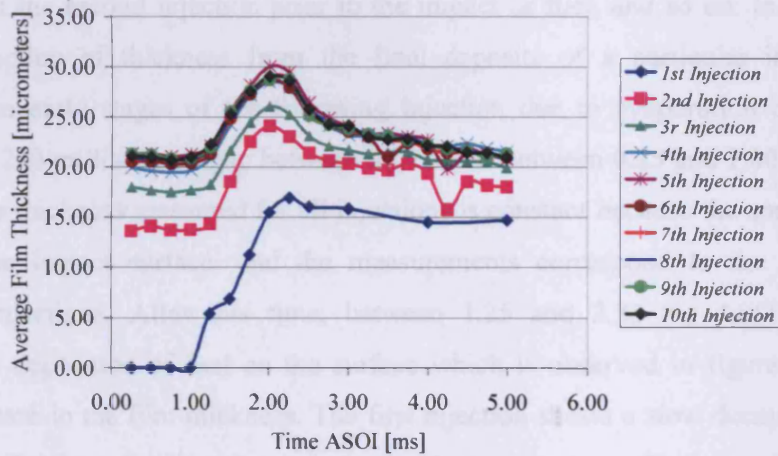
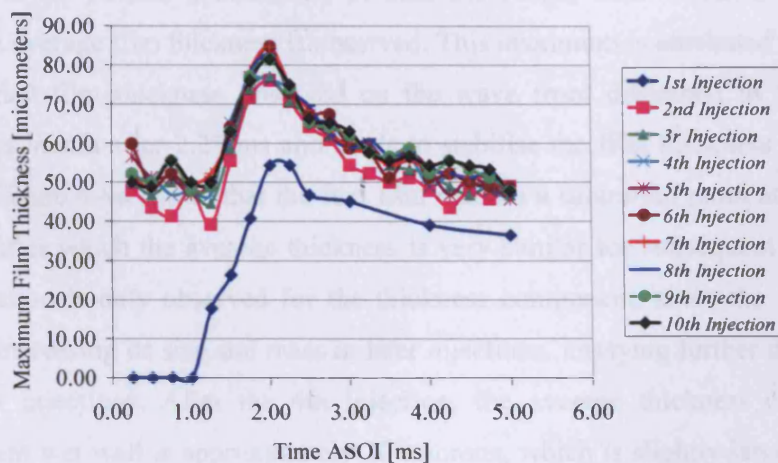


Figure 4-8: Transient fuel thickness measurements for multiple injections for selected times ASOI: (a) 1.00 ms, (b) 1.25 ms, (c) 1.50 ms, (d) 1.75 ms; (e) 2.00 ms, (f) 2.25 ms

Additionally, a ‘crescent moon’ shape region with higher thickness can be identified in both images to the left of the crater which describes a large accumulation of fuel in the cone impact region. Subsequent timebins describe the development of a surface wave as a result of the elevated deposits during the cone impact as can be seen in the sequence of images 4-8dii, 4-8eii and 4-8fii (or 4-8diii, 4-8eiii and 4-8fiii for the tenth injection). During this time, from 1.75 to 2.25 ms ASOI, there is continuous deposition of fuel on the surface (as described in figure 4-4), which applies momentum to the small wave front forcing it to propagate across the impingement plane. After 2.25 ms, all the pre-impact spray reaches the surfaces marking the end of the deposition phase, for which no more momentum is applied to the wave front.



(a)



(b)

Figure 4-9: Average (a) and Maximum (b) Thickness for multiple injections.

Therefore, after this time, the surface wave propagates across the film for a short period, losing momentum, until it tends to die-out creating a relatively uniform film distribution. Eventually, after sufficient time, they produce a film similar to that on figure 4-8a<sub>ii</sub>, which marks the boundary condition for the next injection.

A time resolved fuel film thickness plot for multiple injections is presented in figure 4-9. The average and maximum thickness of 10 consecutive injections (separated by 200 milliseconds) are superimposed in this figure to illustrate the development of the fuel film. The average thickness is calculated by integrating values of thickness across the impingement plane. Figure 4-9a shows the average thickness of the fuel film, where a good agreement is observed in successive injections. For instance, a similar average thickness is observed in the latter stages of the first injection and the early timebins of the second injection prior to the impact of fuel, and so on. In general, a small reduction of thickness from the final deposits of a particular injection is observed in early stages of the following injection due to evaporation of the fuel during the 200 milliseconds gap between injections. Between 0.25 and 1.00 ms ASOI, the average thickness measured for all injections is constant because the spray has not reached the impact surface, and the measurements correspond to the film from previous injections. After this time, between 1.25 and 2.25 ms ASOI, there is continuous deposition of fuel on the surface which is observed in figure 4-9a as a sharp increase in the film thickness. The first injection shows a slow decay after 2.25 ms as the film is redistributed across the impingement plane. The rest of injections (from 2<sup>nd</sup> to 10<sup>th</sup>) reach a maximum at 2.25 ms ASOI, after which a significant decrease in average film thickness is observed. This maximum is attributed to the high localised fuel film thickness observed on the wave front described in figure 4-8, which loses inertia after 2.25 ms and tends to stabilise the film thickness for further timebins. Figure 4-9a shows that the fuel film reaches a saturation point at the fourth injection, after which the average thickness is very similar for subsequent injections. This saturation is only observed for the thickness component, since the liquid film continues increasing its size and mass in later injections, implying further deposits for subsequent injections. After the 4th injection, the average thickness of the pre-impingement wet wall is approximately 20 microns, which is slightly larger than the global SMD of the pre-impacting spray (approx. 18 microns) reported by Kay (2006). The relative high thickness of the wet wall in comparison with the pre-impact droplet diameters is thought to be the primary cause for the thickness saturation of the liquid

film. However, this, along with other potential explanations, would require further experimental study and analysis to be fully confident of the underlying causes. A maximum fuel film thickness plot is presented in figure 4-9b, which shows a similar trend for early timebins to that discussed for 4-9a (before 2.25 ms). However, after 2.25ms, a sharper decay is observed for all the injections as wave front dies out levelling the thickness across the fuel film.

#### **4.1.6. Analysis of Fuel Impingement for Case A - Summary**

Section 4.1 describes the application of a TIR-LIF for spatial and temporal quantitative analysis of transient liquid fuel films formed after spray impingement of a G-DI spray. Calibrated benchmark results of a transient spray from a gasoline direct injector impinging on a flat quartz crown under atmospheric conditions are presented, with observations and discussion of the transient development of the 3-dimensional fuel film. Results presented show that the TIR-LIF technique is successful in characterising the development of the fuel film qualitatively and quantitatively, particularly in describing the transient effect of the fuel film thickness and shape. Additionally, an analysis of fuel films for multiple injections is presented which illustrates the applicability of this technique for characterisation of fuel films with wet pre-impingement walls.

#### **4.2. Analysis of Fuel Films of an Impinging Spray at Elevated Ambient Pressure (0.4 MPa) – Case B**

The characterisation of transient liquid fuel films formed as a result of spray impingement of a G-DI spray on a quartz crown under elevated ambient pressures is described in this section. The modified TIR-LIF rig for experiments at elevated conditions (figure 3-15) is used for characterisation of fuel film under 0.4 MPa ambient pressure, for the same experimental conditions discussed in section 4.1. The calibration curve for this case is presented in figure 3-12. A complete dataset of fuel film results at elevated pressure can be found in appendix B, which includes time resolved two-dimensional distribution maps of fuel film thickness. Selected times After Start of Injection (ASOI) are presented in figure 4-10 to compare the development of the transient fuel film for two different ambient (0.1 and 0.4 MPa).



Chapter 4: Analysis of Transient Liquid Fuel Films from a GDI Spray Impinging Upon a Solid Surface

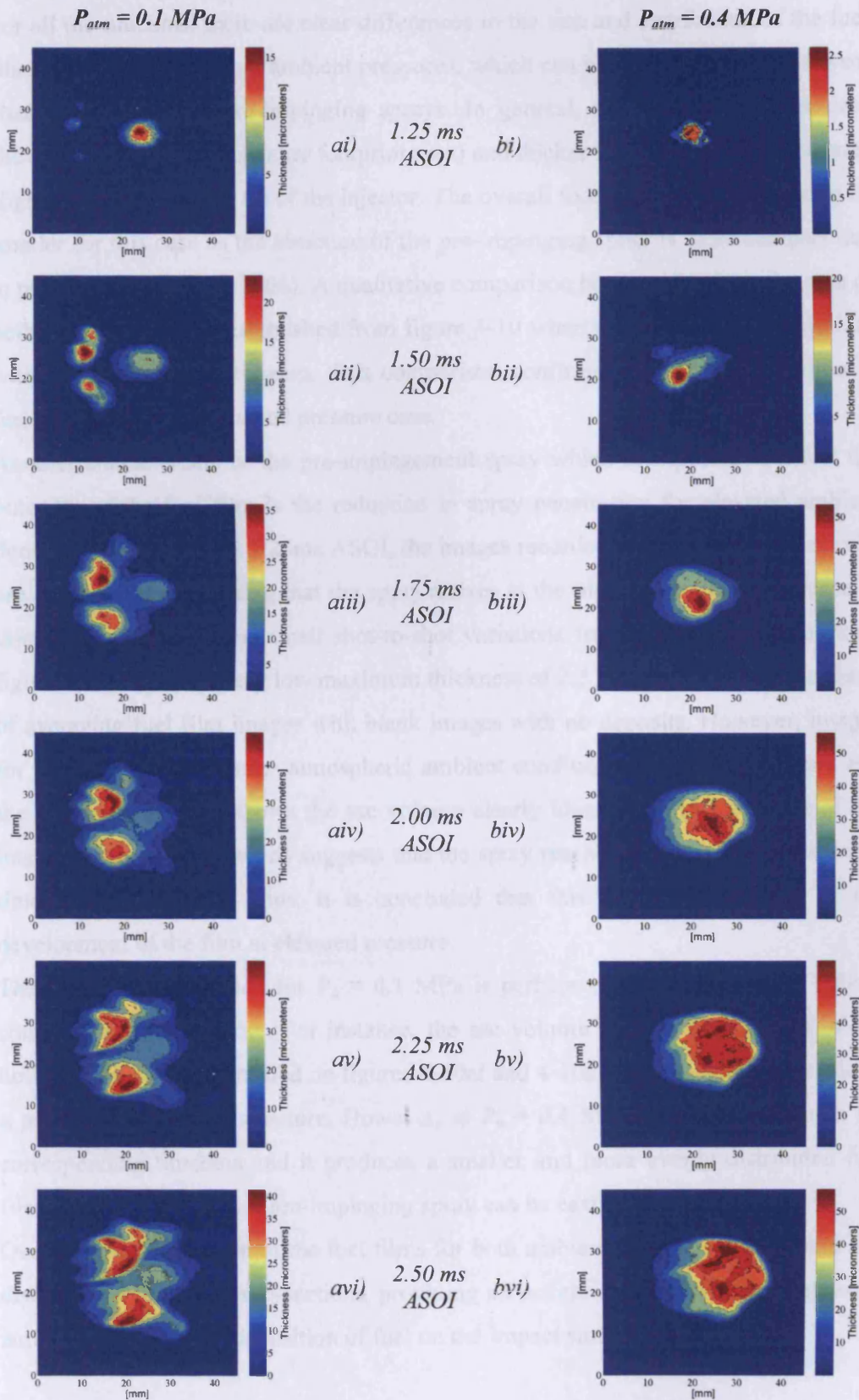


Figure 4-10: Comparison between transient fuel thickness measurements under 0.1 and 0.4 MPa ambient pressures for selected times after start of injection.

For all the timebins, there are clear differences in the size and distribution of the fuel films produced at different ambient pressures, which can be attributed to the different characteristics of the pre-impinging sprays. In general, the elevated pressure case shows a more compact (smaller footprint area) and thicker fuel film, which propagates slightly further from the tip of the injector. The overall footprint area is expected to be smaller for this case as the structure of the pre-impinging spray is more compact due to pressure effects (Kay 2006). A qualitative comparison between the footprint area of both fuel films can be established from figure 4-10 when comparing each liquid film with its corresponding timebin. This comparison confirms a significant reduction in fuel film size for the elevated pressure case.

Another characteristic of the pre-impingement spray which is expected to affect the outcome of the fuel film is the reduction in spray penetration for elevated ambient density (Kay 2006b). At 1.25ms ASOI, the images recorded for the high pressure case are intermittent, suggesting that the spray arrives at the piston at a time very close to this timebin, hence some small shot-to-shot variations from the injector. Therefore, figure 4-10bi shows a very low maximum thickness of 2.5 microns, which is the result of averaging fuel film images with blank images with no deposits. However, images for the same timebin under atmospheric ambient conditions are very consistent, and the calibrated average shows the sac volume clearly identifiable in the centre of the image (figure 4-10ai), which suggests that the spray reached the impact surface some time before 1.25 ms. Thus, it is concluded that this represents a delay in the development of the film at elevated pressure.

The fuel film distribution for  $P_a = 0.1$  MPa is perhaps more intuitive for a hollow cone pre-impinging spray. For instance, the sac volume and the bottom half of the hollow cone can be identified on figures 4-10ai and 4-10aai, which is characteristic of a pressure swirl spray structure. However, at  $P_a = 0.4$  MPa, the spray collapses for corresponding timebins and it produces a smaller and more evenly distributed fuel film, where no features of pre-impinging spray can be easily identified.

Quantitative comparison of the fuel films for both ambient pressures is presented and discussed in following sub-sections, providing an insight on the influence of elevated ambient density in the deposition of fuel on the impact surface.

### 4.2.1. Total Mass Deposits

Figure 4-11 shows a time resolved cumulative total mass deposits plot generated by integrating the fuel film thickness over the spatial domain for each timebin, as explained in section 4.1.1. The figure shows that between 1.00 and 1.25 ms ASOI the fuel film starts developing. At 1.25 ms, the graph shows a delay in the development of the film at elevated pressure, which is attributed to the reduced penetration of the pre-impinging spray which takes longer to reach the wall. After 1.25 ms there is a rapid accumulation of fuel for both cases up to a peak at 2.00 ms ASOI of about 9 and 10.5 mg of fuel deposited on the piston surface for ambient pressures of 0.1 and 0.4 MPa respectively.

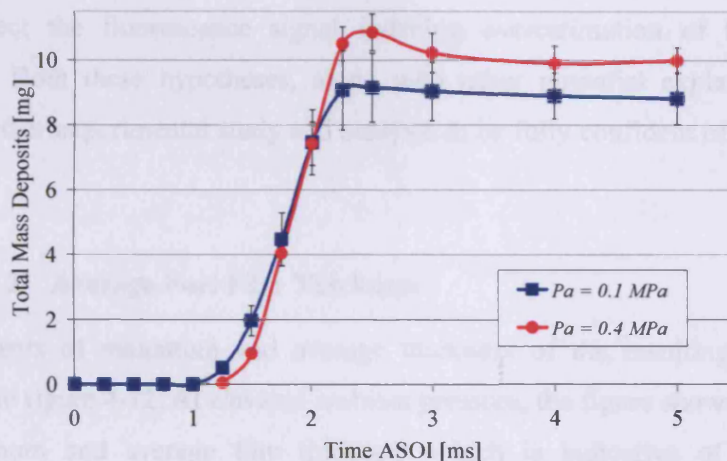


**Figure 4-11:** Comparison of cumulative total mass deposits at 0.1 and 0.4 MPa ambient pressures.

This corresponds to approximately 80 and 95 % of the total mass injected. Since the experiments were performed at ambient conditions, the temperature of the fuel, piston crown, and atmosphere was 295 K, which largely accounts for such large total deposited mass. The trends after 2.5ms ASOI show a relatively slow decay of total mass deposited due to post impingement evaporation (figure 4-11). This film evaporates less quickly for the elevated pressure case due to the decrease in vapour pressure, though the absolute difference in aggregated deposit is greater at elevated pressure due to the dominance of pre-impact spray dynamic variations over thermodynamic differences. However, between 2.00 and 3.00 ms ASOI, there is a surprising increase in mass deposits for the elevated pressure case. One possible

explanation would be the transient nature of the well-known splashing-crown mode of secondary atomisation, created when larger droplets impact on liquid pools. Another possible explanation for such increase in deposits could be explained by changes in the photo-physical properties of the tracer not accounted for during the calibration process. For instance, during the calibration of this technique, known volumes of fuel are deposited on the quartz crown quasi-statically for calibration. However, the impinging fuel travels with high kinetic energy which is dissipated during the impact with the wall. Experiments by Magnusson et al (2008) showed that the fuel temperature increases up to 6 K in the moment of impact for a diesel application. Even though the injection pressure is significantly higher, it illustrates the fact that the spray conditions during the impact could change significantly. Therefore, the photo-physical properties of the tracer might be affected during the impact process, which might affect the fluorescence signal inducing overestimation of the total mass deposited. Both these hypotheses, along with other potential explanations, would require further experimental study and analysis to be fully confident of the underlying causes.

#### **4.2.2. Average Fuel Film Thickness**

Measurements of maximum and average thickness of the resulting fuel film are presented in figure 4-12. At elevated ambient pressure, the figure shows an increase in the maximum and average film thickness which is indicative of the fuel film evaporation time. Thus, even though the overall area of the film is smaller for the high pressure case, the film is thicker, for which it would take longer to evaporate.

In figure 4-12, both the mean and maximum thickness increase gradually between 1.25 and 2.25 ms ASOI and there is continuous deposition of fuel on the wall. After 2.25 ms the fuel film is redistributed showing a gradual decrease in the maximum thickness recorded for both cases. The average thickness for  $P_a = 0.4$  MPa also shows a decay after 2.25 ms, while the lower ambient pressure case reaches a plateau of approximately 15 micrometers after this time. Finally, between 4.00 and 5.00 ms ASOI the maximum and average thickness of both fuel films stabilises at around 40 and 18 micrometers respectively.



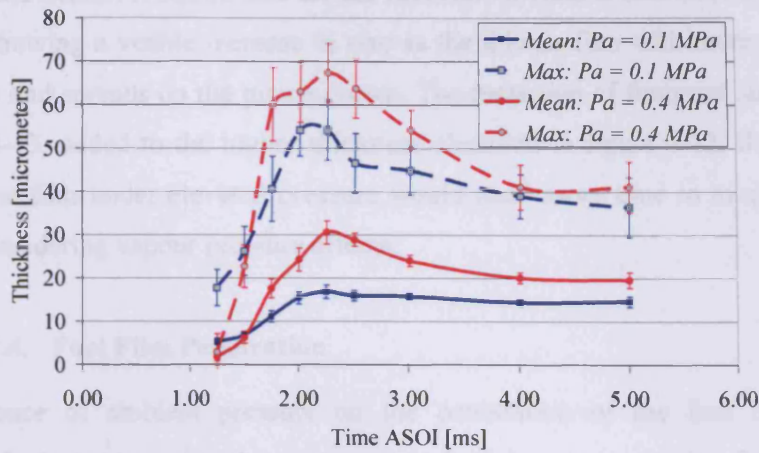


Figure 4-12: Comparison between average and maximum thickness of the fuel film at 0.1 and 0.4 MPa ambient pressures.

### 4.2.3. Footprint Size

Similarly to section 4.1.3, the overall footprint size was calculated for the fuel film under elevated pressure. A comparison between the footprint area of Case A and Case B fuel films presented in figure 4-13. This figure confirms a significant reduction in fuel film footprint size for the elevated pressure case, also observed qualitatively in figure 4-10. Figure 4-13 shows a sharp increase in the overall footprint size for both cases between 1.25 and 2.50 ms, after which the overall footprint size of Case A stabilises at around 6 cm<sup>2</sup>.

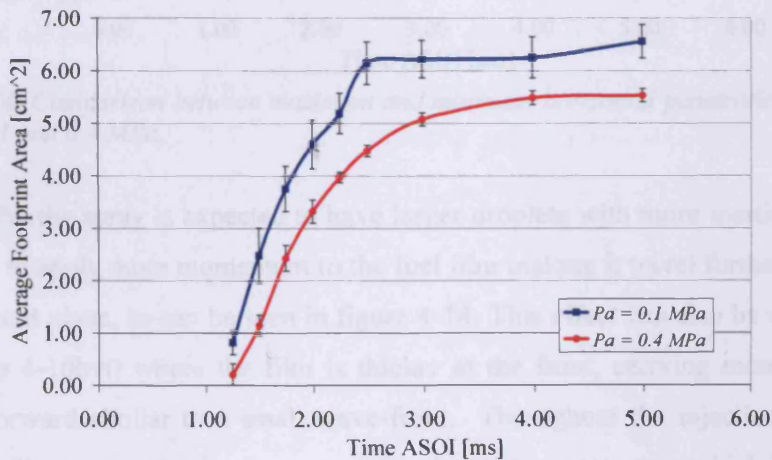
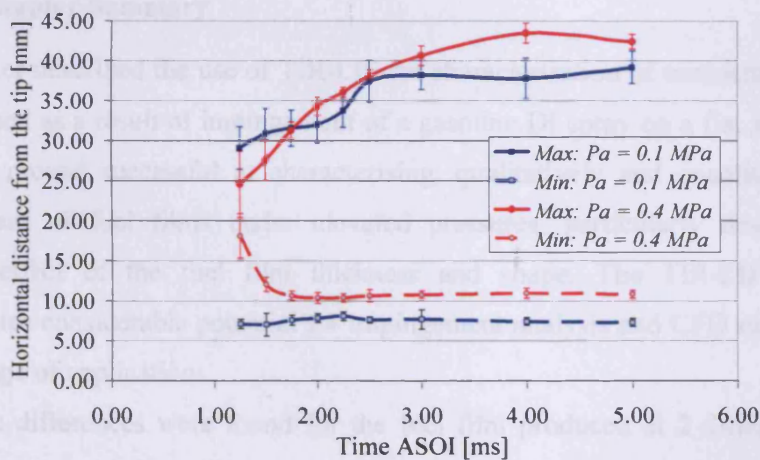


Figure 4-13: Comparison between footprint area of the fuel film at 0.1 and 0.4 MPa ambient pressures

However, the overall footprint size for the fuel film of Case B continues to grow after 2.50 ms, showing a visible increase in size as the thicker film with more momentum propagates and spreads on the piston crown. The reduction of footprint size observed in figure 4-13, added to the higher thickness observed in figure 4-12, illustrates the fact that the film under elevated pressure would need more time to evaporate, even without considering vapour pressure effects.

#### 4.2.4. Fuel Film Penetration

The influence of ambient pressure on the penetration of the fuel film can be appreciated when comparing the maximum and minimum penetration for both cases in figure 4-14. The maximum and minimum penetration of the film is defined as the maximum and minimum horizontal distances from the tip of the injector, as described in section 4.1.4.



**Figure 4-14:** Comparison between maximum and minimum horizontal penetration of the film for  $P_a = 0.1$  and  $0.4$  MPa

At 0.4 MPa, the spray is expected to have larger droplets with more inertia which are presumed to apply more momentum to the fuel film making it travel further across the impingement plane, as can be seen in figure 4-14. This effect can also be seen at 2.50 ms (figure 4-10bvi) where the film is thicker at the front, carrying momentum and moving forward similar to a small wave-front. Throughout the injection event, the minimum film penetration is also greater for elevated pressure case which is attributed

to the reduced footprint area, and reduced distance between the impact symmetry axis and the back edge of the film.

#### **4.2.5. Analysis of Fuel Impingement for Case B - Summary**

Results presented in section 4.2 show that the TIR-LIF technique, integrated within the adapted high-pressure/temperature spray facility at Cardiff, provides a valuable integrated system for characterisation of fuel films due to spray impingement under elevated ambient conditions. Calibrated results for a representative 0.4 MPa ambient pressure case describe a fuel film thicker and smaller than that described in section 4.1, for the same experimental configuration, at atmospheric ambient pressure. The film also travels further from the tip of the injector. Cumulative mass deposits reveal higher average fuel thickness and higher total deposits for elevated ambient pressure due to variation in the momentum exchange process.

#### **4.3. Chapter Summary**

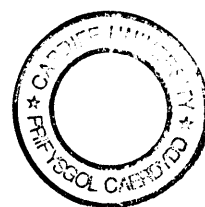
This chapter described the use of TIR-LIF for characterisation of transient liquid fuel films formed as a result of impingement of a gasoline DI spray on a flat surface. The technique proved successful at characterising, qualitatively and quantitatively, the development of fuel films under elevated pressures, particularly describing the transient effect of the fuel film thickness and shape. The TIR-LIF technique demonstrates considerable potential for impingement analysis and CFD validation for a wide range of applications.

Noticeable differences were found for the fuel film produced at 2 different sets of ambient pressures, due to differences in the pre-impingement spray dynamics such as the known collapse of the spray under increased ambient pressure (Kay, 2006). For elevated ambient pressures (0.4 MPa) a thicker and smaller film which travels further from the tip of the injector is identified. Cumulative mass deposits reveal higher average fuel thickness and higher total deposits for elevated ambient pressure due to variation in the momentum exchange process. As expected, extremely high quantities of residual fuel-film are measured under the atmospheric temperature conditions of this experimental programme. Further work is required to explain a few unusual trends, and utilisation of smaller pixel size afforded by future hardware improvements will assist in further refinement of the technique.



# **Chapter 5:**

## **Analysis of Vapour Fractions of a Gasoline Direct Injection Spray at Elevated Ambient Conditions**



Quantitative measurements of liquid and vapour fractions of a pressure-swirl gasoline direct injection spray are presented and discussed in this chapter. The LIEF technique discussed in section 3.3 is used for spectral separation of liquid and vapour phases. The experimental configuration is presented in figure 3-19, which involves the characterisation of a BOSCH C2-70 pressure swirl injector with a line pressure of 10 MPa and injection duration of 1.50 ms. In order to account for systematic errors intrinsic to laser sheet diagnostics in dense sprays, such as power attenuation or multiple scattering, only the half cone of the spray was investigated. Quantitative results include time resolved two-dimensional distribution maps of vapour concentration, spray penetration of liquid and vapour phases, and relative area of the liquid and vapour regions.

A solution of TEA and benzene in isooctane is used throughout the experiments with relative concentration of: 2 %, 2.9 %, and 95.1 % respectively (all percentages by weight). The experiments are performed in a nitrogen atmosphere, at three sets of ambient conditions, to investigate the influence of ambient pressure and temperature in the evaporation of the spray. Selected times after start of injection (ASOI) are presented in this chapter with observations of the liquid and vapour distribution and fuel concentration for the vapour fractions. Figure 5-1 shows the development of the evaporating spray for three different ambient conditions:

- Case 1 (column *a*) with  $P_a = 0.14$  MPa and  $T_a = 423$  K.
- Case 2 (column *b*) with  $P_a = 0.58$  MPa and  $T_a = 423$  K.
- Case 3 (column *c*) with  $P_a = 0.10$  MPa and  $T_a = 373$  K.

The ambient temperature selected for Case 1 and Case 2 is the same, which enables analysis of the influence of ambient pressure in the evaporation of the spray. Additionally, a lower temperature of 373 K (with slightly different pressure to compensate for air density effects) is used for Case 3 to investigate the evaporation of the spray at a lower temperature. Images presented in figure 5-1 are phase-averaged over 30 injections. In general, a higher penetration is observed for the vapour phase for all cases at any given time, showing that the vapour fractions travel ahead of the liquid. Comparing Cases 1 and 2 (columns *a* and *b*), the figure shows a significant change on spray pattern and penetration due to the change in ambient pressure. For elevated ambient pressure, case 2, both the liquid and vapour phases show a more compact spray structure.

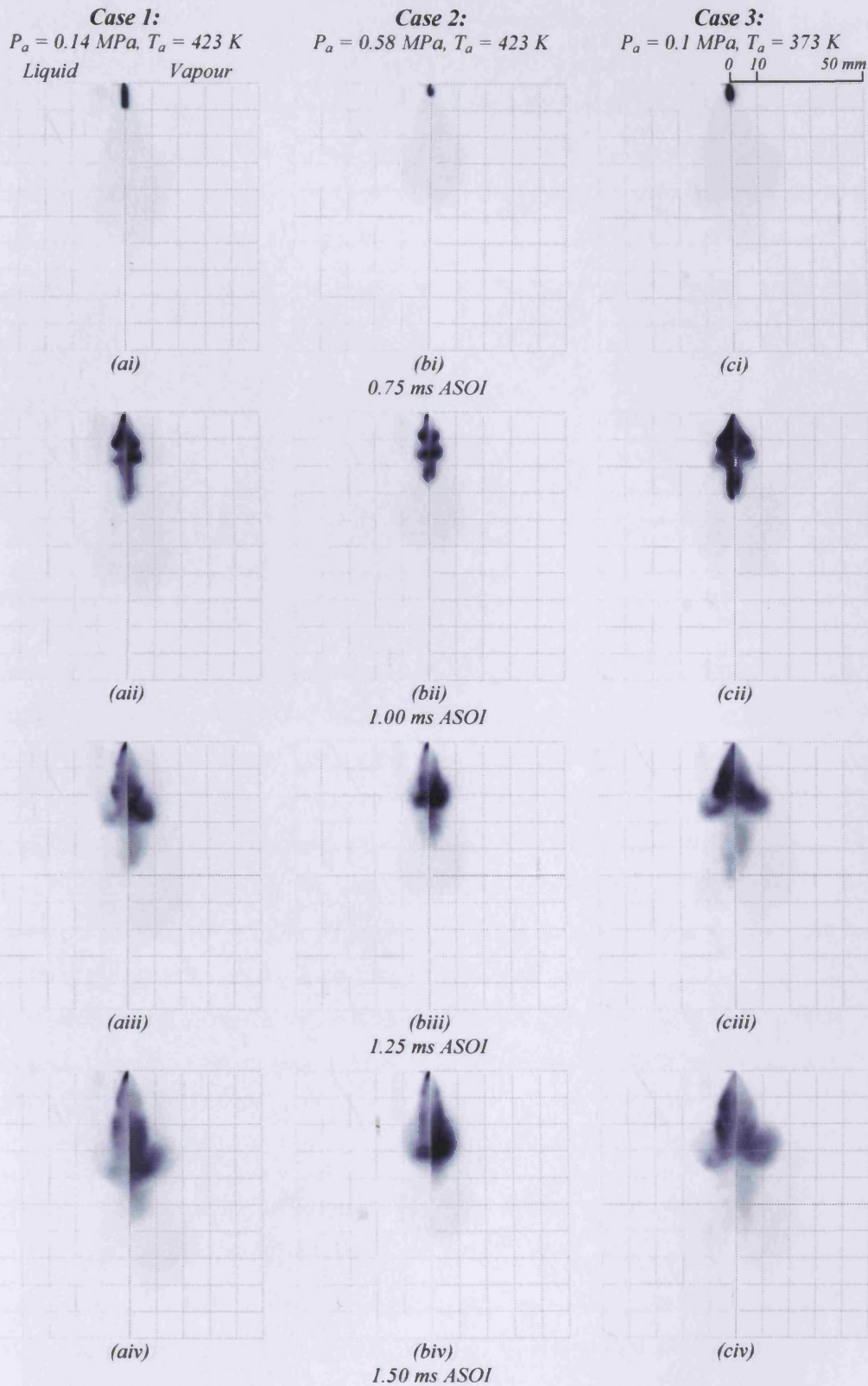


Figure 5-1: Development of the gasoline DI pressure swirl spray under three different ambient conditions

Chapter 5: Analysis of Vapour Fractions of a Gasoline Direct Injection Spray at Elevated Ambient Conditions

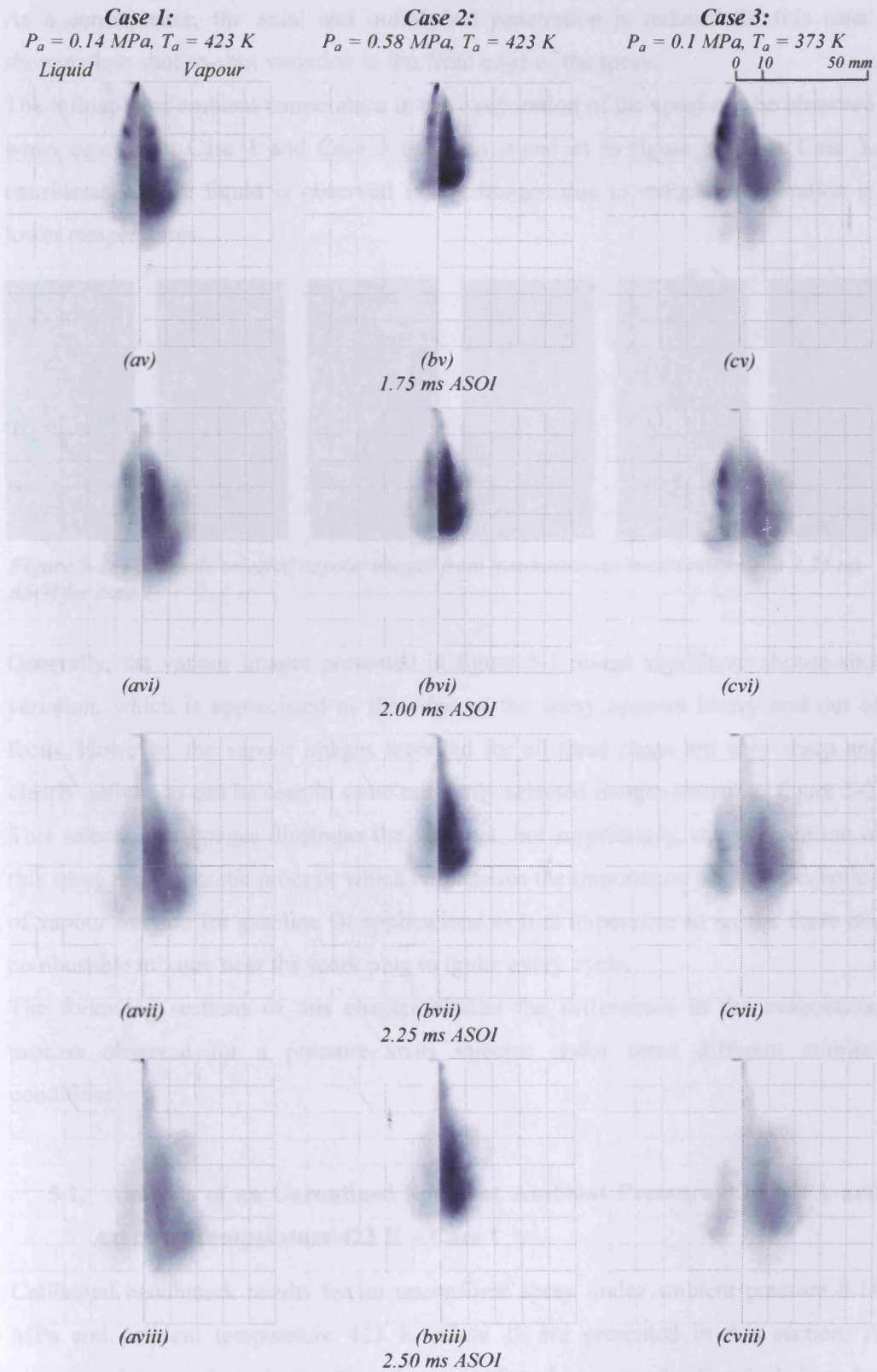
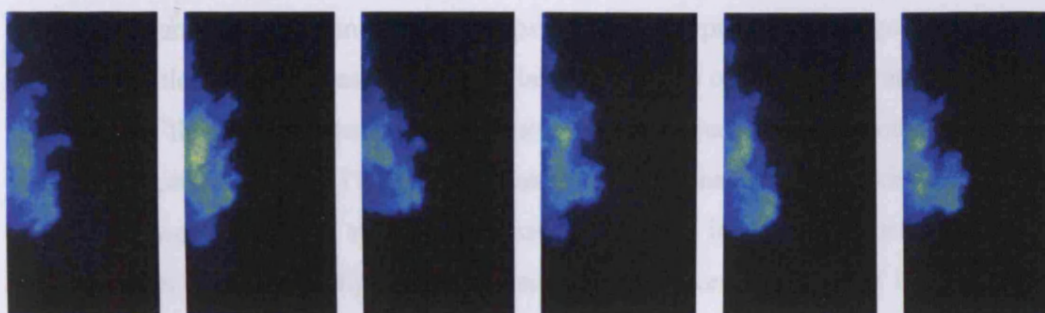


Figure 5-1: Continued...



As a consequence, the axial and radial fuel penetration is reduced for this case, showing less shot-to-shot variation in the front edge of the spray.

The influence of ambient temperature in the evaporation of the spray can be observed when comparing Case 1 and Case 3 (column *a* and *c*) in figure 5-1. For Case 3, considerably more liquid is observed in the images due to reduced evaporation at lower temperatures.



*Figure 5-2: Randomly selected vapour images from instantaneous measurements at 2.25 ms ASOI for case 1*

Generally, the vapour images presented in figure 5-1 reveal significant shot-to-shot variation, which is appreciated as the edge of the spray appears blurry and out of focus. However, the vapour images recorded for all three cases are very sharp and clearly defined as can be seen in some randomly selected images shown in figure 5-2. This selection of images illustrates the fact that, not surprisingly, the evaporation of this spray is a stochastic process, which emphasises the importance of characterisation of vapour fraction for gasoline DI applications as it is imperative to ensure there is a combustible mixture near the spark plug to ignite every cycle.

The following sections of this chapter discuss the differences in the evaporation process observed for a pressure swirl injector under three different ambient conditions.

### **5.1. Analysis of an Unconfined Spray at Ambient Pressure 0.14 MPa and Ambient Temperature 423 K – Case 1**

Calibrated benchmark results for an unconfined spray under ambient pressure 0.14 MPa and ambient temperature 423 K (Case 1) are presented in this section. A complete dataset of results for Case 1 can be found in appendix C, which includes time-resolved two-dimensional distribution maps of vapour concentration.

Quantitative results discussed in this section were obtained using the LIEF technique discussed in section 3.3, and include analysis of spray penetration for liquid and vapour phases, distribution of liquid and vapour regions, and vapour concentration measurements. The calibration curve for this case is shown in figure 3-23.

### 5.1.1. Spray Penetration

Temporal changes in axial and radial fuel penetration are presented in figure 5-3. The axial penetration is defined as the distance between the tip of the injector and the axial front edge of the spray (furthest axial distance from the injector tip) for both the liquid and vapour phase images. The radial penetration is defined as the maximum radial distance between the spray and injector axis. Due to the inherent stochastic shot-to-shot variation discussed in figure 5-2, the spray penetration is calculated individually for each of the thirty images obtained for each timebin, and then phase averaged to obtain figure 5-3. The error bars in figure 5-3a show the standard deviation.

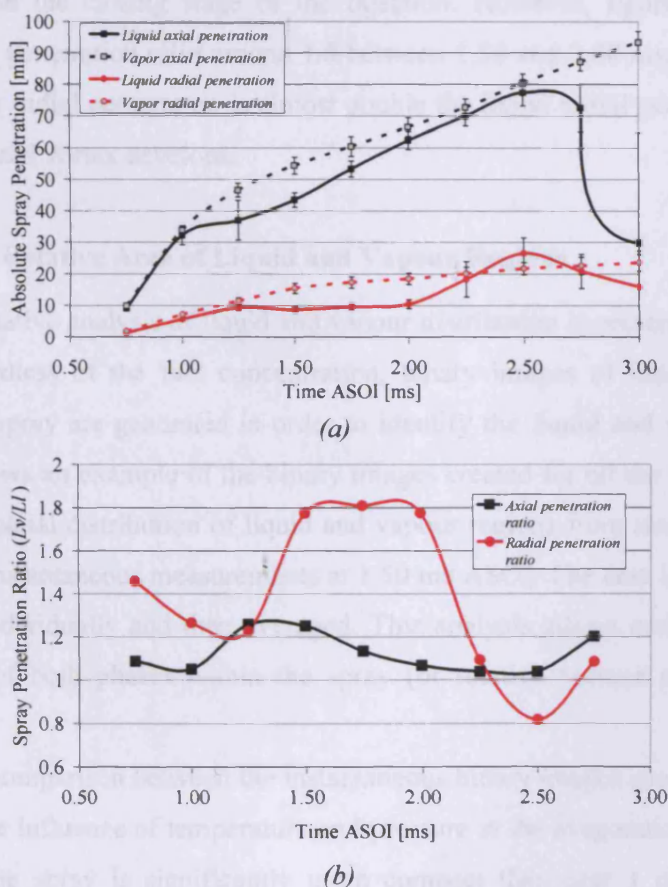


Figure 5-3: Absolute (a) and relative (b) penetration of liquid and vapour phases for case 1



Figure 5-3a describes the axial and radial absolute penetration of the liquid and vapour phases of the spray. The ratio between vapour and liquid penetration  $L_v/L_l$  is presented in figure 5-3b. Clearly, if this ratio is equal to one, the liquid and vapour phases penetrate concurrently. However, this ratio is mostly greater than unity throughout the injection event. This implies that the growth of the vapour phase is dominant at any given time, suggesting that the vapour fractions travel ahead of the liquid ones. This trend, also observed in figure 5-3a, is also reported by Bae et al (2004) for a gasoline pressure swirl spray with similar experimental conditions.

At the very early stages of the injection, between 0.75 and 1.00 ms ASOI, figure 5-3b shows a decrease in the penetration ratio, suggesting that the rate of growth of the liquid phase is greater within this timescale. However, there is an increase in the axial and radial penetration ratio between 1.00 and 1.50ms, reaching a maximum at around 1.50 ms where there is maximum separation between vapour and liquid spray. After 2.00 ms ASOI, the axial penetration ratio remains constant around unity. This indicates that both the liquid and vapour phases of the spray developed axially at a constant rate in the closing stage of the injection. However, figure 5-3b show a constant radial penetration ratio around 1.8 between 1.50 and 2.00 ms, which implies that the vapour radial penetration is almost double the liquid radial penetration as the recirculation head vortex develops.

### 5.1.2. Relative Area of Liquid and Vapour Regions

A semi-quantitative analysis of liquid and vapour distribution is presented in this subsection. Regardless of the fuel concentration, binary images of liquid and vapour phases of the spray are generated in order to identify the liquid and vapour regions. Figure 5-4 shows an example of the binary images created for all the test conditions, showing the spatial distribution of liquid and vapour regions from randomly selected images from instantaneous measurements at 1.50 ms ASOI. The area is calculated for each region individually and then averaged. This analysis allows comparison of the relative area of both phases within the spray (or relative volume assuming spray symmetry).

A qualitative comparison between the instantaneous binary images shown in figure 5-4 illustrates the influence of temperature and pressure in the evaporation of the spray. For case 2, the spray is significantly more compact than case 1 due to elevated

ambient pressure. Also, the image of case 3 reveals a significantly higher presence of liquid over the image for case 1 due to the retarded evaporation at lower temperature.

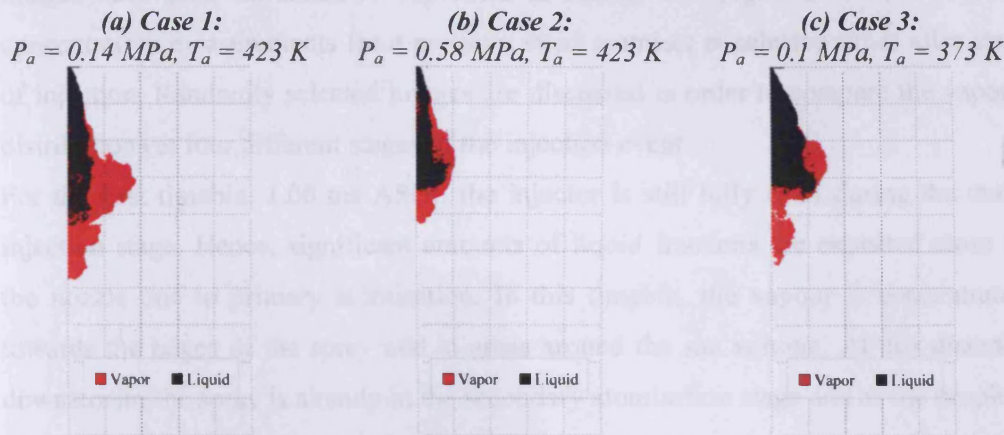


Figure 5-4: Spatial distribution of liquid and vapour regions (Randomly selected images from instantaneous measurements at 1.50 ms ASOI)

The relative area of the liquid and vapour region is presented in figure 5-5a, which illustrates the evaporation process of the spray. The distribution of fuel before 1.50 ms shows that around 50 % of the area of the spray fuel is in liquid phase. However, after 1.50 ms there is substantial evaporation of liquid fuel, thus the area of the vapour fraction increases as the liquid fuel evaporates. The ratio between vapour and liquid area  $A_{vap}/A_{liq}$  is presented in figure 5-5b. In this plot, values below one imply that the area of liquid phase is greater than the area of the vapour region. This is true for all timebins before 1.5ms ASOI, which is expected for the early stages of the injection as there is a large presence of liquid fractions in the spray. For subsequent timebins the injection has already ended, and the relative area of vapour region increases exponentially due to the evaporation of the liquid spray.

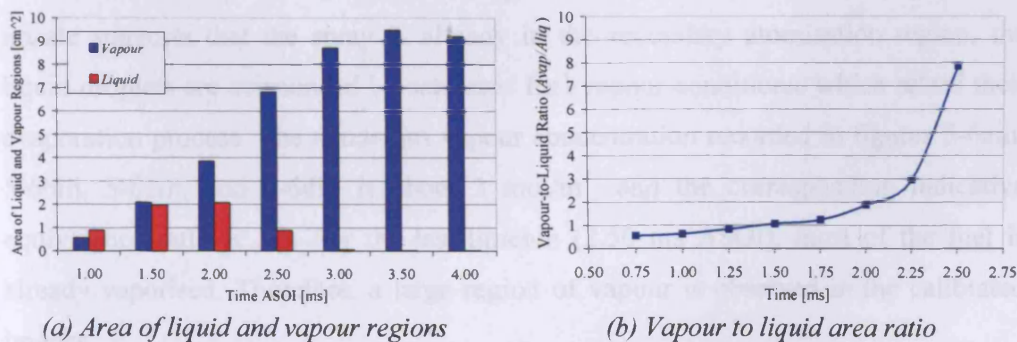


Figure 5-5: Relative area of liquid and vapour regions for case 1

### 5.1.3. Vapour Fractions Quantification

An analysis of distribution and concentration of vapour fractions is possible after the images have been calibrated as explained in section 3.3. Figure 5-6 shows vapour concentration measurements for a pressure swirl atomiser at selected times after start of injection. Randomly selected images are discussed in order to compare the vapour distributions at four different stages of the injection event.

For the first timebin, 1.00 ms ASOI, the injector is still fully open during the main injection stage. Hence, significant amounts of liquid fractions are expected close to the nozzle due to primary atomisation. In this timebin, the vapour is concentrated towards the edges of the spray and in areas around the sac volume. At this distance downstream the spray is already in the secondary atomisation stage and as the droplets get smaller they will evaporate more rapidly creating vapour rich zones. According to the d-squared law for evaporation (equation 2-6), a single 20 micron drop would take approximately 1 millisecond to evaporate completely, which is consistent with the global arithmetic mean diameter of the spray and the evaporation timescales observed at this time. At 1.50 ms ASOI, figure 5-6ii (a, b, c and d), a vapour rich zone is revealed in the centre of the recirculation head vortex, showing an indicative equivalence ratio  $\Phi'$  of approximately 3.75, which describes a very rich mixture. The vapour concentration in this region is in the order of  $3.5 \text{ mol/m}^3$ . For this timebin, there is still a substantial fraction of fuel in the liquid phase which compromises the detection of vapour in the regions close to the injector tip.

Later in the injection, at 2.00 ms ASOI, the injection event has already ended. After correcting for liquid fluorescence, it is possible to identify a hole in the calibrated images shown for this timebin between 20 and 50 mm downstream. This is the result of a large region of liquid fuel, separated 20 mm from the tip of the injector, which corresponds to the last fraction of fuel injected. Even though the distance from the nozzle suggests that the spray is already in the secondary atomisation region, the liquid droplets are surrounded by saturated fuel-vapour conditions, which retard their evaporation process. The maximum vapour concentration recorded in figures 5-6aiii, 5-6biii, 5-6ciii, and 5-6diii is about  $3 \text{ mol/m}^3$ , and the corresponding indicative equivalence ratio is 3.3. For the last timebin (2.50 ms ASOI), most of the fuel is already vaporised. Therefore, a large region of vapour is observed in the calibrated images.

Chapter 5: Analysis of Vapour Fractions of a Gasoline Direct Injection Spray at Elevated Ambient Conditions

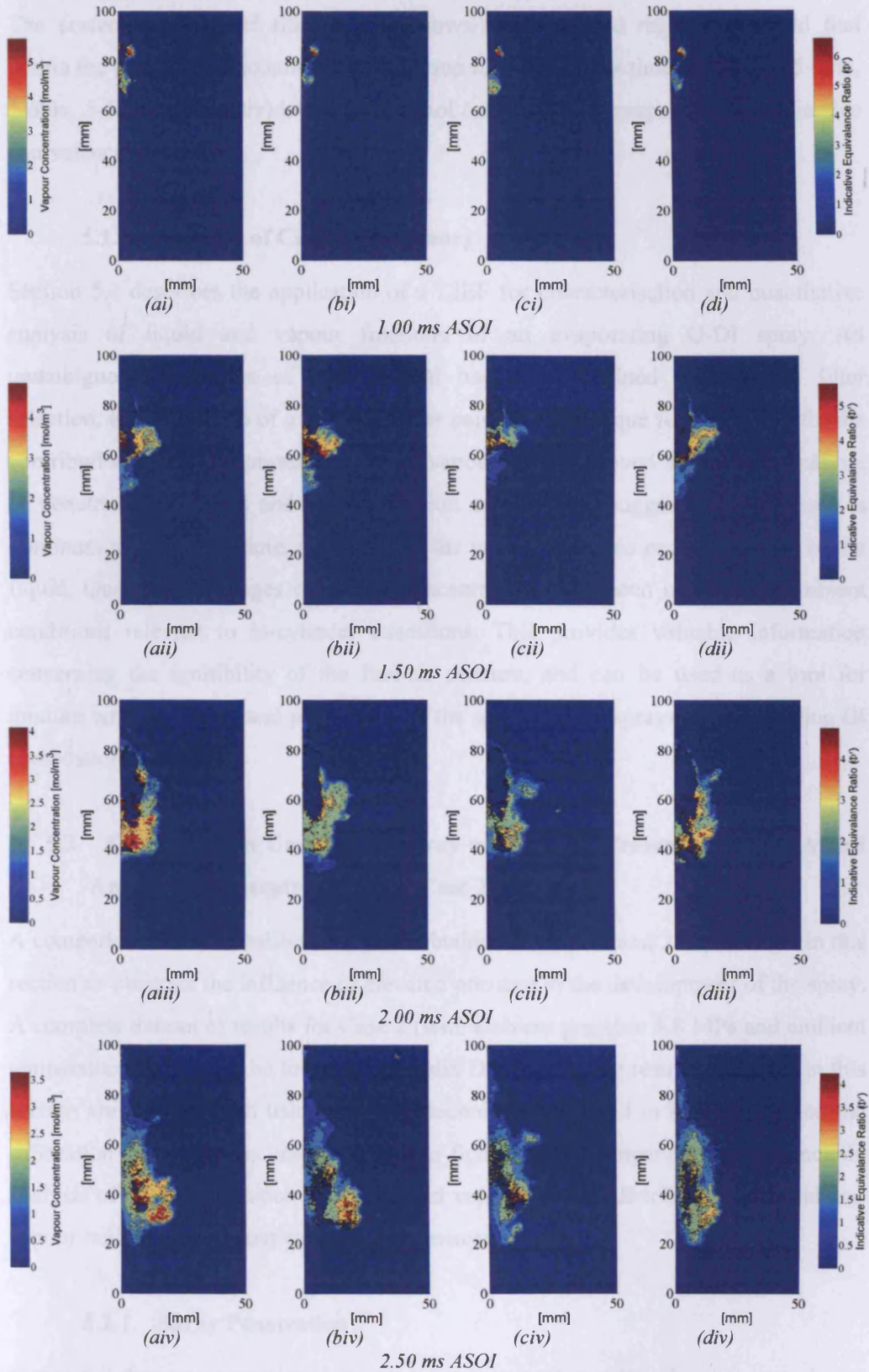


Figure 5-6: Vapour concentration measurements for selected timebins of Case 1 (all images are randomly selected from instantaneous measurements)

The correction of liquid fluorescence shows small isolated regions of liquid fuel within the spray. The maximum concentration recorded at this timebin (figures 5-6aiv, 5-6biv, 5-6civ, and 5-6div) is about 2.75 mol / m<sup>3</sup>, which corresponds to an indicative equivalence ratio of 3.

#### **5.1.4. Analysis of Case 1 – Summary**

Section 5.1 describes the application of a LIEF for characterisation and quantitative analysis of liquid and vapour fractions of an evaporating G-DI spray. An unambiguous separation of liquid signal has been obtained with careful filter selection, and utilisation of a suitable tracer pair. The technique for correcting for the contribution of liquid fluorescence in the vapour images proved successful. Analysis of penetration of liquid and vapour fraction of the spray suggests vapour phase is dominant at any given time, showing that the vapour fractions penetrate ahead of the liquid. Quantitative images of vapour concentration have been obtained at ambient conditions relevant to in-cylinder conditions. This provides valuable information concerning the ignitibility of the fuel-air mixture, and can be used as a tool for mixture ignition timing and positioning of the spark plug in spray-guided gasoline DI combustion systems.

#### **5.2. Analysis of an Unconfined Spray at Ambient Pressure 0.58 MPa and Ambient Temperature 423 K – Case 2**

A comparison between calibrated results obtained for case 1 and 2 is presented in this section to illustrate the influence of elevated pressure in the development of the spray. A complete dataset of results for Case 2 (with ambient pressure 5.8 MPa and ambient temperature 423 K) can be found in appendix D. Quantitative results discussed in this section are also obtained using the LIEF technique discussed in section 3.3, and the calibration curve for this case is shown in figure 3-23. Comparative results include analysis of spray penetration for liquid and vapour phases, distribution of liquid and vapour regions, and vapour concentration measurements.

##### **5.2.1. Spray Penetration**

Figure 5-7 shows a comparison between spray penetration of liquid and vapour phases for cases 1 and 2. As described in section 5.1.1, the axial penetration is defined as the



maximum axial distance between the injector tip and the front edge of the spray, and the radial penetration is defined as the maximum radial distance between the spray and injector axis. Figure 5-7a confirms the influence of ambient pressure on fuel penetration, as the absolute axial penetration of both the liquid and vapour phases is significantly reduced for the high pressure case.

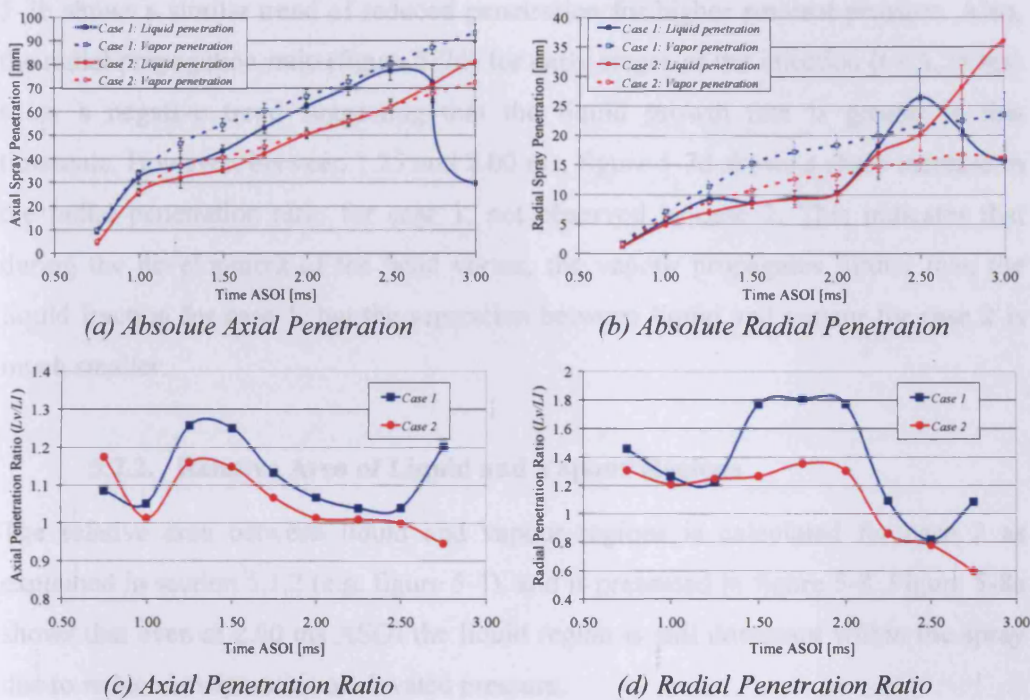


Figure 5-7: Comparison between spray penetration of liquid and vapour phases for cases 1 and 2

The ratio between vapour and liquid axial penetration ( $L_v/L_l$ ) is presented in figure 5-7c. Regardless of the ambient conditions, this ratio is mostly greater than unity throughout the injection event. This implies that the growth of the vapour phase is still dominant at elevated ambient pressure. Between 0.75 and 1.00 ms ASOI, there is a decrease in the axial penetration ratio for both cases, suggesting a faster rate of growth of the liquid phase due to the pre-spray (sac-spray) characteristics, which is largely formed by large droplets with high axial momentum and minimal radial velocity. After this time, the axial penetration ratio (figure 5-7c) for case 2 follows the same trend observed for case 1 (discussed in section 5.1.1). However, this ratio is significantly reduced for case 2 throughout the injection event suggesting a smaller

separation between vapour and spray for this case, indicating that, as to be expected, increasing the ambient density reduces the evaporation rate.

Figure 5-7b shows the absolute radial penetration for the liquid and vapour phases of the spray, and figure 5-7d shows the radial penetration ratio between both phases. The radial growth tendency observed for both phases in this plots (5-7b and 5-7d) is similar to that observed for the axial penetration case (figures 5-7a and 5-7c). Figure 5-7b shows a similar trend of reduced penetration for higher ambient pressure. Also, the radial propagation ratio (figure 5-7d) for early stages of the injection ( $t < 1,25$  ms) show a negative trend suggesting that the liquid growth rate is greater in this timescale. However, between 1.25 and 2.00 ms, figure 5-7d shows a sharp increase in the radial penetration ratio for case 1, not observed in case 2. This indicates that during the development of the head vortex, the vapour propagates further than the liquid fraction for case 1, but the separation between liquid and vapour for case 2 is much smaller.

### 5.2.2. Relative Area of Liquid and Vapour Regions

The relative area between liquid and vapour regions is calculated for case 2 as explained in section 5.1.2 (e.g. figure 5-4), and is presented in figure 5-8. Figure 5-8a shows that even at 2.00 ms ASOI the liquid region is still dominant within the spray due to reduced evaporation at elevated pressure.

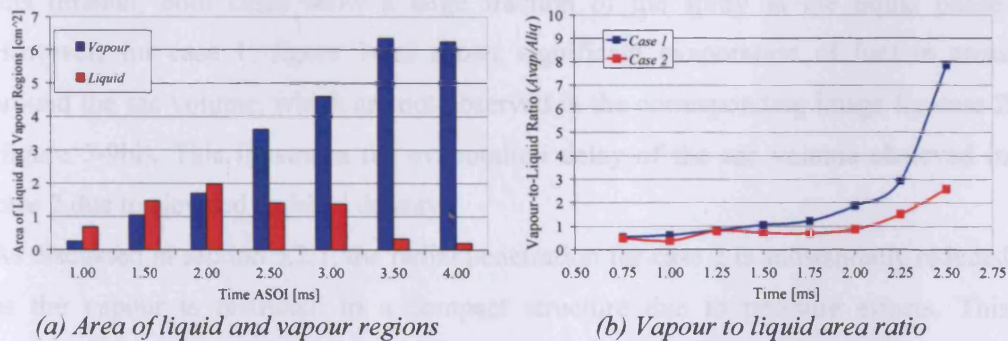


Figure 5-8: Relative area of liquid and vapour regions for case 2

Comparing figure 5-8a with figure 5-5a, it is clear that there is a significant increment in the fraction of liquid fuel region observed for case 2 (especially after 1.50 ms) as the elevated pressure retards the evaporation process. Figure 5-8b shows that, in general, the growth of the vapour region is significantly retarded for the high pressure case, as the liquid is more dominant up to 2.00ms ASOI. At this timebin, the vapour-

to-liquid ratio is approximately 2.0 for case 1 ( $P_a = 0.14$  MPa) and almost 1.0 for case 2 ( $P_a = 0.58$  MPa). This indicates that the vapour region occupies about 66 % and 50 % of the total area of the spray respectively. At 0.58 MPa, the vapour-to-liquid area ratio for case 2 increases slowly throughout the injection, showing that the higher ambient density prevents the spray from penetrating and restricts it to a compact spray region.

### 5.2.3. Vapour Fractions Quantification

Similar to section 5.1.3, calibrated images of vapour concentration are obtained for case 2, as explained previously in the post processing section (section 3.3). Figure 5-9 shows a quantitative comparison of vapour concentration measurements for selected timebins of Cases 1 and 2 (all images are randomly selected from instantaneous measurements). The figure, at any given time (5-9i, 5-9ii, 5-9iii, and/or 5-9iv), demonstrates the influence of ambient pressure in the evaporation of the spray. As the spray collapses under elevated pressures, there is a significant difference in size, distribution, and concentration of the vapour fraction. The collapse of the spray under elevated pressure is well known for pressure-swirl sprays (Kay 2006) under current experimental conditions.

For the first timebin, 1.00 ms ASOI, a very high concentration of vaporised fuel is observed around the edges of the compacted spray at high pressure (figure 5-9bi). At this timebin, both cases show a large fraction of the spray in the liquid phase. However, for case 1, figure 5-9ai shows significant evaporation of fuel in areas around the sac volume, which are not observed in the corresponding image for case 2 (figure 5-9bi). This illustrates the evaporation delay of the sac volume observed in case 2 due to elevated ambient density.

As discussed in section 5.2.1, the radial penetration for case 2 is substantially reduced as the vapour is restricted to a compact structure due to pressure effects. This phenomenon can be observed when comparing figures 5-9aii and 5-9bii. The area of the recirculation head vortex is significantly reduced at high pressure, showing a mean concentration of approximately 6 mol/m<sup>3</sup> in the centre of the vortex, which is significantly more than the concentration of around 3.5 mol/m<sup>3</sup> exhibited at lower ambient pressure (figure 5-9aii). The corresponding indicative equivalence ratio ( $\Phi'$ ) for case 1 is approximately 3.5, which defines a very rich mixture.



## Chapter 5: Analysis of Vapour Fractions of a Gasoline Direct Injection Spray at Elevated Ambient Conditions

Case 1:  $P_a = 0.14 \text{ MPa}$ ,  $T_a = 423 \text{ K}$

Case 2:  $P_a = 0.58 \text{ MPa}$ ,  $T_a = 423 \text{ K}$

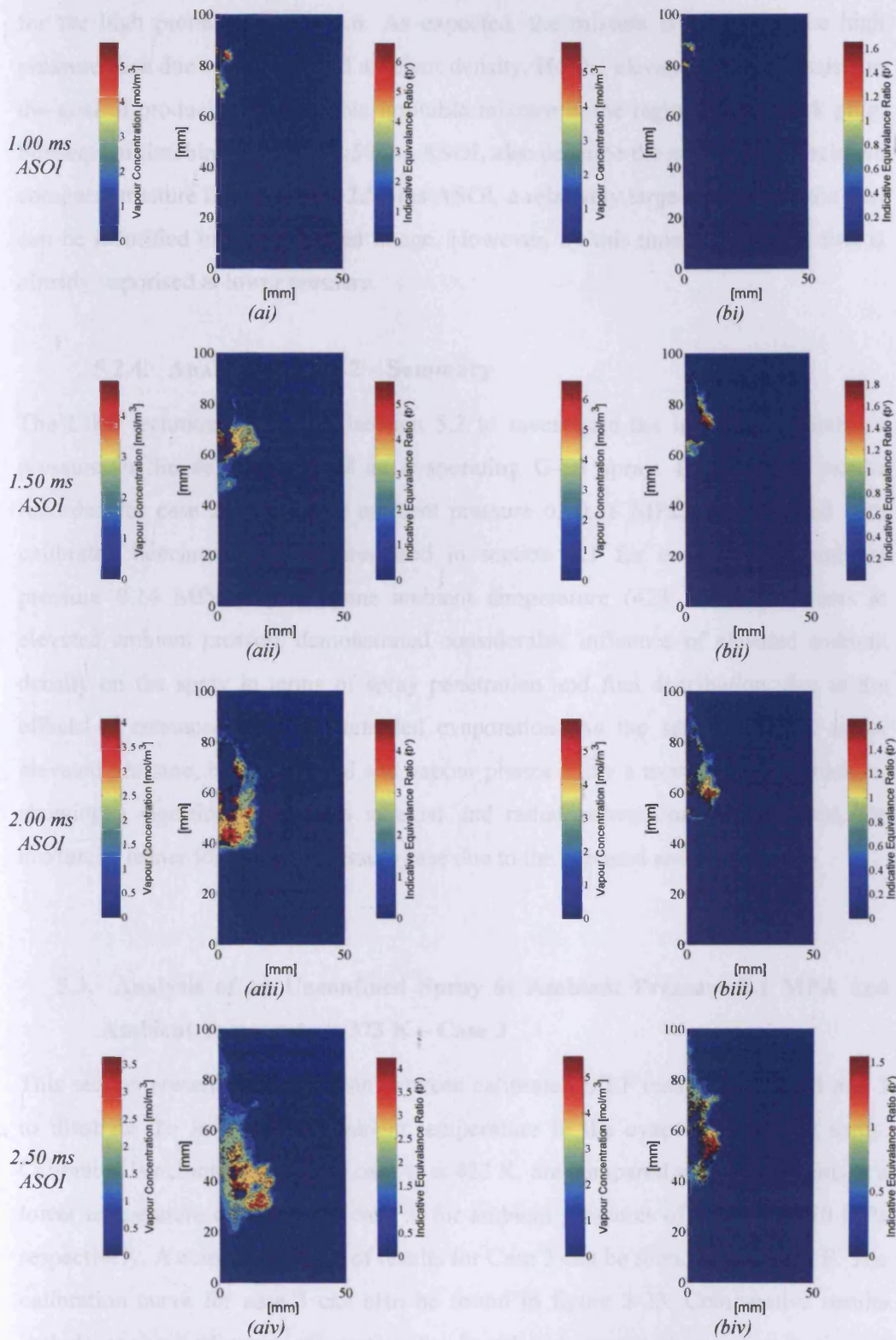


Figure 5-9: Comparison of vapour concentration measurements for selected timebins of Cases 1 and 2 (all images are randomly selected from instantaneous measurements)

In contrast, for the same timebin the maximum indicative equivalence ratio recorded for the high pressure case is 1.6. As expected, the mixture is leaner for the high pressure case due to the elevated ambient density. Hence, elevated pressure assists in the goal of producing a repeatable ignitable mixture in the region of the spark plug. Subsequent timebins, 2.00 and 2.50 ms ASOI, also describe the same trend of relative compact structure for case 2. At 2.50 ms ASOI, a relatively large region of liquid fuel can be identified in the calibrated image. However, by this time, most of the fuel is already vaporised at lower pressure.

#### **5.2.4. Analysis of Case 2 – Summary**

The LIEF technique is used in section 5.2 to investigate the influence of ambient pressure in the development of an evaporating G-DI spray. Experimental results recorded for case 2, at elevated ambient pressure of 0.58 MPa, are compared with calibrated benchmark results presented in section 5.1 for case 1, with ambient pressure 0.14 MPa, for the same ambient temperature (423 K). Experiments at elevated ambient pressure demonstrated considerable influence of elevated ambient density on the spray in terms of spray penetration and fuel distribution, due to the effects of enhanced drag and retarded evaporation. As the spray collapses under elevated pressure, both the liquid and vapour phases show a more compact structure, showing a significant reduction in axial and radial penetration. As expected, the mixture is leaner for the high pressure case due to the elevated ambient density.

#### **5.3. Analysis of an Unconfined Spray at Ambient Pressure 0.1 MPa and Ambient Temperature 373 K – Case 3**

This section presents a comparison between calibrated LIEF results for cases 1 and 3 to illustrate the influence of ambient temperature in the evaporation of the spray. Calibrated benchmark results for case 1, at 423 K, are compared with experiments at a lower temperature of 373 K for case 3, for ambient pressures of 0.14 and 0.10 MPa respectively. A complete dataset of results for Case 3 can be found in appendix E. The calibration curve for case 3 can also be found in figure 3-23. Comparative results include analysis of spray penetration for liquid and vapour phases, distribution of liquid and vapour regions, and vapour concentration measurements.



### 5.3.1. Spray Penetration

A quantitative time-resolved comparison of axial and radial spray penetration for cases 1 and 3 is presented in figure 5-10. As described previously, the axial and radial penetrations are defined as the maximum axial and radial distances from the tip to the edges of the spray. In general, case 3 shows a slightly reduced penetration when compared to case 1 due to ambient density effects, as discussed qualitatively in figure 5-1. This is also observed in figure 5-10a, as the absolute axial penetration of both liquid and vapour phases show a slight reduction for case 3.

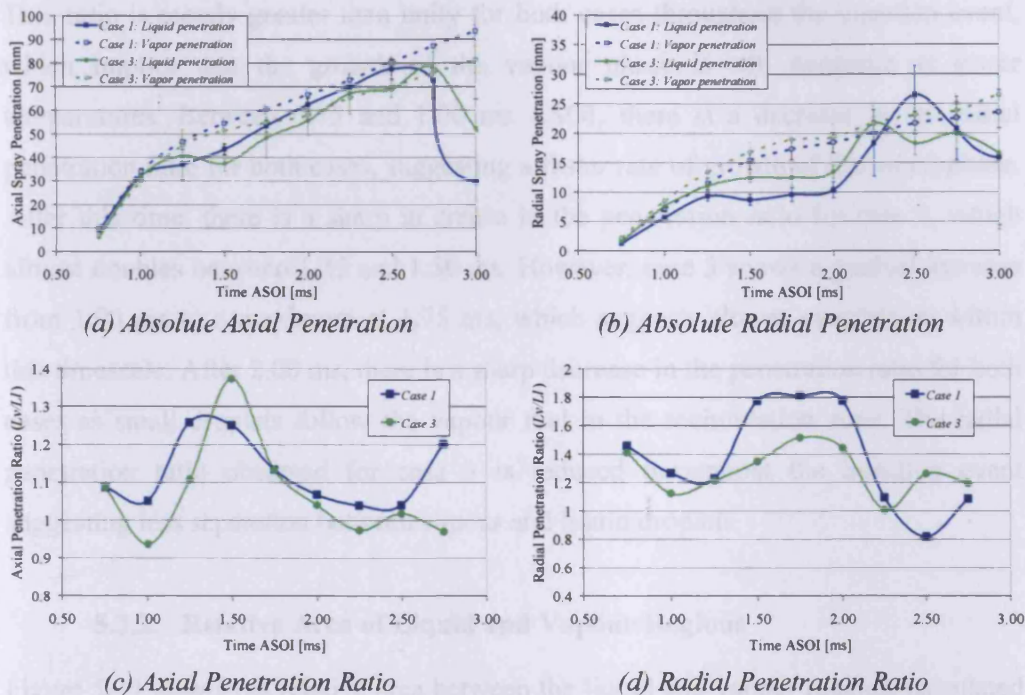


Figure 5-10: Comparison between spray penetration of liquid and vapour phases for cases 1 and 3

The vapour-to-liquid penetration ratio for the axial component (figure 5-10c) shows a similar trend to that observed for case 1. Between 0.75 and 1.00 ms ASOI, there is a sharp decay in the axial penetration ratio for both cases, suggesting a faster penetration of the liquid phase due to the sac-spray characteristics. After 1.00 ms ASOI, the ratio increases for both cases to a maximum at around 1.50 ms. However, figure 5-10c shows a delay for case 3 within this timescale, which is attributed to retarded evaporation of the sac volume. Subsequent timebins show a relatively slow decay of axial penetration ratio due spray evaporation after the end of injection.

Interestingly, the absolute radial penetration shown in figure 5-10b, describes higher radial penetration for case 3 for both the liquid and vapour fractions of the spray, contrary to that observed for the axial component. Therefore, the spray structure observed for case 3 can be described as shorter (axially) but wider (radially) for a lower ambient temperature. This is likely to be due to reduced evaporation at lower ambient temperature, as the remaining droplets within the spray follow the recirculation vortex with relatively high momentum, thus increasing the radial global penetration of the fuel.

Figure 5-10d, shows the ratio between vapour and liquid radial penetration ( $L_v/L_l$ ). This ratio is mostly greater than unity for both cases throughout the injection event, which implies that the growth of the vapour phase is still dominant at lower temperatures. Between 0.75 and 1.00 ms ASOI, there is a decrease in the radial penetration ratio for both cases, suggesting a faster rate of growth of the liquid phase. After this time, there is a sharp increase in the penetration ratio for case 1, which almost doubles between 1.25 and 1.50 ms. However, case 3 shows a gradual increase from 1.00 ms to a maximum at 1.75 ms, which suggests slower evaporation within this timescale. After 2.00 ms, there is a sharp decrease in the penetration ratio for both cases as small droplets follow the vapour fuel in the recirculation zone. The radial penetration ratio observed for case 3 is reduced throughout the injection event suggesting less separation between vapour and liquid droplets.

### 5.3.2. Relative Area of Liquid and Vapour Regions

Figure 5-11 shows the relative area between the liquid and vapour regions, calculated as explained in section 5.1.2. The distribution of relative area observed for case 3 (figure 5-11a) is similar to that observed for case 1 (figure 5-5a). However, the liquid phase appears to be even more dominant for case 3 at early stages of the injection (between 1.00 and 1.50 ms), which is expected due to retarded evaporation at lower temperatures. Since the injection ends at 1.50 ms, further timebins show a sharp increase in the area of vapour fuel as the liquid fuel within the rig evaporates.

Figure 5-11b shows that ratio between the area of vapour and liquid fuel ( $A_{vap}/A_{liq}$ ) is slightly smaller for case 3, which indicates that the area of liquid fuel is more dominant in case 3, and also illustrates the slower evaporation of fuel at lower temperatures. At 373 K, case 3 shows a vapour-to-liquid area ratio below unity for

times before 1.75 ms. After this time, the ratio increases exponentially at a higher gradient than case 1, suggesting a faster evaporation after the injection has ended.

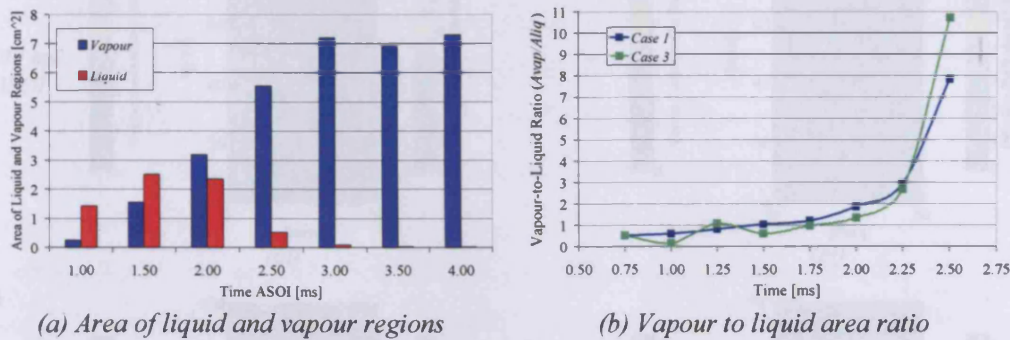


Figure 5-11: Relative area of liquid and vapour regions for case 3

### 5.3.3. Vapour Fractions Quantification

Calibrated images of vapour concentration for cases 1 and 3 are presented and compared in figure 5-12 (all images are randomly selected from instantaneous measurements). Similar to section 5.1.3 and 5.2.3, an analysis of concentration of vapour fractions is possible after the images have been calibrated as explained in section 3.3. Figure 5-12, illustrates the influence of reduced ambient temperature in the evaporation of the spray at four different stages of the injection event.

For the first timebin, 1.00 ms ASOI, a relatively small area of vapour fuel is observed for case 3, similar to that observed for case 2 in figure 5-9. However, the compact vapour structure observed for case 3 is less concentrated ( $4 \text{ mol/m}^3$ ) than the vapour region of case 1 ( $5 \text{ mol/m}^3$ ), contrary to the comparison between cases 1 and 2. This implies that the reduced area of vapour is the result of retarded evaporation within this timescale. At this timebin, case 1 (figure 5-12ai) shows rich vapour regions around the edges of the spray and around the sac volume, while the vapour region for case 3 (figure 5-12bi) is concentrated only at the front edge of the hollow cone. The following timebin, a vapour rich zone is revealed in the centre of the recirculation vortex for both cases. Figure 5-12aai and figure 5-12bii show an indicative equivalence ratio  $\Phi'$  of approximately 3.75, and 6 for cases 1 and 3 respectively. For this timebin, at 1.50 ms, there is a substantial fraction of fuel in liquid phase for both cases which makes difficult the detection of vapour in the regions close to the injector tip.



Chapter 5: Analysis of Vapour Fractions of a Gasoline Direct Injection Spray at Elevated Ambient Conditions

Case 1:  $P_a = 0.14 \text{ MPa}$ ,  $T_a = 423 \text{ K}$

Case 3:  $P_a = 0.10 \text{ MPa}$ ,  $T_a = 373 \text{ K}$

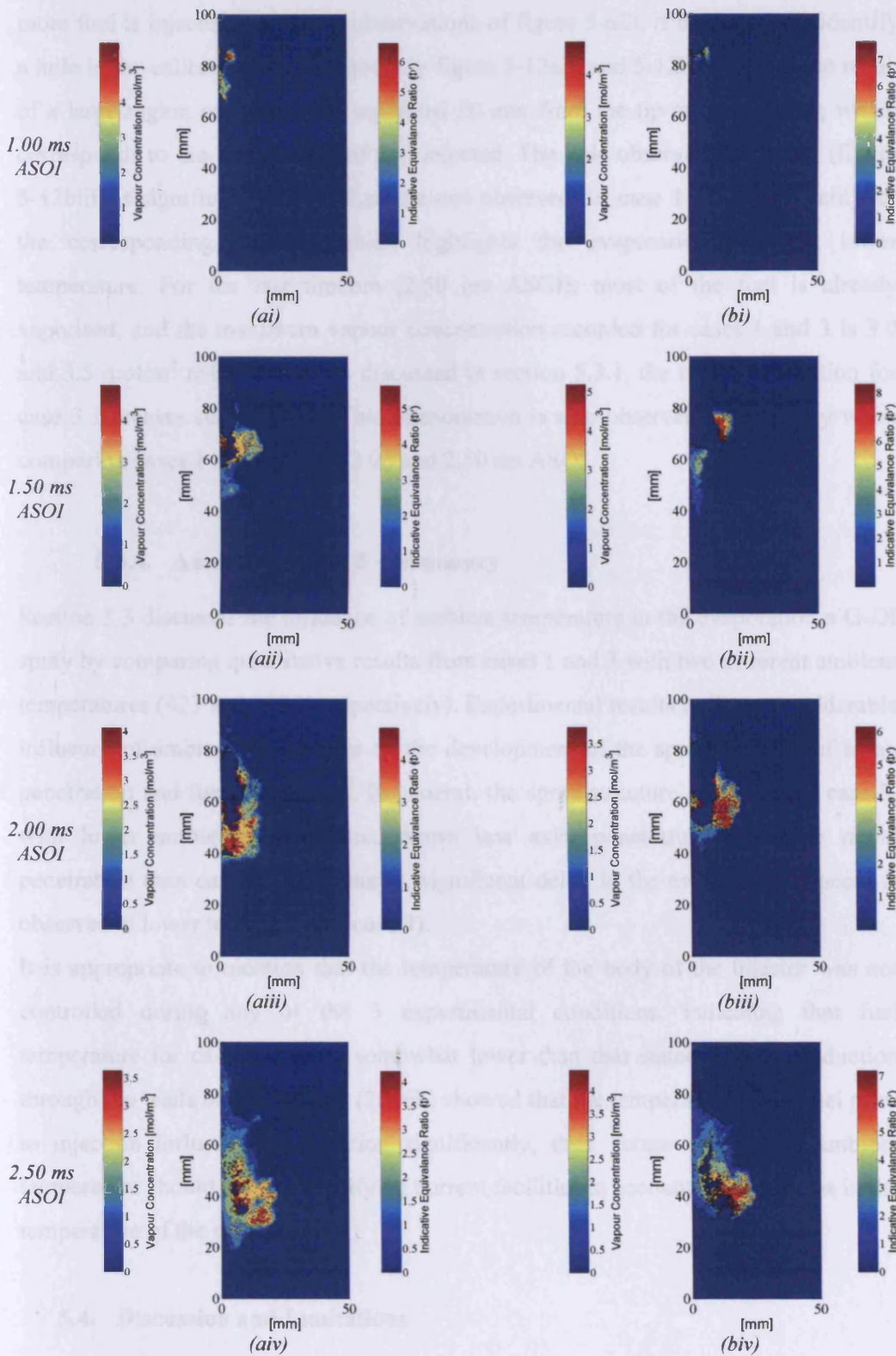


Figure 5-12: Comparison of vapour concentration measurements for selected timebins of Cases 1 and 3 (all images are randomly selected from instantaneous measurements)

Later in the injection, at 2.00 ms ASOI, the injection event has already ended and no more fuel is injected. Similar to observations of figure 5-6iii, it is possible to identify a hole in the calibrated images shown in figure 5-12aiii and 5-12biii. This is the result of a large region of liquid fuel, separated 20 mm from the tip of the injector, which corresponds to the last fraction of fuel injected. The hole observed for case 3 (figure 5-12biii) is significantly larger than the one observed for case 1 (figure 5-12aiii) for the corresponding timebin, which highlights the evaporation delay at lower temperature. For the last timebin (2.50 ms ASOI), most of the fuel is already vaporised, and the maximum vapour concentration recorded for cases 1 and 3 is 3.0 and 3.5 mol/m<sup>3</sup> respectively. As discussed in section 5.3.1, the radial penetration for case 3 increases substantially. This phenomenon is also observed qualitatively when comparing cases 1 and case 3 at 2.00 and 2.50 ms ASOI.

#### 5.3.4. Analysis of Case 3 – Summary

Section 5.3 discusses the influence of ambient temperature in the evaporation a G-DI spray by comparing quantitative results from cases 1 and 3 with two different ambient temperatures (423 and 373 K respectively). Experimental results indicate considerable influence of ambient temperature on the development of the spray in terms of spray penetration and fuel distribution. In general, the spray structure observed for case 3, with lower ambient temperature, shows less axial penetration but more radial penetration than case 1. Additionally, significant delay in the evaporation process is observed at lower temperatures (case 3).

It is appropriate to mention that the temperature of the body of the injector was not controlled during any of the 3 experimental conditions, indicating that fuel temperature for case 3 may be somewhat lower than that stated due to conduction through the walls of the rig. Kay (2006b) showed that the temperature of the fuel prior to injection influences atomisation significantly, thus, future analysis of ambient temperature should involve modifying current facilities to account for variations in the temperature of the injector.

#### 5.4. Discussion and Limitations

Unambiguous separation of liquid signals has been achieved, which provides valuable information about the location of liquid droplets in the vapour images. This



information allows for correction of the vapour images for quantitative results. However, significant errors are introduced to the corrected images due to the comparatively large size of the pixels being disregarded by the binary liquid images. For instance, the final pixel size of these experiments is around 100 x 100 microns, so ignoring 1 pixel generates a hole of 100 x 100 microns in the corrected image, however, this pixel could be the result of the fluorescence of a single 40micron droplet, for which a much larger area than required is ignored. Therefore, to increase accuracy a camera with a much larger pixel resolution should be used in order to apply this criterion for separation of vapour fluorescence, or a smaller area of interrogation should be considered.

### **5.5. Chapter Summary**

This chapter discussed the applicability of the laser induced exciplex fluorescence (LIEF) technique described in chapter for the characterisation of vapour fractions in gasoline DI sprays. Simultaneous, unambiguous spectrally-separated signals for liquid and vapour fractions were obtained with careful selection of optical filters. The technique for correcting for the contribution of liquid fluorescence in the vapour images proved successful. Experimental results recorded at three different ambient conditions showed that the technique was successful in describing liquid and vapour fractions qualitative and quantitatively. This technique provides novel insights to the applicability of LIEF for quantitative measurements of vapour concentration and air-to-fuel ratios in the vicinity of spark plug for gasoline DI applications. Recommendations for future improvement in accuracy have been discussed.

# **Chapter 6:**

**CFD modelling of a Gasoline Impinging Spray**

This Chapter describes the comparison of a simulated impinging spray from a G-DI pressure swirl atomiser and experimental data presented and discussed in Chapter 4. The chapter aims to demonstrate the potential of the TIR-LIF technique, developed in this thesis, for appraisal of current computational models and for development of new empirical numerical models to describe the atomisation and spray impact processes. Preliminary CFD modelling results of an impacting spray are presented in this chapter for corresponding experimental conditions discussed in chapters 4.

### 6.1. Computational Fluid Dynamics

The objective of Computational Fluid Dynamics (CFD) is to solve numerically the partial differential equations that govern the motion of fluid flow. The equations describing the Newtonian fluid flow motion are the Navier-Stokes equations, the continuity equation, and the energy equation. Although many of the key ideas for numerical solution methods of partial differential equations were established more than a century ago, they were of little use before computers appeared. Once the power of computers was recognized, interest in numerical techniques increased dramatically. Nowadays, CFD is a very powerful technique and spans a wide range of industrial and non-industrial application areas such as: automotive engineering, aeronautics, hydrodynamics, turbomachinery, electrical and electronic engineering, power generation, chemical process engineering, marine engineering, meteorology, environmental engineering, and biomedics among others.

In principle, solutions of any desired accuracy can be obtained, subject to numerical convergence. However for many practical fluid flow problems such as turbulent, combusting or multiphase flows, the accurate numerical solution is not always practicable. This makes necessary the introduction of mathematical or empirical models. These submodels can be used even when the exact treatment of the governing equations is possible, to reduce the computational cost. The validation of empirical models and sub-models requires careful experimentation. The chapter aims to demonstrate the potential of the TIR-LIF technique, developed in this thesis, for appraisal of current computational models which describe the spray impact process.

Among the several commercial CFD packages available, this study uses 'Ricardo VECTIS 3.8' to simulate the impact process of a G-DI pressure swirl spray. VECTIS is a CFD code developed by Ricardo Software. It is a general-purpose tool for solving

industrial fluid flow problems, with particular attention given to requirements of engine and automotive applications. It uses an Euler-Lagrangian approach to model sprays. Sub-models are used to describe droplet break-up, droplet evaporation, impingement, and coalescence. More information about the models used in VECTIS CFD code can be found in Ricardo-Software (2004a and 2004b). A key summary of the governing equations and spray sub-models is presented in the following section.

### 6.2. Governing Equations

The full set of equations used in Ricardo VECTIS to describe sprays can be found in Ricardo-Software (2004a). A key summary of those equations is presented in this section. The equation governing the momentum of a droplet of mass  $m_d$ , which is described by Newton's Law, is shown in equation 6-1:

$$m_d \frac{dU_d}{dt} = \frac{1}{2} (C_p \rho_g A_d) \cdot (U - U_d)^2 \quad (6-1)$$

where,  $C_p$  is the drop drag coefficient,  $\rho$  is the gas density,  $A_d$  is the drop frontal area, and  $(U-U_d)$  is the relative velocity of between the ambient and the drop. The drag coefficient is calculated from the correlation proposed by Putnam (1961), as described in equation 6-2.

$$C_d = \begin{cases} \frac{24}{Re_d} \left( 1 + \frac{1}{6} Re_d^{2/3} \right) & \text{---} Re_d \leq 1000 \\ 0.424 & \text{---} Re_d \geq 1000 \end{cases} \quad (6-2)$$

The drop Reynolds number is defined as:

$$Re = \frac{\rho U_d D_d}{\mu} \quad (6-3)$$

where  $\mu$  is the gas dynamic viscosity.

The evaporation of drops within a spray involves simultaneous heat and mass transfer processes. The heat of evaporation is transferred to the drop by conduction and convection from the surrounding gas. Then, the vapour is transferred back to the gas stream by convection and diffusion. The mass and temperature are calculated from the following equations:

$$\frac{dm_d}{dt} = -A_d Sh \frac{D_{AB}}{D_d} \rho_v \ln \left( \frac{p - p_{v,\infty}}{p - p_{v,s}} \right) \quad (6-4)$$

$$m_d \frac{dc_{p,d} T_d}{dt} = A_d Nu (T_d - T) \cdot K_m F_z + h_{fg} \frac{dm_d}{dt} \quad (6-5)$$

where  $D_{AB}$  is the mass diffusivity,  $K_m$  is the thermal conductivity,  $C_{p,d}$  is the gas specific heat of liquid fuel,  $h_{fg}$  is the latent heat of evaporation,  $p$  is the pressure of the gas mixture, and  $p_{v,s}$  and  $p_{v,\infty}$  stand for the partial pressure at the drop surface and ambient respectively. Additionally, the fuel vapour density  $\rho_v$  is calculated from the gas pressure and mean temperature ( $T_m = (T_d - T)/2$ ). The Nusselt number ( $Nu$ ) is the ratio of convective to conductive heat transfer across the boundary, and the Sherwood number ( $Sh$ ) represents the ratio of convective to diffusive mass transport, and they are calculated by the correlation by Ranz and Marshall (1952):

$$Nu = 2 \left( 1 + 0.3 Re_d^{1/2} \cdot Pr^{1/3} \right) \quad (6-6)$$

$$Sh = 2 \left( 1 + 0.3 Re_d^{1/2} \cdot Sc^{1/3} \right) \quad (6-7)$$

where the Schmidt and Prandtl numbers are:

$$Sc = \frac{\mu}{\rho D_d} \quad (6-8)$$

$$Pr = \frac{C_p \mu}{K_m} \quad (6-9)$$

where  $C_p$  is the specific heat and  $\mu$  the gas viscosity. Finally, the quantity  $F_z$  is obtained from:

$$F_z = \frac{\ln \left( 1 + \frac{(p_t - p_{t,\infty})}{(p_t - p_{t,s})} \right)}{\frac{(p_t - p_{t,\infty})}{(p_t - p_{t,s})}} \quad (6-10)$$

VECTIS offers a selection of models to describe mechanical break-up within the spray: the Reitz-Diwakar break-up model, the Liu-Mather-Reitz model, and the Patterson-reitz break-up model. In this study, the Reitz-Diwakar (1986) break-up



model is used. The model proposes a critical value of Weber number after which the droplet breaks-up using a bag break-up mechanism. A second critical value based on the drop Weber and Reynolds numbers is used to determine the transition between bag and stripping breakup. Further information about mechanical break-up can be found in Lefebvre (1989).

### 6.3. Spray Impact Modelling

Extensive research has been undertaken over the past couple of decades to formulate and validate numerical models to describe the spray impact phenomenon (see Cossali et al 2005). A number of spray impact models have been proposed in the literature, the most popular being: Bai and Gosman (1995), Mundo et al (1998), and the Stanton and Rutland model (1998). The formulation of spray impact models is generally based on experiments of single droplets impacting normally onto dry or wet walls, where the impact conditions are carefully controlled. Results from single droplets impact are then extrapolated to multiple droplet impact (spray impact) by simple superimposition of multiple individual droplets. However, such simplification neglects to consider various effects of the spray impact process such as: the influence of the deposited film on the post-impact spray, the tangential momentum of oblique impacting droplets, the effect of multiple droplets interaction, the effect of film fluctuations on the outcome of impacting drop-lets, and the creation of secondary droplets due to break up of the liquid film (Kalantari and Tropea 2007). For instance, the literature shows that a single drop impact differs from the impact of a train of drops on a stationary film (Cossali et al 1997). Also, observations by Sivakumar and Tropea (2002) show that the impact from a single drop differs significantly from the impact resulting from a drop within a spray. Therefore, the development of new empirical spray impact models often involve the analysis of more challenging experimental configurations involving the interaction of multiple drops (e.g. Kalantari and Tropea 2007).

VECTIS offers a 'Spray Wall Impingement' model to predict the outcome of secondary spray formed upon impact. Considering the potential post-impingement outcomes discussed in section 2.4.4, the model includes three sub-models for possible post-impact regimes:

a) *Stick sub-model:*

Similar to figure 2-10a, and 2.10c, this sub-model assumes that all drops sticks to the wall once they reach the wall, and they are removed from the calculation.

b) *Rebound sub-model:*

Similar to figure 2-10b and 2-10e, this sub-model proposes that all droplets bounce back with the same speed as the incoming jet.

c) *Comprehensive sub-model:*

Based on the model proposed by Bai et al (1995 and 2002), this sub-model considers four potential outcomes resulting from a drop impacting a solid surface: Stick (figure 2-10a), Rebound (figure 2-10b), Spread (figure 2-10c), and Splash (figure 2-10f). In the normal regime, the behaviour of an outgoing droplet depends on the impinging Weber number and whether the wall is dry or wet. In this study, the comprehensive sub-model is used to predict post impingement spray characteristics. A summary of this impingement sub-model is presented in table 6-1:

Table 6-1: Summary of the comprehensive sub-model used by Ricardo VECTIS

	<i>Wet Wall</i>	<i>Dry Wall</i>
<i>Regime</i>	<i>Transition Criteria</i>	<i>Transition Criteria</i>
Stick	$We_d < 5$	$We_d < (A).La^{-0.18}$
Rebound	$5 \leq We_d \leq 10$	...
Spread	$10 \leq We_d \leq (1320).La^{-0.18}$	...
Splash	$We_d \geq (1320).La^{-0.18}$	$We_d \geq (A).La^{-0.18}$

where, the drop Laplace number is:

$$La = \frac{\rho_d \sigma D_d}{\mu_d^2} \tag{6-11}$$

and  $A$  is a function of the surface roughness:

- $A = 5264$  If surface roughness  $\Delta_s \leq 0.05 \mu m$
- $A = (2629.536) / \Delta_s^{0.24}$  If surface roughness  $0.05 \mu m \leq \Delta_s \leq 12 \mu m$
- $A = 1332$  If surface roughness  $\Delta_s \geq 12 \mu m$

When stick or spread happens, the drops are removed from the calculation, and the total mass of the pre-impact droplet is added to the surface film. When splash occurs, part of the drop mass deposits on the surface film and the rest of the mass bounces back as secondary spray. The mass of the secondary drops can be estimated by:

$$\frac{m_s}{m_i} = 0.2 + 0.6N_r \quad \text{For dry walls} \quad (6-12)$$

$$\frac{m_s}{m_i} = 0.2 + 0.9N_r \quad \text{For wet walls} \quad (6-13)$$

where  $m_i$  is the mass of impinging droplets,  $m_s$  is the total mass of the secondary droplets, and  $N_r$  is a random number between 0 and 1. This sub-model also include empirical correlations for heated wall above the Leidenfrost regime. These equations can be found in Ricardo-Software (2004a).

VECTIS offers a ‘Wall Film’ model to predict the outcome of the resulting liquid film formed on the impact surface as a result of spray impingement. The wall-film model is based on the model proposed by Bai and Gosman (2006). It adopts an Eulerian approach and seeks the solution of film characteristics by solving continuous film transport equations. A major assumption of this model involves the hypothesis that the film is ‘thin’ enough so that the film transport equations can be cast into depth-averaged equations, which are two-dimensional in the sense that one needs to deal with surface meshes only. A full set of equations describing this model can be found in Ricardo-Software (2004a). However, some key equations are reproduced in this section. The discretised continuity equation is presented in equation 6-9.

$$\frac{((\rho A \delta)_p^{+\Delta t} - (\rho A \delta)_p)}{\Delta t} + \sum_f \delta_f l_f F_f = \dot{m}_d - \dot{m}_v \quad (6-14)$$

where  $\sum_f$  stands for the summation over all sides of each patch cell,  $l_f$  is the length

of cell side  $f$ ,  $\dot{m}_d$  is the droplet mass evaporation rate,  $\dot{m}_v$  is the film evaporation rate at the interface, and the film face flux at side  $f$  is given by:

$$F_f = \rho \bar{U} \cdot \bar{n}_f \quad (6-15)$$

where  $\bar{n}_f$  is the unit vector tangentially normal to the side  $f$ .

The discretised momentum equation is given by:

$$\frac{((\rho \bar{U} A \delta)_p^{+\Delta t} - (\rho \bar{U} A \delta)_p)}{\Delta t} + \sum_f \delta_f l_f F_f \bar{U}_f = -\sum_f p_f \delta_f l_f \bar{n}_f + \vec{\sum}_{\text{int}} - \vec{\sum}_w + S_{\bar{U},d} \quad (6-16)$$

in which the subscript  $f$  refers to the value evaluated at the side  $f$ ,  $S_{\bar{U},d}$  is the droplet tangential momentum source,  $\vec{\sum}_{\text{int}}$  and  $\vec{\sum}_w$  are the shear stresses at the film interface and wall respectively. They are given by:

$$\vec{\sum}_{\text{int}} = \mu \left. \frac{\partial \bar{U}_t}{\partial Z} \right|_{\text{int}} \quad (6-17)$$

$$\vec{\sum}_w = \mu \left. \frac{\partial \bar{U}_t}{\partial Z} \right|_w \quad (6-18)$$

where  $\bar{U}_t$  is the tangential resultant velocity, and  $Z$  the distance from the surface normal. The total film pressure is the sum of the impingement pressure ( $p_{\text{imp}}$ ), the gas pressure ( $p_g$ ), and the capillary pressure ( $p_\sigma$ ), and is given by:

$$p = p_{\text{imp}} + p_g + p_\sigma \quad (6-19)$$

Finally, the discretised enthalpy equation is given by:

$$\frac{((\rho h A \delta)_p^{+\Delta t} - (\rho h A \delta)_p)}{\Delta t} + \sum_f \delta_f l_f F_f h_f = \dot{q}_{\text{int}} - \dot{q}_w + S_{h,d} \quad (6-20)$$

where  $\dot{q}_{\text{int}}$  and  $\dot{q}_w$  are the heat fluxes at the film interface and the wall respectively, and  $S_{h,d}$  is the droplet enthalpy source.

## 6.4. Spray Model Development

This section discusses the development of the computational mesh, and the development of the spray model used to simulate the pressure swirl injector used in the TIR-LIF experiments discussed in chapter 4. The spray model is then used as initial input data for the CFD simulation.

### 6.4.1. Mesh Development

In order to reduce computational requirements during the simulation, a relatively simple control volume was selected for this study. Even though the experimental setup discussed in chapter 4 involves the use of the TIR-LIF rig within the HP-HT rig, it can be assumed that the spray is not affected by wall effects of the resulting gas flow. Therefore, a simple box is used in this simulation, with dimensions such that the spray is unaffected by these effects. The schematic of the control volume used for the simulation can be seen in figure 6-1, with dimensions (100 by 100 by 40 mm). The injector tip for the simulation is located 21 mm above the impact surface to match the experimental conditions. Since the spray impact angle is  $45^\circ$ , the position of the tip was selected so that the spray impinges at the centre of the impact plane (28 mm from the back of the control volume and 50 mm from the side). The structured discretisation of the control volume produced 511904 cells of approximately  $1.00 \text{ mm}^3$ . However, within the impact surface, a grid refinement produced elements of approximately  $0.62 \text{ mm}^3$ . This level of grid refinement is a sufficient compromise between accuracy and computational cost (Ricardo-Software 2004b).

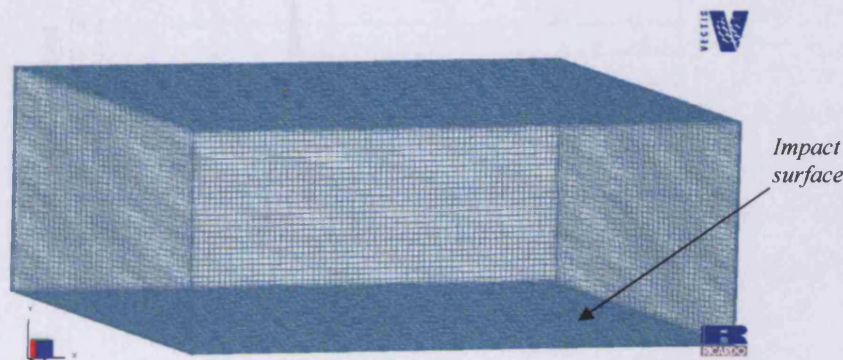


Figure 6-1: Schematic of the computational mesh used for an impingement spray



### 6.4.2. Spray Model

In order to describe the initial conditions of the spray model for CFD simulation it is required to define the following parameters:

- a) Mass Injection Rate Profile.
- b) Droplet Velocity Distribution.
- c) Droplet Diameter Distribution.
- d) Mass Injected.
- e) Initial Liquid Temperature.
- f) Nozzle Diameter.

A spray model was produced from experimental measurements of the free spray, and is later used as initial input data for the CFD simulation. Experiments by Kay (2006) studied the transient development of the spray in study and the influence of elevated ambient temperatures and pressures on spray characteristics. Using Phase Doppler Anemometry, he characterised droplet diameters and flowfield for the injector in study under a range of ambient conditions, including corresponding ambient conditions for TIR-LIF experiments. Additionally, he obtained instantaneous mass rate measurements of the injector in study using a Bosch type injector rate test described in detail by Morris (2003). Figure 6-2 shows the variation of mass rate of injection with time recorded by Kay (2006). PDA data and instantaneous mass rate measurements are complemented with high speed imaging in Kay's dataset which are used to build the spray model for the simulation presented in this chapter.

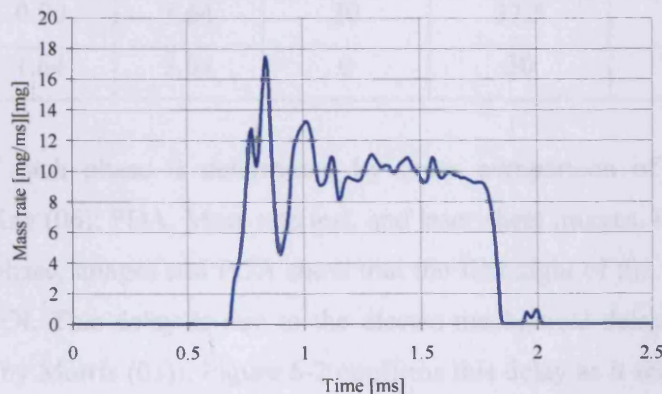


**Figure 6-2:** Variation of mass injection rate with time for the Bosch C2 pressure swirl injector (Kay 2006)

In order to simulate accurately the development of the transient pressure swirl spray, the injection is divided into four different phases:

1. **Sac-Spray:** this phase corresponds to the injection of the sac volume, which is the small amount of fuel left in the injector from the previous injection.
2. **Opening Phase:** describes the development of the hollow cone as the injector opens.
3. **Steady Phase:** describes a relatively steady phase in which the injector is fully open.
4. **Closing Phase:** describes the process of closure of the injector.

Each of these phases is modelled separately, with its own initial conditions, and is later superimposed in the same spray model to describe the complete injection event. To ensure continuity, the timing for each phase follows seamlessly from one phase to the next. Table 6-2 shows a summary of the initial conditions and corresponding times for all the different phases of the injection:

Table 6-2: Summary of the initial conditions and corresponding times for all the different phases of the spray model.

Phase	Opening time [ms]	Closing time [ms]	Inner Cone angle [°]	Outer Cone angle [°]	Parcel injection rate [parcel/s]
Sac-Spray	0.68	0.75	0	3	$3 \cdot 10^6$
Opening 1	0.75	0.82	0	7.5	$3 \cdot 10^6$
Opening 2	0.82	0.90	22.5	27.5	$3 \cdot 10^6$
Steady	0.90	1.64	30	37.5	$3 \cdot 10^6$
Closing	1.64	2.04	0	30	$3 \cdot 10^6$

The timing of each phase is determined by cross comparison of the three tests performed by Kay (06): PDA, Mass rate test, and laser sheet images. For example, for the Sac-spray phase, images and PDA show that the first sight of the fuel is observed at 0.68 ms ASOI. This delay is due to the electro-mechanical delay of the injector (also observed by Morris (03)). Figure 6-2 confirms this delay as it shows that no fuel is injected before this time. Therefore, this is the time at which the initial fuel is injected for the sac-spray phase. The closing time for the sac-spray phase is determined by velocity magnitude of the droplets recorded by PDA at a line very

close to the tip of the injector (2.5 mm downstream). The Sac-spray is characterised by droplets with strong axial velocity and relatively small radial velocity. Droplets with these characteristics are observed until 0.75 ms ASOI. Therefore, this time is selected as the closing time for the pre-spray model. The start of the opening phase corresponds to the end of the sac-spray phase. This phase is divided into 2 stages because some differences in spray angle were observed by high speed imaging. The end of this stage is determined by a combination of imaging and mass rate trace. After 0.9 ms ASOI, images show that the injector is fully open, which marks the start of the steady phase of the injection. During this phase, the injection duration can be selected as desired to simulate longer injections. However, for this injection, at 1.64 ms ASOI, a collapse in the hollow cone is observed by images and PDA, which describes the end of the steady phase and the beginning of the closing phase of the injection. The mass rate test, figure 6-2, shows that there is fuel being injected up to 2.04 ms ASOI. Some resonance is observed in this test, which is also confirmed by the corresponding images.

Once the timing of each phase has been defined, the exact amount of fuel injected on each phase can be determined by integrating the mass injected within each phase on figure 6-2. Consequently, the mass injected for each phase is:

Sac-Spray Phase:	0.23 mg
Opening Phase 1:	0.75 mg
Opening Phase 2:	0.98 mg
Steady Phase:	7.42 mg
Closing Phase:	1.77 mg
<hr/>	
<b>Total Mass Injected:</b>	<b>11.15 mg</b>

Using experimental data reported by Kay, most of the input parameters required for the CFD simulations can be defined. However, to ensure continuity, equation 6-21 (the continuity equation) is used to calculate either the mass flow rate, the injection velocity, or the cross sectional area of the nuzzle, using the other two experimental parameters as input:

$$\dot{m} = \rho \cdot V \cdot \left( \pi \left( \frac{d_n}{2} \right)^2 \right) \quad (6-21)$$

where  $d_n$  is the diameter of the nozzle,  $\dot{m}$  is the mass flow rate of the fuel exiting the nozzle, and  $V$  is the injection velocity and  $\rho$  the fuel density.

For the opening, steady, and closing phases of the injection, the initial velocity of the droplets was calculated using experimental measurements of mass flow rate and cross sectional area of the nozzle. However, Kay (06) reported that this method produced misleading representation of the sac-spray phase. Therefore, the cross sectional area was calculated using mass flow rate and velocity measurements close to the tip of the injector. Kay proposed using the 2.5 mm line to define a velocity profile for this phase of the spray. The velocity profile used to model the sac-spray is shown in figure 6-3.



**Figure 6-3:** Velocity profile input for sac-spray (Kay 2006)

In the spray model, the droplet diameter distribution used for each phase was determined from PDA data 10 mm downstream of the tip of the injector. At this distance, Kay (2006) reported a good compromise between being close enough to the injector that the droplet diameter distribution is realistic (and unaffected by secondary factors), while being far enough downstream that good quality data is used (considering PDA limitations).

Considering atmospheric conditions, the ambient temperature and pressure were introduced manually corresponding to the experimental conditions discussed in Chapter 4 (295 K and 0.1 MPa). The initial liquid temperature was also selected manually, and the fluid properties were extrapolated from pre-specified gasoline property files within the VECTIS code (Ricardo-Software 2004b).



### 6.5. Preliminary Results of a Simulated Impinging Spray

In this section, a comparison between spray impact experiments by TIR-LIF (discussed in chapter 4) and a corresponding CFD simulation is presented and discussed.

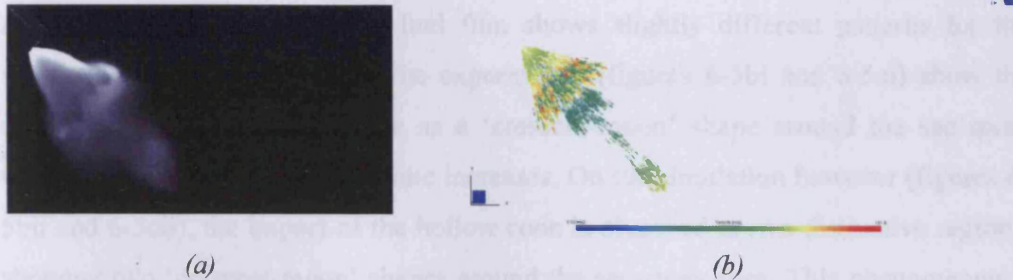


**Figure 6-4:** Qualitative comparison of the spray side view at 1.00 ms ASOI: (a) Planar laser image, (b) CFD simulation

Figure 6-4 shows a qualitative comparison of the spray side view, prior to impact, for a experimental laser sheet image (figure 6-4a) and the corresponding CFD simulation (Figure 6-4b). For early stages of the injection, the sac volume and hollow can be clearly identified in figure 6-4b. The figure shows a good qualitative agreement between the experiments and CFD simulation, illustrating a good representation of the transients in the spray development process. A good representation of the spray prior to impact is crucial for the ‘spray-impact’ simulation as it marks the initial condition for the fuel film development process.

Fuel film impingement results obtained by TIR-LIF for Case A ( $P_a = 0.1$  MPa, and  $T_a = 295$  K) are compared with a corresponding CFD simulation in figure 6-5. The column on the left (column *i*) shows two-dimensional distribution maps of fuel film thickness, obtained by TIR-LIF, for selected times After Start of Injection (ASOI). Comparative fuel film simulation results obtained with Ricardo VECTIS are presented on the right column for corresponding times ASOI. The simulation images are cropped to the same size of the experimental images (45 x 45 mm) to facilitate qualitative comparison of footprint sizes. As discussed in chapter 4, the first sight of fuel film deposits is observed at 1.25 ms ASOI. The delay incurred is attributed to the electro-mechanical opening delay of the injector, plus the travelling time of the spray from the nozzle to the impact surface. Figure 6-5ai shows clearly the impact of the sac volume at the centre of the image, and the impact of the bottom half of the hollow



cone to the left of the sac-spray film. However, on the corresponding CFD simulation (figure 6-5a<sub>ii</sub>) only the impact of the sac volume can be observed in the centre of the image. For this timebin, the film resulting from the sac-spray has a similar size, thickness, and location to that measured by TIR-LIF. However, the absence of any impact from the hollow cone indicates a slight delay of the timing selected for the 'opening phase' of the simulation. For the following timebins, 1.50 and 1.75 ms ASOI, the development of the fuel film shows slightly different patterns for the simulation and measurements. The experiments (figures 6-5b<sub>i</sub> and 6-5c<sub>i</sub>) show the development of the hollow cone as a 'crescent-moon' shape around the sac-spray film, which increases in size as time increases. On the simulation however (figures 6-5b<sub>ii</sub> and 6-5c<sub>ii</sub>), the impact of the hollow cone is observed at two distinctive regions, showing two 'crescent-moon' shapes around the sac-spray film. This phenomenon is attributed to the sharp transition between the two opening phases of the simulation, with different angles selected for the inner and outer cone angle. One possible solution would be to use more than two steps to describe accurately the development of the opening phase of the injection. This suggestion, along with other potential solutions, would require further simulation studies and analysis.

From 2.00 to 2.50 ms ASOI, there is a good transient comparison of experiments and simulation in terms of footprint size, shape, and thickness. During this period there is continuous deposition of fuel on the wall, which compares well as the film increases in size and thickness at a similar rate. Although the simulation suggests a slightly more dispersed fuel film, the comparative overall size of the footprint is similar to that measured, while the thickness is in the same order of magnitude. This suggests that the main (steady) and closing phases of injection are well represented within the simulation. Figure 6-5g<sub>i</sub> and 6-5g<sub>ii</sub> show the residual fuel deposits on the wall, which compares well the TIR-LIF experimental results and the VECTIS CFD simulation.

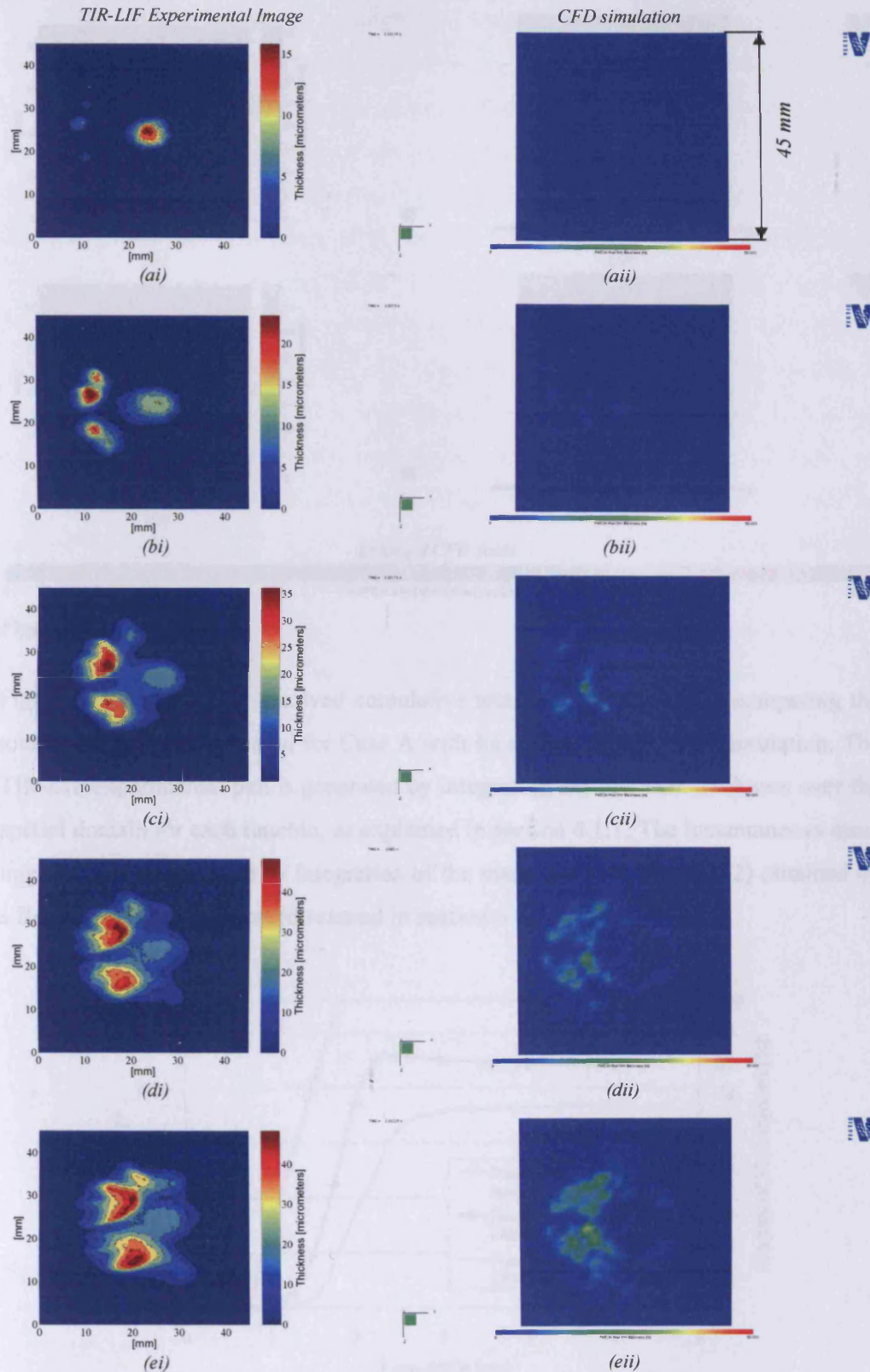


**Figure 6-5:** Comparison between (i) TIR-LIF measurements at atmospheric pressure and (ii) CFD predictions using Ricardo VECTIS, for different times after start of injection (ASOI): (a) 1.25 ms, (b) 1.50 ms, (c) 1.75 ms, (d) 2.00 ms, (e) 2.25 ms, (f) 2.50 ms, (g) 3.00ms

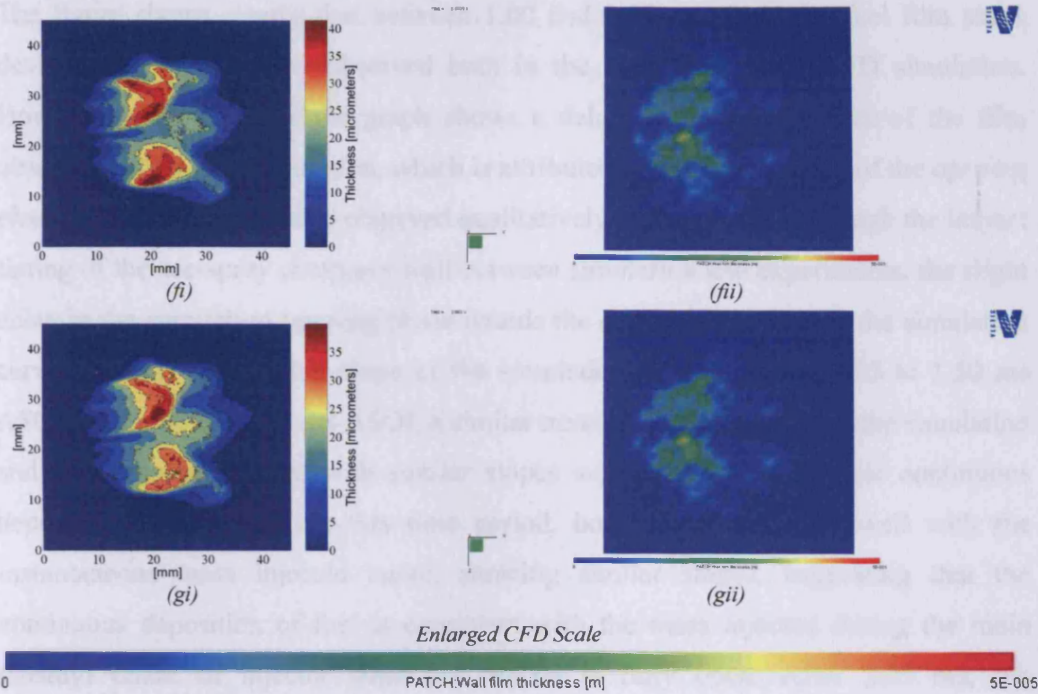


Figure 6-5: Continued...

Figure 6-6 shows a time resolved cumulative total mass deposits plot comparing the total mass deposits measured for Case A with its corresponding CFD simulation. The TIR-LIF experimental plot is generated by integrating the fuel film thickness over the spatial domain for each timebin, as explained in section 4.1.1. The instantaneous mass injected plot is generated by integration of the mass rate plot (figure 6-2) obtained by a Bosch type mass rate test (discussed in section 6.4.2).

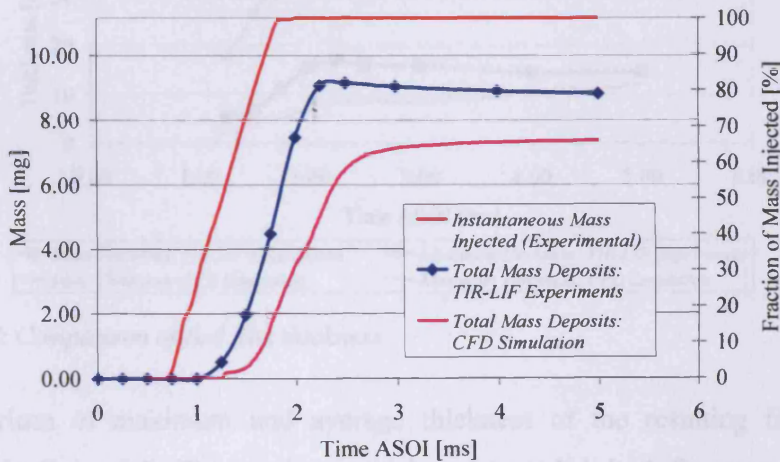


Figure 6-6: Comparison of cumulative mass deposits for experiments at atmospheric pressure and CFD simulation



The figure shows clearly that between 1.00 and 1.25 ms ASOI the fuel film starts developing. This trend is observed both in the experiments and CFD simulation. However, after 1.25 ms, the graph shows a delay in the development of the film observed in CFD the simulation, which is attributed to the timing delay of the opening phase of the simulation, also observed qualitatively in figure 6-5. Although the impact timing of the sac-spray compares well between simulation and experiments, the slight delay in the simulation opening phase retards the deposition of fuel in the simulation curve, thus the slow rising slope of the simulation curve between 1.25 to 1.50 ms ASOI. From 1.75 to 2.25 ms ASOI, a similar trend is observed both for the simulation and experimental curves, with similar slopes suggesting a comparable continuous deposition on the wall. In this time period, both curves compare well with the instantaneous mass injected curve, showing similar slopes, suggesting that the continuous deposition of fuel is consistent with the mass injected during the main (steady) phase of injector when the nuzzle is fully open. After 2.25 ms, the experimental cumulative mass deposits curve shows a sharp transition as the impingement process finishes and the resulting fuel film reaches its maximum mass deposits. This transition is also observed in the simulation curve, although more gradually.

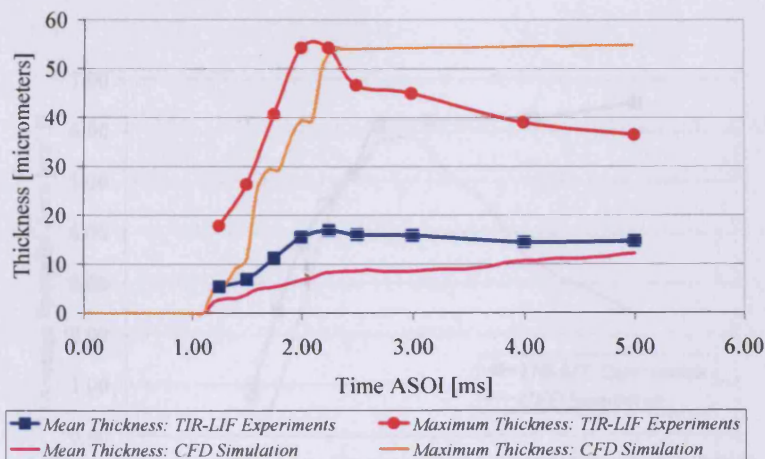
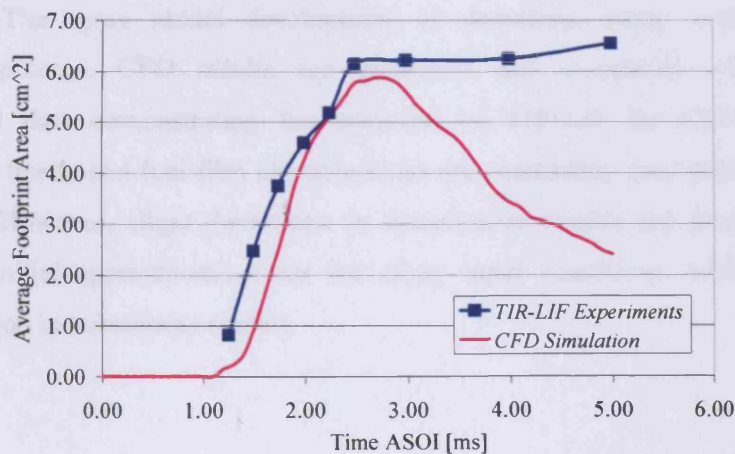


Figure 6-7: Comparison of fuel film thickness

A comparison of maximum and average thickness of the resulting fuel film is presented in figure 6-7. The maximum thickness recorded, both for experiments and simulation, is significantly higher than the average thickness due the uneven

distribution of the film observed in figure 6-5, with high localised deposits. The graph shows that the mean thickness increase gradually between 1.25 and 2.25 ms ASOI. During this time there is continuous deposition of fuel on the wall. The maximum thickness measured and predicted compare well in magnitude. However, for the simulation, the maximum thickness curve shows a ‘stepped shape’, instead of a smooth curve observed in TIR-LIF measurements, which is attributed to the representation of the input spray model as five distinctive phases. After 2.25 ms ASOI, the experimental measurements show that the fuel film is redistributed showing a significant decrease in the maximum thickness recorded, while the average thickness reaches a plateau of approximately 15 micrometers. For the simulation however, the average thickness continues to increase gradually until 5.00 ms ASOI, and the maximum thickness reaches a plateau of approx. 55 microns at 2.25 ms. The continuous gradual increase in average thickness in the CFD simulation is attributed to the evaporation of ‘thin’ dispersed films observed in figure 6-5. As discussed before, the CFD simulation predicts a slightly more dispersed fuel film. The model predicts that the isolated thin films would evaporate quicker while the thicker sections of the film take longer to evaporate, thus increasing the overall average thickness of the film. The average thickness of the residual fuel film is measured to be approx. 15 microns, which is similar to the 13 microns predicted by CFD.



**Figure 6-8:** Comparison fuel film footprint area for TIR-LIF experiments at atmospheric pressure and corresponding CFD simulation



A comparison between the footprint area of the fuel film recorded by TIR-LIF experiments at atmospheric pressure, and the corresponding CFD simulation is presented in figure 6-8. The figure shows a sharp increase in the overall footprint size between 1.25 and 2.50 ms observed both for the simulation and experimentally. Such increase in footprint size is expected within this timescale as it represents the deposition phase of the injection, also observed in figure 6-6. The trend of sharp increase in the overall size of the fuel film for early timebins can also be appreciated qualitatively when comparing calibrated TIR-LIF images in figure 6-5. At 2.50 ms ASOI, the maximum amount of deposits recorded experimentally is reached, after which the overall footprint size stabilises, showing only a slight increase in size for subsequent timebins as the film moves / spreads due to inertial effects. However, after 2.50 ms ASOI, the CFD simulation predicts a gradual decrease of the fuel film wetted area. Again, this decrease is attributed to the evaporation of 'thin' dispersed sections of the film.

### 6.6. Chapter Summary

This Chapter described the comparison of experimental fuel film measurements presented and discussed in chapter 4, with a corresponding simulated impinging G-DI pressure swirl spray. A commercially available CFD code specifically designed for the automotive sector was used to simulate the spray under atmospheric ambient conditions. The spray model development is described, along with the mesh generation process. CFD results are presented and compared with TIR-LIF experimental data demonstrating the potential of TIR-LIF for CFD validation. Quantitative trends and fuel film characteristics are reasonably well predicted by the simulation. However, slight deviations in quantitative results are presumed to be caused by initial approximations for the spray input conditions, which could be improved upon in subsequent studies.

# **Chapter 7:**

## **Conclusions and Future Work**

### 7.1. Conclusions

The main conclusions of the thesis are now summarised:

- Concerning development of the TIR-LIF technique for characterisation of fuel films resulting from spray impact:
  - Calibrated benchmark results presented in chapter 4 show that the TIR-LIF technique, developed in this thesis, proved successful in quantifying the transient fuel film formed as a result of spray impingement on a flat surface. The technique describes, qualitatively and quantitatively, the successful development of the fuel film particularly quantifying the transient effect of the fuel film thickness and shape.
  - Errors from illuminating airborne droplets observed by Kay (2006) are corrected through controlling the propagation of the laser beam by total internal reflection (TIR-LIF). Further corrections are made to account for variations in laser beam profile and shot-to-shot intensity.
  - Significant differences were found for the fuel film produced at 2 different sets of ambient pressures, due to differences in the pre-impingement spray dynamics such as the known collapse of the spray under increased ambient pressure. For elevated ambient pressures (0.4 MPa) a thicker and smaller film which travels further from the tip of the injector is identified. Cumulative mass deposits reveal higher average fuel thickness and higher total deposits for elevated ambient pressure due to variation in the momentum exchange process. As expected, extremely high quantities of residual fuel-film are measured under the atmospheric temperature conditions of this experimental programme.
  - The TIR-LIF technique demonstrated considerable potential for impingement analysis and CFD validation for a wide range of applications. The dataset produced for two experimental conditions is robust and self-consistent, providing an excellent benchmark for spray impact model appraisal.
  
- Concerning development of the LIEF technique for characterisation of vapour fractions of thermofluid sprays:

- Experimental results recorded at three different ambient conditions showed that the technique was successful in describing liquid and vapour fractions of the spray.
  - Unambiguous separation of liquid signals was achieved by utilisation of a suitable tracer pair and careful selection of optical filters, which provides valuable information about the location of liquid droplets in the vapour images. The technique for correcting for the contribution of liquid fluorescence in the vapour images proved successful. Thus, quantitative images of vapour concentration were obtained at ambient conditions relevant to in-cylinder conditions.
  - Experiments at elevated ambient pressure (Case 2) demonstrated considerable influence of elevated ambient density on the spray in terms of spray penetration and fuel distribution, due to the effects of enhanced drag and retarded evaporation. As the spray collapses under elevated pressure, both the liquid and vapour phases show a more compact structure, showing a significant reduction in axial and radial penetration.
  - A significant delay in the evaporation process is observed in experiments at lower ambient temperature (Case 3). Experimental results indicate considerable influence of ambient temperature on the development of the spray in terms of spray penetration and fuel distribution. In general, the spray structure observed for case 3, with lower ambient temperature, shows less axial penetration but more radial penetration than case 1.
  - The dataset produced to support this technique shows consistent trends and offers an excellent platform for analysis of spray evaporation.
- 
- A CFD simulation was performed on a commercially available CFD code to explore the potential of TIR-LIF for validation of spray impact models. The spray model was produced from experimental measurements of the free spray, and was later used as initial input data for the simulation. Preliminary CFD results are presented and compared with TIR-LIF experimental data. Quantitative trends and fuel film characteristics are reasonably well predicted by the simulation. However, deviations in quantitative results are presumed to be caused by incorrect determination of the spray input conditions, although there is

undoubtedly scope for improvements in spray impingement submodeling now that quantitative validation data is available.

### **7.2. Recommendations and Future Work**

- As discussed in chapter 4, further work is required on TIR-LIF to explain a few unusual trends observed on the elevated pressure case, particularly the elevated peak deposits observed around 2.25 ms ASOI, for which a couple of hypothesis have been suggested. To facilitate the understanding of this trend, it is proposed to use a less complicated experimental setup, studying a less dense spray or a single drop impact, to analyze the fundamentals of the impact process under elevated ambient pressure.
- It is recommended to perform impingement tests at elevated ambient temperatures to demonstrate the potential of TIR-LIF for characterisation of fuel films under more realistic operational conditions.
- Given the progress and confidence on results produced by TIR-LIF, and the expertise in post-impingement spray diagnostics within the research group, the ultimate aim of this project should be to evaluate the performance of all spray impact models available in the literature and, if necessary, to propose a new / improved impact model from empirical correlations deduced by careful experimentation.
- As discussed in chapter 5, future work regarding LIEF should concentrate in studying the interference of liquid and vapour signals at different pressures and temperatures. It is proposed to use a less complicated experimental setup, studying a less dense spray or single drop evaporation within the chamber, to analyze the fundamentals of the evaporation process and thus improve the methodology for interference correction.
- The possibility of substituting benzene as one of the tracers must be considered as a priority due to its notorious hazardous association.
- In order to improve the accuracy of both techniques, utilisation of smaller pixel sizes afforded by future hardware improvements should increase the spatial resolution of the interrogation zone, and thus, reduce errors associated with the image resolution.



---

## List of Publications by the Author:

Alonso M., Kay P.J., Bowen P.J., Gilchrist R., and Sapsford S. (2009a). A Laser Induced Fluorescence Technique for Quantifying Transient Liquid Fuel Films Utilising Total Internal Reflection (TIR-LIF). Submitted for publication on *Experiments in Fluids* on 22-09-2008. Manuscript number EXIF-D-08-00166.

Alonso M., Kay P.J., Bowen P.J., Gilchrist R., and Sapsford S. (2009b): Quantification of Transient Fuel Films for a Gasoline Direct Injection Spray under Elevated Ambient Pressure Utilising Total Internal Reflection Laser Induced Fluorescence (TIR-LIF). Submitted for publication on *Experiments in Fluids* on 07-11-2008. Manuscript number EXIF-D-08-00246.

Alonso M., Kay P.J., Crayford A.P., Bowen P.J., Gilchrist R., and Sapsford S. (2009c). Characterisation of the Vapour Fractions of a Gasoline Direct-Injection Spray using Laser Induced Exciplex Fluorescence. Submitted for publication on *Atomization and Sprays* on 08-10-2008. Manuscript number AAS-350.

Alonso M., Kay P.J., Bowen P.J., Gilchrist R., and Sapsford S. (2009d). TIR-LIF: a Validation Tool for Spray Impact Models. *11th International Annual Conference on Liquid Atomization and Spray Systems (ICLASS)*, July 2009, Vail-Colorado, USA

Alonso M., Kay P.J., Bowen P.J., Gilchrist R., and Sapsford S. (2008a). Quantification of 3D Transient Fuel Films for G-DI Sprays Under Elevated Ambient Conditions. *22nd European Conference on Liquid Atomization and Spray Systems*, 8-10 September 2008, Como Lake, Italy

Alonso M., Kay P.J., Crayford A.P., Bowen P.J., Gilchrist R., Sapsford S. (2008b). On the Quantitative Analysis of Vapour Fuel Fractions of Spark Ignition DI Sprays by use of LIEF. *22nd European Conference on Liquid Atomization and Spray Systems*, 8-10 September 2008, Como Lake, Italy

Alonso M., Kay P.J., Bowen P.J., Gilchrist R., Sapsford S., Owen N. (2007): Development of a 2-D Quantitative LIF Technique for Measurement of Transient Liquid Fuel Films Utilising Total Internal Reflection. *21st European Conference on Liquid Atomization and Spray Systems*, 10-12 September 2007, Mugla, Turkey

---

## References:

Bae C., Choi D.S. and Kim D.J. (2004). Characterisation of an Evaporating Direct-Injected Gasoline Spray Using Laser-Induced Exciplex Fluorescence and Particle Image Velocimetry, *Proc. Inst Mech. Engrs., J. Automobile Engineering*, Vol 218 Part D

Bai C. X. and Gosman A.D (1995): Development of Methodology for Spray Impingement Simulation, *SAE paper 950283*

Bai C. X. and Gosman A.D (1996): Mathematical Modelling of Wall Films Formed by Impinging Sprays, *SAE paper 960626*

Bai C. X., Rusche, H., and Gosman A.D (2002): Modelling of Gasoline Spray Impingement, *Atomization and Sprays*, 12:1-27

Berrocal E., (2006) Multiple scattering of light in optical diagnostics of dense sprays and other complex turbid media, PhD Thesis, Cranfield University.

Bruneaux G. (2001) Liquid and vapor spray structure in high-pressure common rail injection, *Atomization and Sprays*, Vol 11, n 5, pp p 533-556.

DECC. *Statement - Carbon Capture & Storage - 23 Apr 09*. Available at: <[http://www.decc.gov.uk/en/content/cms/news/090423\\_ccs\\_sta/090423\\_ccs\\_sta.aspx](http://www.decc.gov.uk/en/content/cms/news/090423_ccs_sta/090423_ccs_sta.aspx)>.

[Accessed on 26th April 2009]

Chale H.G., Georjon T., Brun M. (1997). Flow characteristics of impinging transient diesel sprays using Phase Doppler Anemometry. *ASME Fluids Engineering Division Summer Meeting FEDSM'97*. June 22-26.

Cho H., Min K. (2003). Measurement of liquid fuel film distribution on the cylinder liner of a spark ignition engine using the laser-induced fluorescence technique. *Measurement Science and Technology*. 14:975-982.

## References

---

Coleman R. (2002). Developing characterisation techniques for gasoline direct injection (G-DI) engines. Cardiff School of Engineering. Cardiff.

Comer M., (1999): Transient G-DI fuel spray characterization, PhD thesis, University of Wales, Cardiff.

Cossali G.E., and Coghe A., and Marengo M. (1997). The impact of a single drop on a wetted surface, *Experiments in Fluids*, 22:463–472.

Cossali G.E., Marengo M., and Santini M. (2005) Single-drop empirical models for spray impact on solid walls: a review, *Atomisation and Sprays*, 15:699-736

Cossali G.E., Marengo M., Santini M. (2007) Thermally induced secondary drop atomisation by single drop impact onto heated surfaces. *International Journal of Heat and Fluid Flow*. 29: 167-177

Crayford, A.P. (2004). Suppression of methane-air explosions with water in the form of 'fine' mists, PhD Thesis, Cardiff University.

De Sarcey G., (2004) Laser Induced Fluorescence for the measurement of air-to-fuel ratios in gasoline direct injection engines, PhD thesis, Brighton University.

De Sarcey G., Awcock G., and Heikal M. (2005): Use of LIF image acquisition and analysis in developing a calibrated technique for in-cylinder investigation of the spatial distribution of air-to-fuel mixing in direct injection gasoline engines. *Computers in Industry*. 56: 1005 – 1015.

Dodge L.G., Biaglow J.A. (1985). Effect of Elevated Temperature and Pressure on Sprays from Simplex Swirl Atomisers. *American Society of Mechanical Engineers*. 1-7.

Einecke S., Schulz C., Sick V. (2000): Measurement of temperature, fuel concentration and equivalence ratio fields using tracer LIF in IC engine combustion. *Applied Physics B: Lasers and Optics*. 71 (5): 717-723

## References

---

Eichlseder H., Wimmer A. (2003) Potential of IC-engines as minimum emission propulsion system. *Atmospheric Environment*. 37: 5227 – 5236.

EU-ACEA. COMMISSION RECOMMENDATION: on the reduction of CO<sub>2</sub> emissions from passenger cars. *Official Journal of the European Communities*. Available at: < <http://ec.europa.eu/environment/air/transport/co2/99125/en.pdf> >. [Accessed on 12<sup>th</sup> January 2009]

Fansler T.D., and Drake M.C., (2006) “*Designer Diagnostics*” for developing direct-injection gasoline engines. *Journal of Physics: Conference Series* 45: 1–17

Fardad, D., Ladommatos, N. (1999). Evaporation of Hydrocarbon Compounds, Including Gasoline and Diesel fuel, on Heated Metal Surfaces, *Proceedings of the Institute of Mechanical Engineers*, 213(D): 625-645

Felton P.G., Bracco F.V., and Bardsley M.E.A., (1993). On the quantitative application of Exciplex Fluorescence to Engine Research, *SAE paper*, 930870.

Fujikawa T., Hattori Y., Koike M., Akihama K., Kobayashi T., Matsushita S. (1999). Quantitative 2D Fuel Distribution Measurements in a Direct-Injection Gasoline Engine Using a Laser-Induced Fluorescence Technique. *JSME International Journal*. 42 (4):760-767.

Fujikawa T., Fukui K., Hattori Y., Akihama K. (2006): 2-D Temperature Measurements of Unburned Gas Mixture in an Engine by Two-line Excitation LIF Technique. *SAE paper* 2006-01-3336

Fujimoto H., Choi D., Shima Y., and Senda J., (2002). Two-dimensional imaging of fuel-vapour concentration by use of LIEF technique during mixture formation process in a DI diesel engine. *Meas. Sci. Technol.* 13: 391-400

Gao J.J.D., Huang Z., and Wang X., (2005) Experimental and Numerical Study of High-Pressure-Swirl Injector Sprays in a Direct Injection Gasoline Engine.

## References

---

*Proceedings of the Institute of Mechanical Engineering Part A: Journal of Power and Energy*. 219: 617-629

Gervais D., and Gastaldi P. (2002). A comparison of two quantitative laser induced fluorescence technique applied to a new air guided direct injection SI combustion chamber, *SAE paper*, 2002-01-0750.

Ghandhi J.B., Felton P.G., Gajdeczko B.F. and Bracco F.V. (1994). Investigation of the Fuel Distribution in a Two-Stroke Engine with an air-assisted Injector, *SAE paper* 940304

Greenhalgh D.A., Le Gal P., Farrugia D.A. (1999). Laser Sheet Dropsizing of Dense Sprays. *Optics & Laser Technology*. 31: 75-83.

Gruenberger T.M. (2000). Studies of Soot and Carbon Black Formation by Incomplete Combustion and Thermal Decomposition of Natural Gas, PhD Thesis, Cardiff University.

Hardalupas Y., Domann R. (2001). Spatial distribution of fluorescence intensity within large droplets and its dependency on dye concentration. *Applied Optics*. Vol 40, No. 21, pp 3586 – 3597.

Hentschel N., Grote A., and Langer O. (1997). Measurement of wall film thickness in the intake manifold a standard production SI engine by a spectroscopic technique. *SAE Paper* 972832.

Jiang Y.J., Umemura A., and Law C.K., (1992). An experimental investigation on the collision behaviour of hydrocarbon droplets. *Journal of Fluid Mechanics*. 234: 171-190

Kalantari D., Tropea C. (2007). Spray impact onto flat and rigid walls: Empirical characterisation and modelling. *International Journal of multiphase Flow*. 33:525-544.



## References

---

Kay P.J., Bowen P.J., Gold M., Sapsford S. (2005). Impingement studies of G-DI Sprays at Atmospheric and Elevated Ambient Densities. *Annual conference on Liquid Atomisation and Spray Systems, North and South America*, Irvine, California.

Kay P.J., Bowen P.J., Gold M., Sapsford S. (2006). Development of a 2D quantitative LIF technique towards Measurement of Transient Liquid Fuel Films. *10th International Congress on Liquid Atomisation and Spray Systems*. Kyoto, Japan.

Kay P.J. (2006) Characterising Thermofluid Spray Dynamics for Energy-Efficient Automotive Engines, PhD Thesis, Cardiff University

Khavkin Y., (2004) The Theory and Practice of Swirl Atomizers, *Taylor & Francis Press*, 203-280.

Kim T., and Gandhi J.B. (2003). Characterization of evaporating diesel sprays using exciplex laser-induced fluorescence measurements, *Atomization and Sprays*, 13, part 5/6, pp 535-560

Kornmesser C., Muller T., Beushausen V., Hentschel W., and Andresen P. (2001). Applicability of different exciplex tracers and model fuels for investigation of mixture formation in direct injection gasoline engines. *The Fifth Symposium on Diagnostics and Modeling of Combustion in Internal Combustion Engines*. COMODIA, July 1-4, Nagoya-Japan.

Kull E., Wiltafsky G., Stolz W., Min K.D., Holder E. (1999). Two-Dimensional visualization of liquid Layers on transparent walls. *Optics Letters*. 22:645-647.

Landry E.S., Mikkilineni S., Paharia M., McGauhey A.J.H. (2007). Droplet evaporation: A molecular dynamics investigation. *Journal of Applied Physics*. 102: 124301.

Le Coz J.F., Baritaud T. (1994). Application of Laser Induced Fluorescence for Measuring the Thickness of Evaporating Gasoline Liquid Films. *Proceeding of Applications of Laser Techniques to Fluid Mechanics*. Lisbon, 113-131

## References

---

Lefebvre, A.H. (1989). *Atomization and Sprays*. Hemisphere Publishing Corporation.

Leipertz A., Froba A.P., Rabenstein F., and Munch U. (1998). Mixture of Triethylamine (TEA) and Benzene as a New Seeding Material for the Quantitative Two-Dimensional Laser-Induced Exciplex Fluorescence Imaging of Vapor and Liquid Fuel Inside SI Engines, *Combustion and Flame*, 112, pp 199-209

Magnusson A., Joelsson T., Turcan F., and Andersson S. (2008). Characterization of Diesel Model Fuel Sprays Impinging on a Temperature Controlled Wall Using Rapid Thermocouples and PDPA. *22nd European Conference on Liquid Atomization and Spray Systems*, 8-10 September 2008, Como Lake, Italy

Meingast U., and Renz U. (2001): Fuel Film Thickness Measurements Under Diesel Engine Conditions, *ILASS Europe 2001*, Zurich, Switzerland.

Melton L., (1983). Spectrally Separated Fluorescence emissions for diesel fuel droplets and vapour, *Applied Optics*, 22: 2224-2226.

Melton L. A., (1993). Exciplex-Based Vapor/Liquid Visualization Systems Appropriate for Automotive Gasolines. *Applied Spectroscopy*. Vol 47, No. 6, pp 782-786.

Melton L.A., and Verdick J.F., (1984). Vapor/Liquid Visualization in Fuel Sprays, *Twentieth Symposium on Combustion*, The Combustion Institute, pp. 1283-1290

Morris D., (2003). Temporal Characterisation of Various G-DI Fuel Injector Concepts, PhD thesis, Cardiff University.

Mundo C., Sommerfeld M., and Tropea C. (1995) Droplet-Wall collisions: Experimental Studies of the Deformation and Break-up Processes. *International Journal of Multiphase Flow*, 21(2): 151-173.

Mundo C., Sommerfeld M., and Tropea C. (1998) On the Modeling of Liquid Sprays Impinging on Surfaces. *Atomization and Sprays*, 8: 625-652.

## References

---

- Panao M.R.O., Moreira A.L.N. (2007). Interpreting the influence of fuel spray impact on mixture preparation for HCCI combustion with port-fuel injection. *Proceedings of the Combustion Institute*, 31 (2007): 2205-2213
- Pilch M., Erdman C.A. (1987). Use of breakup time data and velocity history data to predict the maximum size of stable fragments for acceleration-induced breakup of a liquid drop. *International Journal of Multiphase Flow*. 13: 741–757.
- Putnam, A. (1961). Integrable Form of Droplet Drag Coefficient. *Journal of the American Rocket Society*, 31:1467-1468
- Ranz W.E., and Marshall W.R. (1952). Evaporation from Drops. *Chemical Engineering Progress*. Vol 48. Part 1: 141 – 146, Part 2: 173 – 180.
- Reitz, R.D., Diwakar, R. (1986) Effect of Drop Brea-up on Fuel Spray. *SAE Publications*, 860469.
- Ricardo-Software (2004a). VECTIS Computational Fluid Dynamics Release 3.8 Theory Manual.
- Ricardo-Software (2004b). VECTIS User Manual, Release 3.8
- Richter M., Axelsson B., and Alden, M. (1998): Engine Diagnostics Using Laser Induced Fluorescence Signals Collected Through an Endoscope Detection System. *SAE paper 982465*
- Rioboo, R., Tropea, C., and Marengo, M. (2001). Outcomes from a Drop Impact on Solid Surfaces, *Atomisation and Sprays*, 19:223-228
- SAE. *Bosch's illustration of spark-ignition-engine mode with direct injection*. Available at: < [http://www.sae.org/automag/techbriefs\\_01-00/08.htm](http://www.sae.org/automag/techbriefs_01-00/08.htm) >. [Accessed on 15<sup>th</sup> January 2009]

## References

---

- Schäfer A., Heywood J.B., Weiss M.A. (2006) Future fuel cell and internal combustion engine automobile technologies: A 25-year life cycle and fleet impact assessment. *Energy*. 31: 2064 – 2087.
- Schulz C., Sick V. (2005). Tracer-LIF diagnostics: quantitative measurement of fuel concentration, temperature and fuel/air ratio in practical combustion systems. *Progress in Energy and Combustion Science*. 31:75-121.
- Schulz C., Koban W., Koch J.D., Sick V., Wermuth N., Hanson R.K. (2005). Predicting LIF signal strength for toluene and 3-pentanone under engine-related temperature and pressure conditions. *Proceedings of the Combustion Institute*. 30:1545–1553.
- Seitzman J.M., Hanson R.K. (1993): Instrumentation for flows with combustion. *A.M.K.P. Taylor. Academic Press*, 405-466.
- Senda J., Tanabe Y., and Fujimoto H., (1992). Visualization of evaporative diesel spray impinging upon wall surface by exciplex fluorescence method, *SAE paper* 920578, 1-10.
- Sick V., Zhang R., Stanislav V.B. (2005). Stability of iso-octane with 3-pentanone and biacetyl as fluorescence tracers in combustion experiments. *Experiments in Fluids*. 40:161-173.
- Sivakumar, S., Tropea, C., (2002). Splashing impact of a spray onto a liquid film. *Phys. Fluids Lett.*, 14, L85–L88.
- Stanglmaier R.H., Li J., Matthews R.D. (1999) The effect of in-cylinder wall wetting location on the HC emissions from SI engines. *SAE paper*. 1999-01-0502.
- Stanton, D.V., Rutland, C.J., (1998). Multi-dimensional modeling of thin liquid films and spray-wall interactions resulting from impinging sprays. *Int. J. Heat Mass. Transfer*, 41:3037–3054.

## References

---

Stern, N., (2008) Key elements of a global deal on climate change. London School of Economics and Political Science, London, UK.

Taylor A.M.K.P. (2008). Science Review of Internal Combustion Engines. *Energy Policy*. 36: 4657 – 4667

Tropea C., Roisman I.V., (2006) Droplet Breakup, Coalescence, and Wall Impact. *Multiphase Flow Handbook*. CRC Press, Taylor and Francis. 12: 35-51.

UNFCCC. *Key GHG data - greenhouse gas emissions data for 1990 - 2003*. Available at: < [http://unfccc.int/resource/docs/publications/key\\_ghg.pdf](http://unfccc.int/resource/docs/publications/key_ghg.pdf) >. [Accessed on 12<sup>th</sup> January 2009]

Wieske P., Wissel S., Grunefeld G. and Pischinger S. (2006). Improvement of LIEF by wavelength-resolved acquisition of multiple images using a single CCD detector-Simultaneous 2D measurement of air / fuel ratio, temperature distribution of the liquid phase and quantitative distribution of the liquid phase with the Multi-2D technique, *Applied Physics B*, 83, pp 323-329.

Weiss M.A., Heywood J.B., Drake E.M., Schafer A., AuYeung F.F. (2000) *On the road in 2020: A life-cycle analysis of new automobile technologies*. Energy Laboratory Report MIT EL 00-003, Energy Laboratory, Massachusetts Institute of Technology, Cambridge, MA, 02139-4307.

Yarin, A.L., Weiss, D.A. (1995). Impact of drops on solid surfaces: self-similar capillary waves, and splashing as a new type of kinematic discontinuity, *Journal of Fluid Mechanics*, 283:141-173.

Yule A.J, Filipovic I. (1992): On the breakup times and length of diesel sprays. *International Journal of Heat and Fluid Flow*. 13(2): 197-206

Zhao F., Lai M.C., Harrington D.L. (1999) Automotive Spark-Ignited Direct-Injection Gasoline Engines. *Progress in Energy and Combustion Science*, 25:437-562.



## References

---

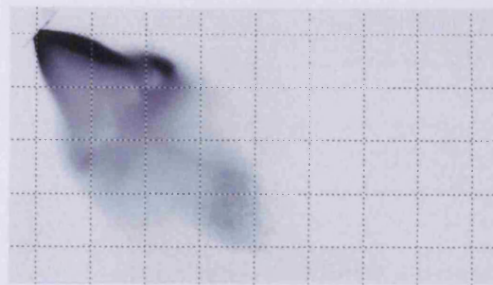
Zhao H., and Ladommatos N., (1998). Optical diagnostics for In-Cylinder mixture formation measurements in IC engines, *Progress in Energy and Combustion Science*, 24: 297-336.

## Appendix A: Transient Fuel Film Measurements for Case A

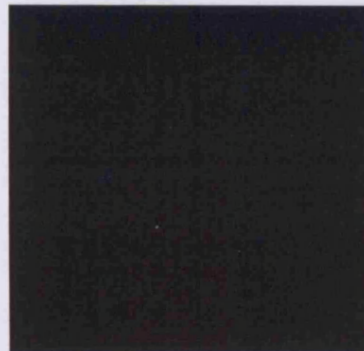
This Appendix shows a full set of fuel film TIR-LIF measurements for Case A. The experimental conditions for Case A are highlighted in the following table:

Table A-A: Summary of experimental conditions for Case A

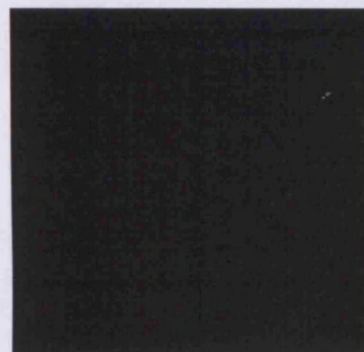
	<i>Case</i>	<i>Ambient Pressure [MPa]</i>	<i>Ambient Temperature [K]</i>
<i>Fuel Film Studies (TIR-LIF)</i>	<i>A</i>	<i>0.1</i>	<i>293</i>
	<i>B</i>	<i>0.4</i>	<i>293</i>
<i>Vapour Fraction Studies (LIEF)</i>	<i>1</i>	<i>0.14</i>	<i>423</i>
	<i>2</i>	<i>0.58</i>	<i>423</i>
	<i>3</i>	<i>0.10</i>	<i>373</i>



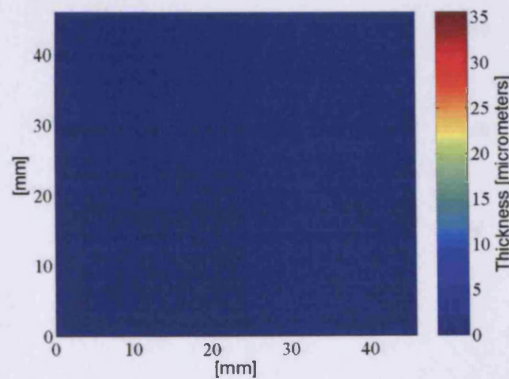
*Side View Image of  
the Spray  
(size 45 x 25 mm)*



*Average Fuel Film  
Image  
(size 45 x 45 mm)*



*COV Image  
(size 45 x 45 mm)*

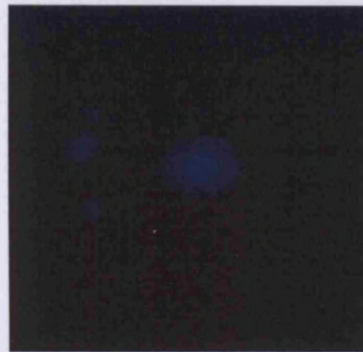


*Calibrated fuel  
film image*

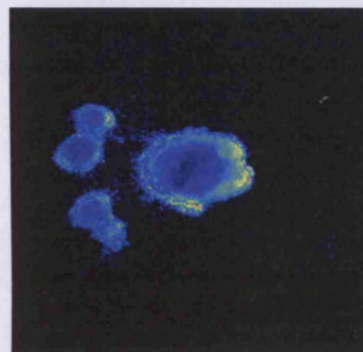
**Figure A1:** Fuel film thickness measurements for Case A at 1.00 ms after start of injection



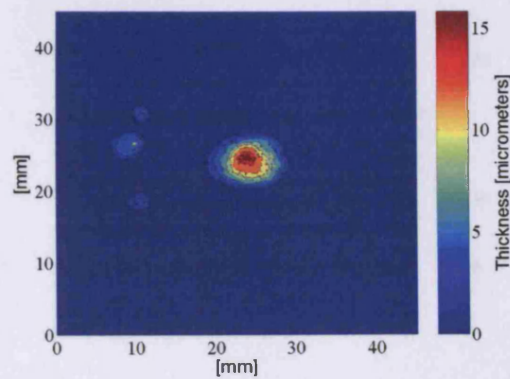
*Side View Image of the Spray  
(size 45 x 25 mm)*



*Average Fuel Film Image  
(size 45 x 45 mm)*



*COV Image  
(size 45 x 45 mm)*

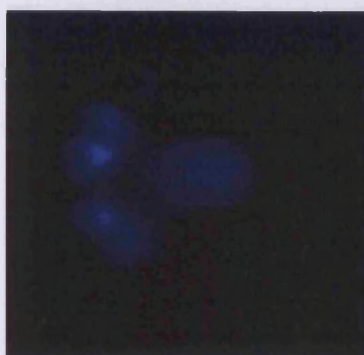


*Calibrated fuel film image*

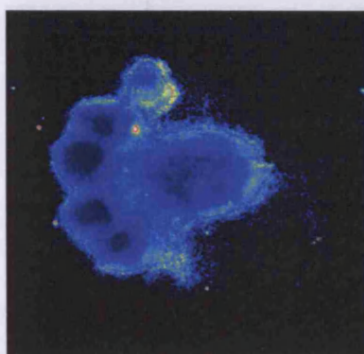
**Figure A2:** Fuel film thickness measurements for Case A at 1.25 ms after start of injection



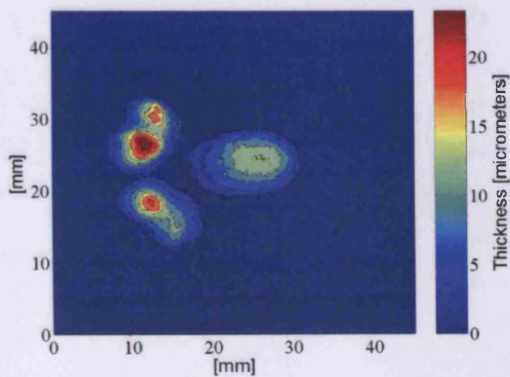
*Side View Image of the Spray  
(size 45 x 25 mm)*



*Average Fuel Film Image  
(size 45 x 45 mm)*



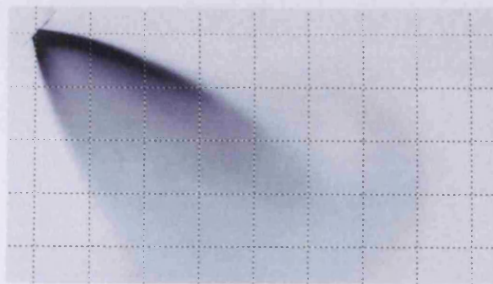
*COV Image  
(size 45 x 45 mm)*



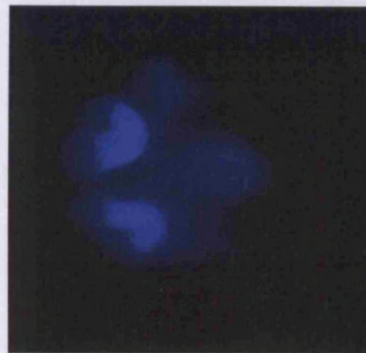
*Calibrated fuel film image*

**Figure A3:** Fuel film thickness measurements for Case A at 1.50 ms after start of injection

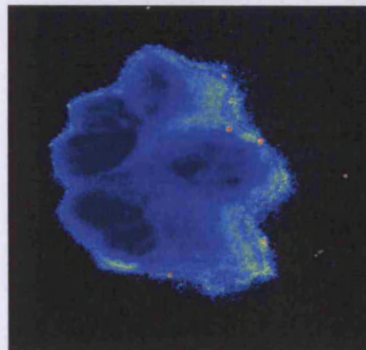




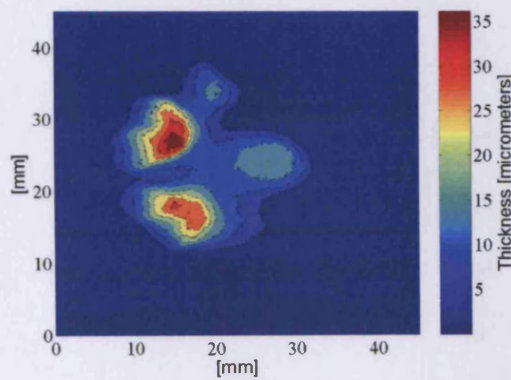
*Side View Image of  
the Spray  
(size 45 x 25 mm)*



*Average Fuel Film  
Image  
(size 45 x 45 mm)*



*COV Image  
(size 45 x 45 mm)*



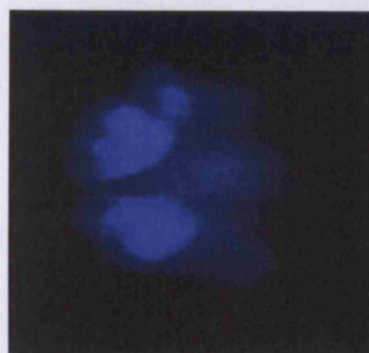
*Calibrated fuel  
film image*

**Figure A4:** Fuel film thickness measurements for Case A at 1.75 ms after start of injection

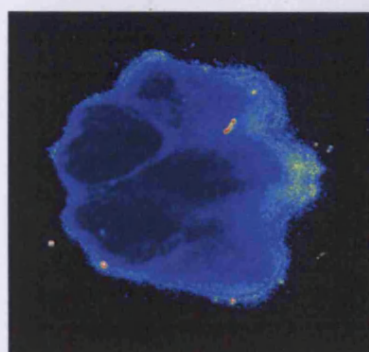




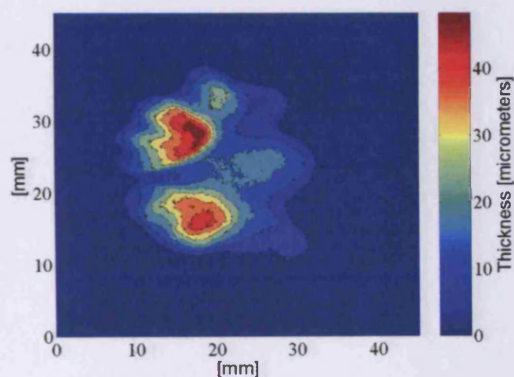
*Side View Image of  
the Spray  
(size 45 x 25 mm)*



*Average Fuel Film  
Image  
(size 45 x 45 mm)*

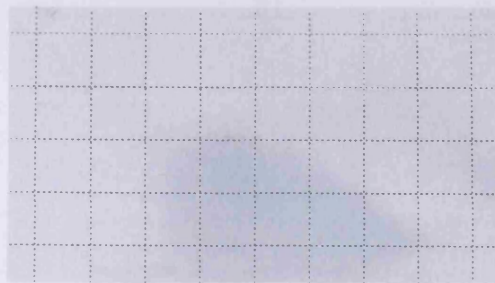


*COV Image  
(size 45 x 45 mm)*

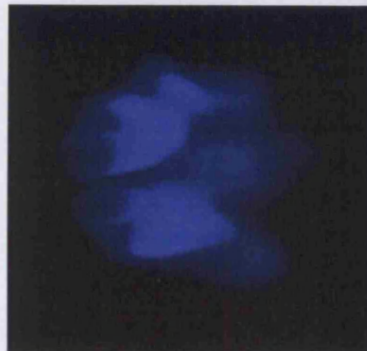


*Calibrated fuel  
film image*

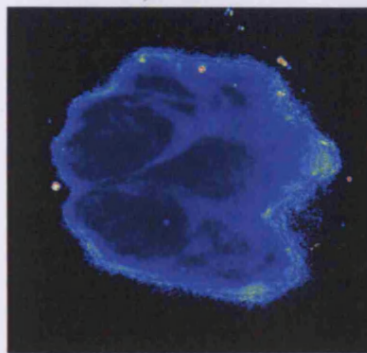
**Figure A5:** Fuel film thickness measurements for Case A at 2.00 ms after start of injection



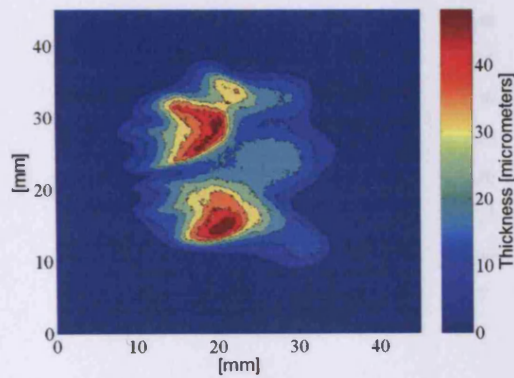
*Side View Image of the Spray*  
(size 45 x 25 mm)



*Average Fuel Film Image*  
(size 45 x 45 mm)



*COV Image*  
(size 45 x 45 mm)

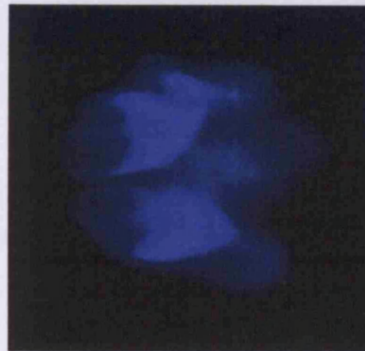


*Calibrated fuel film image*

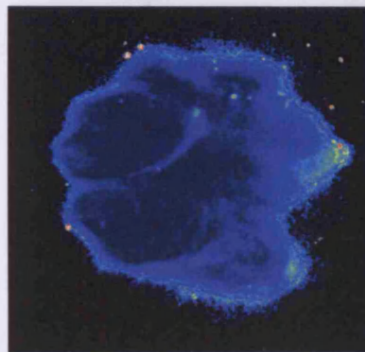
**Figure A6:** Fuel film thickness measurements for Case A at 2.25 ms after start of injection



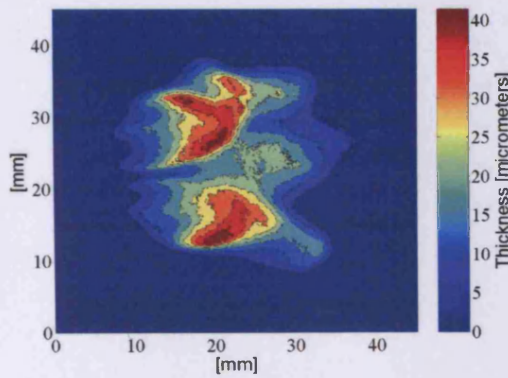
*Side View Image of the Spray  
(size 45 x 25 mm)*



*Average Fuel Film Image  
(size 45 x 45 mm)*

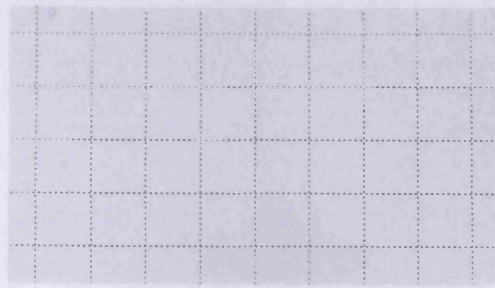


*COV Image  
(size 45 x 45 mm)*

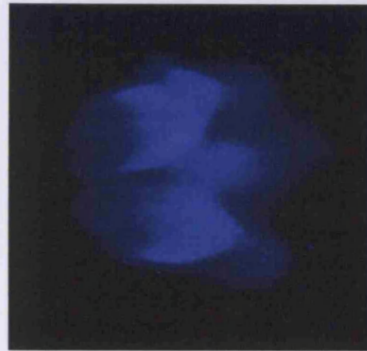


*Calibrated fuel film image*

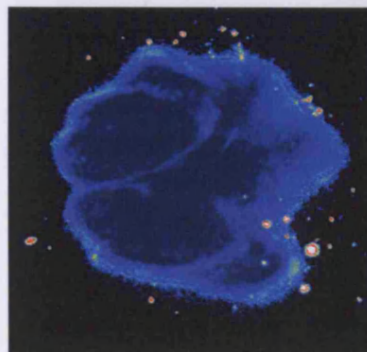
**Figure A7: Fuel film thickness measurements for Case A at 2.50 ms after start of injection**



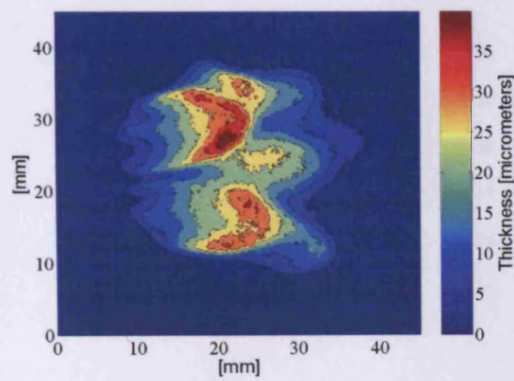
*Side View Image of the Spray  
(size 45 x 25 mm)*



*Average Fuel Film Image  
(size 45 x 45 mm)*



*COV Image  
(size 45 x 45 mm)*



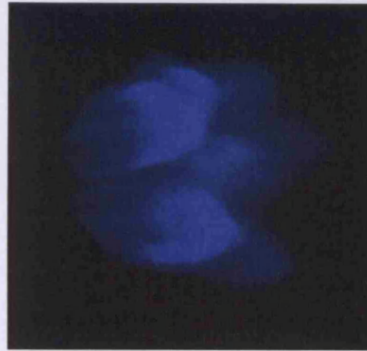
*Calibrated fuel film image*

**Figure A8:** Fuel film thickness measurements for Case A at 3.00 ms after start of injection

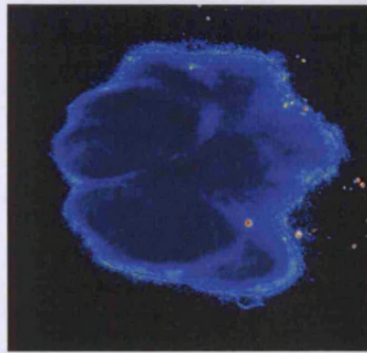




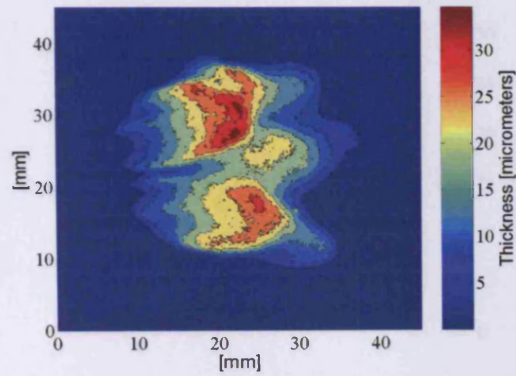
*Side View Image of the Spray  
(size 45 x 25 mm)*



*Average Fuel Film Image  
(size 45 x 45 mm)*

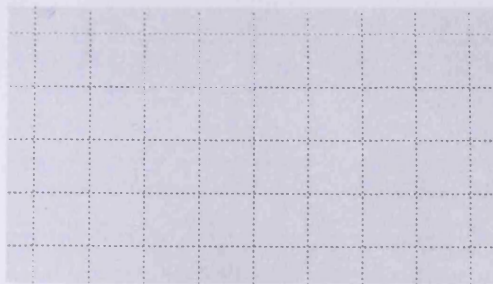


*COV Image  
(size 45 x 45 mm)*

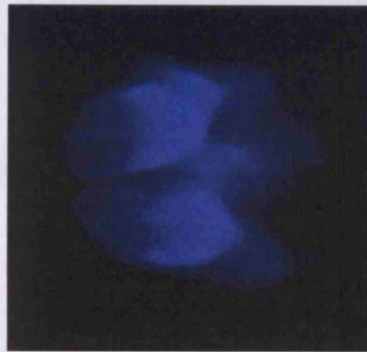


*Calibrated fuel film image*

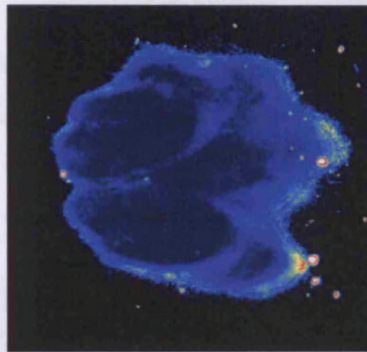
**Figure A9:** Fuel film thickness measurements for Case A at 4.00 ms after start of injection



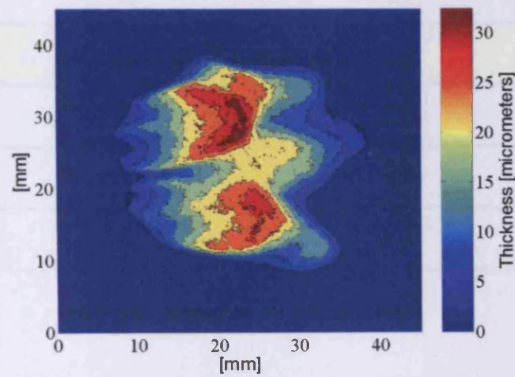
Side View Image of the Spray  
(size 45 x 25 mm)



Average Fuel Film Image  
(size 45 x 45 mm)



COV Image  
(size 45 x 45 mm)



Calibrated fuel film image

Figure A10: Fuel film thickness measurements for Case A at 5.00 ms after start of injection

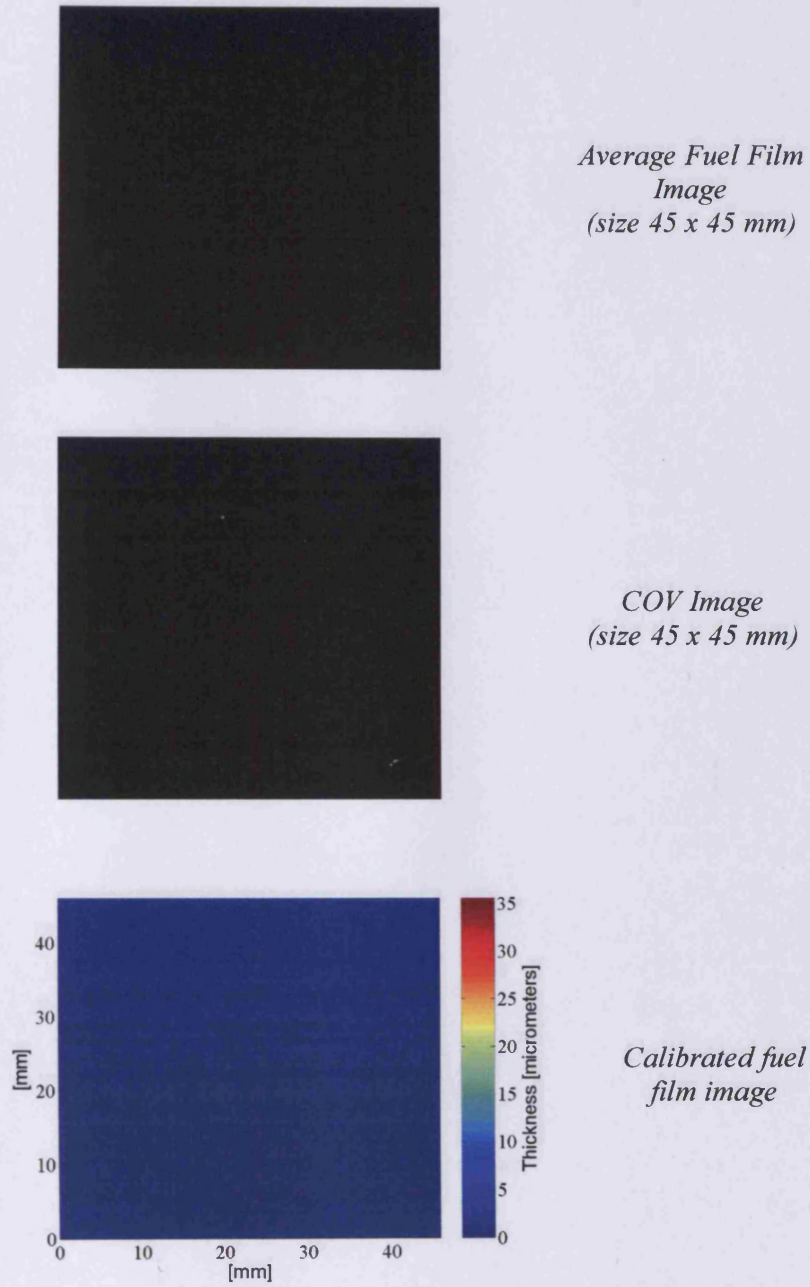


## Appendix B: Transient Fuel Film Measurements for Case B

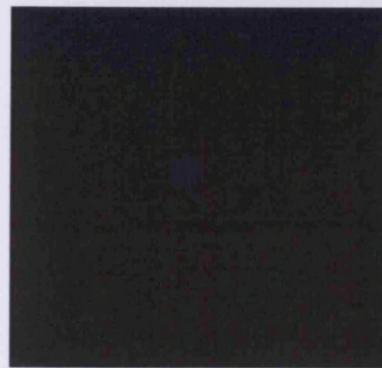
This Appendix shows a full set of fuel film TIR-LIF measurements for Case B. The experimental conditions for Case B are highlighted in the following table:

Table A-B: Summary of experimental conditions for Case B

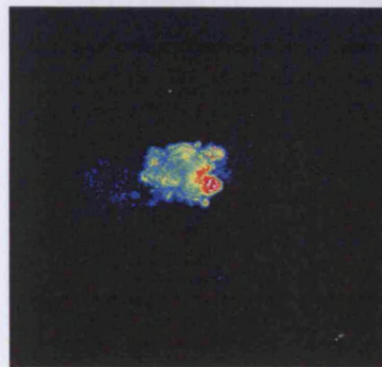
	<i>Case</i>	<i>Ambient Pressure [MPa]</i>	<i>Ambient Temperature [K]</i>
<i>Fuel Film Studies (TIR-LIF)</i>	<i>A</i>	<i>0.1</i>	<i>293</i>
	<i>B</i>	<i>0.4</i>	<i>293</i>
<i>Vapour Fraction Studies (LIEF)</i>	<i>1</i>	<i>0.14</i>	<i>423</i>
	<i>2</i>	<i>0.58</i>	<i>423</i>
	<i>3</i>	<i>0.10</i>	<i>373</i>



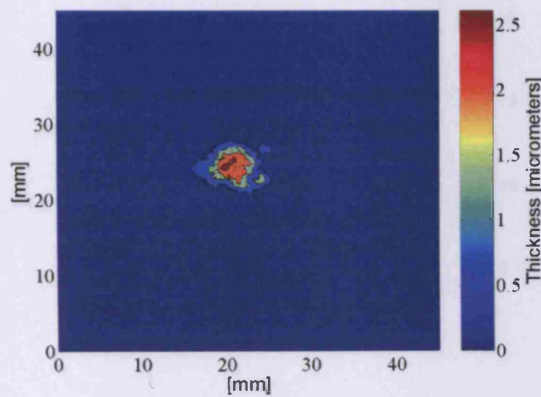
*Figure B1: Fuel film thickness measurements for Case B at 1.00 ms after start of injection*



*Average Fuel Film  
Image  
(size 45 x 45 mm)*

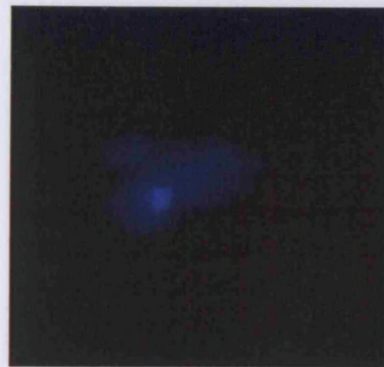


*COV Image  
(size 45 x 45 mm)*

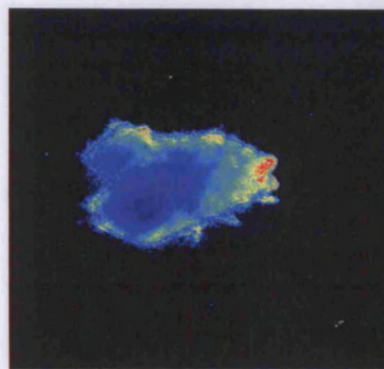


*Calibrated fuel  
film image*

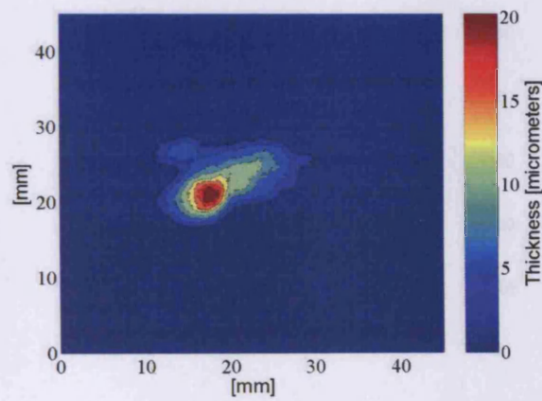
**Figure B2:** Fuel film thickness measurements for Case B at 1.25 ms after start of injection



*Average Fuel Film  
Image  
(size 45 x 45 mm)*



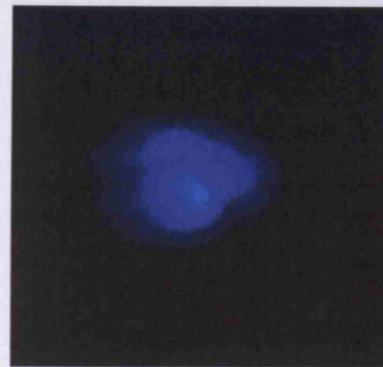
*COV Image  
(size 45 x 45 mm)*



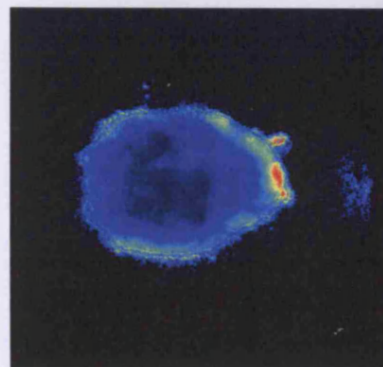
*Calibrated fuel  
film image*

**Figure B3:** Fuel film thickness measurements for Case B at 1.50 ms after start of injection

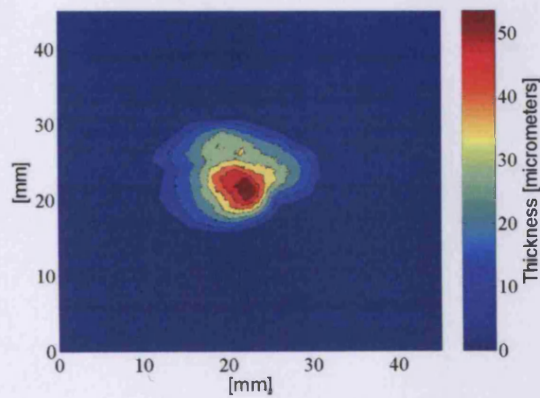




*Average Fuel Film  
Image  
(size 45 x 45 mm)*



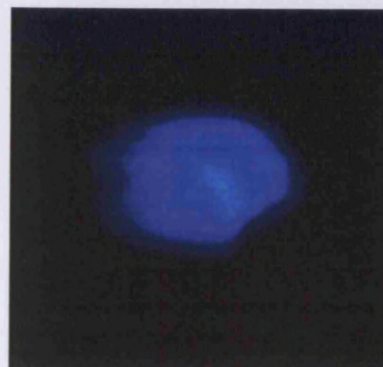
*COV Image  
(size 45 x 45 mm)*



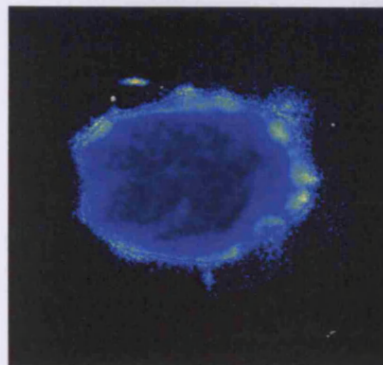
*Calibrated fuel  
film image*

**Figure B4:** Fuel film thickness measurements for Case B at 1.75 ms after start of injection

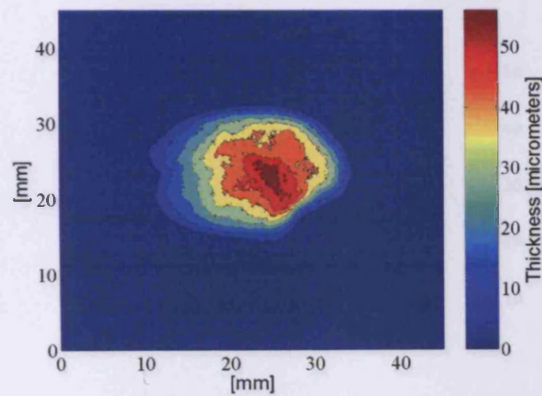




*Average Fuel Film  
Image  
(size 45 x 45 mm)*

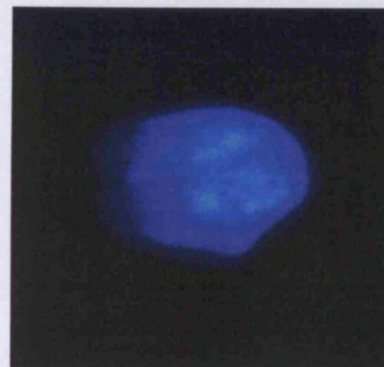


*COV Image  
(size 45 x 45 mm)*

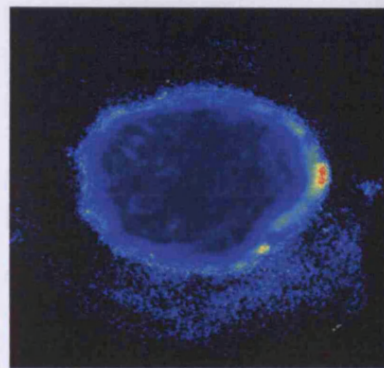


*Calibrated fuel  
film image*

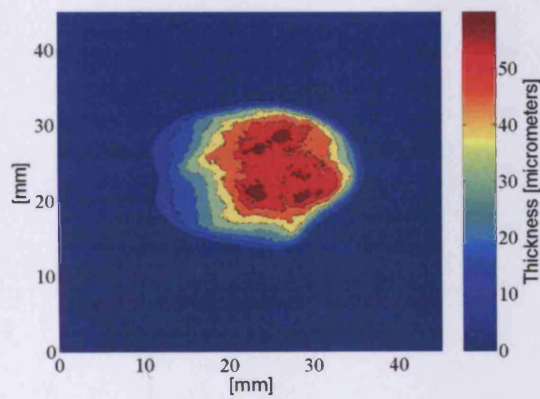
**Figure B5:** Fuel film thickness measurements for Case B at 2.00 ms after start of injection



*Average Fuel Film  
Image  
(size 45 x 45 mm)*

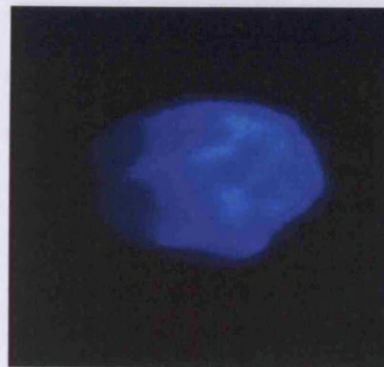


*COV Image  
(size 45 x 45 mm)*

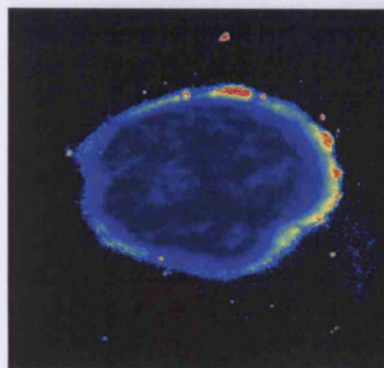


*Calibrated fuel  
film image*

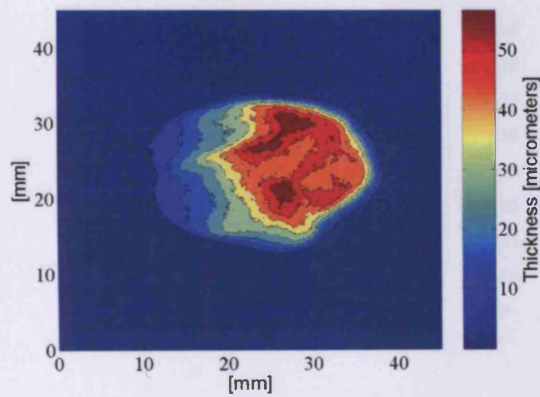
**Figure B6:** Fuel film thickness measurements for Case B at 2.25 ms after start of injection



*Average Fuel Film  
Image  
(size 45 x 45 mm)*



*COV Image  
(size 45 x 45 mm)*



*Calibrated fuel  
film image*

**Figure B7:** Fuel film thickness measurements for Case B at 2.50 ms after start of injection

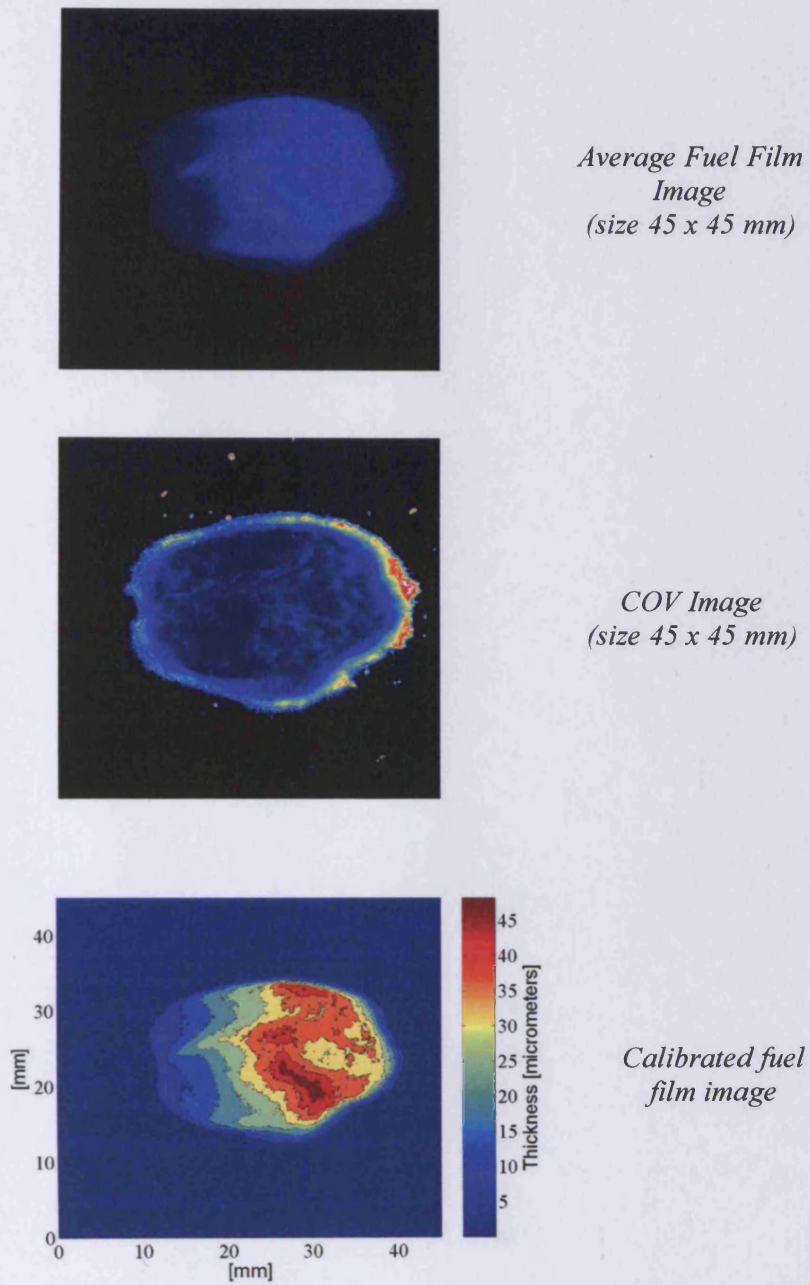
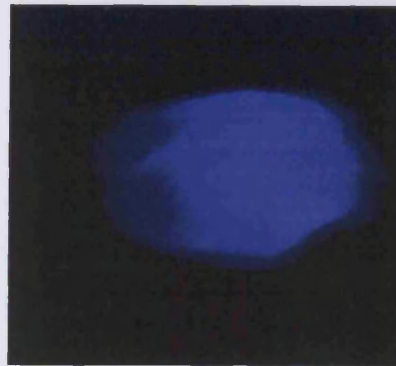
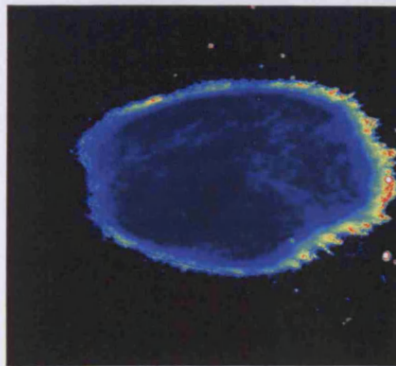


**Figure B8:** Fuel film thickness measurements for Case B at 3.00 ms after start of injection

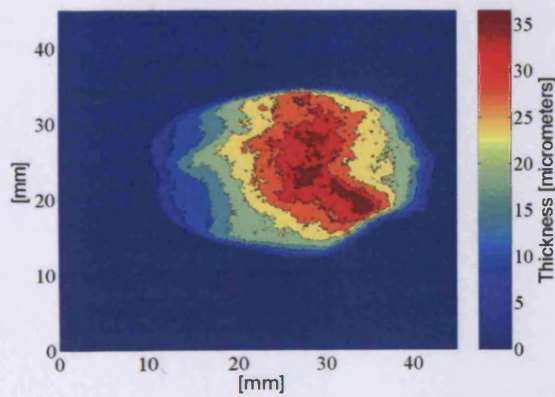




*Average Fuel Film  
Image  
(size 45 x 45 mm)*



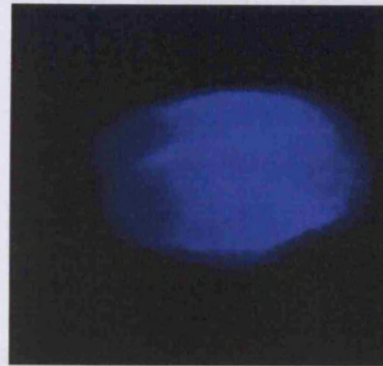
*COV Image  
(size 45 x 45 mm)*



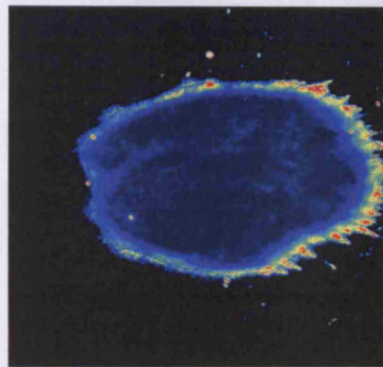
*Calibrated fuel  
film image*

**Figure B9:** Fuel film thickness measurements for Case B at 4.00 ms after start of injection

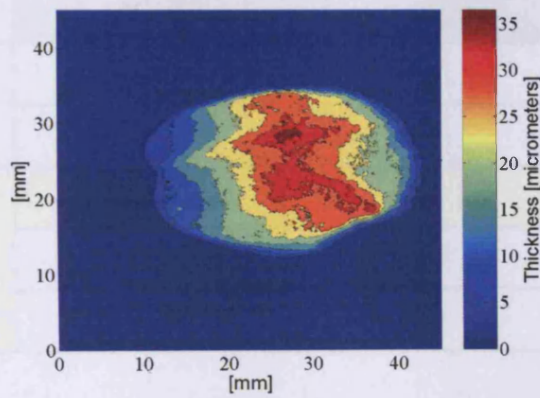




*Average Fuel Film Image  
(size 45 x 45 mm)*



*COV Image  
(size 45 x 45 mm)*



*Calibrated fuel film image*

**Figure B10:** Fuel film thickness measurements for Case B at 5.00 ms after start of injection

## Appendix C: Transient Vapour Concentration Measurements for Case 1

This Appendix shows a full set of vapour concentration LIEF measurements for Case 1. The experimental conditions for Case 1 are highlighted in the following table:

Table A-C: Summary of experimental conditions for Case 1

	<i>Case</i>	<i>Ambient Pressure [MPa]</i>	<i>Ambient Temperature [K]</i>
<i>Fuel Film Studies (TIR-LIF)</i>	<i>A</i>	<i>0.1</i>	<i>293</i>
	<i>B</i>	<i>0.4</i>	<i>293</i>
<i>Vapour Fraction Studies (LIEF)</i>	<i>1</i>	<i>0.14</i>	<i>423</i>
	<i>2</i>	<i>0.58</i>	<i>423</i>
	<i>3</i>	<i>0.10</i>	<i>373</i>

Figure C1: Vapour concentration measurements for Case 1 at 7.06 ms after start of injection (image taken from instantaneous image)

Appendix C: Transient Vapour Concentration Measurements for Case 1

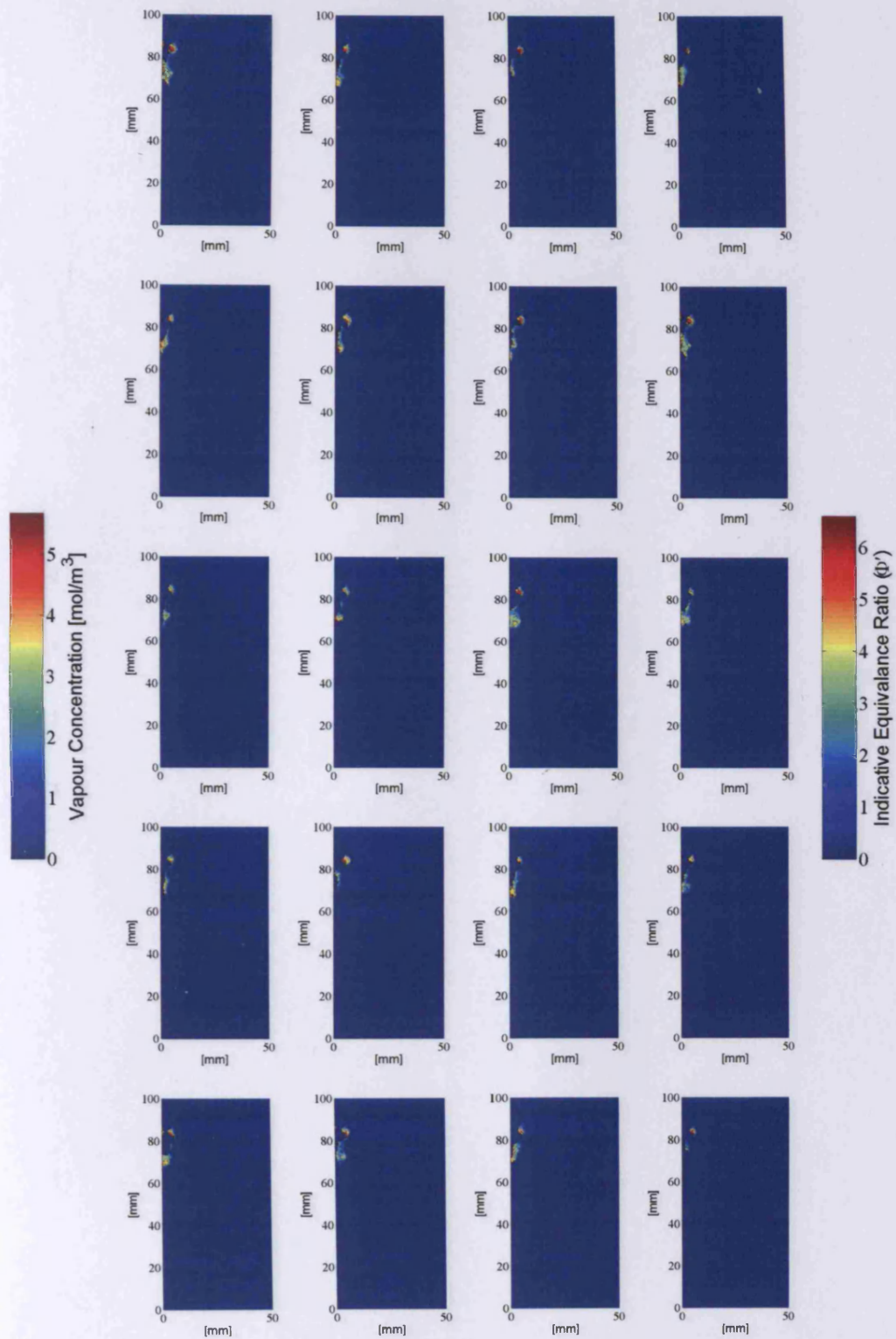
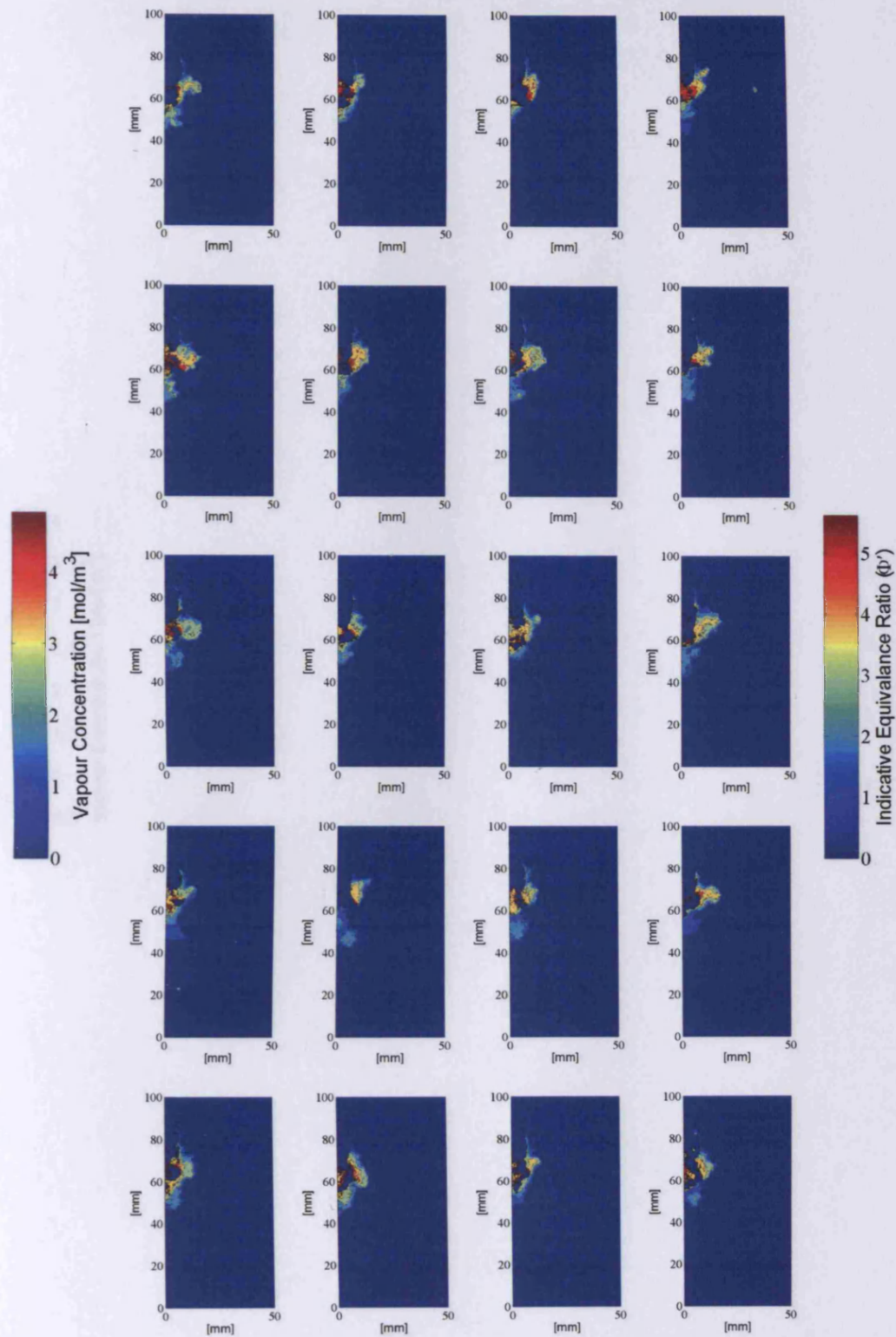


Figure C1: Vapour concentration measurements for Case 1 at 1.00 ms after start of injection (measurements from instantaneous images)





*Figure C2: Vapour concentration measurements for Case 1 at 1.50 ms after start of injection (measurements from instantaneous images)*

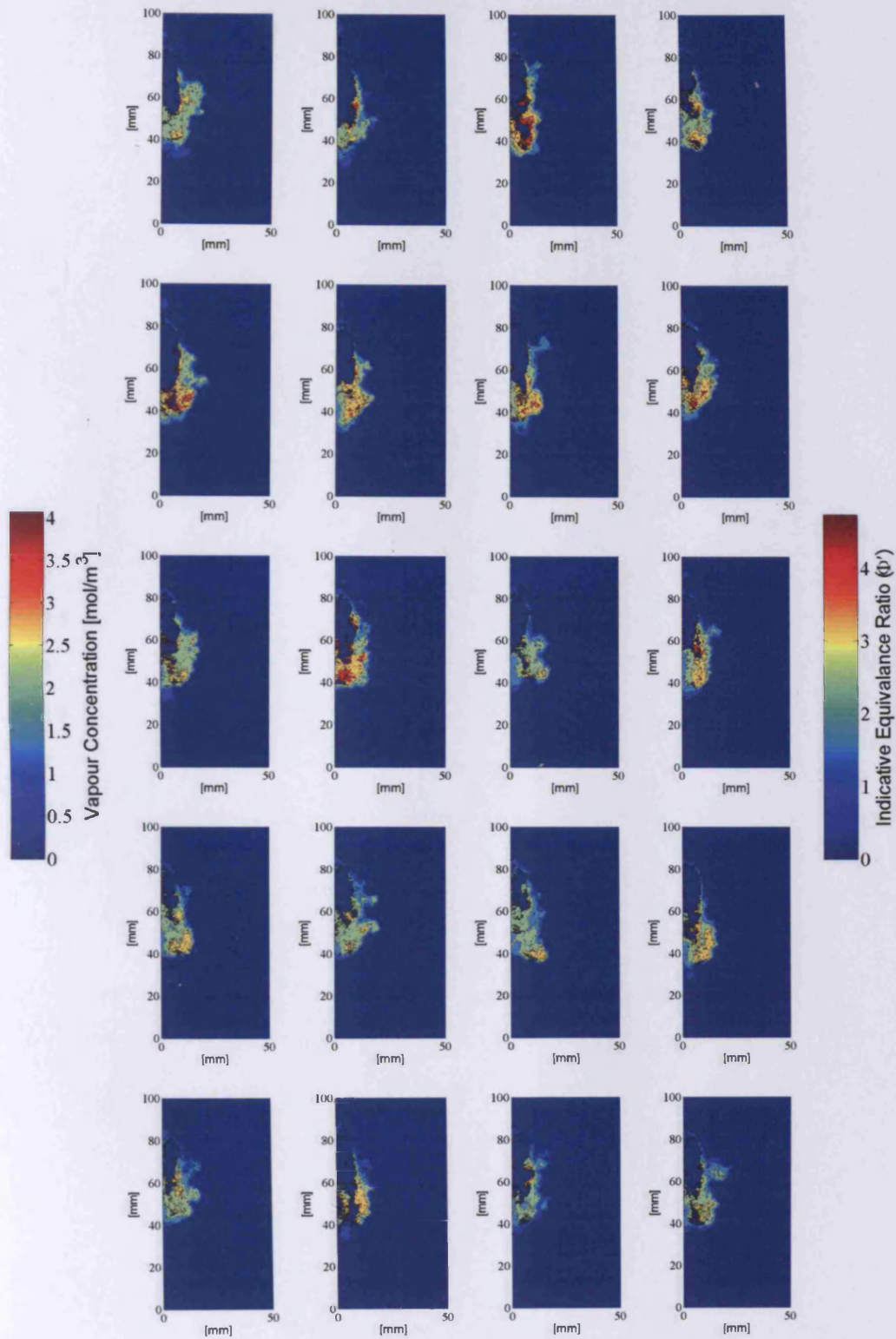
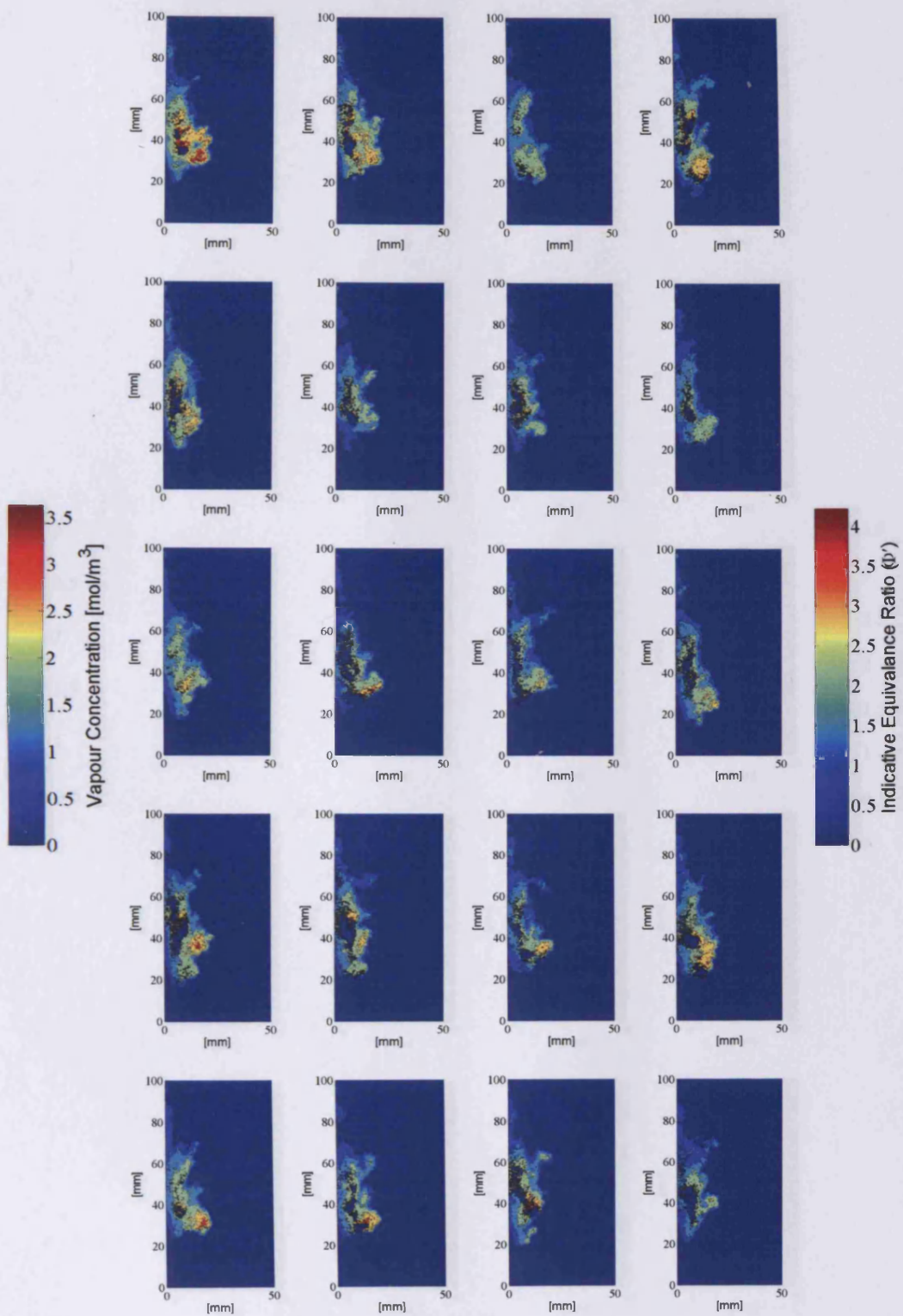


Figure C3: Vapour concentration measurements for Case 1 at 2.00 ms after start of injection (measurements from instantaneous images)



Appendix C: Transient Vapour Concentration Measurements for Case 1



**Figure C4:** Vapour concentration measurements for Case 1 at 2.50 ms after start of injection (measurements from instantaneous images)

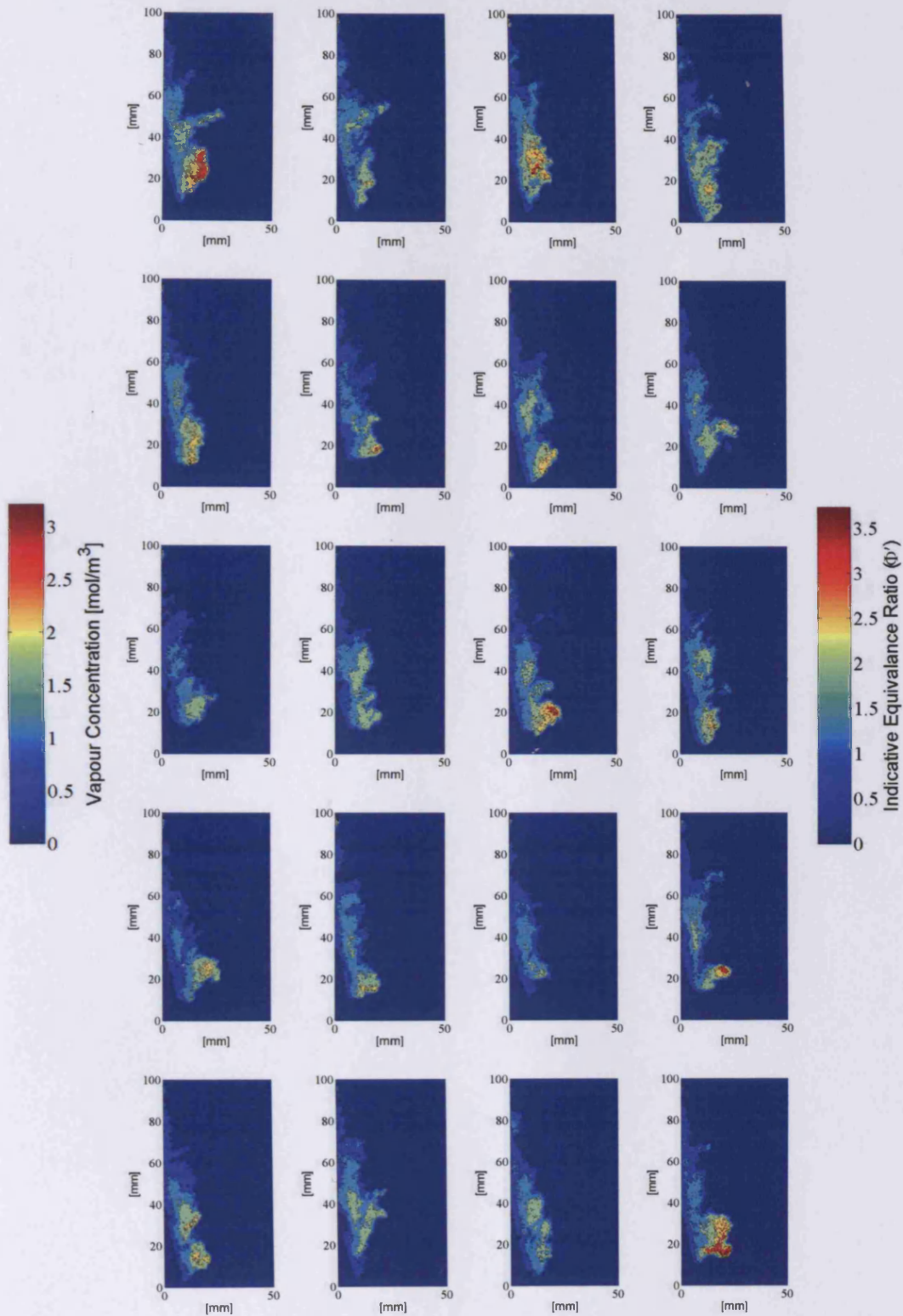


**Figure C5:** Vapour concentration measurements for Case 1 at 3.00 ms after start of injection (measurements from instantaneous images)

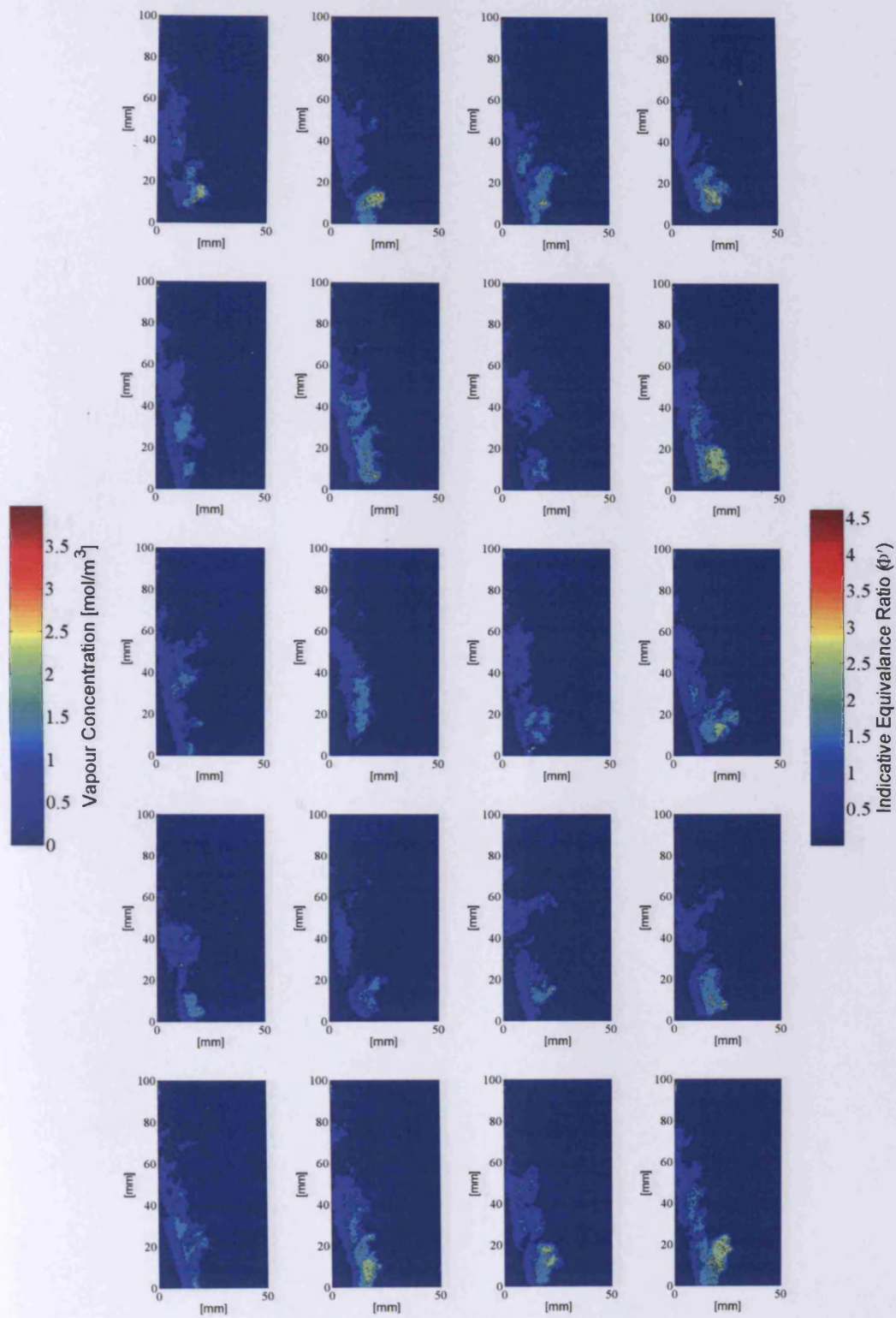


Figure C6: Vapour concentration measurements for Case 1 at 3.50 ms after start of injection (measurements from instantaneous images)



Appendix C: Transient Vapour Concentration Measurements for Case 1

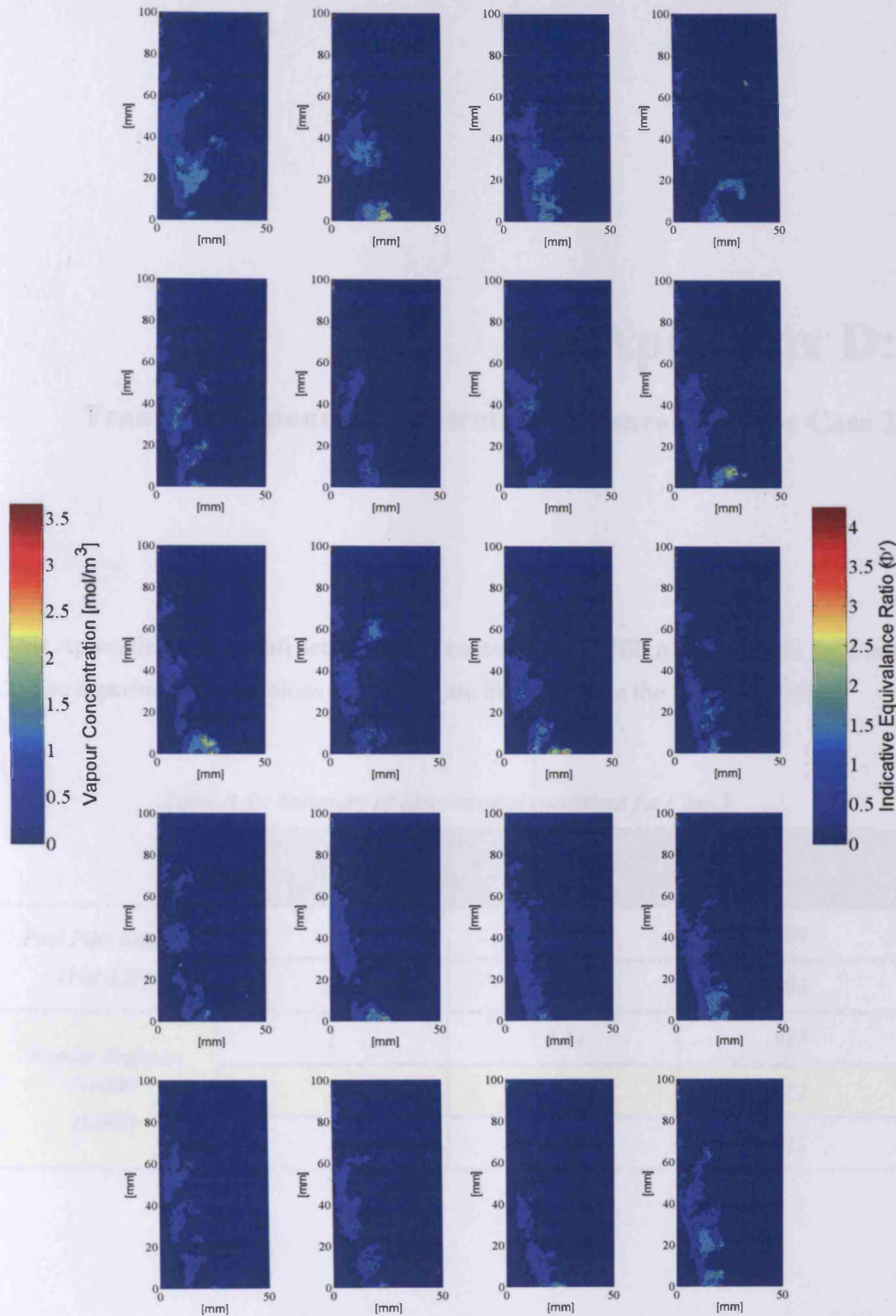


Figure C7: Vapour concentration measurements for Case 1 at 4.00 ms after start of injection (measurements from instantaneous images)

## Appendix D: Transient Vapour Concentration Measurements for Case 2

This Appendix shows a full set of vapour concentration LIEF measurements for Case 2. The experimental conditions for Case 2 are highlighted in the following table:

Table A-D: Summary of experimental conditions for Case 2

	<i>Case</i>	<i>Ambient Pressure [MPa]</i>	<i>Ambient Temperature [K]</i>
<i>Fuel Film Studies (TIR-LIF)</i>	<i>A</i>	<i>0.1</i>	<i>293</i>
	<i>B</i>	<i>0.4</i>	<i>293</i>
<i>Vapour Fraction Studies (LIEF)</i>	<i>1</i>	<i>0.14</i>	<i>423</i>
	<i>2</i>	<i>0.58</i>	<i>423</i>
	<i>3</i>	<i>0.10</i>	<i>373</i>

Figure D1: Vapour concentration measurements for Case 2 at LIEF (fraction of vapour concentration) (see Table A-D for experimental conditions)



Appendix D: Transient Vapour Concentration Measurements for Case 2

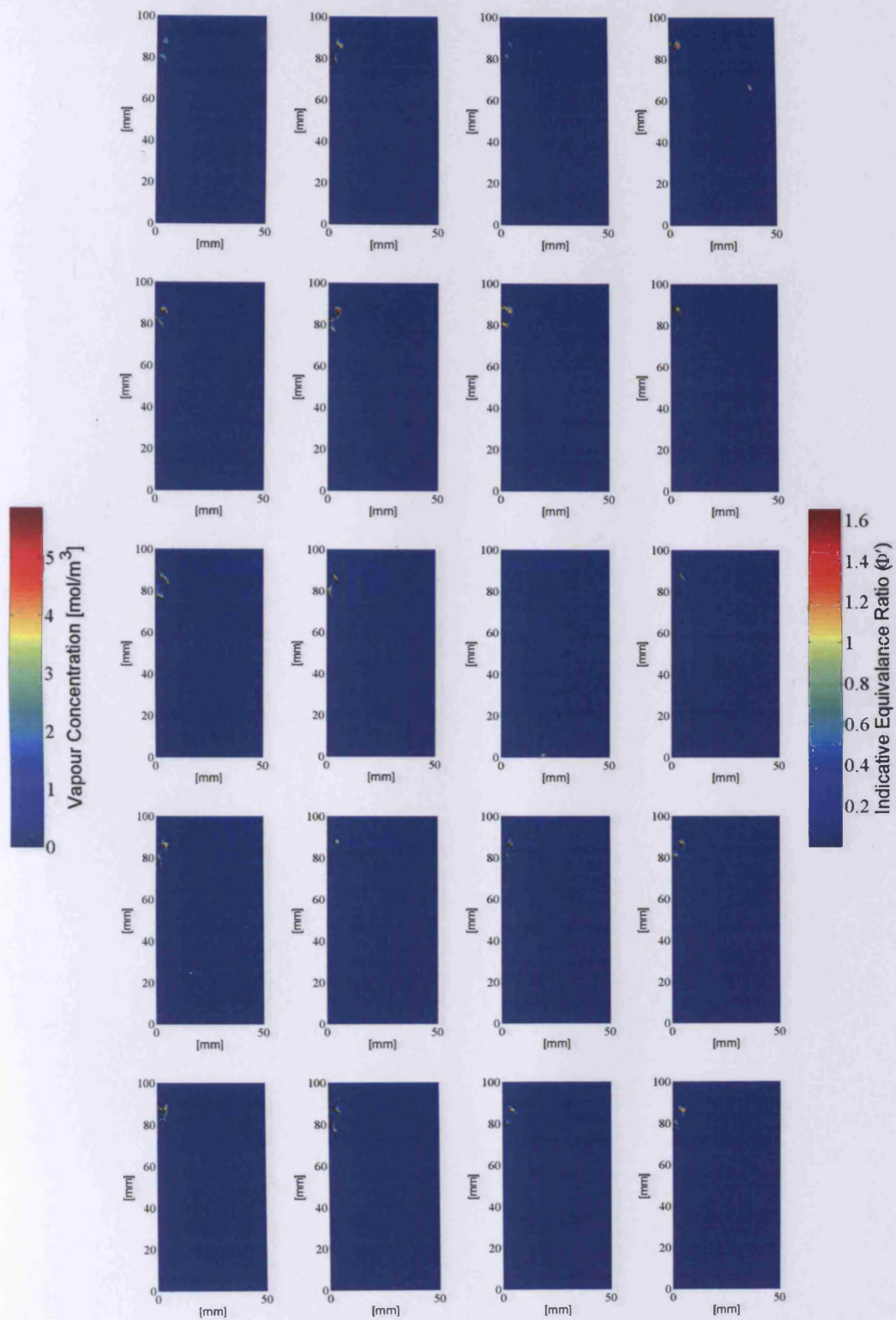


Figure D1: Vapour concentration measurements for Case 2 at 1.00 ms after start of injection (measurements from instantaneous images)

Appendix D: Transient Vapour Concentration Measurements for Case 2

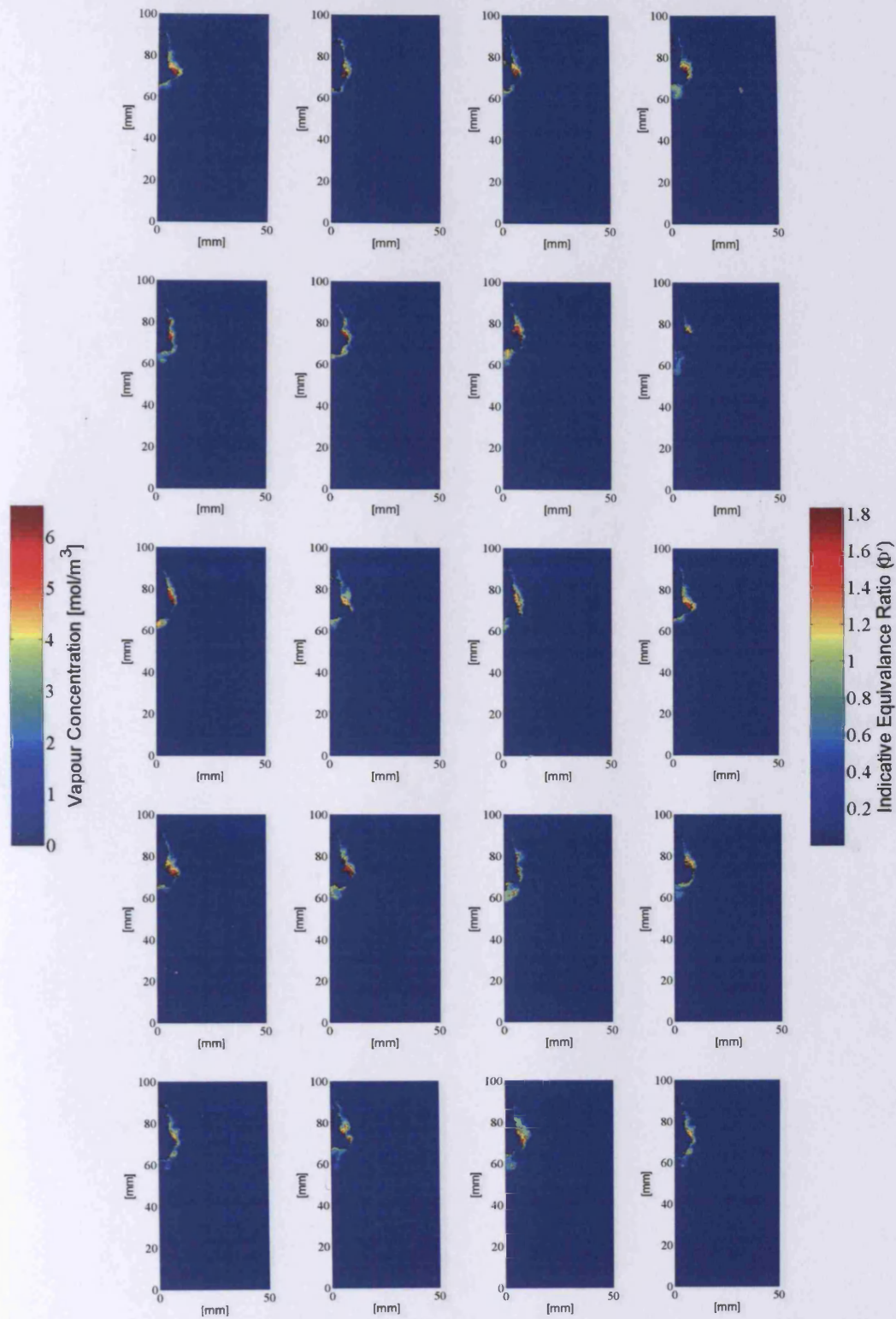
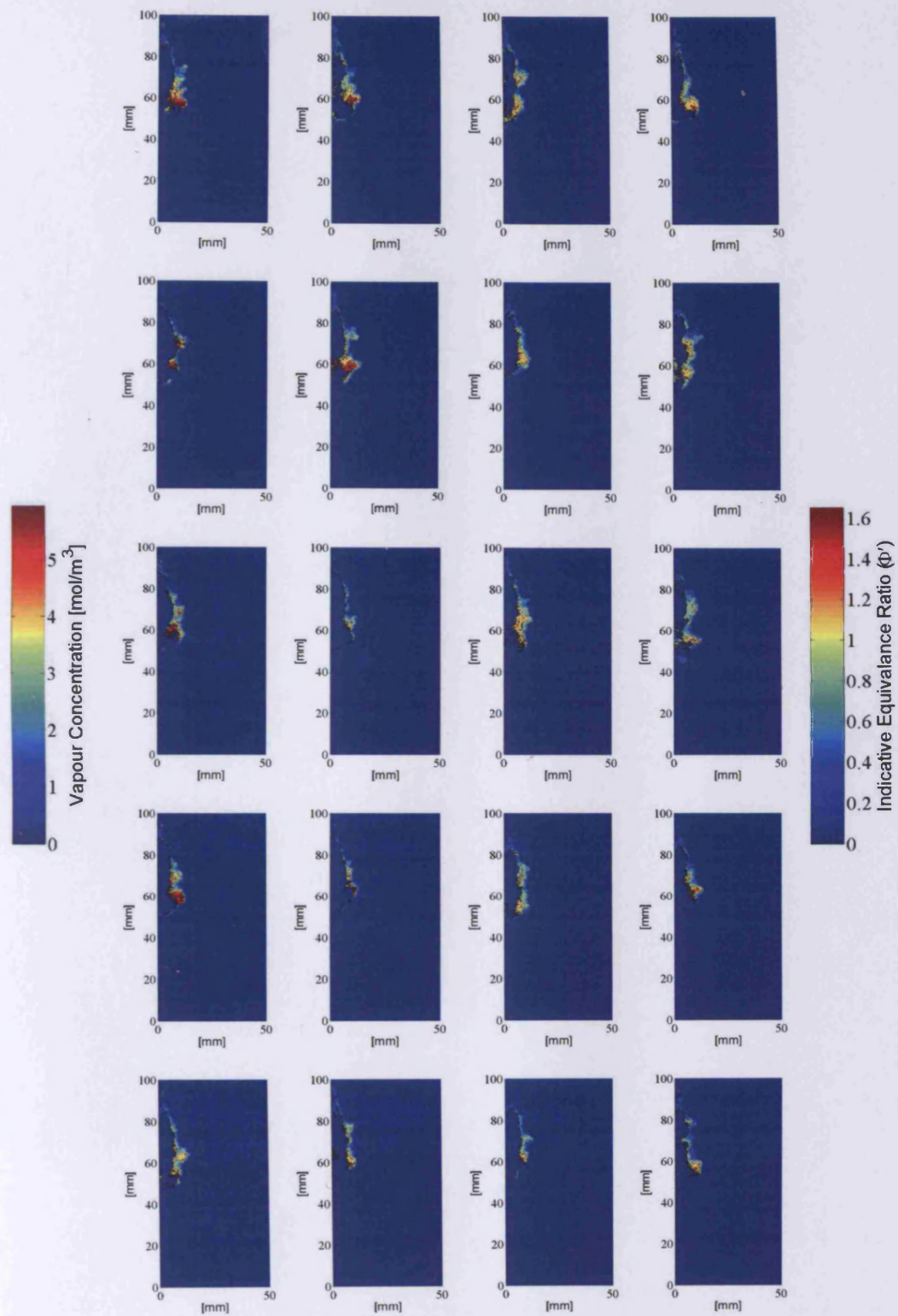


Figure D2: Vapour concentration measurements for Case 2 at 1.50 ms after start of injection (measurements from instantaneous images)

Appendix D: Transient Vapour Concentration Measurements for Case 2



*Figure D3: Vapour concentration measurements for Case 2 at 2.00 ms after start of injection (measurements from instantaneous images)*



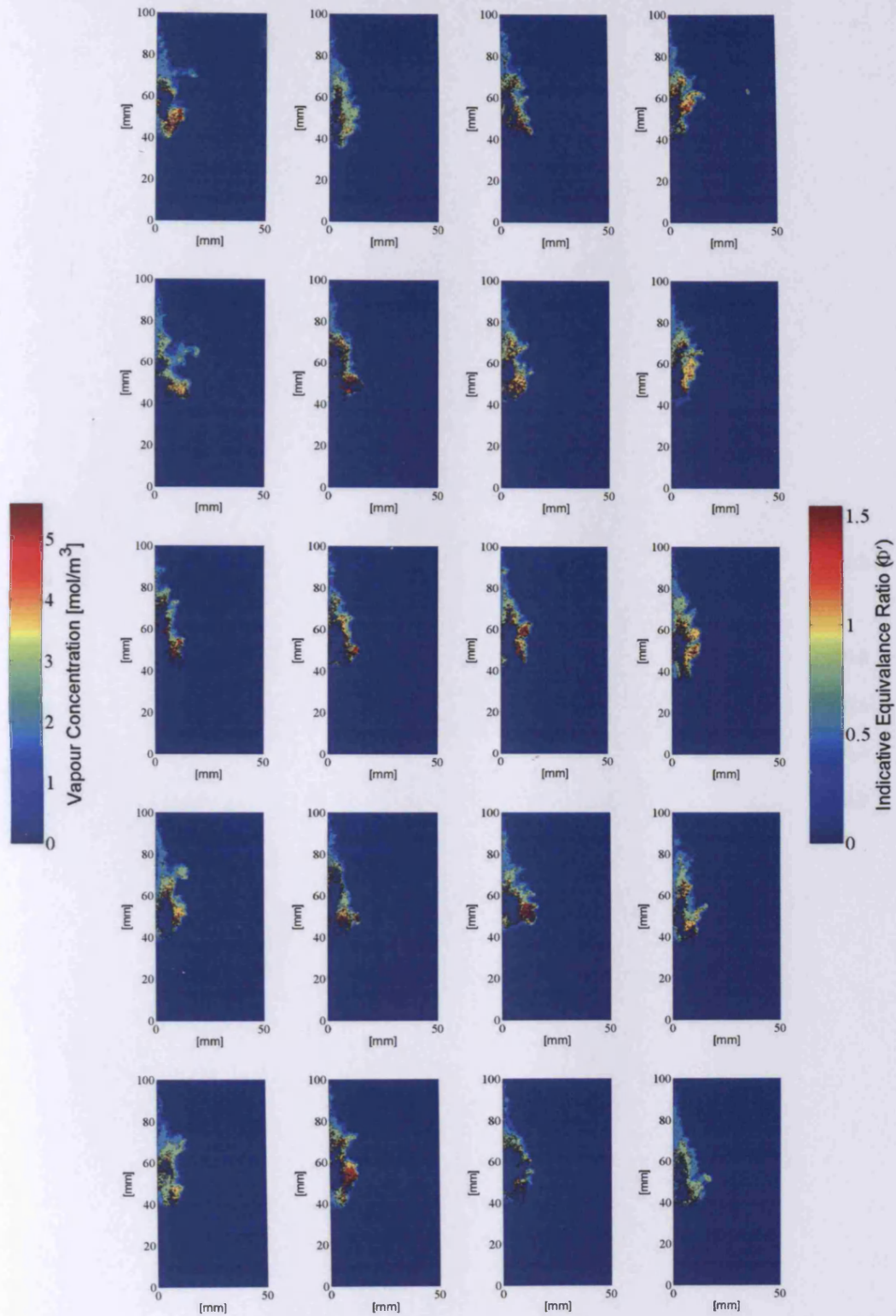


*Figure D4: Vapour concentration measurements for Case 2 at 2.50 ms after start of injection (measurements from instantaneous images)*

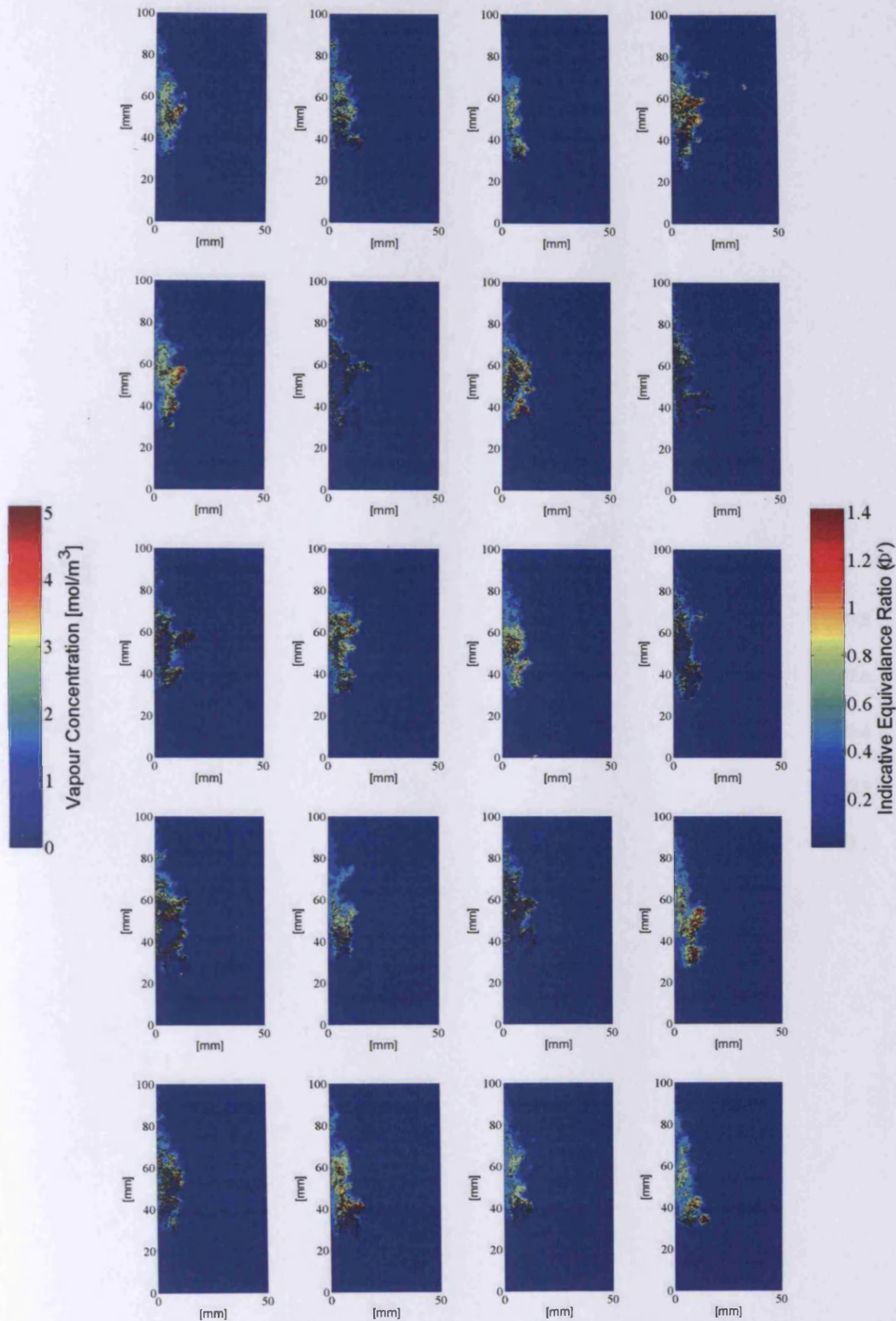
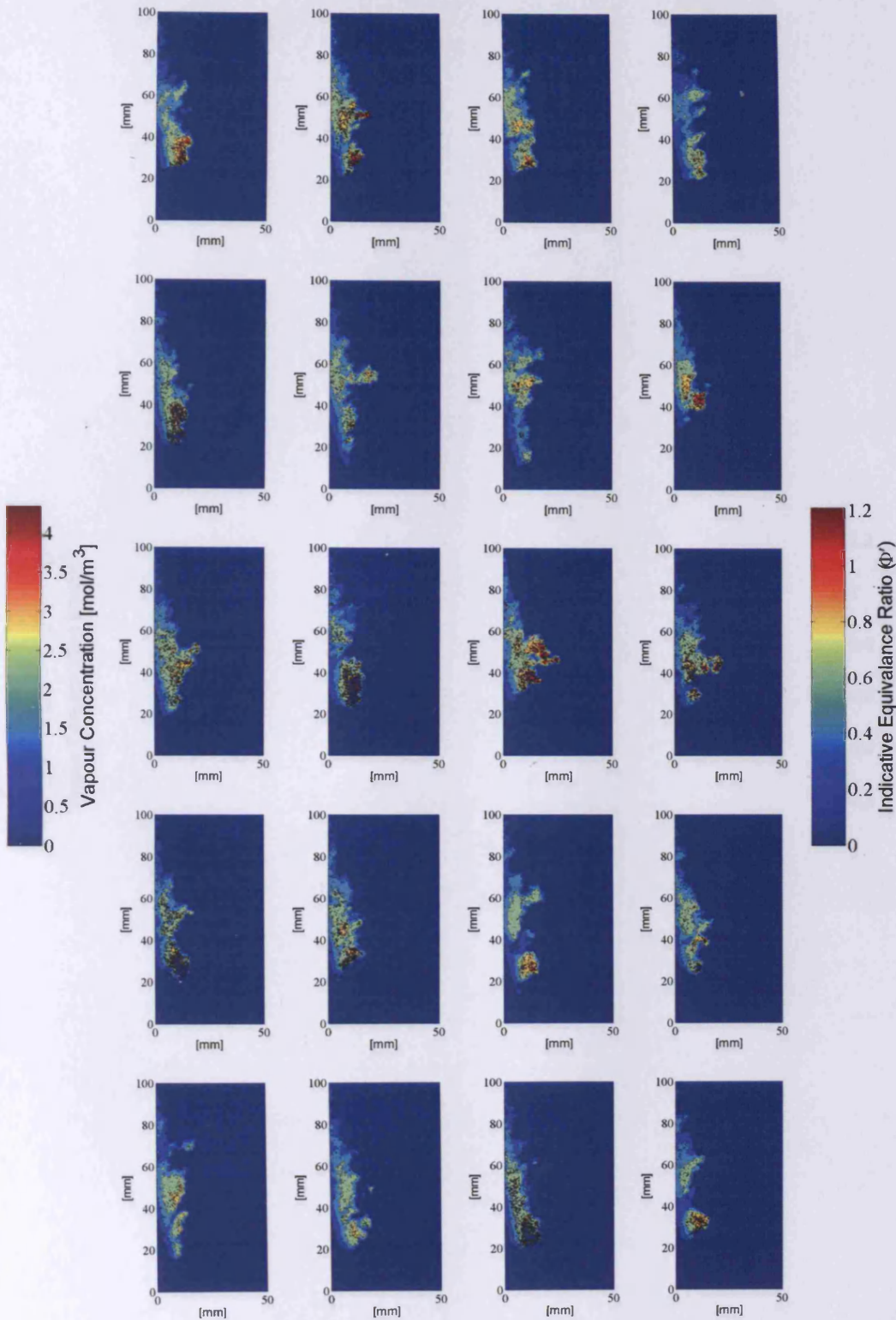


Figure D5: Vapour concentration measurements for Case 2 at 3.00 ms after start of injection (measurements from instantaneous images)





**Figure D6:** Vapour concentration measurements for Case 2 at 3.50 ms after start of injection (measurements from instantaneous images)

Appendix D: Transient Vapour Concentration Measurements for Case 2

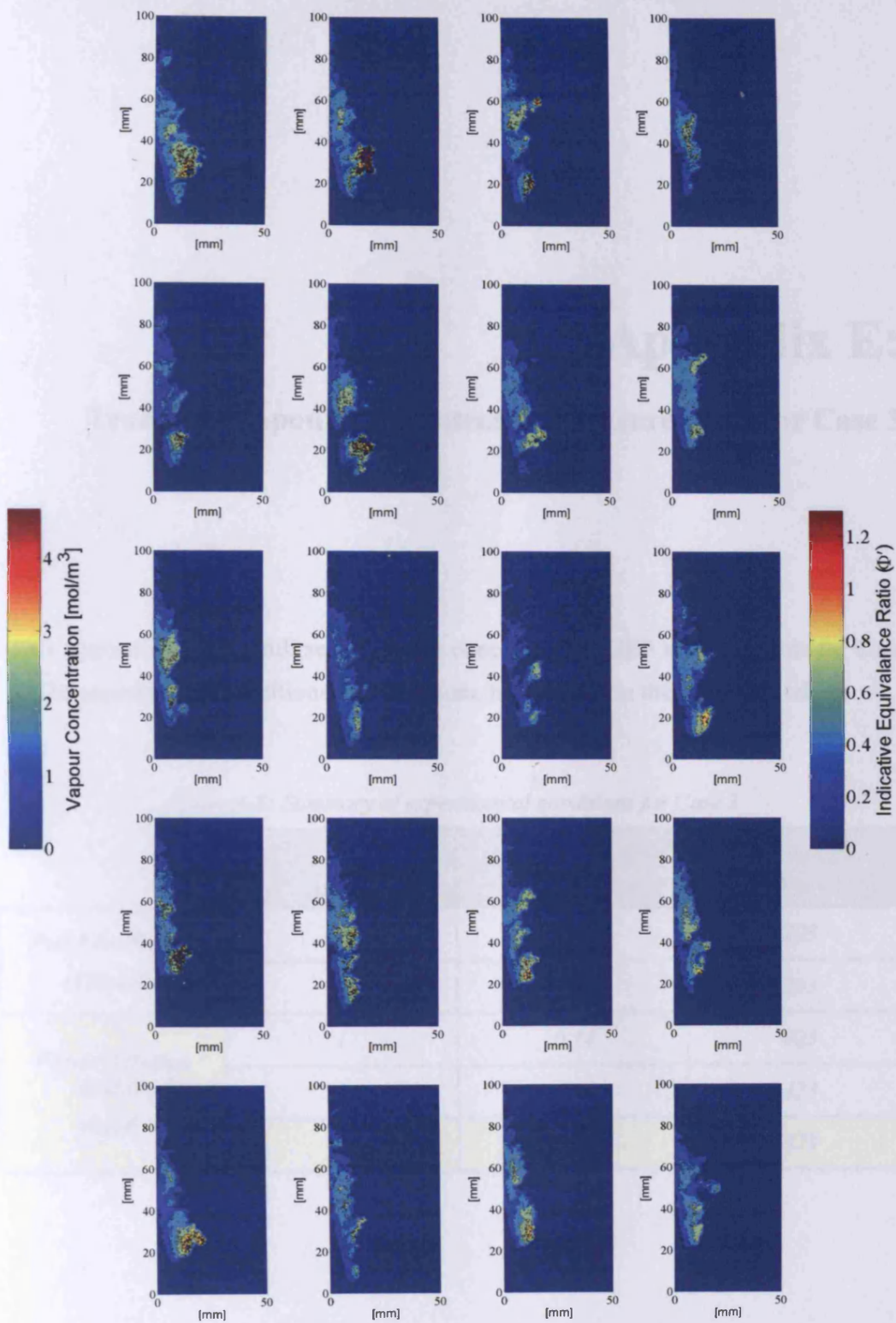


Figure D7: Vapour concentration measurements for Case 2 at 4.00 ms after start of injection (measurements from instantaneous images)

## Appendix E:

### Transient Vapour Concentration Measurements for Case 3

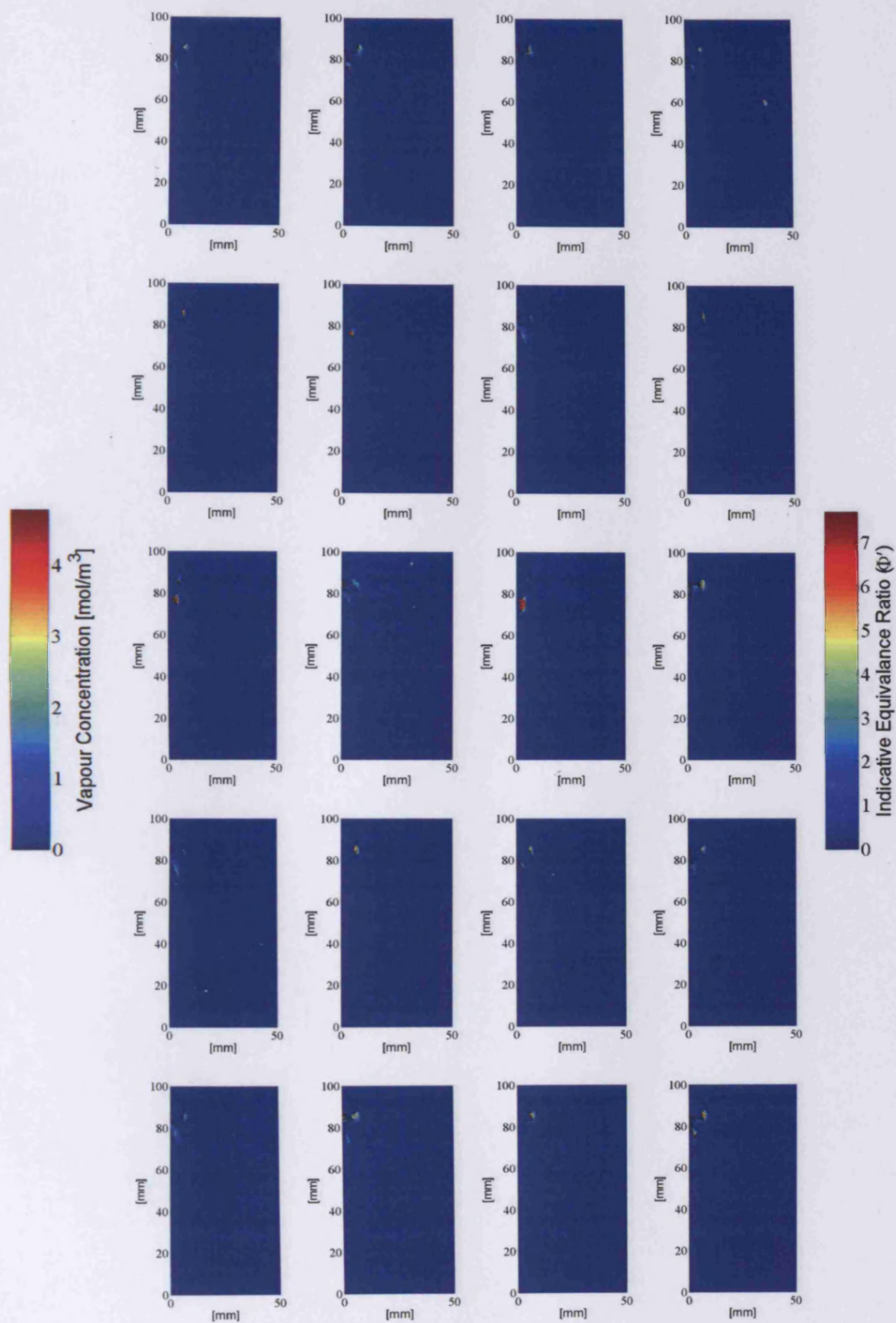
This Appendix shows a full set of vapour concentration LIEF measurements for Case 3. The experimental conditions for Case 3 are highlighted in the following table:

Table A-E: Summary of experimental conditions for Case 3

	<i>Case</i>	<i>Ambient Pressure [MPa]</i>	<i>Ambient Temperature [K]</i>
<i>Fuel Film Studies (TIR-LIF)</i>	<i>A</i>	<i>0.1</i>	<i>293</i>
	<i>B</i>	<i>0.4</i>	<i>293</i>
<i>Vapour Fraction Studies (LIEF)</i>	<i>1</i>	<i>0.14</i>	<i>423</i>
	<i>2</i>	<i>0.58</i>	<i>423</i>
	<i>3</i>	<i>0.10</i>	<i>373</i>



## Appendix E: Transient Vapour Concentration Measurements for Case 3



**Figure E1:** Vapour concentration measurements for Case 3 at 1.00 ms after start of injection (measurements from instantaneous images)

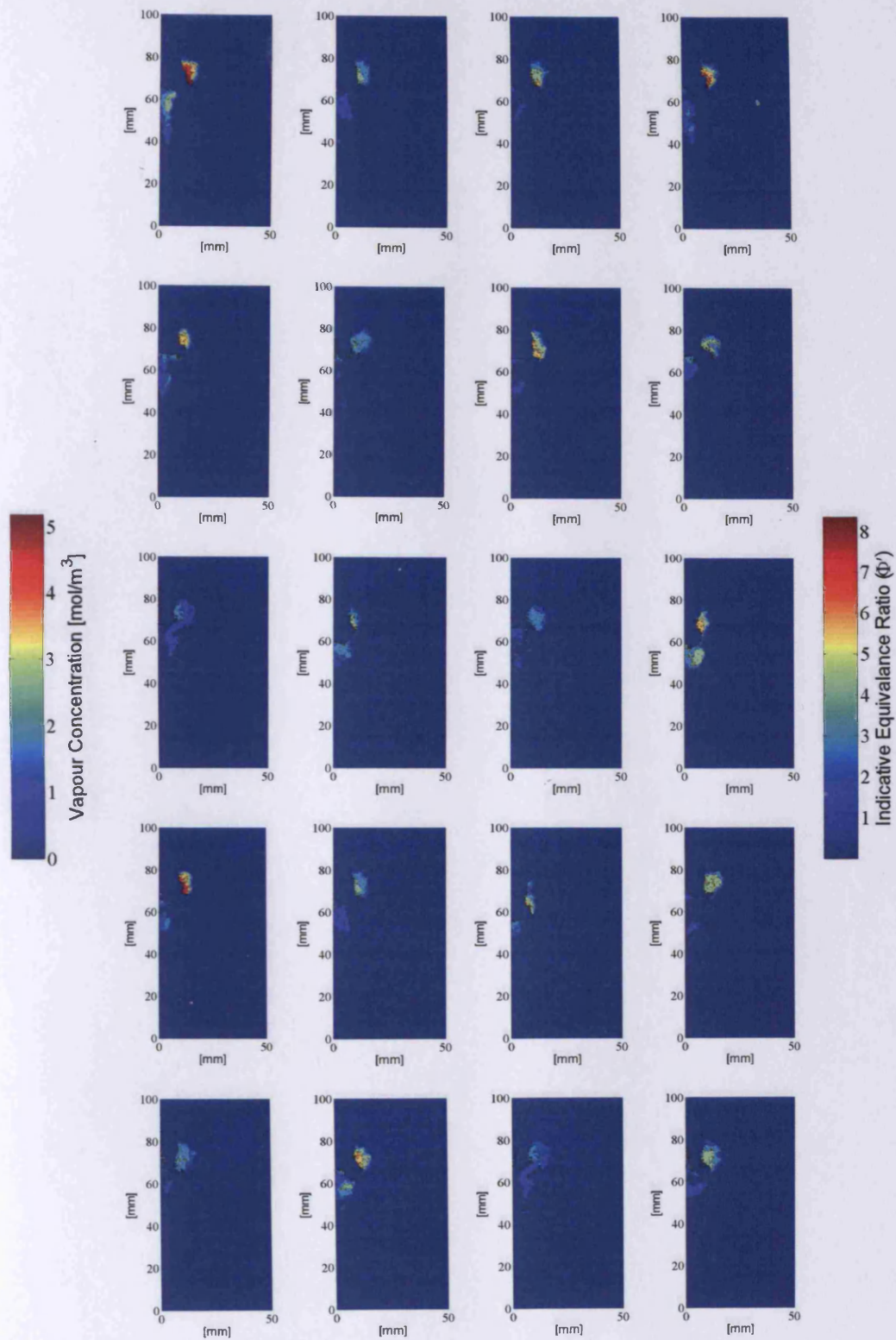


*Figure E2: Vapour concentration measurements for Case 3 at 1.50 ms after start of injection (measurements from instantaneous images)*



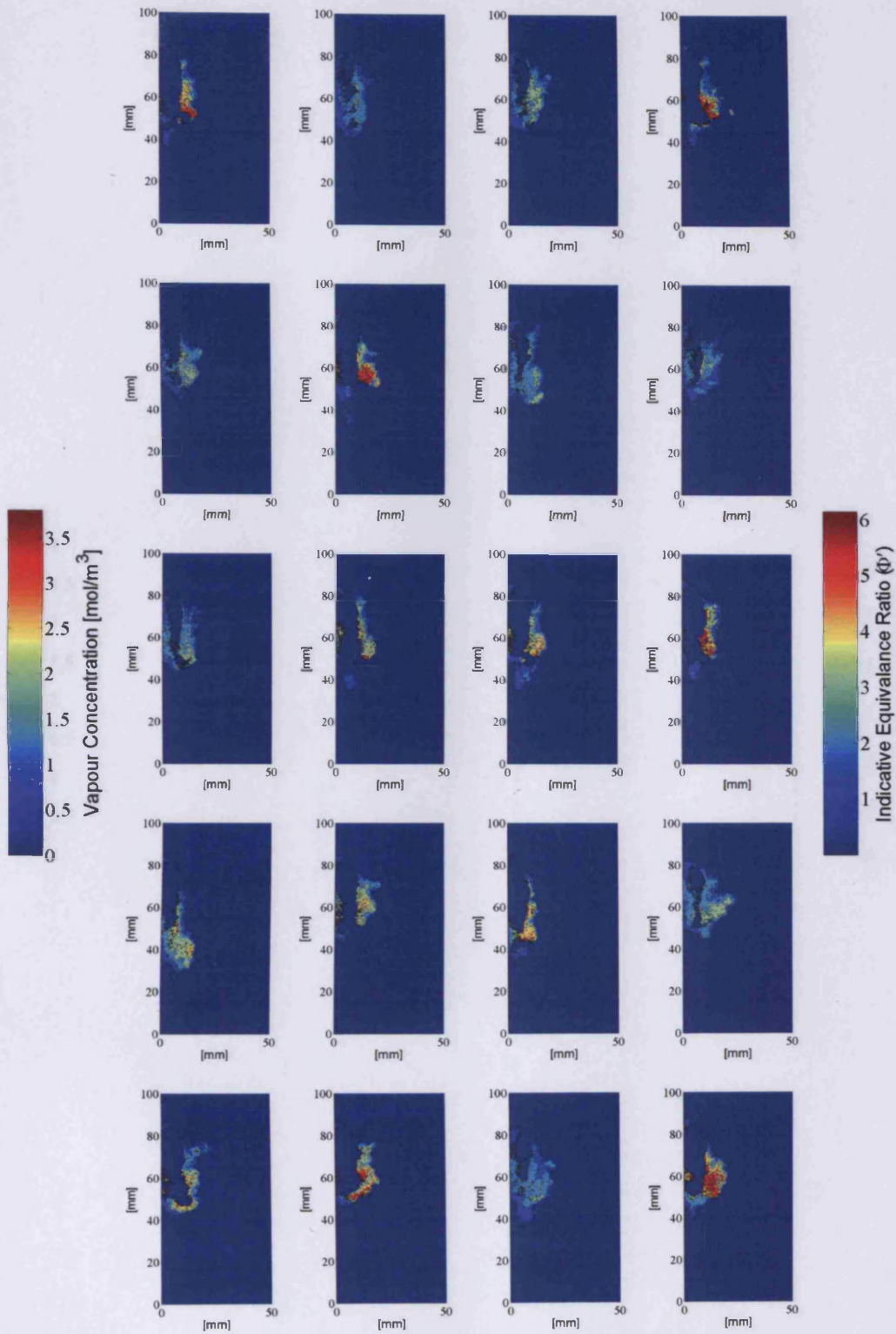


**Figure E3:** Vapour concentration measurements for Case 3 at 2.00 ms after start of injection (measurements from instantaneous images)

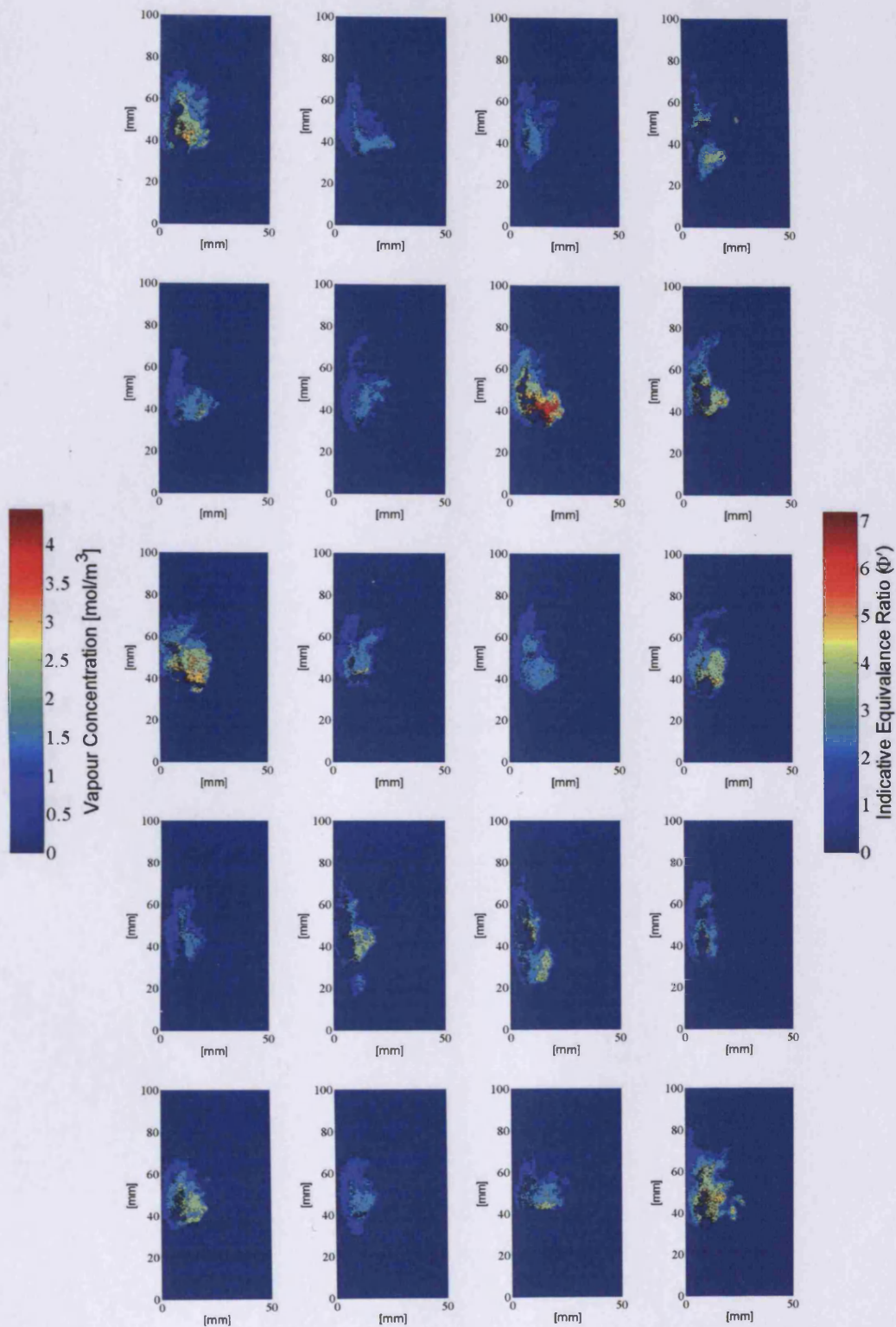


Figure E4: Vapour concentration measurements for Case 3 at 2.50 ms after start of injection (measurements from instantaneous images)

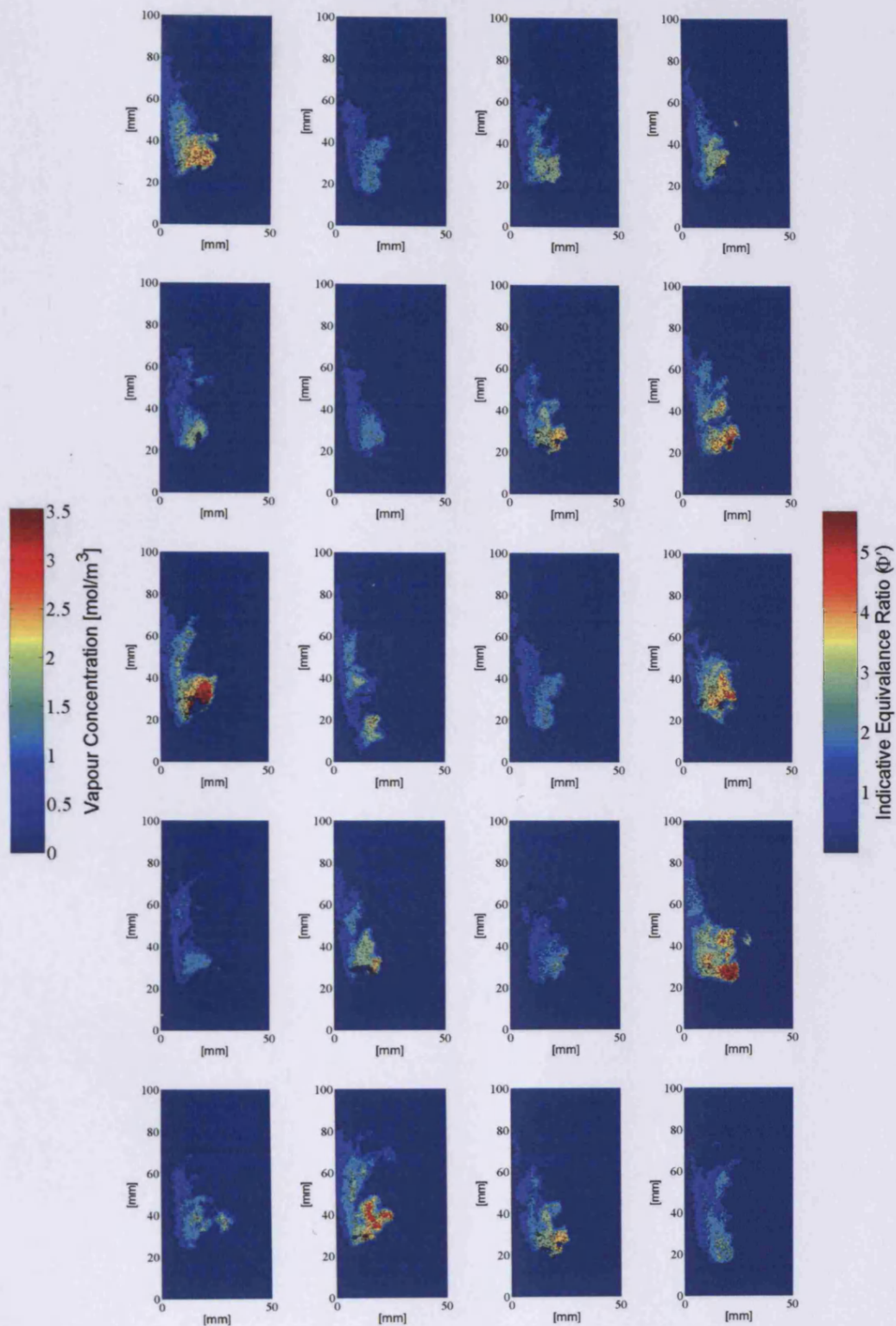


Figure E5: Vapour concentration measurements for Case 3 at 3.00 ms after start of injection (measurements from instantaneous images)



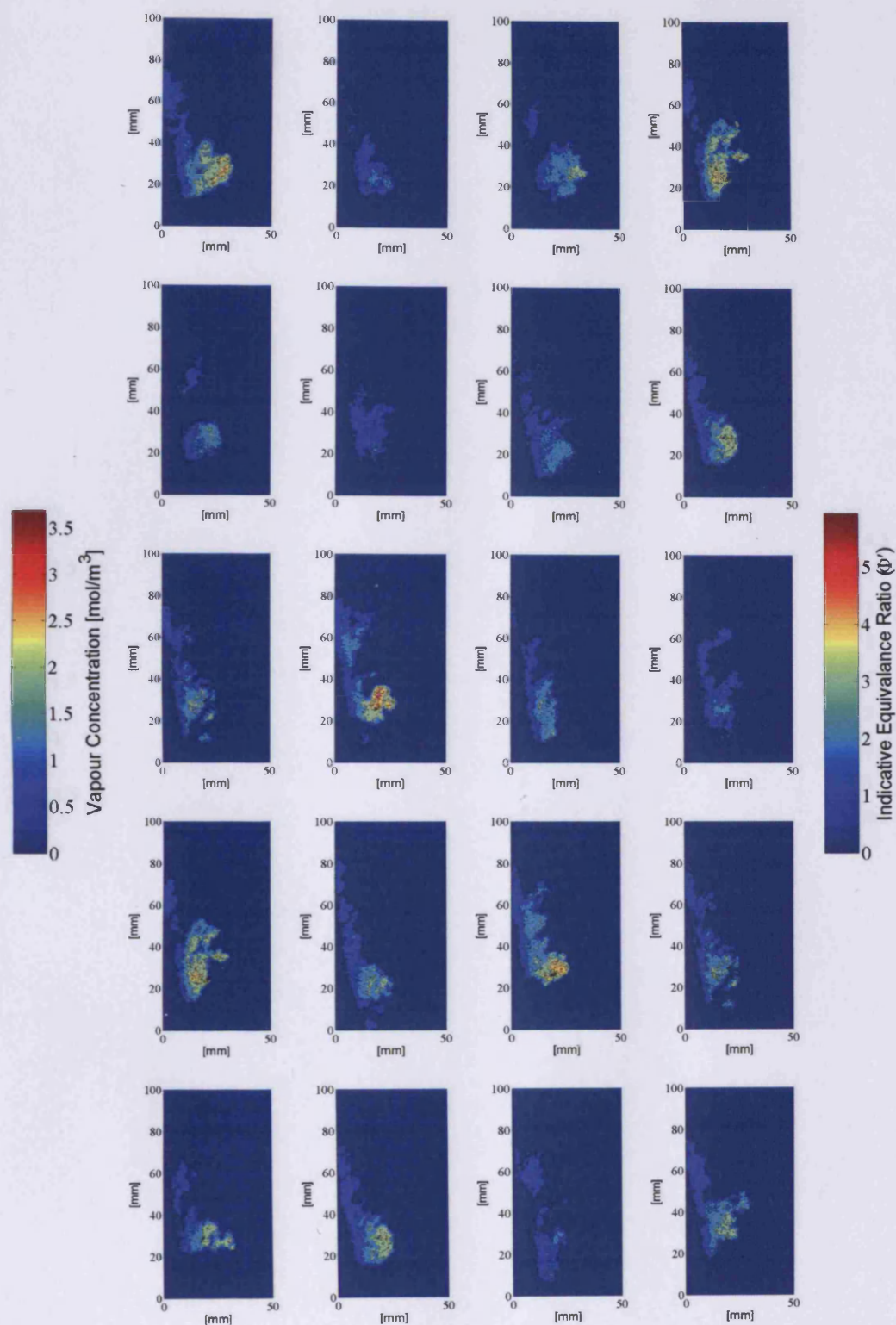


Figure E6: Vapour concentration measurements for Case 3 at 3.50 ms after start of injection (measurements from instantaneous images)

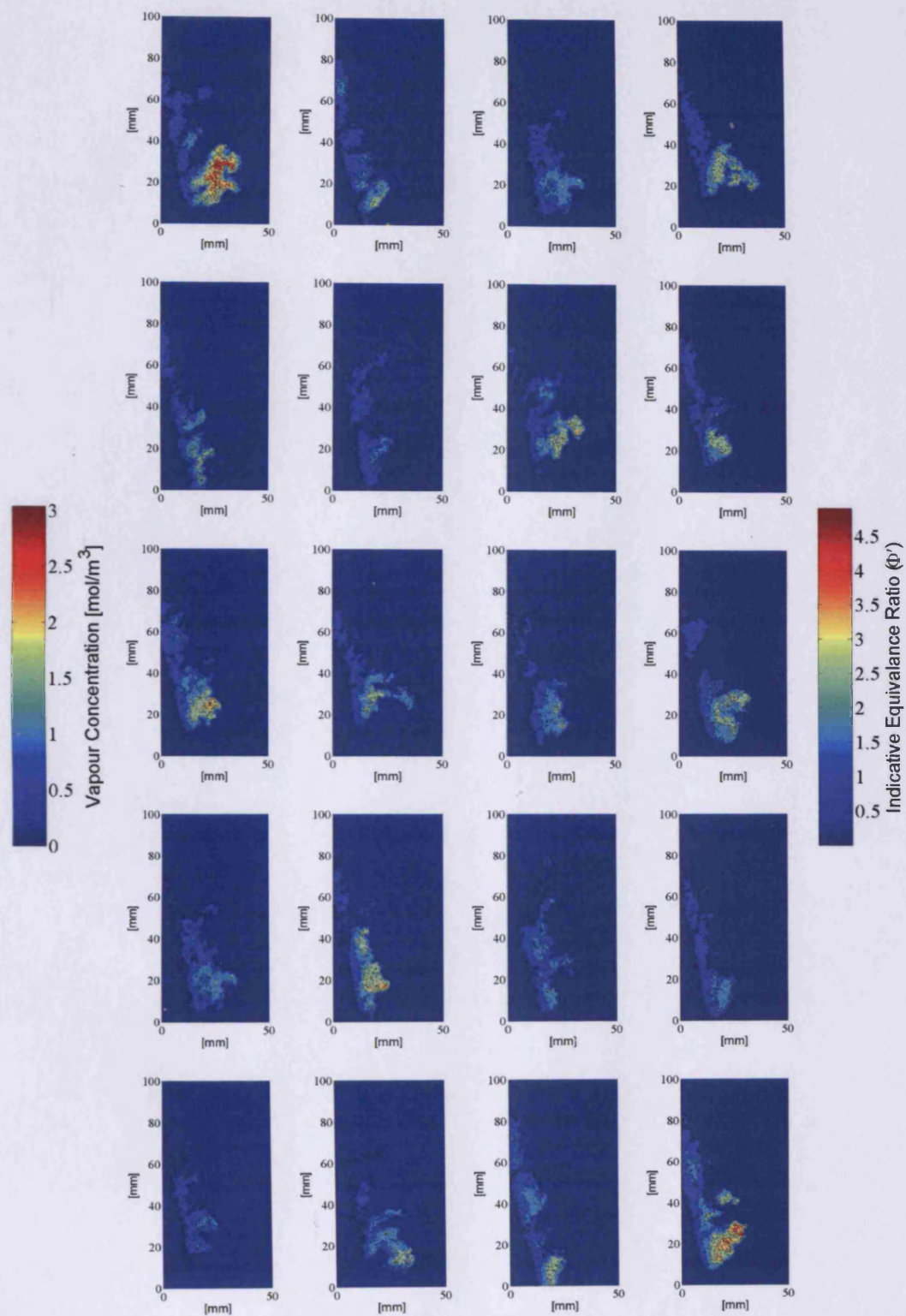


Figure E7: Vapour concentration measurements for Case 3 at 4.00 ms after start of injection (measurements from instantaneous images)

